IMPROVING SEISMIC FOUNDATION MODELS OF JACK-UPS

ERIK EMONDT

TU Delft

TU Delft

Improving seismic foundation models of jack-ups

Author:
Erik Emondt

To obtain the degree of Master of Science at the Delft University of Technology.

Student number: 4219031
Project duration: August 1, 2019 – September 30, 2020
Thesis Committee: Prof. Dr. Ir. Andrei V. Metrikine
Dr. Ir. Apostolos Tsouvalas
Ir. Athanasios Tsetas
Dr. Ir. Ronald van der Meulen
Ir. Perry van Uchelen

This thesis is confidential and cannot be made public until October 1st, 2020

Abstract

Jack-up designers, owners and operators are expanding their activities into seismically active areas such as Japan and Taiwan. Further development of expertise in seismic analysis of jack-ups is required to improve safety and reduce costs. At present, a linear elastic foundation model is used in seismic assessments. Improved understanding of foundation behaviour can lead to a significant reduction in conservatism. In this thesis a brief comparison of available foundation models is made. The radiation damping model has been improved, which is found to have minor effect on jack-up response. To capture non-linear foundation behaviour, a hypoplastic macro-element has been implemented in seismic simulation software OpenSees. This results in reduced non-linear resonance and an amplitude-dependent resonance-shift. The modelled loads at critical locations in the structure consistently decrease more than 25% as a result. Plastic displacements and hardening are found to be significant for highly non-linear soils and severe earthquakes. This thesis demonstrates significant conservatism in the linear foundation model. Implementation of the proposed hypoplastic macro-element can thus reduce costs and increase demonstrated capabilities of jack-ups significantly.

Preface

With this thesis I conclude a wonderful time at TU Delft. I could not think of a better environment to grow, both on professional and personal level.

It has been a challenging but rewarding experience, to write a thesis that aims to push the engineering capabilities of an innovative company such as GustoMSC. It has been a true pleasure to do this under supervision of Ir. Perry van Uchelen and Dr. Ir. Ronald van der Meulen. Above all, this thesis learnt me to tackle a problem that seems daunting and unsolvable. Ronald has been an excellent guide in peeling away the complexity, layer by layer. Perry, the brain behind the seismic assessment procedure at GustoMSC, has been a great inspiration and motivator throughout my research. I would like to thank them both for being excellent supervisors and hope our career paths cross again. A big thanks also to the thesis committee, for setting the bar high at TU Delft and igniting my passion for structural dynamics.

I am also grateful for having Manuela by my side, who pushes me to be my best self and never fails to put a smile on my face. But most importantly, I want to thank my parents and other family. Their support, through good times and bad, enabled me to graduate as engineer at the Delft university of Technology.

Contents

Chapter 1

Introduction

Decades of research indicates that global temperature is rising due to human emission of greenhouse gasses. The Paris Climate Agreement was signed by almost all nations, aiming to keep global temperature rise this century well below 2 degrees Celsius compared to pre-industrial levels. This has spurred the demand for new, sustainable energy sources. As the price of offshore wind energy decreases, Taiwan and Japan are emerging as large markets. Taiwan aims to have 5.7 Gigawatts (GW) of offshore wind capacity by 2025, and 15.7 GW in 2035 [10]. Japan has set the goal of 10 GW in 2030. They aim for 39 GW by 2050, of which 19 GW bottom-founded [26]. Attractive feed-in tariffs spur development in this region, but the industry faces new engineering challenges here. Structures should be designed to withstand typhoons, and much of Japans offshore wind potential is in deep waters. The region is situated around large fault lines, causing strong seismic activity along the coastlines of Japan and Taiwan. In order to meet safety standards, offshore structures should be subjected to seismic analysis. Jack-up operators also require seismic analyses as input for risk analyses, insurance and mitigation measures. The seismic response of a jack-up is however not fully understood. GustoMSC is developing expertise to perform extensive seismic analyses of jack-ups for severe earthquakes.

1.1 Problem definition

Improving safety of personnel and minimizing environmental and economic damage during an earthquake has led to the development of seismic design procedures and criteria. These have been defined by the International Organization for Standardization (ISO). The procedure consists of assessing the structure in an Extreme Level Earthquake (ELE) against the Ultimate Limit State (ULS) criteria. The objectives of ULS design are to ensure that there is little or no damage to the structure during the ELE event. ULS design procedures are primarily based on linear elastic methods of structural analysis, ensuring a sufficient safety margin for the next ELE event. If the ULS criteria are not satisfied, the ISO standard allows for performing Abnormal Level Earthquake (ALE) analyses instead. The objective of an ALE design check is to ensure that progressive collapse will be avoided. For offshore Japan and Taiwan, the ELE screening needs to be performed on all sites. Assessing the structure against ALE criteria allows for non-linear plastic structural and foundation behavior, contrary to the ULS assessment. ISO 19901-2 indicates it is often uneconomic to design a structure that is able to resist an ALE event without including non-linear behaviour [18].
In order to assess seismic loads, GustoMSC developed a linear dynamic model for site-specific assessments of jack-ups. The soil and foundation response is currently represented by linear springs in all 6 Degrees Of Freedom (DOF). This foundation model is simplistic and based on the assumption of small soil shear strains ($<0.01\%$) [47]. It has been recognized [22] that non-linear soil displacement behaviour is certain to occur during heavy seismic loading. This behaviour includes plastic deformation of the soil, hardening, hysteretic damping, cyclic stiffness degradation, cyclic strength degradation and ratcheting. ***The currently linear modelled foundation behaviour is unrealistic and expected to be overly conservative.*** By more realistic foundation modelling, significant improvements in seismic response analyses could be achieved. Additionally, the foundation stiffness significantly affects the eigen periods of the jack-up. As some potential mitigating measures are tuned to the eigen periods, they perform optimally in a certain frequency range. Im-

proving the foundation model makes it possible to better estimate the occurring vibration frequencies during an earthquake. The new foundation model could therefore be beneficial to the effectiveness of mitigating measures. Current industry practice does not include non-linear foundation behaviour into their engineering processes. The traditional approach to include these phenomena is to perform expensive FE analyses on discretised soil. In this thesis the new macro-element method is implemented. This method is mainly used in academic research, but provides an easy and computationally efficient way to capture non-linear behaviour. Additionally, the radiation damping model is improved. The current method reduces the input ground motion, is time consuming and prone to human error. By replacing this method with a viscous damper, the foundation model can quickly be improved.

1.2 Scope

1.2.1 Research questions

This research aims to quantify the effect of improved foundation behaviour modelling on the modelled seismic response of a jack-up unit. The main research question is:

What is the effect of improved foundation behaviour modelling on the modelled seismic response of a jack-up unit?

In order to answer this question, the following additional research questions have been defined :

- *What is the effect of explicitly incorporating linear foundation damping in the model as opposed to reduced input ground motion?*
- *What methods are suitable for modelling nonlinear force-displacement relations in the foundation?*
- *Can a suitable foundation model be implemented as a macro-element in OpenSees?*
- *What is the effect of modelling non-linear foundation behaviour on the jack-up?*
- *What is the sensitivity of the seismic response to empirical foundation parameters?*

1.2.2 Contents

Chapter 2 provides theoretical context to this research. Relevant parts of design standards are summarised and a description of dominant physical effects is given. Methods to model radiation damping and impedance are described. In Chapter 3 the two available macro-elements are extensively described, followed by a comparison. This comparison resulted in selection of the Salciarini macro-element [35] [36] [43] [13].

The thesis compares two available macro-elements in Chapter 3, but the focus is on the implementation, verification and results of the improved model. The seismic analysis will be performed using OpenSees software. OpenSees is an open source seismic analysis software framework that uses object oriented methodology. It allows the user to create an FE model of the structure using nodes and elements. The OpenSees software and currently used FE model is explained in Chapter 4. In Chapter 5 the effect of explicitly incorporating linear foundation damping as a viscous damper in the model is assessed. In order to simulate non-linear behaviour of the foundation in soil, the macro-element developed by Diana Salciarini and Claudio Tamagnini ([35] [36] [43] [13]) will be implemented. Macro-elements condense the behaviour of the foundation and supporting soil body to a non-linear, coupled force-displacement relation. Compared to soil discretisation with Finite Element (FE) models, macro-elements are computationally efficient and easy to use. The computational efficiency is orders of magnitude faster, allowing for implementation in risk analyses [40]. Using a macro-element does not require additional software knowledge, making it easy to implement in engineering processes. The macro-element could therefore be an attractive method for the simulation of seismic foundation behaviour. A comparison is made between two available macro-elements. The most suitable macro-element is selected in Section 3.4.

To the best of the authors knowledge, no published work is available on the implementation of macro-elements in OpenSees. In Section 4.3 a description of the software implementation is provided. Modifications

have been made to the OpenSees ZeroLengthND element, to allow for macro-element implementation. The implementation of the macro-element in OpenSees has been verified in Chapter 6. The macro-element is then attached to the jack-up model and verified again.

The effect of the non-linear foundation model on the jack-up response is assessed by means of 4 case studies with different soil parameters. These four cases are studied extensively to gain insight in the dynamic behaviour resulting from non-linear foundation modelling. Both time-domain and frequency-domain effects are described in detail.
Some material parameters in the macro-element require empirical determination using experimental data or FE analyses. The determination of these parameters is outside the scope of this study, and are chosen here based on available literature. A small sensitivity analysis has been performed to quantify the effects of these parameters on the jack-up response. It also provides clarity on whether conservative parameter selection is possible. The entire case study is performed on sand. Both the case study and sensitivity analysis can be found in Chapter 7.

The main research findings are summarised in Chapter 8. In this chapter results are extensively discussed. Recommendations for further research are provided in Chapter 9.

1.3 Framework

This research is carried out for a four legged jack-up intended for wind turbine installation. The dynamic model is developed by Linthorst [27], and is tuned to match the real weight distribution of the jack-up. The structure is founded on homogeneous sand and damped by means of Rayleigh damping. In this research the effect of dynamic behaviour of the crane is not considered. Plastic deformation in the structure is not accounted for. The assessment of the impact of the explicit radiation damper is performed in combination with a linear foundation. The non-linear case study is based on Yellow Leighton Buzzard Sand [5][13]. A preliminary assessment indicated that hardening is not significant, and was therefore not included.

Not in scope
Incremental collapse, soil interaction effects between legs , pore water pressure, tsunamis, mud volcanoes, soil liquefaction, gap formation, mudslides (slope instability), subsidence, fault proximity, earthquake induced fire etc.

Chapter 2

Design standards and theoretical background

In this chapter, the relevant design standards are discussed. They provide a starting point for parameter determination and simulation methodology. The design standards also contain an introduction to radiation damping, impedance and non-linear foundation modelling. The chapter proceeds with a description of phenomena occurring in non-linear foundations. Academic work cited in this thesis often has the same experimental background as the ISO standards, so the theory is explained here starting from the ISO standards. The modelling methods to capture non-linear phenomena are further detailed in 3.

2.1 ISO 19901-2

This section reviews the relevant parts of ISO 19901-2: Petroleum and natural gas industries - Specific requirements for offshore structures — Part 2: Seismic design procedures and criteria [18].

ISO 19901-2 describes the entire procedure required for seismic analysis of offshore structures: design principles and methodology, seismic actions procedures and performance requirements. The requirements are applicable to fixed steel and concrete structures. The seismic assessments for jack-up units are described in ISO 19905-1 [19] (Section 2.2), but these rely heavily on ISO 19901-2. The relevant sections of ISO 19901-2 are thus described here.

2.1.1 Seismic risk category (SRC)

The seismic risk category is defined based on the seismic zone and the exposure level. ISO 19901-2 provides maps displaying the rock outcrop spectral accelerations at oscillator periods of 0.2 s and 1.0 s . More detailed maps have been published in 2018, and may be used alternatively. These are displayed in Figure 2.1. Manned platforms are always in the highest exposure category (L1), requiring an annual probability of failure of less than 1/2500. Combined with seismic zone 2 or higher, this always leads to SRC 4. Only if the imposed lateral loads are less then 5 % of the total vertical loads, the SRC may be re-categorized as SRC 2. This is for jack-up structures not the case. It can be concluded that for offshore Taiwan and Japan, the SRC is 4. SRC 4 requires a detailed seismic action procedure, site-specific seismic assessments, and non-linear ALE analysis.

2.1.2 Performance requirements

The standard describes two levels of earthquake against which the structure should be tested:

- Extreme Level Earthquake (ELE): "Earthquake with a severity which the structure should sustain without major damage. When exposed to an ELE, a structure is supposed to retain its full capacity for all subsequent conditions." This implies all deformations of the bearing structure should be within the elastic range. Localized and limited non-linear behaviour is allowed. The ELE earthquake is checked

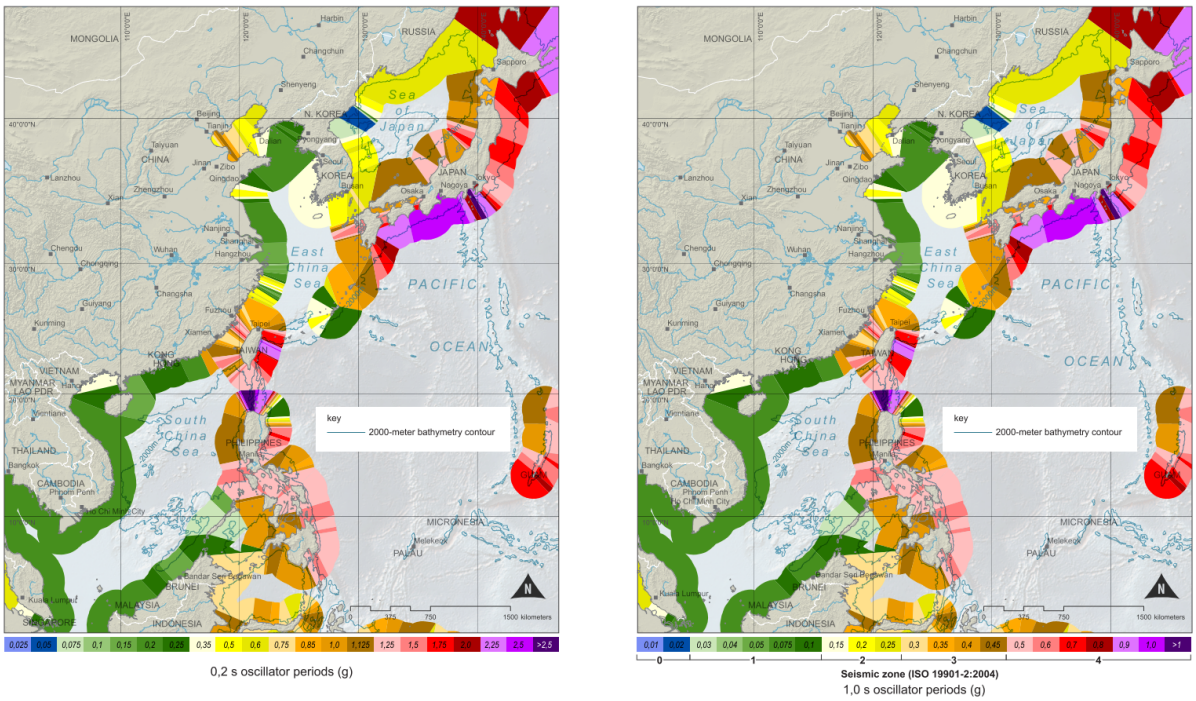

Figure 2.1: Rock outcrop spectral accelerations at oscillator periods of 0.2 and 1.0 [s] [16]

against the Ultimate Limit State (ULS). The ELE earthquake has an average return period of 1000 years.

- Abnormal Level Earthquake (ALE): "Intense earthquake of abnormal severity under the action of which the structure should not suffer complete loss of integrity. When exposed to the ALE, a manned structure is supposed to maintain structural and/or floatation integrity for a sufficient period of time to enable evacuation to take place." The ALE earthquake is checked against the Abnormal Limit State (ALS). The ALE earthquake has an average return period of at least 2500 years.

2.1.3 Performing simulations

In both methods, the base excitation should be in all three directions. At least 4 sets of time history records should be used to capture the randomness in seismic motions. Best practice is to develop a minimum of 7 time history records. These records are created by scaling time traces of historic earthquakes such that their spectra match the required seismic acceleration spectrum. A modal damping ratio up to 5% may be used. Higher damping ratios can be used if these can be substantiated by special studies.

2.2 ISO 19905-1

Petroleum and natural gas industries —Site-specific assessment of mobile offshore units— Part 1: Jack-ups [19].

ISO 19905-1 describes the site-specific assessment of jack-up units. Procedures for earthquake analyses from ISO 19901-2 are tailored to the requirements for jack-ups. The following section reviews the relevant methodologies described in ISO 19905-1. In this standard the HVM yield surface (Section 2.2.2 and corresponding force-displacement curves are defined specifically for jack-up structures.

2.2.1 Earthquake analysis

The following remarks are made on the earthquake analyses of jack-ups.

- Seismic site assessments shall be performed where the seismic zone is 2 or above, as defined in ISO 19901-2. This is the case for virtually the entire coastline of both Japan and Taiwan.
- If the ULS assessment criteria are not met when checked against an ELE, the ALE screening against the ALS can be used. The jack-up is acceptable if it retains its structural integrity to the extend that no loss of life and/or major environmental damage is caused.
- It is not considered possible to ready the jack-up for an earthquake, so all operating configurations should be assessed.
- The uncertainties in foundation modelling should be included by considering a realistic range of for example foundation stiffness, capacities and penetration depths.
- At sites where cohesionless soils dominate, the possibility of earthquake induced soil liquefaction shall be considered.

Radiation damping

As the structure vibrates, stress waves propagate into the soil. These waves radiate energy away from the structure, where it is scattered and ultimately damped out. This radiation damping is linearly related to the velocity difference between soil and structure, and can therefore be modelled as a viscous damper. Normally, the system damping of the superstructure is significantly smaller than the radiation damping in the soil. The effect of soil radiation damping is most dominant for stiff structures with low foundation stiffness and high loading frequency. The first eigen modes of the structure correspond to horizontal footing motions and are not stiff. In combination with the smaller surface area this leads to small horizontal radiation damping. Radiation damping is therefore mainly present in higher modes. Minimal effect of the changed model on the response is expected. The ISO standard allows for inclusion of vertical radiation damping in addition to other foundation damping. The damping coeffient can be estimated from the work of Lysmer and Richart [28]. They analysed the vertical mode of vibration of a rigid circular footing resting on the surface of an elastic half-space, and proposed approximate frequency-independent spring and dashpot as simplified solution for engineers (Lysmer's Analog). This schematisation is representative for a jack-up footing on the seabed. Equation 2.2 is obtained by combining the definition of the damping coefficient, C, with the damping ratio of Equation 2.1 and the corresponding formula for stiffness given by [28].

$$\zeta_{\mathrm{rd}} = R * 0.213 * N_s * B * \omega_n * \sqrt{\frac{\rho}{G_o}} \tag{2.1}$$

$$C_{\mathrm{rd}} = R * (0.85 * B^2/(1-v)) * \sqrt{G_o * \rho} \tag{2.2}$$

Where

- ζ_{rd} is the radiation modal damping ratio to account for spudcan vertical motion;
- R is a reduction factor applied to avoid unconservatism, which should normally be taken as 0.5;
- N_{s} is the number of spudcans;
- B is the equivalent spudcan diameter at uppermost part of bearing area in contact with the soil;
- ω_{n} is the angular eigen frequency of the dominant vertical mode, in radians per second;
- ρ is the total, saturated, (mass) density of the foundation soil;
- G_{o} is the shear modulus of the foundation soil

2.2.2 Yield surface

In Appendix A.9.3.3.2 of ISO 19905-1 the yield surface of the soil bearing the spudcan is defined in the Horizontal-Vertical-Moment (HVM) load space. This yield surface describes the force combination leading to a fully plastic deformation of the bearing soil. The forces are all assumed to act in the same plane, simplifying the 6 DOF loading to a 3 DOF loading scenario. Inside the yield surface the foundation behaviour is considered elastic for small strains, and becomes increasingly plastic as the yield surface is approached. If the force combination lies outside the yield surface, the linearized, rotational stiffness at the spudcan should be reduced using an iterative process until the force combination lies on the yield surface. The cross-sections of the yield surface as displayed in the standard can be seen in Figure 2.2. The yield surface is algebraically described by Equation 2.3, from Templeton [44]. During preloading, the spudcan penetrates deeper into soil due to plastic deformation, causing the yield surface to expand. The plasticity relationship can account for moment softening at high loading levels, unloading behaviour and work-hardening effects. The surface is paraboidal for shallow penetrations, and becomes elliptical for deeper penetrations.

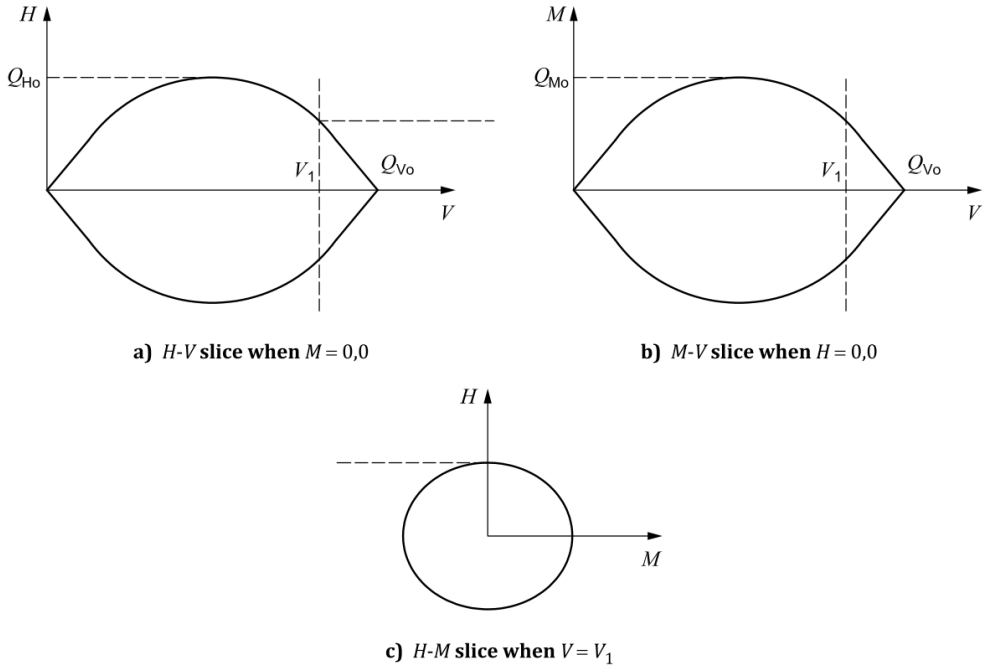

a) *H-V* **slice when** $M = 0{,}0$

b) *M-V* **slice when** $H = 0{,}0$

c) *H-M* **slice when** $V = V_1$

Key

H	horizontal capacity
M	moment capacity
V	vertical capacity

Figure 2.2: Cross sections of yield surface as defined in ISO 19905-1

$$\left(\frac{F_H}{Q_H}\right)^2 + \left(\frac{F_M}{Q_M}\right)^2 - 16(1-a)\left(\frac{F_V}{Q_V}\right)^2\left(1-\frac{F_V}{Q_V}\right)^2 - 4a\left(\frac{F_V}{Q_V}\right)\left(1-\frac{F_V}{Q_V}\right) = 0 \tag{2.3}$$

Where

- F_H, F_V and F_M are the horizontal, vertical and moment forces applied on the spudcan. They are defined in section 8.8 of ISO 19905-1.
- Q_H, Q_V and Q_M are the horizontal, vertical and moment soil bearing capacities. This capacities depend on a large number of foundation properties which are not elaborated here.

2.2.3 Linear vertical, linear horizontal and secant rotational stiffness

A simple method to improve the linear foundation model is to implement a secant rotational stiffness. Rotational loading generally leads to more plastic deformation than the vertical and horizontal loads. By solely including rotational stiffness reduction, the model can be improved without introducing non-linearity. In order to do so, the ISO standard describes a foundation rotational stiffness reduction factor (f_r). This factor should be multiplied with the initial rotational stiffness. The factor can be determined as in Equations 2.4. In this expression, the variable r_f is the failure ratio, as defined in 2.5.

$$f_r = \frac{(1-n) * r_f}{\ln\left[(1 - n * r_f)/(1 - rf)\right]} \tag{2.4}$$

$$r_f = \frac{\left[\left(\frac{F_H}{Q_H}\right)^2 + \left(\frac{F_M}{Q_M}\right)^2\right]^{0.5}}{\left[16(1-a)\left(\frac{F_V}{Q_V}\right)^2\left(1 - \frac{F_V}{Q_V}\right)^2 + 4a\left(\frac{F_V}{Q_V}\right)\left(1 - \frac{F_V}{Q_V}\right)\right]^{0.5}} \leq 1 \tag{2.5}$$

2.2.4 Non-linear vertical, horizontal and rotational stiffness

If a full yield interaction model is implemented, with non-linear stiffness in all directions, the stiffness reduction is implicitly included. For the required force-displacement formulations, the standard refers to Wong et al. [48], Van Langen et al. [46] and Cassidy et al. [6]. A qualitative description of the non-linear force displacement behaviour of the soil is given in Section 2.4.

2.3 Impedance

Mechanical impedance is a measure of how much a structure resists motion when subjected to a harmonic force. The jack-up foundation is found to have a frequency dependent relation between force and displacement. This is effectively a frequency dependent stiffness. This is caused by non-linear and inertial effects in the soil and can be influenced by resonance of soil layers. The stratification of soil has a significant effect on impedance relations due to a complex interplay of added mass and resonance effects. It is worth noting that the soil properties itself are to a good approximation frequency-independent [11]. Generally speaking, the stiffness reduces for increasing frequency. In the range of 0-5 [rad/s] the frequency dependency has been found by GustoMSC to cause equivalent stiffness reductions up to 10%. The effect becomes larger for softer soils.

2.3.1 Modelling methods

The impedance relations are site specific, and mainly determined by the shear moduli of the soil layers. For the simplified case of an embedded disk on a homogeneous elastic half-space, the formulation of impedance relations are given in Gazetas [12]. These simplified relations could be approximated in the model by including an added mass at the spudcan. Now the real part of the force-displacement ratio will follow the curve $k - m * \omega^2$. Modelling the frequency dependent stiffness by means of an added mass could provide an easy tool to improve the modelled foundation behaviour. For homogeneous soils, a back-fitting tool could be developed to tune the added mass to fit the $k - m\omega^2$ curve from Gazetas [11][12].

In conclusion the impedance modelling poses several challenges.

- It would not be possible to account for stratified soils, unless the $k - m\omega^2$ curve is created by means of FE analyses of discretised soils. This would undermine the ease of use of the added mass.
- It is very difficult to combine impedance effects with a non-linear foundation model, as part of the impedance is caused by non-linear soil behaviour. The difficulties were first overcome by Lesgidis et al. [25], and
- Understanding of the foundation behaviour would not be improved, making the scientific basis for resulting load reductions very thin.

- The accuracy of fitting a single mass spring system on the Gazetas curves is very low. It could be improved by using more complex mass-spring systems, but the implementation of these systems in OpenSees would be a time-consuming process.

It is therefor chosen to not mimick impedance by means of an added mass in this research.

2.4 Non-linear soil behaviour

This thesis describes the implementation of a non-linear macro-element foundation. In this section the relevant non-linear foundation characteristics are explained, supported by force-displacement diagrams. For each property the general behaviour, causes, varieties, expected seismic effects and relevant parameters are explained. Design standards recommend excluding plastic behaviour in ULS screenings, but soils can exhibit non-linear behaviour at stress levels as low as 10% of the yield stress and at soil strains of 0.01% [47]. For severe load cases, understanding the non-linear soil behaviour can therefore play a vital role in assessing seismic responses. Jia [22] considers application of linear stiffness and damping modelling not appropriate for strong seismic motions or when shear stresses approach the shear strength. Only at very small shear strains below 0.0005%, soil can be assumed to exhibit fully linear-elastic behaviour [8].

2.4.1 Yield surface and hysteresis

In its most elementary form, a yield surface is a five-dimensional surface in a six-dimensional space of stresses. These stresses are the normal and shear stresses in all three dimensions. When the combined stress increases up to the yield surface, the material has reached its yield point. The material will display fully plastic behaviour, causing the stress state to remain on the yield surface. The yielding will continue until the material breaks or a different physical mechanism (such as reaching a stiffer layer) will expand the yield surface.

Both normal and shear stresses in the soil are caused by the horizontal, vertical and moments (HVM) imposed by the spudcan. It is common engineering practice to describe the yield surface as a function of these forces. The HVM yield surface is extensively described in ISO 19905-1, and the input forces and capacities are readily available.

As the stress state in soils approaches the yield surface, the material will already decrease in stiffness, and display elastoplastic behaviour. This behaviour can lead to several cyclic phenomena, which are captured by the macro-element used in this thesis. These cyclic phenomena are described below.

- Non-linear (secant) stiffness. As the yield surface is approached, the force-displacement ratio reduces. This leads to softer response of the structure, thus shifting the eigen frequencies.
- Plastic deformation. Due to rearrangement of soil grains plastic deformation of the soil occurs. This slipping and sliding is a non-linear phenomenon.
- Hysteretic damping. Caused by friction between sliding grains and water flow through pores.
- Ratcheting. Irreversible, cumulative displacement caused by asymmetric loading. If this loading repeatedly leads to asymmetric plastic deformation, this will lead to an accumulated displacement. An example of ratcheting is given in Figure 2.5.
- Cyclic stiffness reduction (description below)
- Cyclic strength reduction (description below)
- Pinching. Usually the result of crack closure and rivet slip. Pinched hysteretic loops are narrower in the middle and wider at the ends. This is not expected to occur in soils.
- Gap formation. This leads to reduced stiffness at low strains.

A graphical explanation of these phenomena can be found in Figures 2.3 and 2.4. In Figures 2.3 an example is given of a force-displacement relation of a soil exposed to an oscillating load. When the loading initiates at $t = t_o$, the stiffness is approximately linear. At t_1 the stiffness has reduced and the behaviour is elastoplastic. Upon unloading at t_2, the curve does not return on the same path, because energy has been dissipated from the system. The reloading curve at t_2 has the same stiffness as at t_0. At t_3 the load is the same as at t_0, but the displacement different. This difference equals the plastic deformation that has occurred between t_0 and t_3. As the material has been effected by its past loading, the material is sometimes said to have 'memory'. As the oscillation proceeds, the force-displacement relation will repeat the path as displayed in this figure. The hysteretic damping can be determined by calculating the surface of the area enclosed by the loading path. This integral equals the work performed by the exciting force. For small loading, the loading and unloading curves have a shape described by the four Masing's rules. If larger loading occurs, these rules overestimate hysteretic damping [24]. When exposed to prolonged cyclic loading, the soil might have a cyclic capacity lower than the static capacity. This is the result of cyclic loading breaking down the soil structure and tending to volumetric reduction. In undrained seismic conditions the low compressibility of water prevents volumetric changes, resulting in excess pore pressure. The effective stress will decrease accordingly, leading to reduced strength and stiffness [1]. This effect is schematised in Figure 2.4.

The term "hysteresis" is used throughout literature in relation to the effects above. In its most elementary form hysteresis is the dependence of the state of a system on its history. In the application of mechanics, this is caused by plasticity of the material. Hysteretic behaviour in soil causes the phenomena described above. To avoid confusion, the above listed terms are used in this thesis.

These phenomena can traditionally only be captured by discretisation of the soil in large FE analyses. These require much computational power and expertise. In Chapter 3 an alternative approach is extensively described: the macro-element method.

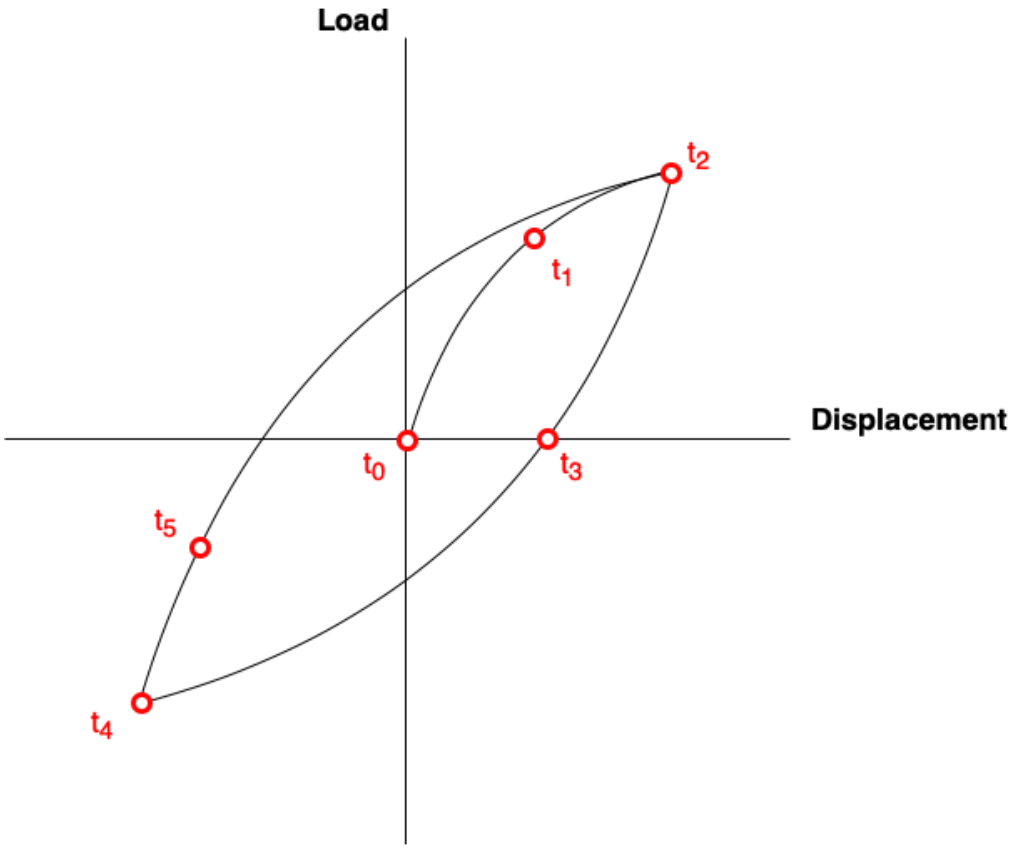

Figure 2.3: Schematised force displacement relation of elasto-plastic material under harmonic forcing

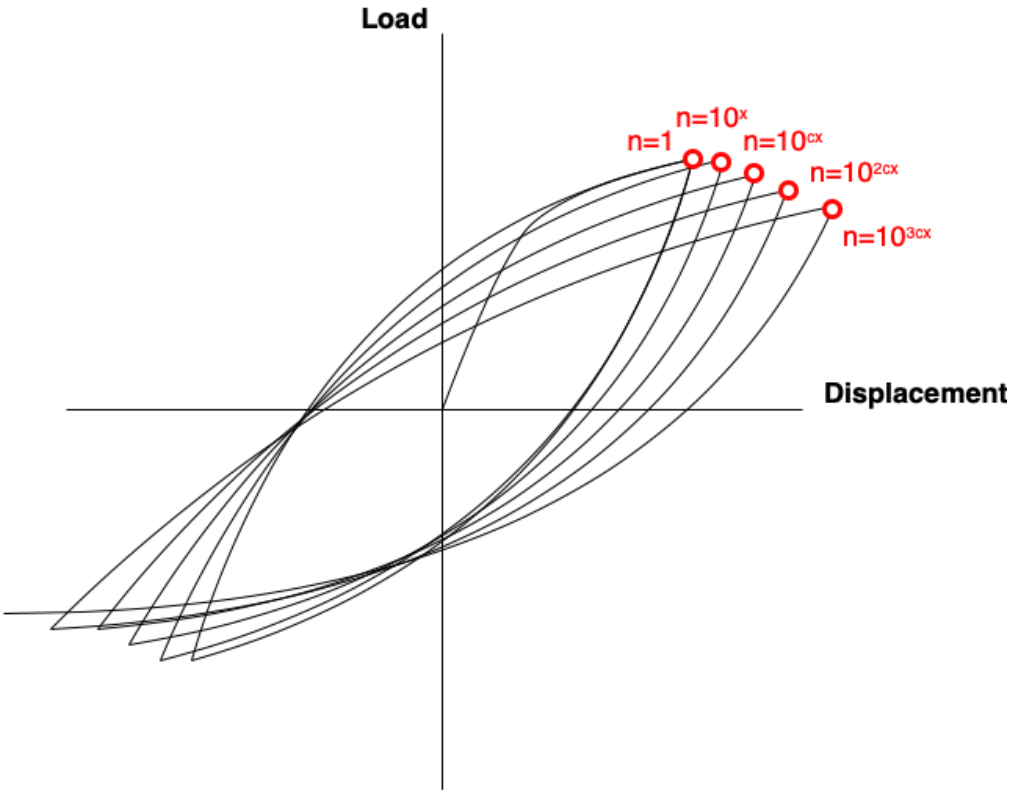

Figure 2.4: Schematised force displacement relation of elasto-plastic material under prolonged harmonic forcing

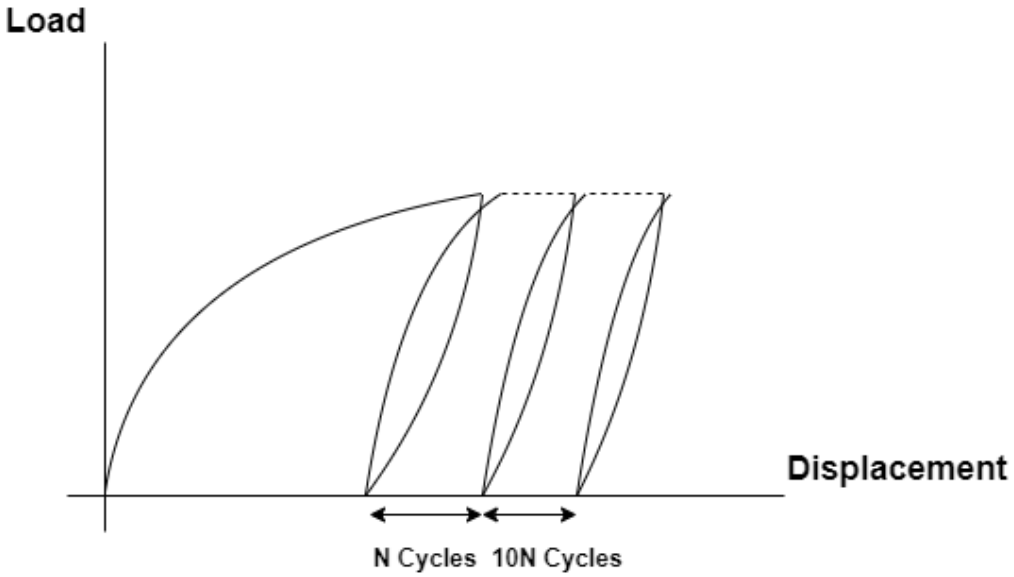

Figure 2.5: Schematised force displacement relation of elasto-plastic material under prolonged asymmetric forcing

Chapter 3

Comparison available modelling methods

3.1 Introduction

In this chapter a comparison is made between two macro-elements available to GustoMSC. These macro-elements both capture non-linear force-displacement behaviour in soil based on the HVM yield surface. Many similar macro-elements have been created and implemented successfully [9][45][7]. This thesis does not aim to find the most optimal macro-element available. A suitable macro-element will be selected and the effects of its implementation analyzed. In OpenSees several hysteretic uniaxialMaterial commands are available, which could hypothetically be adjusted to imitate the effect of the HVM-yield surface. This would require attaching elastoplastic springs to the foundation node in all DOF. Since the yield point in one direction depends on the forces acting in different directions, the yield point in each DOF should be determined based on the occurring forces in the previous time step. If the time step is sufficiently small this should approximate the behaviour a macro-element. This method is not preferred because it potentially leads to excessive computational time, instability and accuracy loss. OpenSees also provides elastoplastic nDMaterial commands, intended for FE analyses. These are based on the combination of normal and shear stresses. The solution algorithms in these material have not been verified for a macro-element approach.

The remaining option is to implement an third party macro-element in OpenSees. Two macro-elements readily available to GustoMSC are briefly assessed based on literature, and a selection is made. The main properties and methodologies used by the macro-element are summarised, and a short description of the validation methods and conclusions is given. In order to select the most suitable method, the elements are given weighted scores for a list of properties, after which the macro-element with the highest score is selected.

3.2 REDWIN foundation model 3

3.2.1 Introduction

Many macro elements presented in literature lack published methodologies for adaptation of the macro-element to different soil conditions. Skau et al. [40] identifies this as a possible reason that macro-elements are rarely used in the design of offshore structures. The macro-element presented addresses this problem by defining a practical-oriented formulation.

In order to present a viable alternative to linear elastic foundation models, the REDWIN project developed three macro-elements. Model 1 and 2 are intended for monopiles, and allows the user to specify p-y curves based on horizontal loading and coupled horizontal an moment loading, respectively. Model 3 is intended for (skirted) Gravity Base Structures (GBS) or bucket foundations, and considers coupled horizontal, vertical and moment loading. Only model 3 is suitable for shallow penetration of the spudcans of a jack-up. Despite being intended for OWT's, it is expected that this model can also be implemented for seismic assessments of jack-ups. Both the spudcan and a GBS supporting an OWT have a load-displacement behaviour that can be modelled as a function of the distance to the HVM yield surface. A complete description of REDWIN foundation model 3 is given in Appendix A.1.

3.2.2 Working principles

REDWIN model 3 has been based on FE analyses of a wide range of soil profiles and bucket geometries. The stress strain behaviour is based on the NGI database on cyclic behavior of over-consolidated clays, as typically found on North Sea offshore wind farm sites. The macro-element presented in this paper has been formulated in the multi-surface plasticity framework [33] [20]. The hardening is defined by subsequent linear curves. In Figure A.1 in A.1 the concept is explained based on a simple 1D model.

The element uses a 3x3 diagonal elastic stiffness matrix. The coupling terms are zero because the z_{LRP} is chosen such that the forces and moments are uncoupled. For low mobilization levels, the contours of plastic work where reasonably approximated by elliptic surfaces. For the purpose of OWT assessment, this is sufficient. The elliptic surfaces are taken as the potential function as specified in Equation A.1 in Appendix A.1. These surfaces are also chosen as the yield surfaces. The yield function f_i is then given by the same function imposing associated flow, for all surfaces, as in A.2 in Appendix A.1. The macro-element includes hysteretic damping, but excludes radiation damping. The hysteretic damping is determined based on the three input curves, following Masing's rule.

A relatively simple hardening rule has been applied, which controls the relation between surface translation and plastic displacement. The hardening is a multi-linear approximation. This means that each surface i has a constant "plastic stiffness". The Koiter rule as in A.3 in Appendix A.1 is used to determine the total amount of plastic displacement.

3.2.3 Limitations and simplifications

Accumulation of displacement (ratcheting) and cyclic stiffness degradation are not considered. The latter is due to difficulties of estimating stiffness degradation and especially accumulation. This simplification is adopted largely because the effects occur over large time spans, while dynamic analysis of a OWT normally consider ten minutes. Pore pressure accumulation and mean stress changes are not computed internally in the model. Skau and Jostad [38] and Andersen and Berre [2] show that "the stress-strain response in sand and clay are reasonably similar if the sand response is predominately undrained during a single cycle and if the loads are relatively small, such that no significant pore- pressure accumulation occurs." The mathematical functions in this model are deliberately implemented without empirical calibration factors. These factors could benefit the accuracy, but the user availability of these factors is limited.

3.2.4 Model performance

Three field tests have been modelled to demonstrate the performance of the macro-element. It resulted in a generally good agreement, with the most significant deviations in the HM-plane. This is due to the simplification of the yield and the potential function, which is less accurate in the HM-load plane. This difference cannot be completely eliminated due to the fundamentally non-symmetric nature of the HM-load plane. The modelled secant stiffness shows a good agreement with the FE Model, but damping has been slightly underestimated.

3.2.5 Conclusion

The macro-element has a simple intuitive input, and was shown to reproduce, with satisfying accuracy, the response computed in FEA and the response observed in the Bothkennar field test. Three examples have been used by the authors to illustrate the macro-element's performance. These examples show that the macro-element:

- reproduces the response computed in FE Analyses of the soil volume and the bucket foundation
- is numerically stable and does not cause numerical ratcheting
- produces a response in good agreement with a large scale field test

The macro-element was however developed with the purpose of being simple. The limited amount of input parameters compromises the accuracy, and it is therefore advised to compare some of the results with a FE Analyses.

3.3 Salciarini model

3.3.1 Introduction

In Salciarini and Tamagnini [35], a macro-element for shallow foundations in sand has been developed based on the theory of hypoplasticity. Previously developed macro-elements ([9][45][7]) have been developed in the framework of the classical theory of plasticity. In the Salciarini model, the theory of hypoplasticity (reviewed in [42]) is used instead. hypoplastic models are a class of incrementally non-linear models. Its aim is "to demonstrate that the same basic principles of continuum hypoplasticity can be used to develop a fully nonlinear and irreversible macro-element model, which is quite effective in reproducing the basic features of the observed behavior of shallow foundations under monotonic and cyclic complex loading paths." This 3 DOF model has later been extended to 6 DOF [36]. Additionally, a new hardening law for the vertical bearing capacity has been adopted to include the effects of accumulated displacements and rotations. The extended model as described in Salciarini and Tamagnini [36] has been used as the subject of comparison in this chapter. This model is validated based on the observed response in a series of laboratory tests performed at 1g on a small-scale circular foundation, subjected to complex loading paths [36]. Dynamic analyses with the macro-element have been performed for a wind turbine loaded by wind in Tamagnini et al. [43].

3.3.2 Working principals

Whereas the REDWIN model adopts a multi-linear approximation of the hardening curve, the Salciarini model adopts a continuous analytical curve within the framework of hypoplasticity [35]. The tangent stiffness varies continuously with the direction of the generalized velocity. This is also known as incremental non-linearity.

In order for any macro-element to correctly reproduce non-linearity, irreversibility and memory, the constitutive equation must be formulated in rate-form:

$$\dot{t} = \hat{t}(t, q, d) \tag{3.1}$$

$$\dot{t} = \kappa(t, q, \eta)d \qquad \kappa = (t, q) + N(t, q)\eta^T \qquad \eta = \frac{d}{||d||} \tag{3.2}$$

Where:

- $d := \dot{u}$ is the generalized velocity factor
- q is a pseudo-vector of internal variables, which captures the effects of loading history.
- The function $\hat{t}$ is assigned properties based on the observed behaviour. In the framework of hypoplasticity it has the structure as defined in Equation 3.2
- (t, q) is a $5x5$ matrix
- N(t,q) is a 5D vector

The full description of the constitutive equations can be found in Appendix A.2.

Yield surface

In this paper the yield surface is normalised against the vertical capacity. Equation 3.3 is different from the one found in ISO19905-1.

Experimental work shows that the ratio of the horizontal to rotational loading influences the combined load capacity of the footing in the HM plane. For $a = 0$ the ellipse is perfectly round, and for $0 < a < 1$ it becomes more and more stretched in the HM plane until it becomes paraboidal. ISO 19905-1 does not consider this effect, thus assumes $a = 0$.

$$\left(\frac{F_{H1}/Q_V}{Q_H}\right)^2 + \left(\frac{F_{H2}/Q_V}{Q_H}\right)^2 + \left(\frac{F_{M1}/Q_V}{Q_M}\right)^2 + \left(\frac{F_{M2}/Q_V}{Q_M}\right)^2 - 2a\left(\frac{F_{H2} * F_{M2} - F_{H1} * F_{M2}}{Q_H * Q_M}\right) + \left(\frac{F_T/Q_V}{Q_T}\right)^2 - B_{12}(F_V/Q_V)^{2B_1}(1-(F_V/Q_V))^{2B_2} = 0 \quad (3.3)$$

$$B_{12} = \left[\frac{(B_1+B_2)^{(B_1+B_2)}}{B_1^{B_1}+B_2^{B_2}}\right]^2 \quad (3.4)$$

[5]

$$a_{ISO} = ADD \quad (3.5)$$

[5]

3.3.3 Required user input

The material constants in the Salciarini model are user defined. The soil is fully characterised by 29 parameters (17 for the 3DOF version). Three additional parameters are used for footing diameter, preload capacity and initial plastic displacement. The material constants defining the shape of the yield surface do not vary greatly with soil type. Typical values for jack-ups are presented in [3] The material parameters can be categorized in five groups:

Physical parameters

- $D[m]$: Spudcan diameter
- $V_0[N]$: Initial (preload) vertical bearing capacity. When hardening has occurred, the vertical bearing capacity is expressed as V_f.
- $\zeta[m]$: Initial vertical plastic displacement at $t = 0$. Only relevant when hardening is activated ($k_1 = 0$). This value should be zero in jack-up simulations, since initial penetration is already accounted for in the definition of capacity and stiffness.

Parameters defining yield surface and initial stiffness

- $k_v[N/m]$: Vertical elastic stiffness at small strains. As specified in ISO 19905-1, Equation A.9.3-46.
- $k_h[N/m]$: Horizontal elastic stiffness at small strains. As specified in ISO 19905-1 Equation A.9.3-47.
- $k_m[Nm/rad]$: Rotational elastic stiffness at small strains. As specified in ISO 19905-1 Equation A.9.3-48.
- $k_q[Nm/rad]$: Torsional elastic stiffness at small strains. As specified in ISO 19905-1 Equation A.9.3-48.
- $k_c[Nm/rad]$: Coupled horizontal-moment elastic stiffness at small strains (non-diagonal terms in stiffness matrix). In ISO 19905-1 the coupled term is implicitly included by the seabed reaction point. Multiply k_h with the distance to the seabed reaction point to get k_c. k_c should be smaller than k_h and k_m to prevent negative stiffness.
- $G[N/m^2]$: Shear modulus of soil.
- $h_0[-]$: Normalised horizontal load capacity compared to V_f. As specified in ISO 19905-1 Equation A.9.3-26, or in Cassidy et al. [6] for clay, dense silica sand and loose carbonate sand.

- $m_0[-]$: Normalised moment capacity compared to V_f. As specified in ISO 19905-1 Equation A.9.3-27, or in Cassidy et al. [6] for clay, dense silica sand and loose carbonate sand.
- $q_0[-]$: Normalised torsion capacity compared to V_0. To be determined from experiments or FE analysis. If no data is available, $q_0 = 1$ should be sufficiently large.
- $a[-]$: Eccentricity of the yield surface ($= 0$). In sand, there is no physical reason to assume the yield surface can not be eccentric, therefore it is desirable for a macro-element to allow for this possibility. For realistic physical cases this parameter is zero [29]. Cassidy and Bienen [3] suggests otherwise. In clay the eccentricity varies slightly with V/V_0 and takes the form as described in Equation 3.6 [6], with $e_1 = 0.518$ and $e_2 = 0.180$ recommended by Martin and Houlsby [15].
- $\beta_1[-]$: Modifies the shape of the yield surface at $FV = 0$. When zero, the yield surface is fully conical. As it increases, the surface becomes closed and pointier. When equal to one, the yield surface ends in a point, and has therefor no horizontal or rotational capacity at $FV = 0$. When the footing is penetrated into the soil, capacity is also increasingly present at $FV = 0$. In soft, clayey soils, low values of β_1 occur.
- $\beta_2[-]$: Equivalent of B_2, but at other side of yield surface where $FV = V_f$.

Parameters describing plastic potential and flow

As described in [6].

- $\alpha_h[-]$: Relates the shape of the plastic potential to the yield surface. If all α equal one, $\beta_1 = \beta_3$ and $\beta_2 = \beta_4$, associated flow is assumed. This means the flow direction is perpendicular to the yield surface. The yield surface and plastic potential are then the same surface. This is the case for non-hardening materials. Please note that the potential lines are perpendicular to the the streamlines. Clay and sand are both observed to have associated flow in the moment–horizontal load plane, but not in the vertical–horizontal and vertical–moment planes [14] [15] [4]. Methods to capture this non-associated behavior are recommended in Cassidy et al. [6].
- $\alpha_m[-]$: Equivalent of α_h, relates the shape of the plastic potential in moment plane to the yield surface.
- $\alpha_q[-]$: Equivalent of α_h, relates the shape of the plastic potential in horizontal plane to the yield surface.
- $\beta_3[-]$: Equivalent of β_1, determining the shape of plastic potential where $FV = 0$.
- $\beta_4[-]$: Equivalent of β_2, determining the shape of plastic potential where $FV = V_f$.

Hardening parameters

As described in Cassidy et al. [5]. Pure vertical hardening can be be determined based on ISO 19905-01 Appendix A.9.3.2, experiments or FE analyses. Hardening as a function of only vertical displacement under predicts the vertical capacity, implying vertical hardening is also a function of radial plastic displacement of the footing [15]. Radial hardening can be determined based on experiments or FE analyses.

- $k_1[-]$: Vertical hardening constant. As the footing penetrates into the soil, V_f increases. Set zero to keep V_f constant. If larger then zero, the hardening constants and ζ are included in the behaviour. The hardening parameters are determined by fitting the curve in Equation 3.7 to experimental or numerical results. In this equation w_p is the plastic component of the vertical displacement.
- $w_1[m]$: Hardening constant. Fitted to the curve in Equation 3.7.
- $w_2[m]$: Hardening constant. Fitted to the curve in Equation 3.7.
- $c_1[rad]$: Radial hardening constant. This effect can be included by fitting the hardening constants in Equation 3.8 and 3.9 to FE or experimental data. In Equation 3.8 the vertical plastic displacement w_p is replaced by the total plastic displacement z_p. Set zero to not include radial hardening.

- $c_2[rad]$: Radial hardening constant. Set zero to not include radial hardening.
- $c_3[rad]$: Torsional hardening constant. Set zero to not include radial hardening.

Degree of non-linearity

Used to calibrate results with measurements. Calibrated with experiments [34] in Salciarini and Tamagnini [35], with an elasto-plastic macro-element on dense sand in Grange et al. [13], and to obtain "realistic behaviour" in Tamagnini et al. [43]. The properties have also been defined based on lab experiments for a skirted caisson foundation in sand [23]. The effect of each of the following parameters has been visualised by performing a small sensitivity analysis on a two-node model and pile model. Results can be found in Appendix F.1 and F.2. The parameters are visually explained in Figure 3.1.

- $\kappa[-]$: Material constant that controls the evolution of the loading function. The degree of non-linearity $Y(t) = \xi^{\kappa}$, where ξ is the normalised distance to between load state and yield surface. Increasing its value leads to less curvature in the stress-strain and a stiffer response. Values of 0.4 [35], 0.25 [13], 1.4 [43], 3.0 [37] and 1.1 [23] are used in literature.
- $m_R[-]$: Controls the amount of stiffness degradation when passing from the small-strain to the medium-strain regime, for full unloading. Increasing m_R leads to a stronger stiffness reduction at small to medium strains. Values of 5.0 [35], 1.1 [13], 3.0 [43] and 10 [23] are used in literature. Always equal or larger than m_R [35] and equal or larger than 1. When equal to one, no stiffness degradation occurs during unloading.
- $m_T[-]$: Controls the amount of stiffness degradation when passing from the small-strain to the medium-strain regime for loading. Decreasing m_T leads to larger vertical stiffness. Always equal or smaller than m_R [35] and equal or larger than 1. When equal to one, no stiffness degradation occurs during loading. Values of 2.0 [35], 1.05 [13], 1.5 [43] and 2 [23] are used in literature.
- $R[m]$: Provides the range at which the material behaves approximately linear. This value of this parameter does not directly relate to physical displacement. Values of 0.0001 [35], 0.005 [13], 0.03 [43] and 0.006 [23] are used in literature.
- β_R: Controls the rate at which the internal displacement vector *delta* tends to align with velocity vector *d*. Values of 0.5 [35], 1.0 [13], 1.0 [43] and 0.5 [23] are used in literature.
- χ: Controls the transition between the small-displacement regime and the full hypoplastic response. Values of 1.0 [35], 1.5 [13], 1.5 [43] and 0.5 [23]are used in literature.

$$a = e1 + e2 * \left(\frac{V}{V_0}\right) * \left(\frac{V}{V_0} - 1\right) \tag{3.6}$$

$$V_0 = k_1 * w_p \left(\frac{1 + w_p/w_1}{1 + w_p/w_1}\right) \tag{3.7}$$

$$V_0 = k_1 * z_p \left(\frac{1 + z_p/w_1}{1 + z_p/w_1}\right) \tag{3.8}$$

$$\dot{z_p} = \dot{w_p} + c_1\sqrt{\dot{u}_{2p}^2 + \dot{u}_{3p}^2} + c_2\sqrt{D * \dot{\theta}_{2p}^2 + D * \dot{\theta}_{3p}^2} \tag{3.9}$$

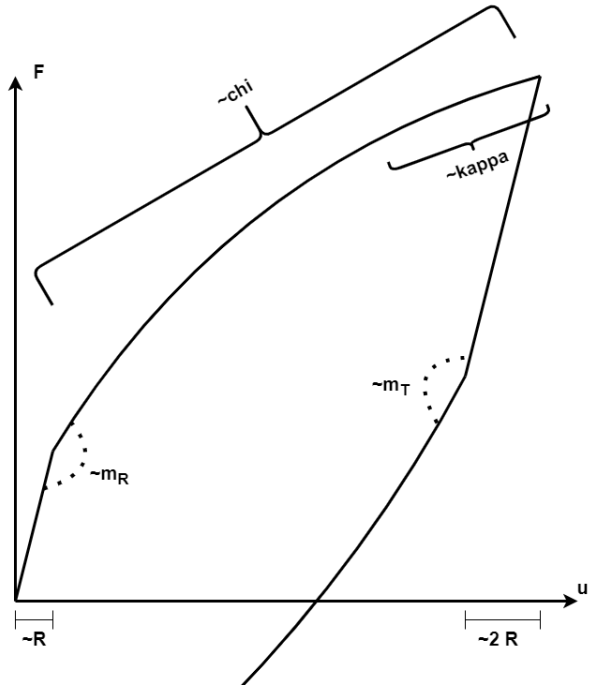

Figure 3.1: Schematised effect of parameters determining non-linearity on force-displacement curve

3.3.4 Model performance

3DOF macro-element [35]

The model performance of the 3DOF macro-element has been compared to experimental data with monotonic and complex loading paths (by Nova and Montrasio [34]) and cyclic loading paths (by Di Prisco et al. [9]) on dry sand. These tests were not used in the calibration. The simulations of monotonic and moment reversal loading paths shows a very good agreement, both qualitatively and quantitatively. For complex loading paths, the results show fairly good agreement, except for an inappropriately soft response between the second and third load reversal. The authors suggest a more accurate definition of model constants R, β_1, β_2 and χ. Due to a lack of cyclic experiment data, the parameters could not be compared well and the observed response is to be considered only from a qualitative point of view. Considering this, the simulations gave good results. For a large number of cycles, Di Prisco et al. [9] shows a decreasing rate of accumulation. This is due to the densification of sand, which is not captured by the macro-element. This effect occurs in the order of 1000 load cycles and is therefore not limiting the applicability of the macro-element for earthquake assessments.

6 DOF macro-element [36]

The combined load capacity and flow direction at shallow embedments were tested by means of swipe tests [5]. The 6-DOF hypoplastic element captures the observed response of the footing reasonably well in terms of load-displacement curves and coupling of loads.

In a second series of tests the footing is subjected to two swipe phases. In these tests the model overestimates the stiffness and the transition between swipe phases is too fast. The model is not capable of obtaining accurate predictions for both tests unless the shape of the failure locus is changed with increasing v_f (vf is a scalar internal variable which controls the dimension of the failure surface of the foundation).

The macro-element presented is an accurate and efficient tool to model fully nonlinear, irreversible and hysteretic relations for shallow foundations on sands. The efficiency of the algorithm tends to decrease for both very large and very small steps, with an optimum choice of the step size located in between the two extremes. The relative error tends to increase with increasing error tolerance, but a reasonable accuracy level

is achieved even for relatively large tolerance values. Increasing TOL has a significant advantage in terms of computational effort. The macro-element uses an RK-4 solver with adaptive sub-stepping.

3.4 Macro-element selection

In this section the most suitable macro-element is selected. The most crucial requirements for the macro-element are the following:

- The macro-element should be able to capture the non-linear force-displacement relationship of the spudcan in soil. This meets the core aim of this thesis.
- The force-displacement relation is dependent on the location of the load-state with respect to the yield surface. The macro-element should allow the definition of the yield surface in accordance with the yield surface described in ISO 19905-1.
- As seismic assessments are performed for many regions, modification of the macro-element for different soils is preferred.
- The macro-element should allow for ratcheting. If different ratcheting magnitudes occur between legs, this can lead to extra loads in the hull and legs, which should be accounted for.
- A macro-element that is able to incorporate hardening is preferred, because significant plastic displacements are expected.
- The algorithm should be numerically stable.
- It is preferred that the macro-element can be implemented in OpenSees.

In order to select the most suitable macro-element, all relevant properties are compared in the matrix in Figure 3.2. All requirements are assigned with a weight and score, both ranging from 1 to 5. Some of these requirements can not be quantified, either do to a lack of sources, or do to the qualitative nature of the requirement. Here, an estimate is given based on the information available.

3.4.1 Conclusion

The Salciarini model is selected as the most suitable macro-element. Major advantages are the wider capabilities regarding capturing physical phenomena, the possibility to include 6 DOF, and the available source code. These advantages outweigh the field test validation and ease of use of REDWIN model 3. The integration with OpenSees software is described in 4.

		Weight (Average)	Score REDWIN	Weighted score	Score Salciarini	Weighted score
Material parameters	Wide range of soil parameters possible	5.0	2	10.0	5	25.0
	Availability input parameters	2.0	5	10.0	4	8.0
Modelling soil behavior	Approximation yield surface	3.3	5	16.7	5	16.7
	Number of DOF	3.0	3	9.0	5	15.0
	Force-displacement curves	5.0	4	20.0	5	25.0
	Ratcheting	4.0	1	4.0	5	20.0
	Hardening	3.0	1	3.0	5	15.0
	Cyclic stifness degradation	2.0	1	2.0	1	2.0
	Cyclic strength degradation	2.0	1	2.0	1	2.0
	Hysteretic damping	4.0	5	20.0	5	20.0
	Radiation damping	1.0	1	1.0	1	1.0
	Tested for clay	1.3	5	6.7	1	1.3
	Tested for sand	1.7	2	3.3	5	8.3
	Inertia effects	1.0	1	1.0	1	1.0
	Calibration method	1.7	3	5.0	4	6.7
	Computational speed	1.0	5	5.0	4	4.0
Stability	Numerical stability	3.7	3	11.0	4	14.7
	Yield surface exceedance	3.0	3	9.0	3	9.0
General	Validation methods	3.0	5	15.0	3	9.0
	Proven methodology	3.0	4	12.0	4	12.0
	Citations authors	1.0	5	5.0	5	5.0
	Citations of describing paper	2.5	2	5.0	5	12.5
	Code ready to use?	3.0	5	15.0	5	15.0
	Implicit/explicit	5.0	5	25.0	5	25.0
	Source code editable?	2.7	1	2.7	5	13.3
	Easy implementation in OpenSees	3.0	4	12.0	4	12.0
	Total			230.3		298.5

Figure 3.2: Comparison between two macro-elements. Both macro-elements have been assigned scores based on available literature

Chapter 4

Model introduction

The aim of the seismic analyses is to assess the response of the jack-up unit to severe earthquakes, and perform unity checks on the results. This requires a model that is easy to use and has limited computational time. In order to be able to add functionalities based on third party developments, OpenSees has been adopted for this research. Both the explicit radiation damping as the non-linear foundation are implemented in this model. This chapter describes the model used at the start of this research, and proceeds with a description of the macro-element implementation in the model.

4.1 OpenSees

OpenSees stands for Open System for Earthquake Engineering Simulation. It is an open source seismic analysis software framework that uses object oriented methodology. It allows the user to create an FE model of the structure using nodes and elements. The user can choose a wide variety of solvers, algorithms and integrators in order to simulate responses to the specified loading conditions. It allows the user to solve complex physical problems, both linear and nonlinear. In this research, Python has been adopted as the command language for the radiation damping assessment. Tcl has been used for implementation of the macro-element.

4.2 Initial model

Linthorst [27] created a model of the jack-up unit in OpenSees, which has been further improved by GustoMSC. The model has been designed such that the mass distribution and eccentricity approximate those of the jack-up unit. The jack-ups eigen frequencies have been verified against FE analysis in MiniFEM. The residual error compared to the detailed model is in the range of $0 - 4\%$ for the first four eigenmodes. The effect of the crane on the jack-up response has been assessed, and has no major influence on the overall jack-up response. When a load is attached to the crane, it even reduces the seismic response (not accounting for potential crane collapse). As it does increase computational time and many crane configurations are possible, the crane is left out of the jack-up model.
Ground accelerations are applied at the soil node, and a transient analysis is performed. The model takes geometric non-linearity into account.

The model consists of fully elastic Timoshenko beams as displayed in Figure 4.1. The soil resistance against spudcan motion is included by applying uncoupled linear springs in every degree of freedom on the soil nodes. A Rayleigh damping of 5% is used to account for material, hydrodynamic and aerodynamic damping. Added water mass is included in the model in accordance with ISO 19905-1. No added soil mass is included in the model.

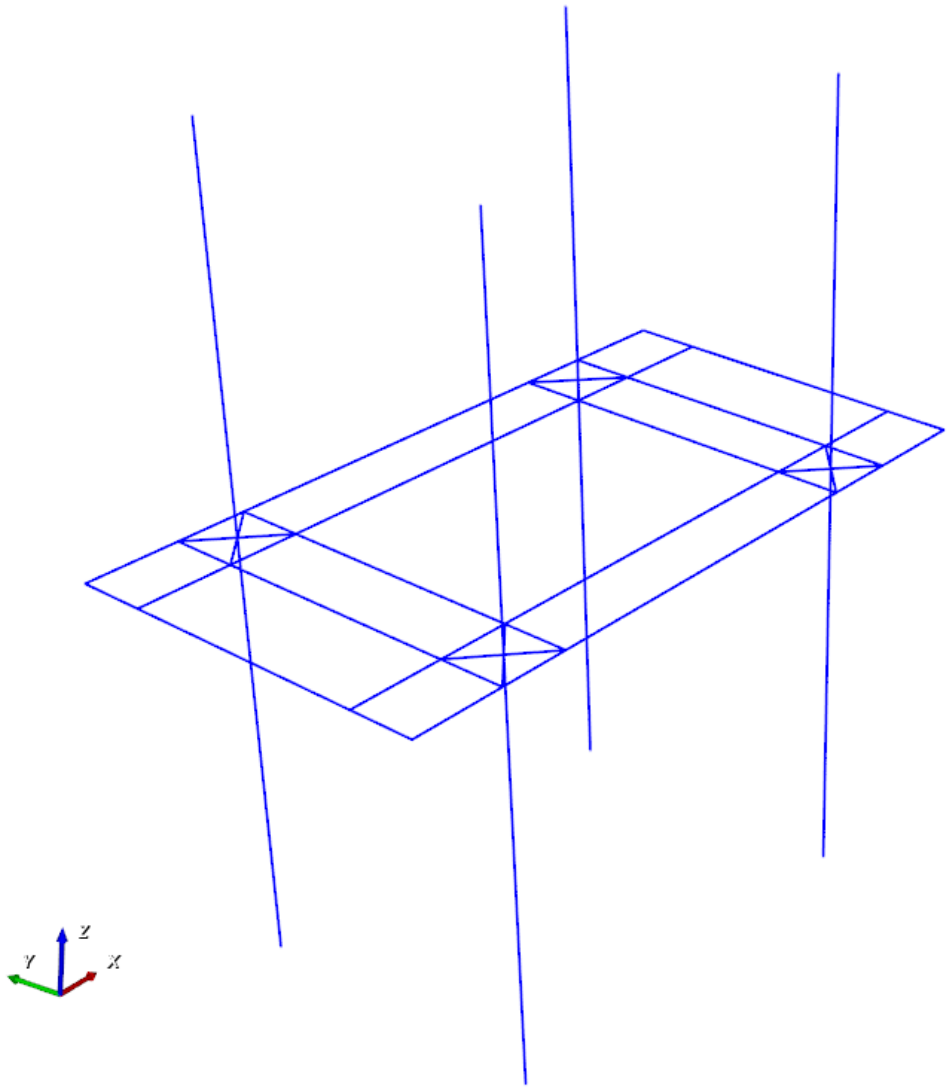

Figure 4.1: Model of jack-up unit as developed by GustoMSC

4.2.1 Seismic loads

The jack-up model is subjected to seismic loading by applying accelerations at the foundation nodes. These acceleration time traces are generated using SeismoMatch software. The accelerations are selected from a database and matched to the target response spectrum (location specific), for a specific return period, with the SeismoMatch software by means of wavelet scaling. At present, the input ground motion is damped beforehand as displayed in 4.3.

In order to illustrate typical effects of the ground motion on the footing node response is displayed below. In Figure 4.2 and 4.3 the horizontal and vertical ground accelerations are plotted. In Appendix B all ground accelerations used in this research are plotted. The horizontal ground motions typically starts with a sequence of high-frequency pressure waves. The time interval between the arrival of P-wave and other destructive waves depends on depth, distance from epicenter and magnitude. It is usually in the order from seconds up to one minute [21]. The severe motions that follow are caused by shear waves. Both pressure waves and shear waves are body waves. Surface waves typically have a longer period and slower decay. They consist of Love and Rayleigh waves, which both cause horizontal motion. Vertical ground motions are generally not preceded by

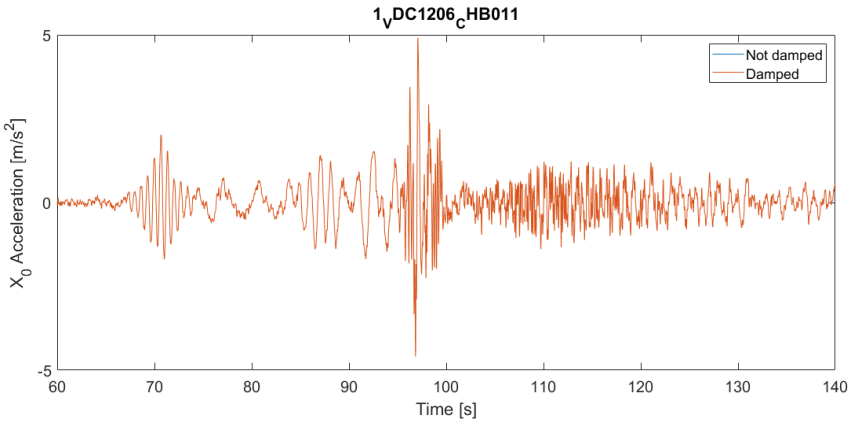

!h]

Figure 4.2: Horizontal ground motion with current (damped) ground motion and undamped ground motion

P-waves, unless the epicenter is near the jack-up location. Shear waves can have a vertical component and Rayleigh waves are the only surface waves inducing vertical ground motion.

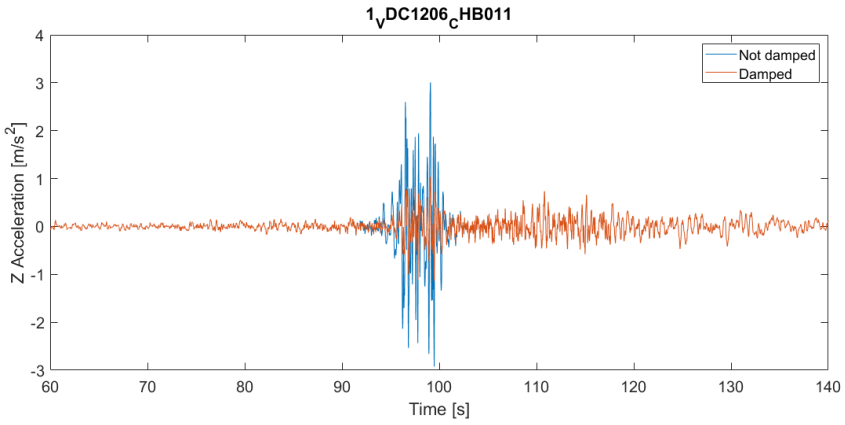

Figure 4.3: Vertical ground motion with current (damped) ground motion and undamped ground motion

4.2.2 Foundation stiffness and radiation damping

In this thesis foundation stiffness is defined as the force-displacement ratio of the spudcan in soil. The foundation stiffness is calculated using the methodology described in ISO19902 [17]. In order to account for vertical radiation damping, the response spectrum to which the time traces are scaled in SeismoMatch is reduced by a factor as determined in Equation 2.1, based on the response spectrum. Generating time traces with this method requires the user to specify the frequency at which the radiation damping is expected to be dominant. This is generally the first eigenmode with high vertical mass participation. In this method, phase information is lost. The explicit radiation damping is therefore more appropriate in time-domain analysis.

By modelling the radiation damping as a linear dashpot, radiation damping can be represented in a more physically correct manner. It would also improve usability of the model.

4.2.3 Other simplifications

The dynamic behaviour of the crane is excluded from the model. The influence of the crane is extensively described by Linthorst [27], and is considered limited. Additionally, the model does not take reserve capacity due to steel plasticity into account. Secondary effects such as incremental collapse and fire damage are not regarded.

4.2.4 Implementation radiation damping

This dashpot is placed in vertical direction under all four footing nodes, parallel to the foundation spring as displayed in Figure 4.4. ISO19905-1 proposes a damping coefficient as determined in Equation 2.2 [28]. In this direction the radiation damping is significantly higher due to the larger soil stiffness and contact area. Although horizontal radiation damping occurs (under assumption of fully elastic soil [12]), design standards recommend to not include it [19]. Implementation of the non-linear foundation might allow application of radiation damping on the far field side in all DOF. This is however considered outside of the scope of this research. The viscous damper is modelled with the Uniaxial Material 'Viscous', as described in Minjie [30]. The material has been assigned a power factor of 1, which ensures linear damping. The material is then implemented in the zeroLength element Minjie [31] connecting the footing node and soil node, parallel to the foundation spring. The adopted damping coefficient is calculated according to 2.2 in all four legs.

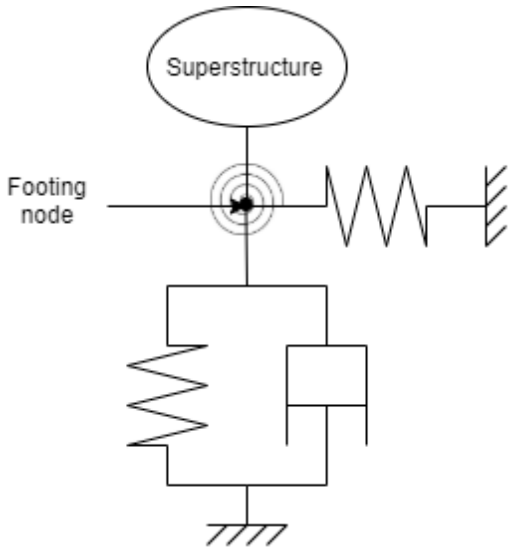

Figure 4.4: Rheological model of foundation, simplified to 3 DOF.

4.3 Implementation macro-element

To the best of the authors knowledge, no published work is available on the implementation of macro-elements in OpenSees. In this subsection two implementation strategies are discussed and the chosen implementation is elaborated.

4.3.1 Compilation strategy

The macro-element made available to GustoMSC is written in Fortran, and could theoretically be implemented in OpenSees in two ways:

- Duplicate an existing OpenSees NDMaterial, which is a material that has properties in multiple DOF. Modify it to an exact C++ equivalent of the Fortran model, while leaving the interface with OpenSees intact. The new material can then be submitted on the OpenSees Github, allowing the developers to include the material in the next OpenSees release.In hindsight, the advantages of this method are as follows:
  - No DLL needs to be compiled, start directly from working OpenSees material
  - No rewriting from UniaxialMaterial to NDMaterial needs to be done
  - The material also functions in the Python environment

- OpenSees provides instruction and an example UniaxialMaterial which should be ready to compile as a C++ DLL. The material should then be modified to be an NDMaterial and stripped from its material properties. Instead, it should call the Fortran DLL. In hindsight, the advantages of this method are as follows:
  - No need to translate Fortran code to C++, preventing human error and saving time
  - Not dependent on OpenSees developers for implementation
  - The DLL will continue to work with future releases of OpenSees, whereas integrated materials require regular maintenance
  - Macro-element remains confidential and within GustoMSC

  The second option appeared to be the easiest to develop, and was therefore the chosen strategy. In hindsight the first option would have been easier to implement.

4.3.2 Approach

The following challenges have been overcome in order to implement the macro-element in OpenSees:

- The example script to compile a C++ UniaxialMaterial DLL provided in the OpenSees package is outdated and not working. Several improvement were made which led to successful compilation.
- OpenSees has been fully compiled, allowing to debug occurring errors effectively.
- As the macro-element has no geometric properties, it should be implemented in a massless ZeroLengthND [32] element. The author identified several errors in the source code and made the outdated element fully functional again.
- The UniaxialMaterial DLL was extended to an NDMaterial that is able to redirect all required material input and state variables to the Fortran DLL. Values returned by the Fortran DLL are correctly implemented back into the OpenSees framework.
- The C++ DLL has been extended to allow for the use of multiple macro-elements (on multiple legs) while using a single C++ DLL and a single Fortran DLL.

4.3.3 Software architecture

In order to implement the hypoplastic foundation model in the jack-up model, the user defines a ZeroLengthND element. An OpenSees element contains the geometric, inertial, damping and stiffness properties. The ZeroLengthND element has no length in any direction, and therefore no mass. After the modifications made by the author it is able to provide a coupled stiffness in all 6 DOF. When OpenSees calculated the displacement at the two nodes connected by an element, it will call the element. The element then calculates the strain, which is sent to the material. The material and its properties have been defined by the user, as described in 3.3.3. Based on the strain and the material properties, the stiffness matrix is determined. In this case, the material is a C++ DLL that provides an interface with the macro-element (Fortran DLL). It passes on the displacement, rate of displacement and time increment to the macro-element. The macro-element then returns the force vector and stiffness matrix. These are returned to the ZeroLengthND element and then passed on the OpenSees solver, which recalculates the displacement. This process is iterated until the force converges to a value which is in balance with all other forces in the structure.

In Figure G.11 in Appendix G a flowchart of the macro-element implementation is provided for developers. In Figure 4.5 a high-level flowchart of the macro-element implementation is provided.

4.3.4 Implementation in OpenSees model

The macro-element effectively replaces the six linear springs that previously modelled the foundation (see Figure 4.4). It is thus placed parallel to the radiation damper. This overestimates radiation damping, but allows for easier comparison between the linear and non-linear model. For engineering practice, it is

recommended to place the viscous damper on the far-field side of the macro-element, in parallel to a spring that has the same stiffness as the elastic range of the macro-element. When performing simulations, OpenSees is not able to perform eigen analysis with the non-linear foundation. This makes it impossible to determine Rayleigh damping. To allow for inclusion of Rayleigh damping, the foundation model initially consists of a linear spring that has the same stiffness as the elastic range of the macro-element. Rayleigh damping is then fitted on the linear model, after which the spring is replaced by the macro-element.

4.4 Conclusion

The macro-element has been successfully integrated in the OpenSees framework. This is a major achievement, and opens a whole new range of OpenSees capabilities. It allows for extensive research into non-linear foundation behaviour while maintaining its industrial applicability. Chapter 5 proceeds however with the linear foundation model, to be able to clearly distinguish effects of the viscous radiation damping. In Chapter 6 the combination of the viscous radiation damping and hypoplastic macro-element is verified.

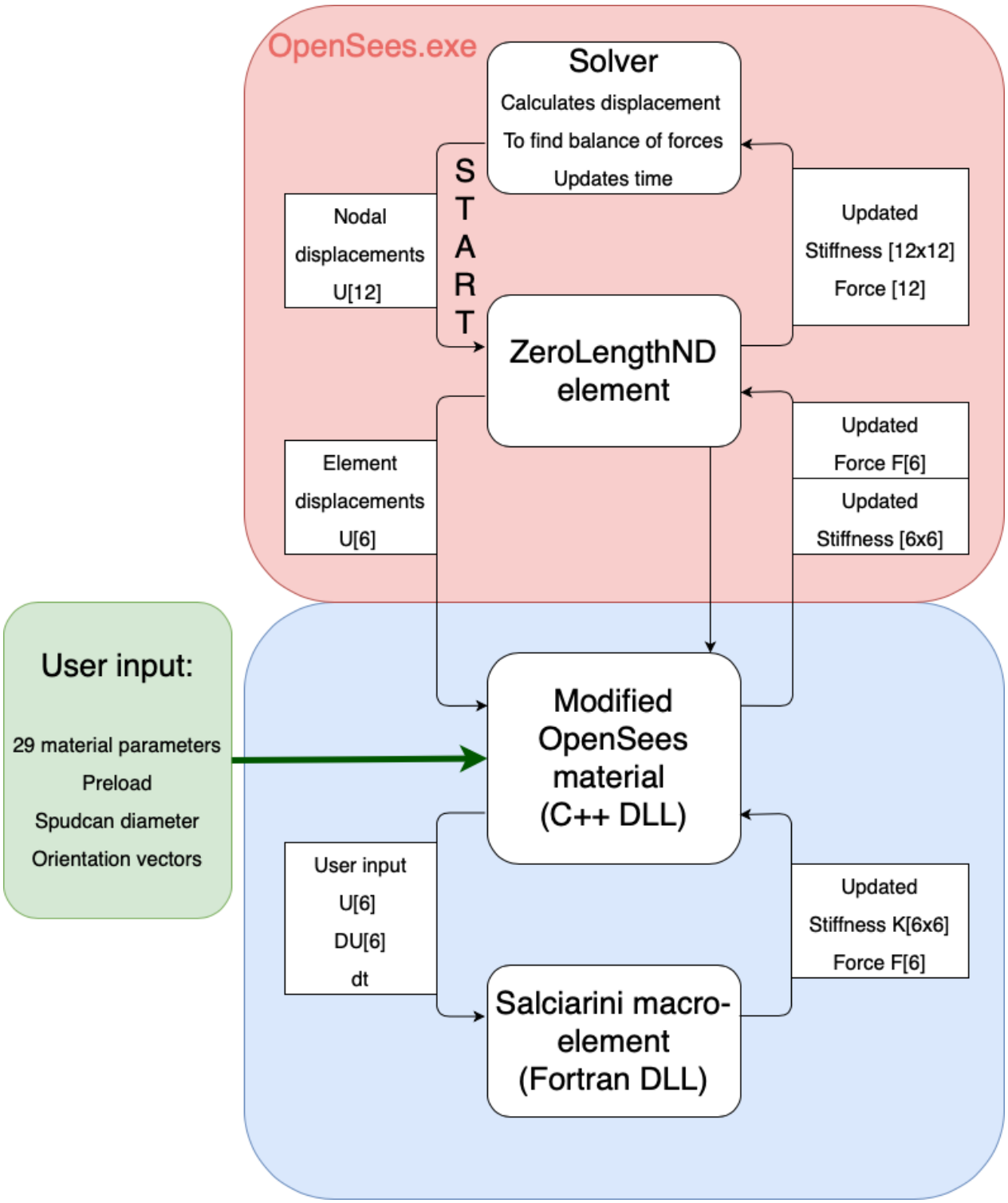

Figure 4.5: Flow chart describing the implementation of the hypoplastic macro-element. In red, the OpenSees main program. In blue, the macro-element implementation

Chapter 5

Explicit radiation damping

5.1 Introduction

As described in Section 4.2.2, radiation damping is currently included by reducing the response spectrum to which time traces are scaled. This requires significant engineering effort. Radiation damping can also be implemented by means of a vertical viscous damper with a damping coefficient as determined by Lysmer and Richart [28]. The model implementation is described in Section 4.2.4. this section discusses the verification and effect of the viscous damper in the OpenSees model.

The macro-element has not yet been implemented in this phase. This allows easier identification of the effects of impedance and viscous damping.

The expected effect of the radiation damper is threefold:

- The current radiation damping is tuned to a single frequency, at which the radiation damping is expected to be most dominant. This results in underestimation of damping at higher frequencies. Theoretically it also leads to overestimation of damping at low frequencies, but radiation damping at these frequencies is negligible.
- The current method directly reduces the ground accelerations. When a viscous damper is included, the velocity difference between soil node and spudcan node is damped, meaning motions of the superstructure are included in the damping as well. This is expected to reduce residual vibrations in the structure when ground motions have decreased.
- As the effect of radiation damping is limited, it is not expected to have a large influence on unity checks. The influence is expected to increase for stiffer configurations.

5.2 Verification

The current model and model with vertical radiation damper have both been subjected to seven ground acceleration time traces. These time traces have been generated in accordance with ISO 19901-2 as described in Section 4.2.1. They are displayed in Appendix B.1.

First, the correctness implementation of the damper is verified by back-calculating the damping coefficient from the velocity and force difference between the footing and soil node See Figure C.1 in Appendix C. This confirmed that the damping coefficient remains correct throughout all simulations.

Then the influence of the damper is checked by setting the damping coefficient to zero and by exaggerating the damping coefficient with multiple orders of magnitude. As expected, zero radiation damping leads to approximately the same response at low frequencies, and a larger response at high frequencies. The exaggerated damping correctly damps all vertical motion of the footing at all frequencies. As expected, the footing response at higher frequencies are fully damped.

The damper has now been verified to work and simulations have been performed for a depth of 30 meters and an airgap of 10 meters. This is a common operational configuration. The results have been analyzed for seven earthquakes, in all directions. In order to explain the effects of explicit damping, the results of a

single earthquake from one single direction are presented below. As the effect of the radiation damper is best observable on the footing node, the motions of this node have been analysed.

5.3 Effect on footing response

In Figure 5.2 the Power Spectral Density (PSD) of the relative (to the ground) mudline node is presented. This node is just above the footing, at the same level as the soil surface. The two horizontal degrees of freedom have a similar response, which is to be expected. In vertical direction it can be observed that at low frequencies the response is similar. The motions at these frequencies are governed by hull motions, which are excited by horizontal forces, and therefore not much effected by the radiation damping. At higher frequencies, in the range where the first vertical modes occur, the explicitly damped system shows a larger response in all seven earthquakes. Due to the the reduced input ground acceleration, 100% of the energy damped by radiation never enters the system. With explicit radiation damping, some of the energy enters the system when the footing and soil velocities are in phase. Likewise, extra energy is absorbed when the velocities are out of phase. It seems likely that the velocities are more often in phase than not, causing a more severe vertical motion. At very high frequencies, beyond the first vertical modes, the reduced input method is too conservative, but effects on the velocity PSD vary. For displacement PSD, the explicit damping clearly has larger response. Please refer to Appendix C.2 for footing displacement and velocity PSD's of all earthquakes. In Figure 5.1 part of the time trace of a footing node response is plotted. The initial vibrations (before t=95 seconds) are caused by horizontal motions, which excite the lower modes. The low frequency of these modes explain the close match of the two models. At 95 seconds, strong vertical ground motions start to occur, exciting the first vertical modes. The higher extremes of the explicitly damped model are explained by the in-phase motions of soil and superstructure. After 110 seconds the earthquake excitation diminishes, and superstructure vibrations are more rapidly damped out by the explicitly damped model. Please refer to Appendix C.3 for all mudline node velocities. The ground motions accelerations are compared to footing accelerations in Appendix C.4 to make phase differences visible.

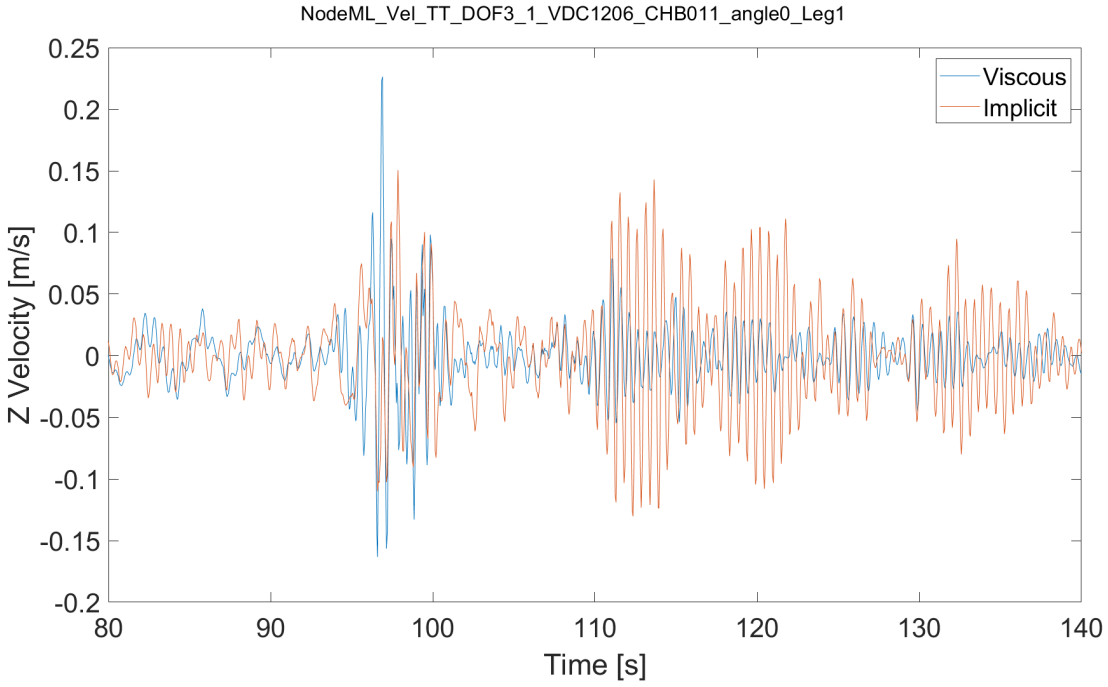

Figure 5.1: Footing node velocity for old (implicit) and new (viscous) model. In horizontal, horizontal and vertical direction (Japan 1000-yr, EQ3, $\theta = 0$, leg 1).

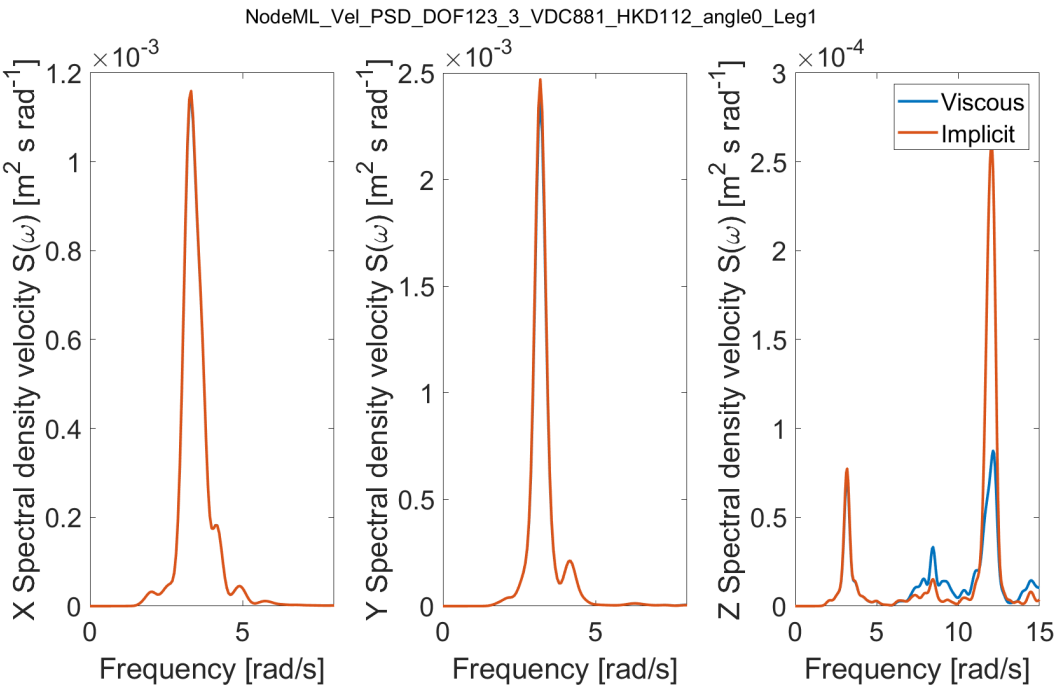

Figure 5.2: Mudline node velocity PSD for old (implicit) and new (viscous) model. In horizontal, horizontal and vertical direction (Japan 1000-yr, EQ3, $\theta = 0$, leg 1)

	Difference [%]
Max UC Sand bearing	0.63
Max UC Sand sliding	-3.67
Max UC Jacking system	-0.02
Max UC Lower Guide	0.05
Max UC Preload exceedance	-3.87
Max UC X-brace	-0.63

Table 5.1: Change in utilization (Unity Check) due to viscous radiation damping

5.4 Effect on utilization

Unity Checks (Load/capacity) are used to quickly assess overall utilization on structure. The structure is subjected to seven earthquakes coming from 12 directions. For each earthquake the highest Unity Check is used. The mean of the seven resulting values is the governing Unity Check. The results of the Unity Checks are presented in Table 5.1. The difference of the explicitly damped model is displayed with respect to the current model. A negative difference means a lower load compared to the current model and is favourable. The Unity Checks have been performed with 30 meter water depth and an airgap of 10 meter.

In general, the difference between the two models is <1.5%, with the exception of failure modes in which vertical forces are dominant. Vertical forces are dominant for the sliding case and preload exceedance.

5.5 Conclusion

The explicit radiation damper has a small but significant effect on the motion of the structure. It is a more physically correct method and improves usability of the model. It can be used in combination with a macro-element by placing it on the the damper on the far end of the macro-element, parallel to a spring with the same stiffness as the macro-element initial stiffness. This applicability makes the viscous damper a significant

improvement of the model, which will be included in analysis of the non-linear foundation in the following chapters.

Chapter 6

Verification macro-element

In this chapter the verification of the hypoplastic macro-element as developed by Salciarini and Tamagnini [36] is described. The hypoplastic macro-element is first verified in a two-node model to easily distinguish effects, which is followed by verification against the pile model as described in Grange et al. [13]. After implementing the macro-element in the jack-up model the orientation and elastic behaviour is verified. Several sets of material parameters from literature [35][13][43][23] are used, which can be found in Appendix D. An explanation for these parameter values is provided in 3.3.3 An in-house developed equivalent of the macro-element has previously been built in Matlab, which has been verified against the pile model and cyclic tests. This Matlab model is used to perform verification of the two-node and pile model.

6.1 Two-node verification

The two-node OpenSees model consists of two massless nodes connected by the hypoplastic macro-element. Node 1 is fixed to its surroundings, and Node 2 can move without constraints. The parameters as in Appendix D.1 are used, with no coupled stiffness and no hardening. The verification performed on the two node model is performed as follows:

- A small single force, exciting only the small strain behaviour is applied to Node 2. After this, small forces in all DOF are applied simultaneously. Additionally, coupled stiffness is activated and verified. Results are presented in Table E.1 in Appendix E.1 The results are clearly elastic, which verifies the orientation and elastic behaviour of the macro-element.
- A single vertical force is applied in combination with a force in each other DOF separately. These forces are increased up to yielding. When no vertical force is applied, the macro-element fails directly due to the load-state being outside of the yield surface. This failure occurs each time the yield surface is exceeded. This is a major disadvantage of the element, as strong earthquakes are likely to lead to full yielding. The stress-strain diagrams are plotted in Figure E.1 and E.2 in Appendix E.1. It can be observed that the response in the OpenSees macro-element implementation deviates slightly from the Matlab equivalent. The error increases closer to the yield surface. The error is step size dependent, which is displayed in Figure 6.1 and E.4 in Appendix E.2. When performing dynamic analysis, the error can be reduced by increasing numerical damping. This error is suspected to result from the different solution algorithm in OpenSees and is considered acceptable.

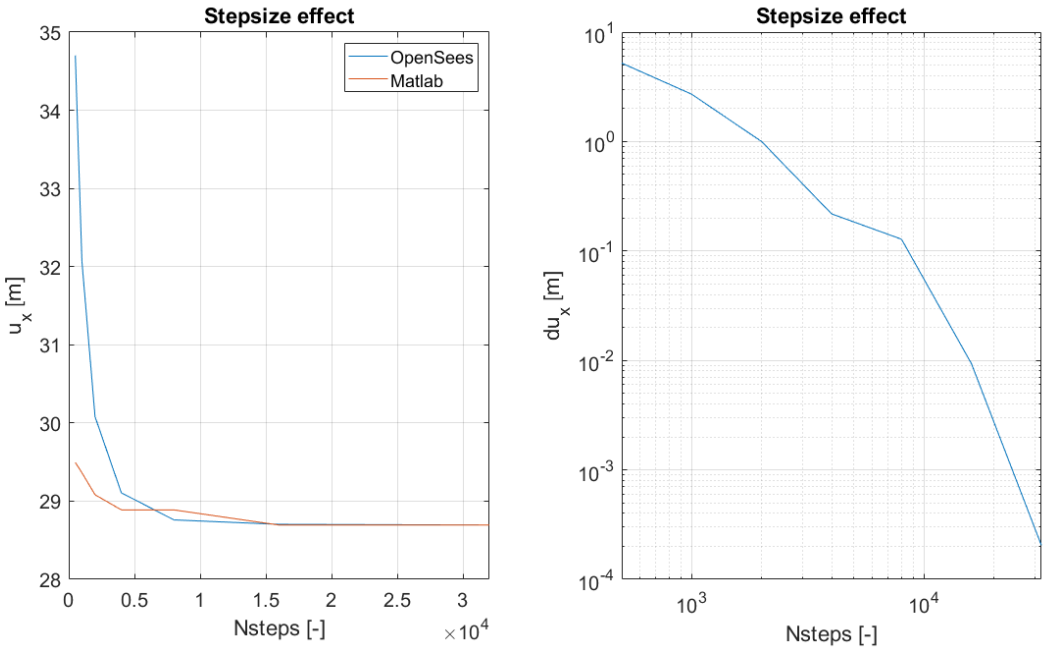

Figure 6.1: Step size convergence of OpenSees macro-element and Matlab equivalent

6.2 Pile model

The pile model as described in Grange et al. [13] is a single 3-DOF pile with circular footing on sand [5]. A constant gravity force has been applied on the structure in combination with an oscillating horizontal force applied at the top. A static analysis has been performed in Abaqus by the authors, and results have been made available to GustoMSC. The material parameters are as specified in Table D.2 in Appendix D.2. The model has been reproduced in OpenSees. The results show a 0.5% error which can be fully reduced by increasing the number of steps tenfold. The error mainly occurs in vertical direction, which is due to more plastic behaviour in this DOF.
The successful verification proves the interface between OpenSees and the macro-element DLL's is working and the modified version of OpenSees can correctly integrate a hypoplastic macro-element. The motions of the foundation nodes are plotted in Figure 6.2 below and in Figure E.3 in Appendix E.2.

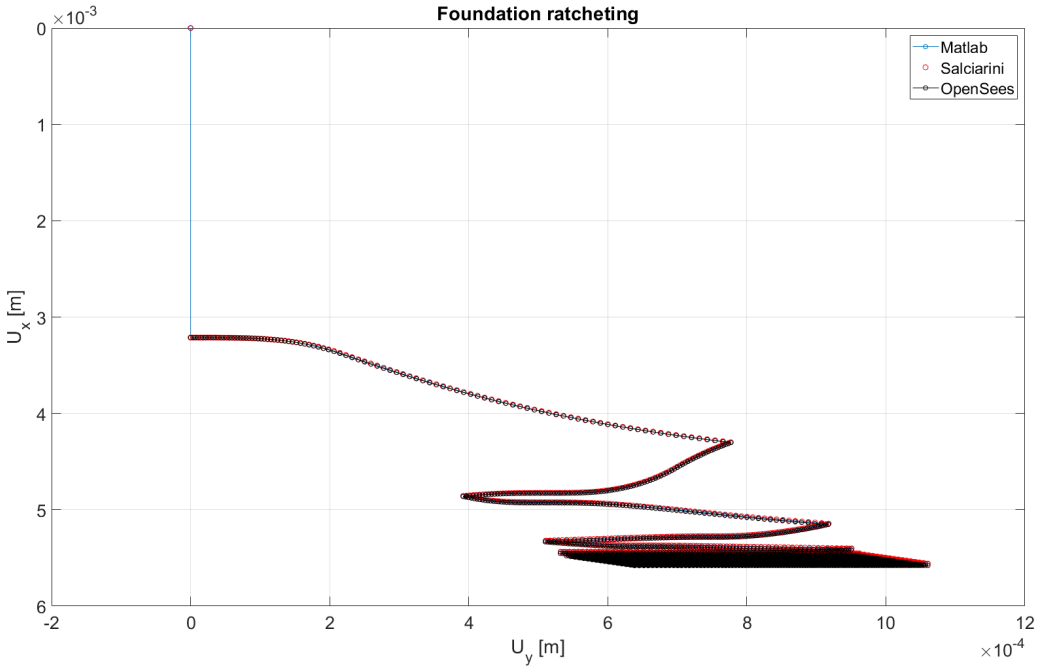

Figure 6.2: Foundation ratcheting in horizontal and vertical direction

6.3 Implementation in jack-up

After implementation of the macro-element in the OpenSees jack-up model, the following aspects require verification:

- The macro-elements should correctly store and call the state variables of the four legs separately, without using a different DLL for each leg
- The orientation should be correct
- The solution algorithm used in dynamic analysis should not introduce errors

These aspects can all be verified by a single simulation, in which the yield surface is expanded orders of magnitude and the elastic nucleus within the yield surface is as large as possible. This should lead to a foundation response exactly equal to the response with linear elastic footing. Parameters are used as in Table D.7 in Appendix D.3. The macro-element produced results exactly equal to the linear elastic model in all six DOF, verifying a proper implementation of the macro-element foundations in the jack-up model. See Figures E.5 and E.6 in Appendix E.3.

6.4 Conclusion

The implementation of the macro-element in the OpenSees jack-up model is now considered fully verified. The next Chapter discusses the effects of the macro-element implementation on the seismic response of the jack-up.

Chapter 7

Case study and sensitivity analysis

7.1 Introduction

In this chapter, the effects of non-linear foundation modelling on the seismic jack-up response are assessed. It aims to provide qualitative understanding of the introduced phenomena and quantifies the impact of varying material parameters on the structural response. The chapter begins with a preliminary investigation is carried out on the two-node and pile model. This is done to gain qualitative understanding of the effect of empirical material parameters on the dynamic behaviour. An extensive case study has been performed for the parameters determining non-linear behaviour. This case study consists of the following components:

- An extensive study of the base case scenario as described in Section 7.3. This section extensively describes the dynamic behaviour introduced by the macro-element in detail for a 200-yr return period earthquake. This analysis is performed to gain understanding in the occurring phenomena and formulate preliminary conclusions and hypotheses. It provides the basis for further parameter analysis.
- The sensitivity study is concluded with simulations using four parameter combinations as found in literature [35][13][43][23]. These simulations are performed with an 100-yr return period earthquake. This Sections aims to verify preliminary conclusions and hypotheses from the preceding section.
- Some material parameters of the macro-element can easily be determined using industry standards. This is for example the case for the initial stiffness and load capacities. The parameters describing flow and non-linearity are not well defined in literature. These material parameters can only be empirically determined by means of FE analyses or experiments. To provide an estimate of the influence of these empirical parameters, a sensitivity study is performed in Section 7.5. In this Section, parameters are varied separately, using parameters found in literature [35][13][43][23]. Simulations are performed with an 100-yr return period earthquake. This improves understanding in the role they play in the jack-up response and checks consistency of the conclusions from preceding sections. It also provides insight on whether there are clearly conservative and unconservative parameter value ranges.

Each parameter combination is simulated using seven earthquakes, which are described in Section 7.3.1. The seismic jack-up analysis produces a vast amount of data. For the single base case, there are 7 earthquakes, 12 jack-up orientations, 422 nodes, 4 legs and 6 DOF. The response can be expressed in terms of force, acceleration, velocity, displacement and spectral density. When example plots are provided, this is always done for earthquake 3. The response is mainly analysed at two nodes: The footing node (spudcan) and the lower guide node, which is positioned at the leg and is connected to the lower guide of the hull. The footing node shows the most direct effect of the macro-element, and allows us to track the load-state within the macro-element. The hull-leg node, which is at the connection of the leg with the hull captures the overall response of the structure very well. Together with the footing node, it is a critical point in the structural integrity during an earthquake.
The loads, motions and spectral densities of the base case are considered in detail. For horizontal motions and forces, the two lateral directions are combined to reveal total horizontal magnitude. The equivalent is done for rotations and overturning moments. Torsion of the legs normally does not limit the bending

mode [−]	Frequency [rad/s]	Frequency [Hz]	Period [s]
1	1.90	0.30	3.31
2	1.92	0.31	3.28
3	1.95	0.31	3.22
4	9.96	1.59	0.63
5	11.05	1.76	0.57
6	11.30	1.80	0.56
7	13.03	2.07	0.48
8	16.98	2.70	0.37
9	17.60	2.80	0.36
10	17.73	2.82	0.35

Table 7.1: Eigenfrequencies and periods based on small-strain stiffness. For a jack-up with 40 meter leg length.

moment strength of the legs [19] and is therefore not considered. This is verified in Figure 7.9, which shows that the torsion at the leg hull connection is three orders of magnitude smaller. Power Spectral Density (PSD) plots are displayed along with the linear foundation model to provide insight in the shifting vibration frequencies and resonance. Overall structural performance is assessed by means of Unity Checks.To check whether different legs and different orientations show significantly different results, maximum values of each time trace are compared. These maximums are averaged over the seven earthquakes and plotted per leg with respect to jack-up orientation. This data can be further condensed by taking the single maximum force or displacement of all legs and orientations and then averaging this value over the seven earthquakes. This value can then be plotted as function of the parameter value. These key figures are used to present the data of the sensitivity analysis in a concise manner.
The ground accelerations and Power Spectral Density (PSD) plots of these earthquakes can be found in B For comparison, the PSD plots of the hull accelerations are plotted together with the PSD plots of the ground motions. The horizontal ground motions peak between $2.5 - 10[rad/s]$, which corresponds to $0.4 - 2.0[Hz]$ or $T = 0.5 - 2.5[sec]$. After this the amount of energy in the spectrum decays to 10% of the peaks around 30 rad/s and to 1% around 50 rad/s. Please note that this ground motion has an atypical response peak around $2.0 - 3.5rad/s$. This is the result of a resonating soil layer at this specific location. It leads to increased resonance of the (linear) model, since the first three eigenmodes of the jack-up are precisely at these frequencies for depths lower than 35 meters. It also leads to less dominant vertical modes.
Eigenfrequencies and eigen periods are provided in Table 7.1. These values are for 30 meters water depth and 10 meter airgap, and are determined based on small-strain foundation stiffness. Corresponding mode shapes can be found in Appendix G.1 Please note that the mode shapes are calculated using the linear foundation model. For the non-linear model, every load state and thus every single moment in time has unique mode shapes and corresponding frequencies. The occurring vibrations could take significantly different forms.

7.2 Preliminary investigation

The effect of each of the following parameters has been visualised by performing a small sensitivity analysis on a two-node model and pile model. This is documented in Appendix F.1. Only κ and m_R appear to have a clear effect on the two-node model response, and are displayed in Figure F.1. Increasing κ reduces the curvature of the force-displacement relation, with its effect evenly distributed. Increasing m_R causes drastic stiffness reduction in the small-strain region, which can only be observed when zooming in by orders of magnitude. In more complex loading scenarios the other parameters reveal their effect more clearly. This is shown in Appendix F.2. All parameters have a major quantitative influence on the displacement path. This has also been described by Figure 3.1 in Section 3.3.3.

7.3 Base case

7.3.1 Description scenario

The base case consists of a jack-up positioned in 30 meter deep water with an airgap of 10 meter. The structure is exposed to an earthquake with a 200-year return period at an offshore location in Taiwan. The time traces and PSD of these earthquakes can be found in B.2. When exposing the structure to stronger earthquakes, the load state exceeds the yield surface in horizontal direction. The macro-element is not able to cope with the zero stiffness that then occurs, and crashes. This also happens while hardening is activated. The numerical instability can be prevented by:

- Increase the horizontal yield capacity by a factor two. This is an undesirable workaround, and not recommended.
- Reduce time step. This significantly slows down the simulation and only helps if the load state does not exceed the yield surface for smaller time step, which is often not the case. This method is not recommended.
- It is recommended to extend the macro-element with a return mapping algorithm. When the load state is exceeded, the load should be reduced to the yield surface. This would lead to full yielding until the load-state reduces again and correctly models the physical behaviour.

Material parameters of the macro-element are displayed in D.4. Please note that the yield surface and stiffness coefficients are provided by literature [19][6].

7.3.2 Analysis strategy

First the footing node time-domain relative displacement is assessed. In this chapter, the term "relative" refers to relative motion with respect to the ground. Absolute motions are used when assessing hull accelerations. The time-domain footing displacements provide qualitative understanding of the effect of the macro-element in spudcan behaviour. Most importantly it contains the maximum and final footing displacement, which are indicative for (post-)earthquake stability, settlement, hardening, and bending moments in legs. An overview of the maximum displacements of all legs, jack-up orientations and earthquakes is provided.
Secondly, the footing time domain loads are assessed. These are the loads occurring in the macro-element, and thus do not include loads imposed by the radiation damper. The horizontal and rotational loads are governing in the structural integrity checks, and not directly influenced by the parallel viscous radiation damper. An overview of the maximum loads of all legs, jack-up orientations and earthquakes is provided. The load states with respect to yield surface are plotted to provide insight in the relevance of shaping parameters of the yield surface. Force-displacement relations are plotted to visualise occurring stiffness reduction and hysteretic damping.
The footing node displacement PSD is provided. In non-linear seismic analysis one should be careful when analysing the PSD, because the time-dependent variations in loading- and vibration frequency are not visible. Non-linear foundations obviously exhibit much time-dependent phenomena, but these have been covered by the preceding analyses. The PSD still provides some clarity regarding the vibration of the structure. For the base case, the relative displacement PSD is shown. The acceleration PSD better displays the effect of the macro-element on high order nodes, but these do not contribute significantly to jack-up motions and is therefore not displayed.
Similar data is shown for the lower guide. The Lower Guide node connects the leg with the lower guide of the hull. The majority of the hull weight is here transferred to the leg. All forces are transferred here by means of a rack and pinion system. In the jack-up model this connection is represented by linear springs in all six DOF. The leg node where these springs are attached are referred to as the "lower guide node" hereafter. The connection is referred to as the "leg-hull connection" or "lower guide springs". The loads at the leg-hull connection are critical in the seismic assessments. especially at large depths. Forces in the leg-hull connection are governing in many load cases, especially at large depths. Additionally, the horizontal displacements and at the lower guide are a good indicator of the global stability of the jack-up.

7.3.3 Footing node displacement time-domain

Time traces of the footing displacements of all 7 earthquakes in 6 DOF on 1 leg and 1 orientation can be found in Appendix F.3.1. The footing node displacement of leg 2 and 3 during earthquake 3 are also plotted here. The footing displacement of earthquake 3, leg 1, is displayed in 7.1. Please note that the ground accelerations belonging to these results can be found in B.

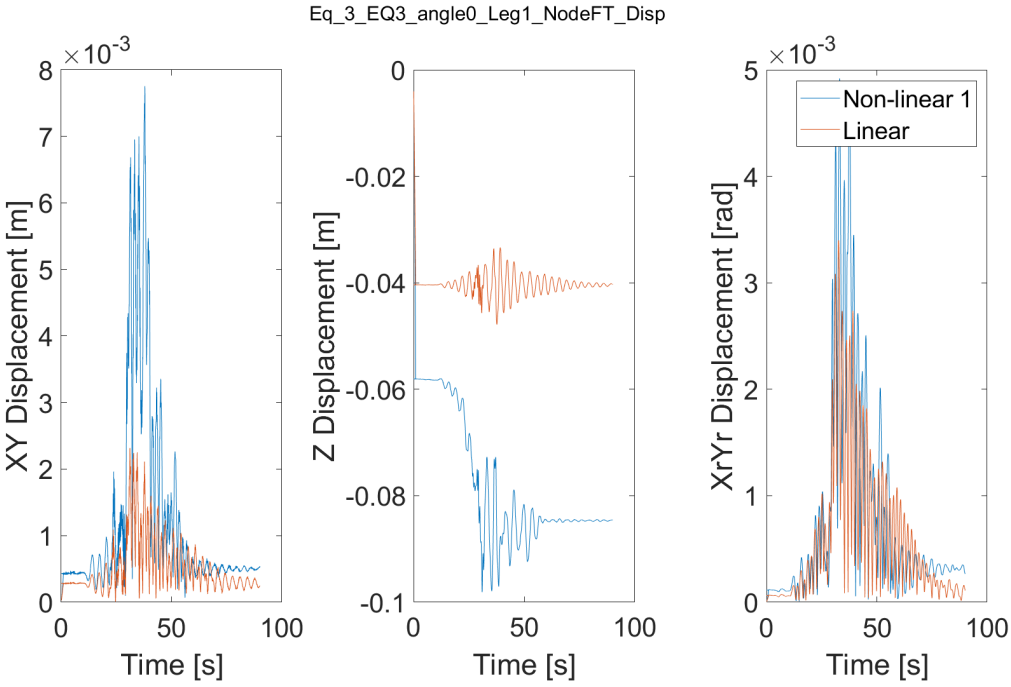

Figure 7.1: Footing displacement (Taiwan-200yr EQ3, $\theta = 0$, Leg 1)

In vertical direction the static loading instantly leads to plastic deformation, which is equal to the difference between the spring and macro-element model. Before the major vibrations of the structure (both footing and hull) reach their maximum magnitude, the structure penetrates further into the soil. This is caused directly by the (vertical) ground accelerations, which reach their maximum magnitude earlier than the jack-up vibrations. If hardening is accounted for, hardening would occur before the structure is fully excited, increasing its influence on the jack-up response. When the structures vibrations reach their maximum magnitude, they do not cause as much settlement. The plastic displacement in vertical direction is in the order of 10 centimeters, which is as expected. In some earthquakes, minor uplift occurs when the ground motions subdue. This is due tilting of the structure as a result of weight eccentricity.
For this parameter combination, the horizontal and rotational displacements are up to twice as large as the liner model. Ratcheting occurs with the final displacement being $10 - 40\%$ of the maximum displacement. This large variation is earthquake dependent and not dependent on legs and orientations. This effect is further visualised and explained in 7.4. In this load case, ratcheting does not cause significant bending moments in hull and legs. The increase in horizontal and rotational footing motions could induce higher bending moments in softer, more non-linear soils, and smaller depths.

Maximum displacements

Maximum displacement magnitude of all legs and orientations, averaged for earthquakes can be found in 7.2. The average maximum displacements are consistent for angles and legs. The most distinctive difference between the two models is the increased displacement at the footing node. Motions are still very limited and are not expected to induce major bending moments due to differential displacement, nor hardening.

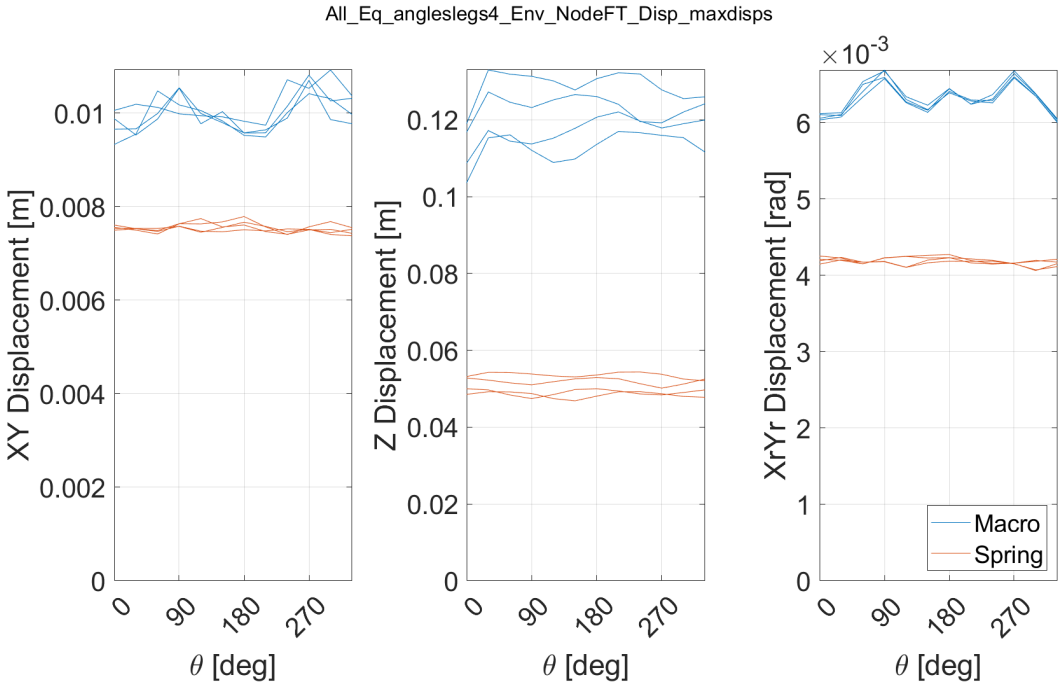

Figure 7.2: Maximum footing displacement, averaged over seven earthquakes for each leg (Taiwan-200yr)

7.3.4 Macro-element loads time-domain

Time-domain macro-element loads of all 7 earthquakes in 6 DOF on 1 leg and 1 orientation can be found in Appendix F.3.2. The loads of earthquake 3 are also displayed in 7.3.
A significant reduction in footing forces is observed. In all DOF, during the entire time span the loads in the macro-element are smaller than in the elastic foundation spring. This results in significantly reduced leg loads. This is caused by effects explained in 7.3.13. An overview of maximum loads is provided in Section 7.5 and 7.4. No significant residual loads are present.

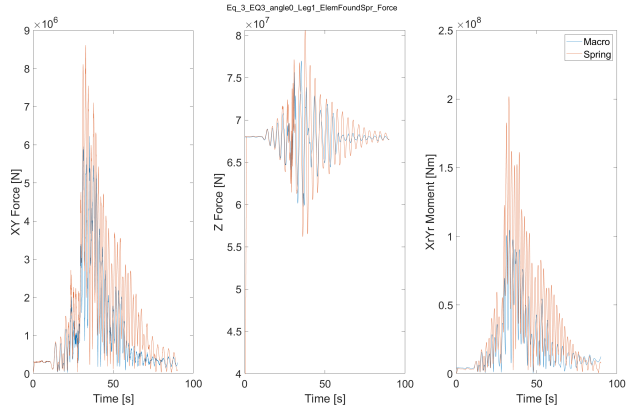

Figure 7.3: Time-domain force in macro-element (Taiwan-200yr, EQ3, $\theta = 0$, Leg 1)

7.3.5 Macro-element force-displacement time-domain

The force-displacement curves provide insight in the degree of stiffness reduction during the earthquake in each DOF. The surface area of hysteretic loops indicates the amount of hysteretic damping. This is mainly relevant when comparing f-u curves from different earthquakes or parameter sets.

In Figure 7.4 the force-displacement curves for earthquake 3 are displayed. The F-u curves for other earthquakes are similar. In Appendix F.4.5 the F-u curves of 4 parameter sets and four earthquakes are displayed. In horizontal directions a clear stiffness reduction is observed between small and medium strain regime. As the yield surface is not approached closely, not much stiffness reduction occurs in the high strain regime. This is underlined in Figure 7.5. It can be concluded that high strain regimes are not dominant for earthquakes with this magnitude.

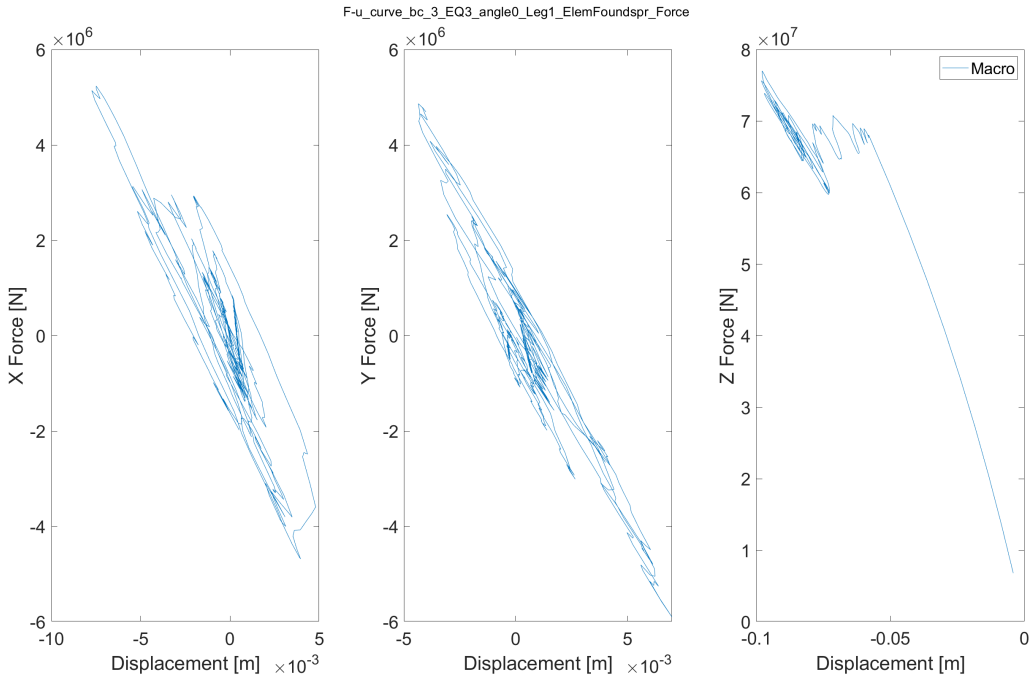

Figure 7.4: Time-domain force-displacement relation for base case (Taiwan-200yr, EQ3, $\theta = 0$, Leg 1)

7.3.6 Macro-element load-state time-domain

Plotting the load-state with respect to yield contours provides insight in the relevance of shaping parameters of the yield surface and plastic flow potential. Figure 7.5 for example shows that the shape of the points of yield contour and flow potential (controlled by β_1-β_4) do not contribute to the behaviour. As the load-state does not approach the yield surface very close, it is still difficult to draw conclusions from these plots. The increased variation in more non-linear behaviour could lead to different conclusions. The load state will therefore also be plotted in Section 7.4 for all parameter sets. The plots for other earthquakes are similar. in Appendix F.4.6 the load-states of 4 parameter sets and all earthquakes are displayed.

7.3.7 Radiation damper loads time-domain

The radiation damper has been incorrectly modelled parallel to the macro-element. Due to the plastic component, spudcan velocities are larger, which leads to overestimation of radiation damping. This section assesses the magnitude of the resulting error. The loads in the radiation damper have been plotted in Figure 7.6. The effect is maximal when vertical loads peak, leading to underestimation of settlement and vertical

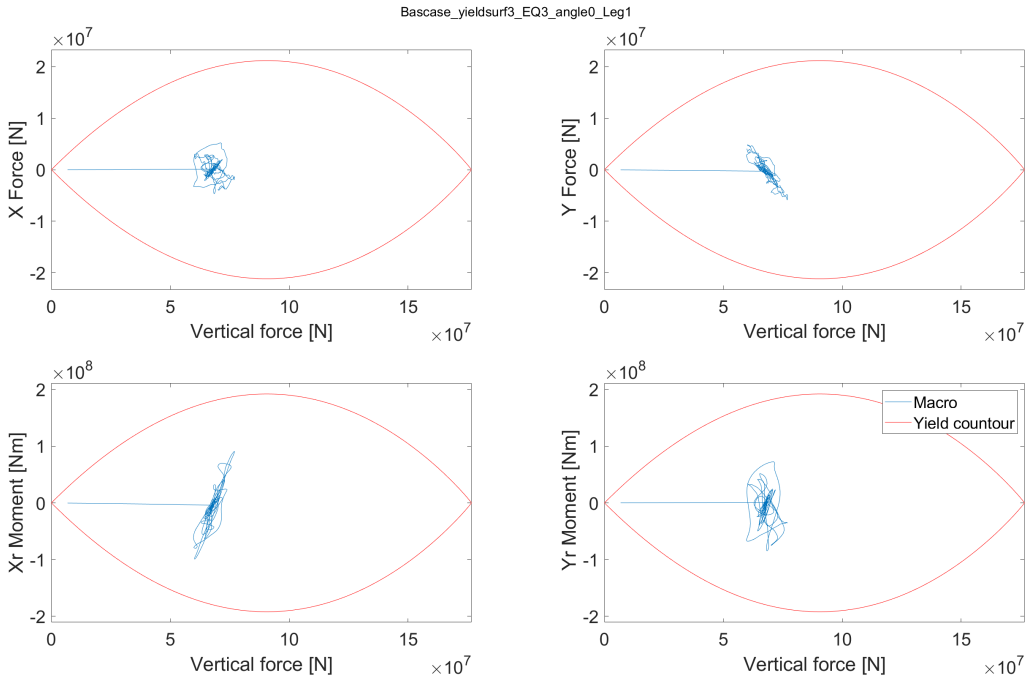

Figure 7.5: Time-domain load-state with respect to yield surface, in horizontal and rotational DOF (Taiwan-200yr, EQ3, $\theta = 0$, Leg 1)

vibration amplitude. From this figure it can be observed that the force overestimation in the radiation damper is much smaller than the force in the macro-element, and has therefore a limited effect. It can be concluded that the induced error acceptable.

7.3.8 Footing node displacement frequency-domain

The power spectral density of the footing node displacement of 7 earthquakes in 3 DOF on 1 leg and 1 orientation can be found in Appendix F.3.3. These are the PSD plots of the displacement **relative** to the ground. This means that only the superstructure effects are visible in the plot. A single example is provided in Figure 7.7 for earthquake 3.

Three major effects of the macro-elements are observed. The first displacement peaks of the first three eigenmodes (at 2 rad/s) have reduced in frequency in all earthquakes. This confirms the hypothesis that the vibration frequency moves away from the most severe ground motion frequencies. As a result, the peaks tend to be lower. Secondly, some PSD show small peaks left and right of the main peak at 2 rad/s. These are caused by peaks ground motions. Ground motions with a frequency of 1 rad/s are also able to modes with a frequency of 2 rad/s, leading to distinct peaks in the footing displacement PSD of earthquake 1, 2 and 4. Higher excitation frequencies can excite the lower modes partly. A peak is also visible at 0 rad/s, which corresponds to ratcheting.

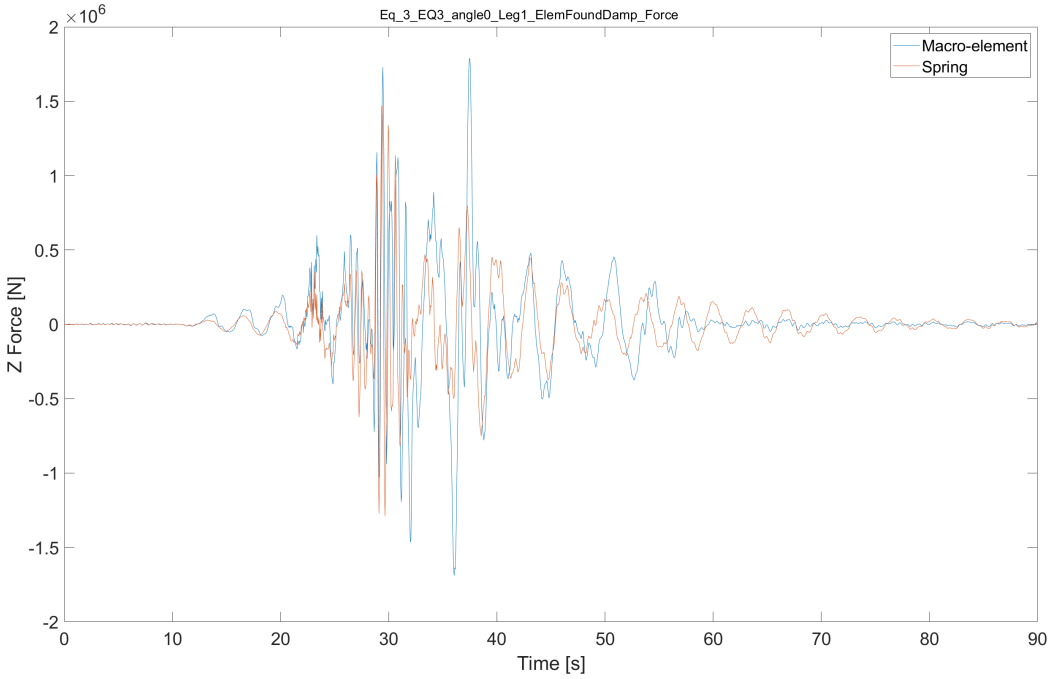

Figure 7.6: Time-domain force in radiation damper (Taiwan-200yr, EQ3, $\theta = 0$, Leg 1)

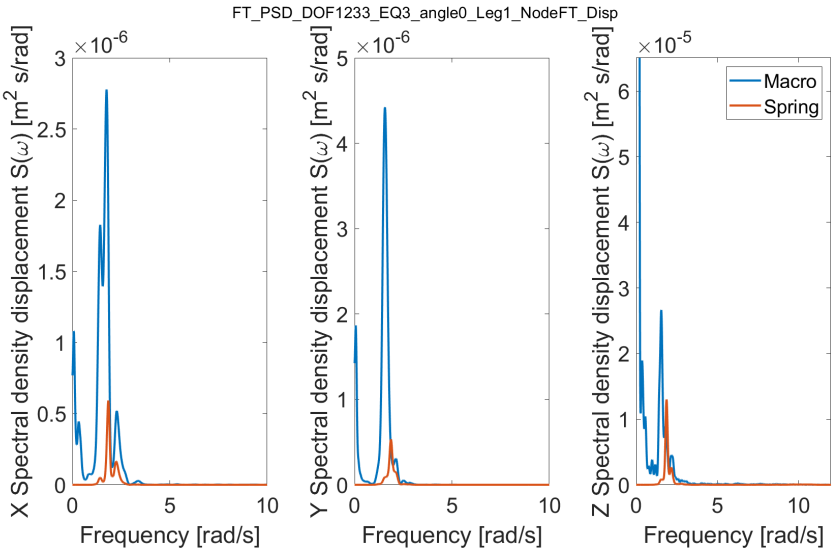

Figure 7.7: PSD of relative footing displacement for base case (Taiwan-200yr EQ3, $\theta = 0$, Leg 1)

7.3.9 Lower guide node displacement time-domain

Time traces of the displacements of 7 earthquakes in 6 DOF on 1 leg and 1 orientation can be found in Appendix F.3.4. The maximum horizontal displacements are approximately equal to the linear spring model, and stability is thus not severely effected in this load case. The faster diminishing displacements in the non-linear model are remarkable, and most probably caused by hysteretic damping. In vertical directions, displacements roughly equal footing node displacement and are not displayed.

7.3.10 Lower Guide loads time-domain

Time traces of the loads acting on the Lower Guide node of 7 earthquakes in 6 DOF on 1 leg and 1 orientation can be found in Appendix F.3.5 The loads occurring during earthquake 3 are plotted in Figure 7.8.

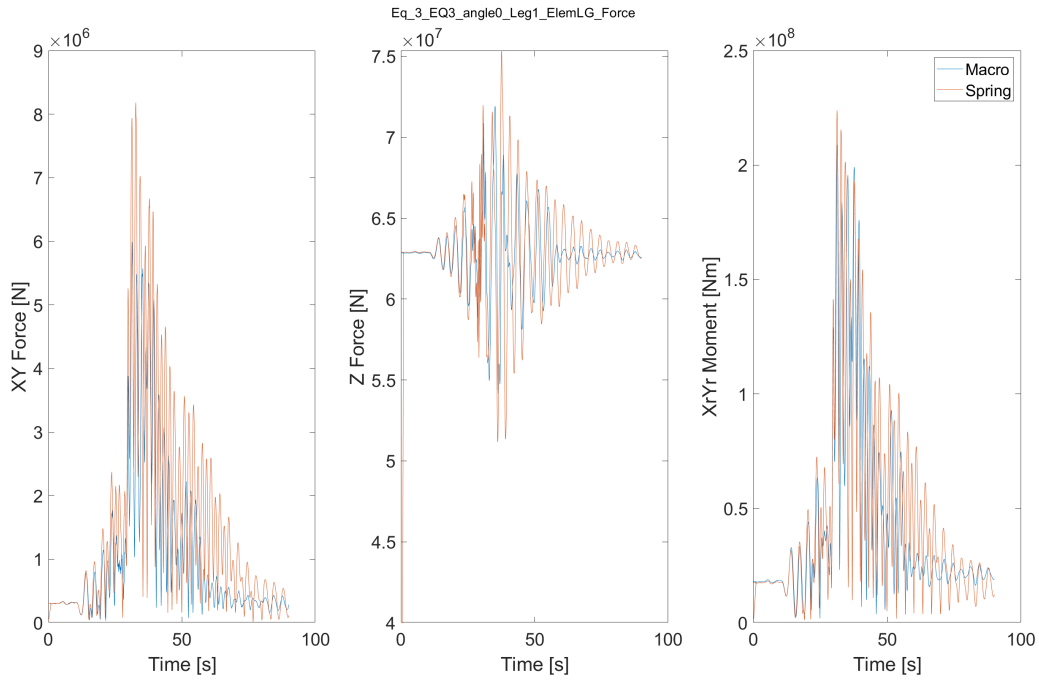

Figure 7.8: Time-domain force of lower guide node loads (Taiwan-200yr EQ3, $\theta = 0$, Leg 1)

The macro-element has a profound effect on the forces at the hull leg connection. In the horizontal plane, forces are $20\% - 40\%$ lower during the entire seismic event. In vertical direction the force reduction is lower because of the large static component in the vertical force. The overturning moments are also significantly smaller. These reduced forces are partly caused by reduced eigenfrequencies. The amplitude-dependent resonance-shift (described in Section 7.3.13) and hysteretic damping also contribute significantly to the reduced loads. The uncertainty of the input parameters is still very large. Although these results are indicate large beneficial effects, the sensitivity study and 4-case study should provide insight on the consistency of this results.

Maximum forces

The average of the maximum forces of all seven earthquakes for each angle and leg is plotted in Figure 7.9. The reduction of horizontal forces retains it significance across legs, orientations and earthquakes, with an average $20 - 30\%$ reduction. The directionality has a minor but significant impact on the difference between models. In this graph, the effect of varying leg length is also included. Vertical forces show no significant difference between the models and fairly large differences between legs. The relatively small difference between the models can be explained by the large static component in the vertical force. Also in larger depth the non-linear model has significantly lower loads in all DOF. Similar effects are expected for smaller depths.

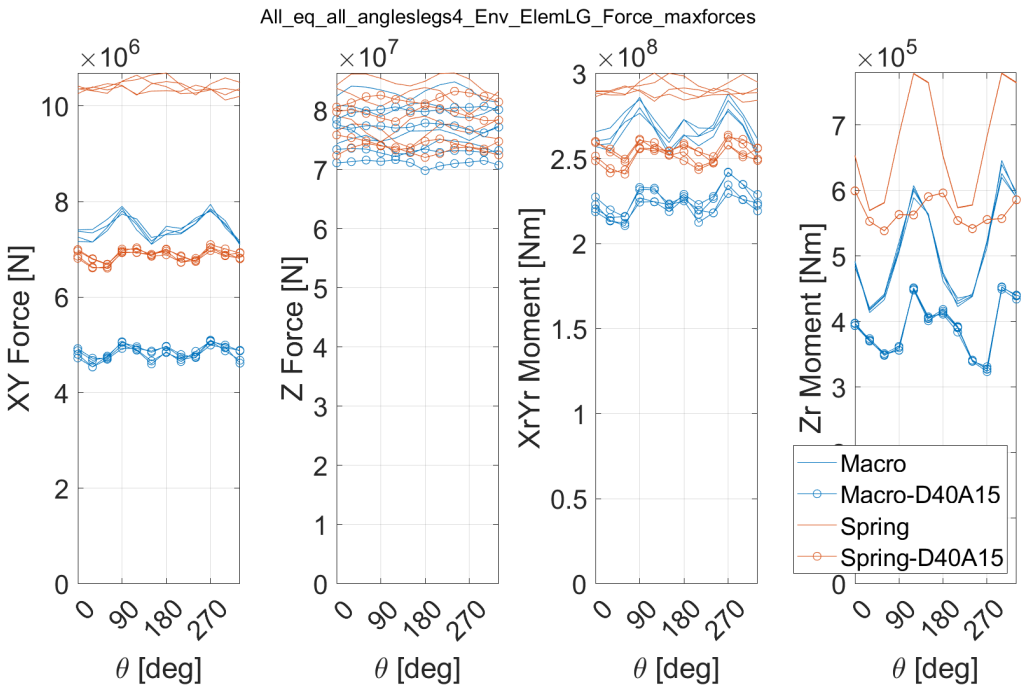

Figure 7.9: Maximum lower guide node loads, averaged over seven earthquakes for each leg. Plotted for depth(D) 30 and airgap (A) of 10 and 15 meters. (Taiwan-200yr)

7.3.11 Lower guide node acceleration frequency-domain

The power spectral density of the lower guide acceleration of 7 earthquakes in 3 DOF on 1 leg and 1 orientation can be found in F.3.6 A single example is provided in Figure 7.10 and Figure 7.11. The PSD plots of the ground accelerations belonging to these results are plotted in the same Figure. These are the PSD plots of the **absolute** acceleration. Acceleration is used instead of displacement, because inertial loads are dominant at hull level and it allows for ease comparison with the ground accelerations. Absolute acceleration is used because inertial loads are independent of ground motion.

The horizontal PSD clearly shows a lack of high frequency modes. The hull motions are fully governed by the first 3 mode shapes, in both models. Higher frequency components are present, but simply follow the ground motions. Also the energy present around 3 rad/s is due to the jack-up following ground motions. The most striking effect that can be observed is the reduction in hull accelerations by the macro-element model. Together with the reduced displacements, this leads to the significant load reduction at the lower guide. The amount of seismic energy present in the earthquake steeply increases up to 2.5-3.0 rad/s after which it gradually declines. The non-linear model vibrates at 0.05-0.5 rad/s lower frequency than the linear model. In vertical direction, similar effects are observed. This is expected to cause a significant reduction in non-linear resonance. This reduction in frequency indicates an overestimation of Rayleigh damping at these modes in the order of $0.1\% - 1.0\%$.

7.3.12 Numerical sensitivity

In Appendix F.3.7 a plot of the footing displacement is provided for two different degrees of numerical damping. this is done by varying the α-value of the Hilber-Hughes-Taylor Integrator. By default, this is 0.67, which corresponds to high numerical damping. The simulation has also been performed with $\alpha = 1$, corresponding to the Newmark method and low numerical damping. The influence of the numerical dmaping is larger than for the non-linear model, but still limited. Given the minor effect of footing displacement on structural loads, this is considered acceptable.

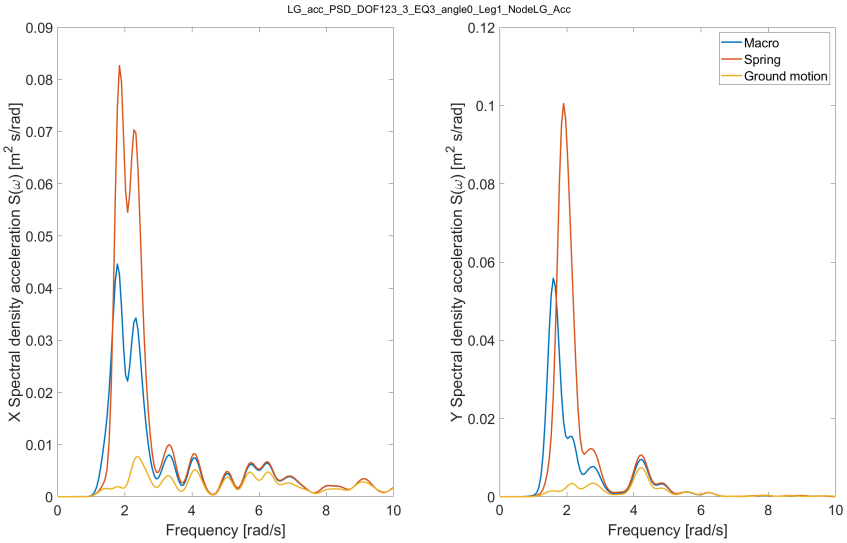

Figure 7.10: PSD of absolute lower guide node horizontal acceleration (Taiwan-200yr EQ3, $\theta = 0$, Leg 1)

7.3.13 Resulting hypotheses

Ratcheting does not lead to excessive displacement. Hardening is not expected to be significant during this research, and therefore excluded in the material model in the next sections. A significant reduction in loads and hull motions is observed. There could be several phenomena leading to these reductions:

- This specific combination of material parameters could "accidentally" have been a beneficial combination, which disappears when other material parameters are used. The consistency of load reduction for different parameter sets is assessed in Section 7.4 and Section 7.5.
- This shift away from seismic energy naturally leads to less resonance which might have a significant effect.
- Hysteretic damping leads to major energy dissipation, thereby reducing the structural response. This is not expected, because hysteric damping is only modelled at the footing, but footing node motions are not dominant in the first eigenmodes.
- As mentioned earlier, the non-linear system does not have a single set of eigenmodes. Each load-state has its own non-linear resonance frequencies, and during loading and unloading, the non-linear resonance frequency shifts. Because of this, when a resonance frequency hits the jack-up, the jack-up moves away from this frequency when loads increase. The resonance-shift is more dominant as resonance increases. This effectively leads to a change of non-linear eigen frequency when resonance builds up. The system therefore tends to move away from resonance. This effect is hereafter referred to as the **"Amplitude-dependent resonance-shift"** of the hypoplastic foundation. Non-linear resonance is still possible, if the loads are below the eigen frequency, and the resonance-shift shifts the frequency into the resonant domain. As soon as resonance start to occur however, the vibration frequency will decrease further, until it falls below the loading frequency. In earthquakes, the majority of seismic energy is above the resonance frequency. The net effect of the resonance-shift leads therefore to a reduction of resonance. Exceptions are observed for ground motions with peaks below 2 rad/s (earthquake 1 and 4).

Section 7.4 verifies the hypotheses listed above, and assesses the effect of these phenomena on the jack-up response. It does so using different parameter sets, causing different vibration frequencies, hysteretic damping, and amplitude-dependent resonance-shifts. Section 7.4 and Section 7.5 aim to verify the consistency of the statements above for a large number of parameter sets.

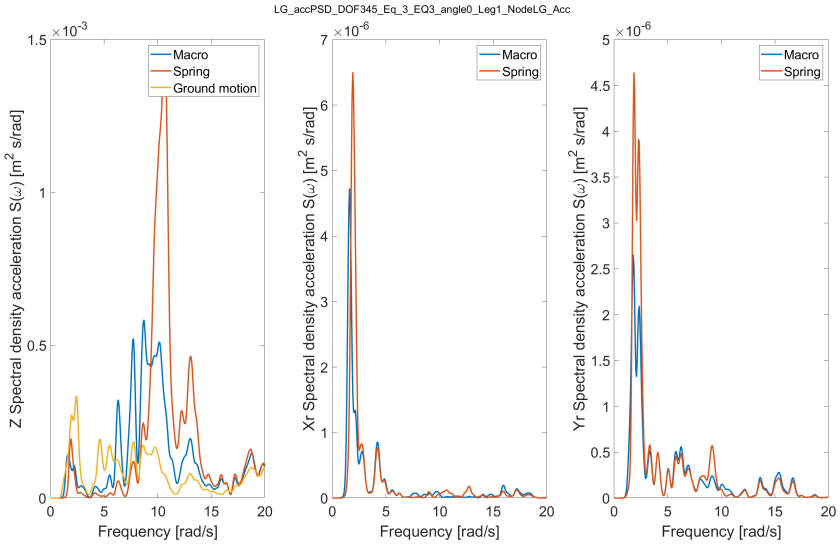

Figure 7.11: PSD of absolute lower guide node vertical and rotational acceleration (Taiwan-200yr EQ3, $\theta = 0$, Leg 1)

7.4 Four parameter sets

Four cases are considered with different parameter sets determining the degree of non-linearity (see Appendix D.5 for parameter combinations). The parameter sets are taken from literature [35][13][43][23] and have different properties:

- Case 1 (blue, same as base case), is most non-linear in medium-high strain regime.
- Case 2 (yellow) and Case 3 (purple), are fairly linear compared to case 1 and 4. Case 2 slightly more non-linear than case 3 in small strain regime and slightly less non-linear in high strain regime.
- Case 4 (green) is highly non-linear at all strains, but less non-linear than case 1 in high strain-regime.

The properties cause different vibration frequencies, hysteretic damping, and amplitude-dependent resonance-shifts. This allows to assess the effect of these phenomena on the lower guide response. Results are again compared with the linear foundation spring. Together with the sensitivity study this section provides understanding of the parameter sensitivity of the jack-up response.
First the time-domain responses are briefly assessed for a single earthquake. This is done for both footing displacement and lower guide forces. To provide visualise the occurring stiffness and hysteretic damping, the force-displacement curves are plotted. The differences in the force-displacement behaviour are then compared to the response of the lower guide to compare the effect of different phenomena. The behaviour with respect to the yield surface is displayed as well.
The response of the two nodes are then further analysed by measuring their maximums in different earthquakes, angles and legs. For both nodes, the Power Spectral Densities of acceleration are studied. The conclusions and recommendations have been summarised at the end of this chapter.

In order to prevent yield surface exceedance, these assessments have been performed using a 100-yr return period earthquake, on the same location as the earthquake used in the base case. The base case in this section has the same material parameters as in Section 7.3.

7.4.1 Footing node displacement time-domain

The different parameter sets show a huge variation in footing displacement. An example is provided in Figure 7.12. Footing node displacements for all earthquakes can be found in F.4.1. Case 4 shows a large plastic

displacements occurring as a result of parameter $m_R = 10$, which leads to a large stiffness reduction when passing from small to medium strain regime. Horizontal displacement peaks at 3cm, and vertical settlement is 35 cm. Given the relatively low strength of the earthquake, hardening is certainly significant in soft and highly non-linear soils. It is therefore recommended to develop a tool to translate penetration curves to macro-element parameters when implementing the macro-element in engineering processes. Parameter set 2 and 3 show a similar response. This is likely due to m_R and m_T being approximately equal.

Interestingly, no vertical settlement occurs when the seismic accelerations peak for parameter set 2,3 and 4. This might indicate that increasing κ and R leads to a settlement increase when the earthquake commences.

These time traces show a clear difference in the extent to which the non-linear parameters allow footing displacement. In general, the footing node shows a large sensitivity to varying parameters. An especially large sensitivity of footing response to m_R is observed. This parameter can however be easily determined based on static displacements.

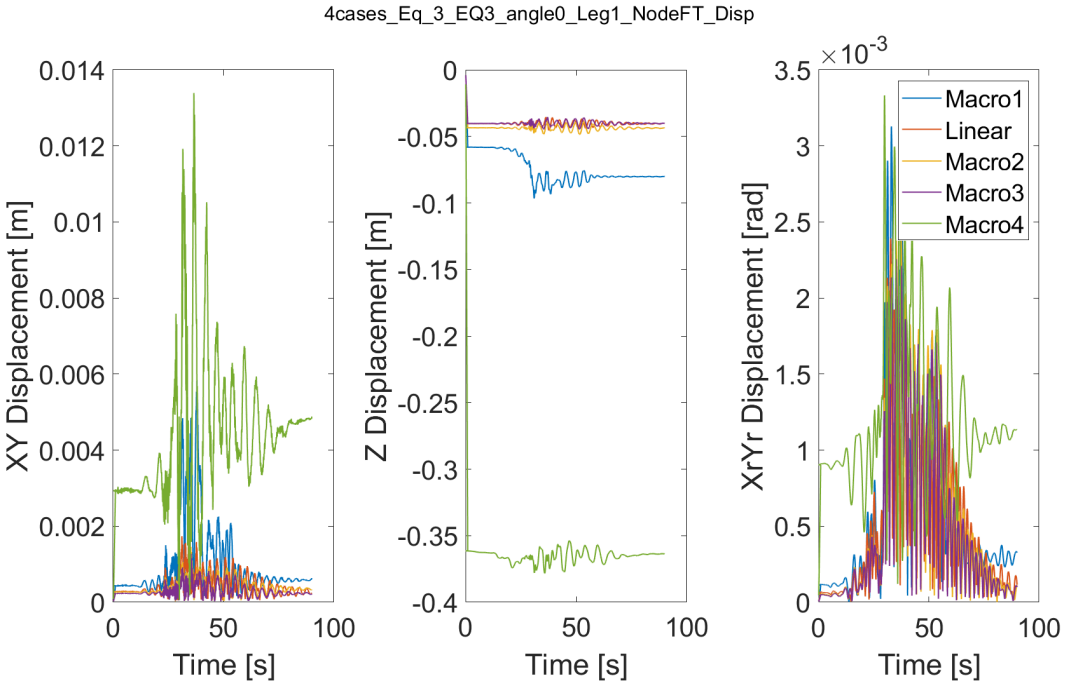

Figure 7.12: Time-domain response of relative footing displacement. Compares 4 sets of parameters and 1 linear foundation model (Taiwan-100yr EQ3, $\theta = 0$, Leg 1)

Maximum displacements

The effect of the different earthquakes on the footing displacements can be condensed by taking the maximum displacement for all legs and orientations in each earthquake. In Figure 7.13 these are shown while taking into account the earlier mentioned variation across earthquakes. Again, the increased degree of non-linearity results in larger variation across earthquakes. Both κ and m_R play a role in this effect.

7.4.2 Macro-element loads time-domain

The loads in the macro-element are severely reduced in highly non-linear soils. See Figure 7.14 and Appendix F.4.2.

Macro-element force-displacement time-domain

The force-displacement curves are plotted In Figure 7.15 and 7.16 to reveal stiffness reduction and hysteretic damping in the different parameter sets. Please note that there is a coupled stiffness present, so the horizontal

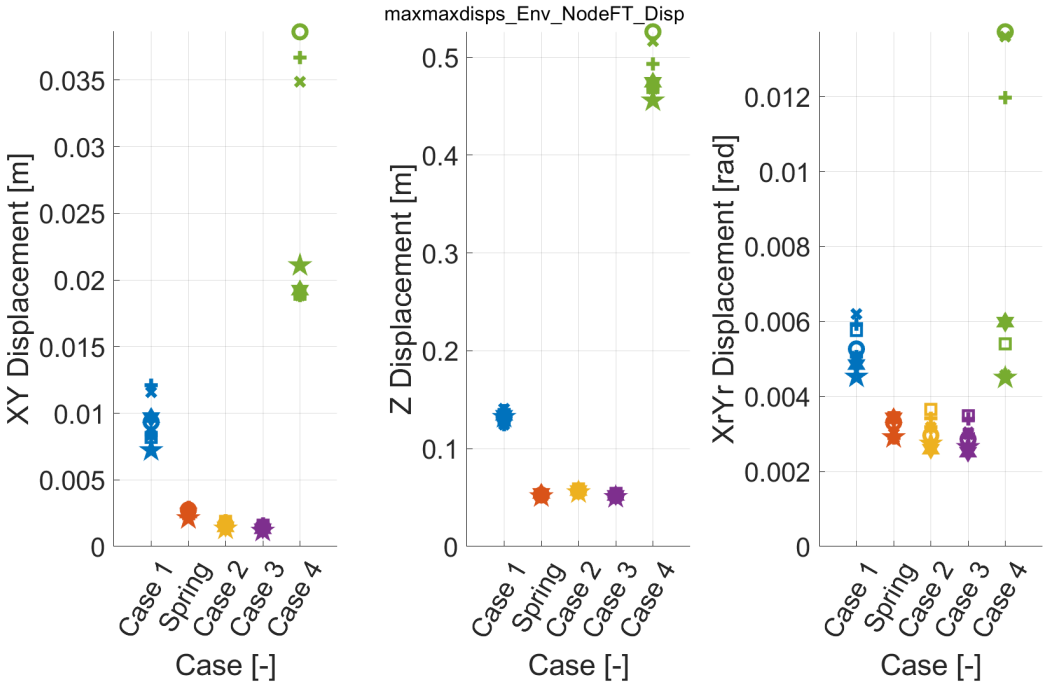

Figure 7.13: Maximum footing displacements, for all legs and angles. Separate earthquakes are represented by separate line types. Compares 4 sets of parameters and 1 linear foundation model (Taiwan-100yr)

loads can influence rotational stiffness and vice versa. This causes the jumps in the curves. Case 1 and 4 clearly have higher hysteretic damping and lower stiffness than case 2 and 3. If amplitude-dependent resonance-shift would not occur, both case 1 and 4 should have much lower guide loads than case 2 and 3. This is verified below. It appears that case 2 and 3 have no stiffness reduction at all. This is not the case. The axes are scaled to case 1 and 4, which clouds the visibility of the stiffness reduction. Separate plots are provided in Appendix F.4.5

The F-u curves in all DOF for all earthquakes can also be found in Appendix F.4.5

Macro-element load-state time-domain

Figure 7.17 confirms the hypothesis that the shape of the yield surface at the pointy ends does not significantly influence yield behaviour. The leg considered here has a relatively low vertical load, so in other legs the vertical load is also centered in the yield surface. Overturning moments lead to the most plastic behaviour. The load states in all DOF for all earthquakes can be found in Appendix F.4.6

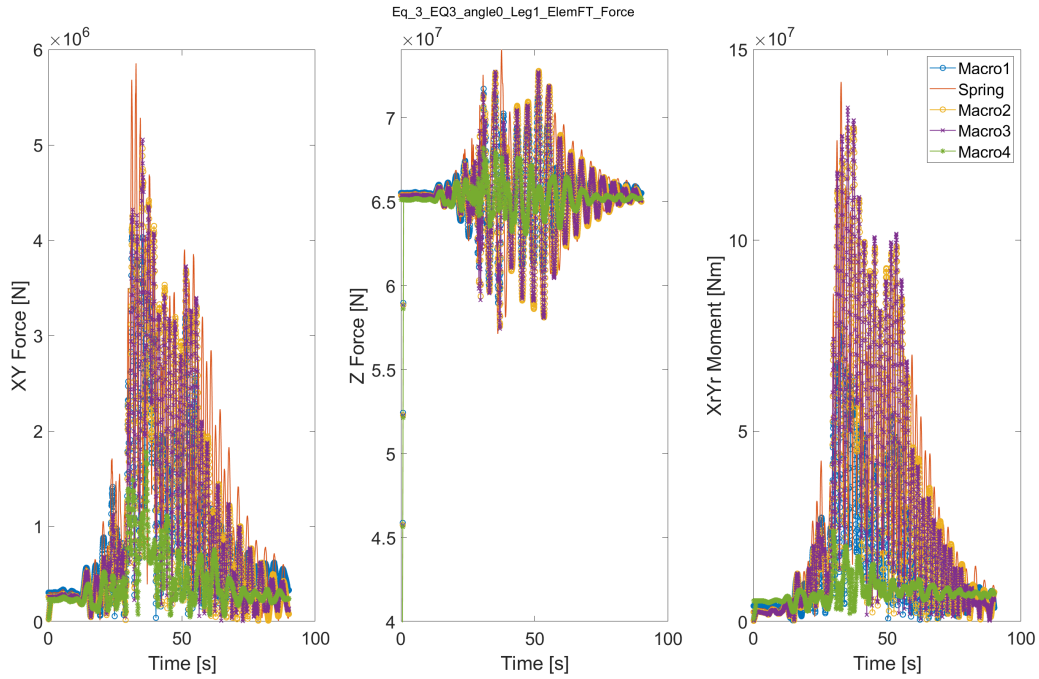

Figure 7.14: Time-domain macro-element loads. Compares 4 sets of parameters and 1 linear foundation model (Taiwan-100yr EQ3, $\theta = 0$, Leg 1)

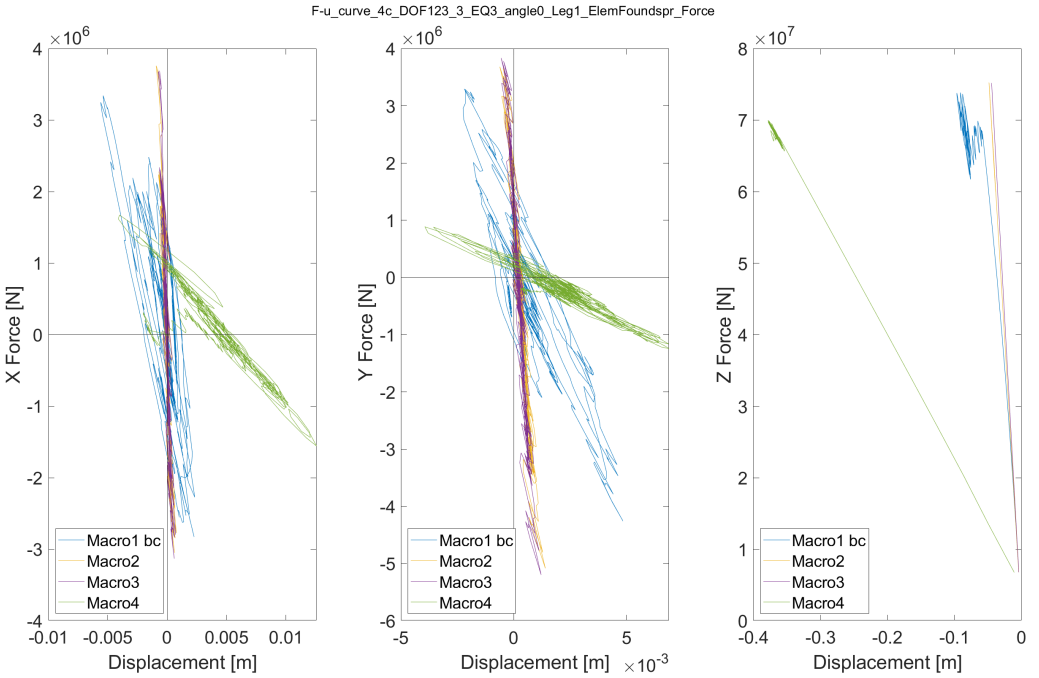

Figure 7.15: Time-domain force-displacement relation for base case translational DOF (Taiwan-200yr, EQ3, $\theta = 0$, Leg 1)

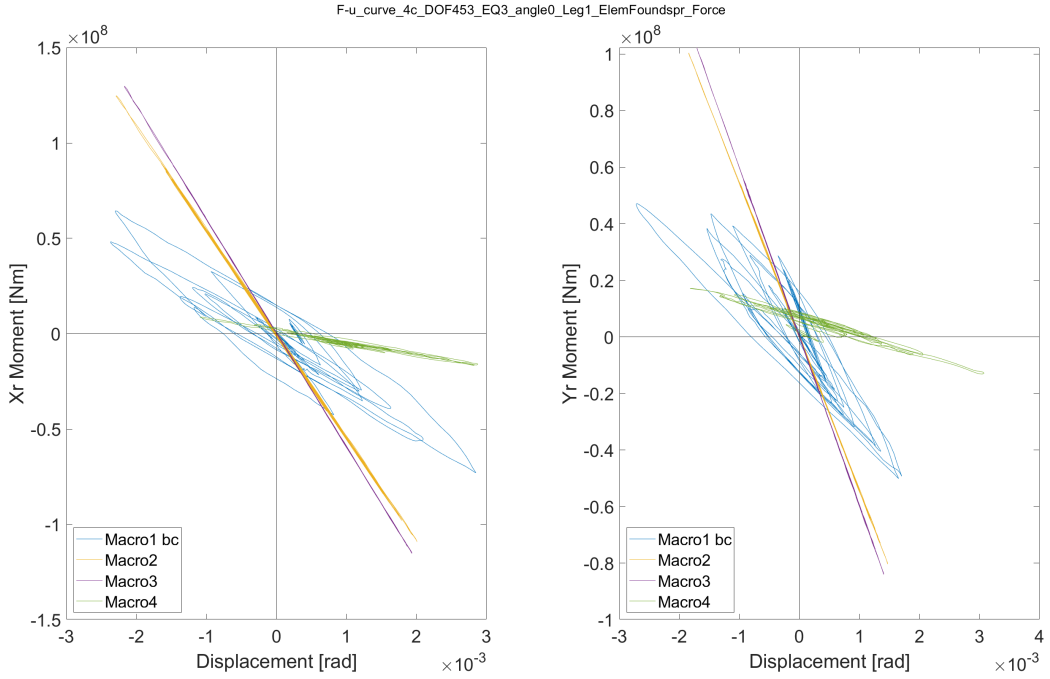

Figure 7.16: Time-domain force-displacement relation for base case rotational DOF (Taiwan-200yr, EQ3, $\theta = 0$, Leg 1)

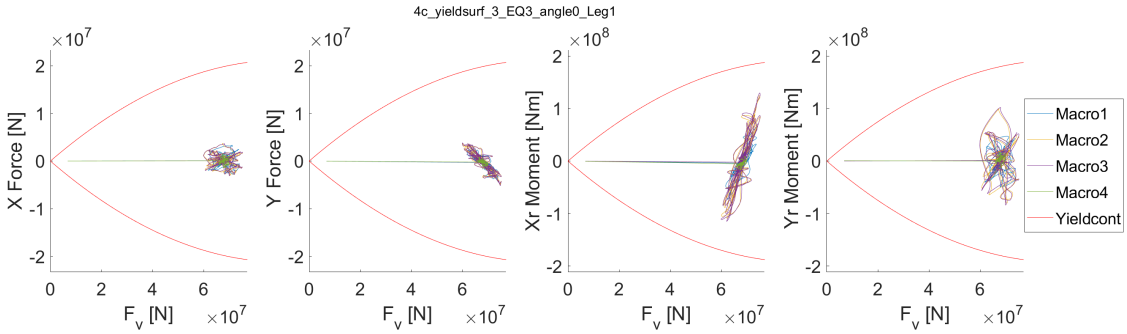

Figure 7.17: Time-domain load-state with respect to yield surface, in translational and rotational DOF (Taiwan-200yr, EQ3, $\theta = 0$, Leg 1)

7.4.3 Lower guide node displacement time-domain

The time traces of lower guide node displacements can be found in Appendix F.4.3. Displacements between different parameter sets are in the same order of magnitude, as the hull displacement is less governed by foundation stiffness. Set 4 is the exception, with in some earthquakes a very large hull displacement, and very low displacement in other earthquakes.

7.4.4 Lower guide node force time-domain

In all DOF, but mainly horizontal and rotational, all four cases reduce the forces in the hull-leg connection. It should be noted that force reduction is maximum at load peaks, and the reduction becomes larger as time increases. The latter is most likely caused by diminishing ground acceleration, making hysteretic damping more dominant in the response.
The highly non-linear case 4 has by far the largest force reduction, but this effect is not consistent across earthquakes. In earthquake 1 and 4 for example, case 4 has much larger loads than the other cases. This is the case for all legs and angles, which is shown in time-domain in Appendix F.4.4 In most earthquakes, the majority of seismic energy is above the resonance frequency. The net effect of the resonance-shift leads therefore to a reduction of resonance. Earthquake 1 and 4 have ground motions with peaks below 2 rad/s (earthquake 1 and 4). It is expected that for this parameter set, the large stiffness reduction at low loads causes resonance at this small load peak. The stiffness reduction in higher loads is too small to cause significant amplitude-dependent resonance-shift.

The observed variations between earthquakes are much larger for highly non-linear foundation models with high values of κ, m_R and possibly m_T. When implementing non-linear foundation behaviour in the design process, caution is required. It is recommended to revisit the current approach of taking the average of seven earthquakes. The number of earthquakes should be increased, and/or the earthquake ID should be a stochastic variable in risk analysis.

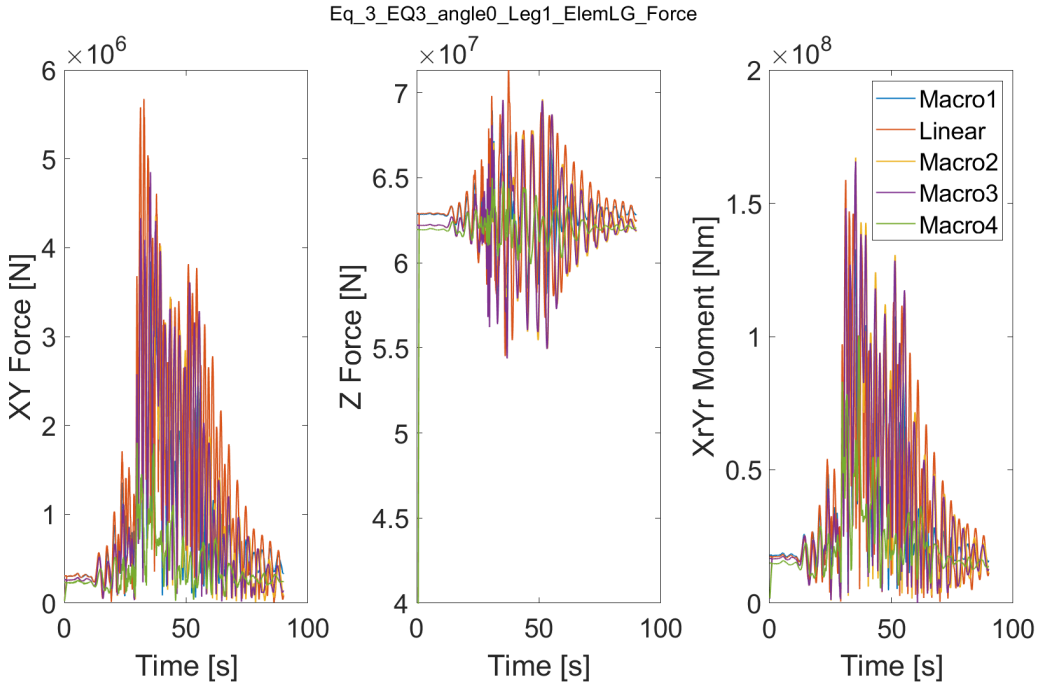

Figure 7.18: Lower guide loads. Compares 4 sets of parameters and 1 linear foundation model (Taiwan-100yr EQ3, $\theta = 0$, Leg 1)

Maximum forces

The effect of the different parameter combinations on the seismic response is best captured in terms of

maximum footing displacement and lower guide forces. In Figure 7.19 these are shown while taking into account the earlier mentioned variation across earthquakes. The values presented here are the maximum values of all legs and angles. A consistent reduction of lower guide forces is observed, with similar variation over earthquakes in parameter sets 1,2 and 3. This confirms that the load-reduction is not only caused by hysteretic damping and reduced overall stiffness.

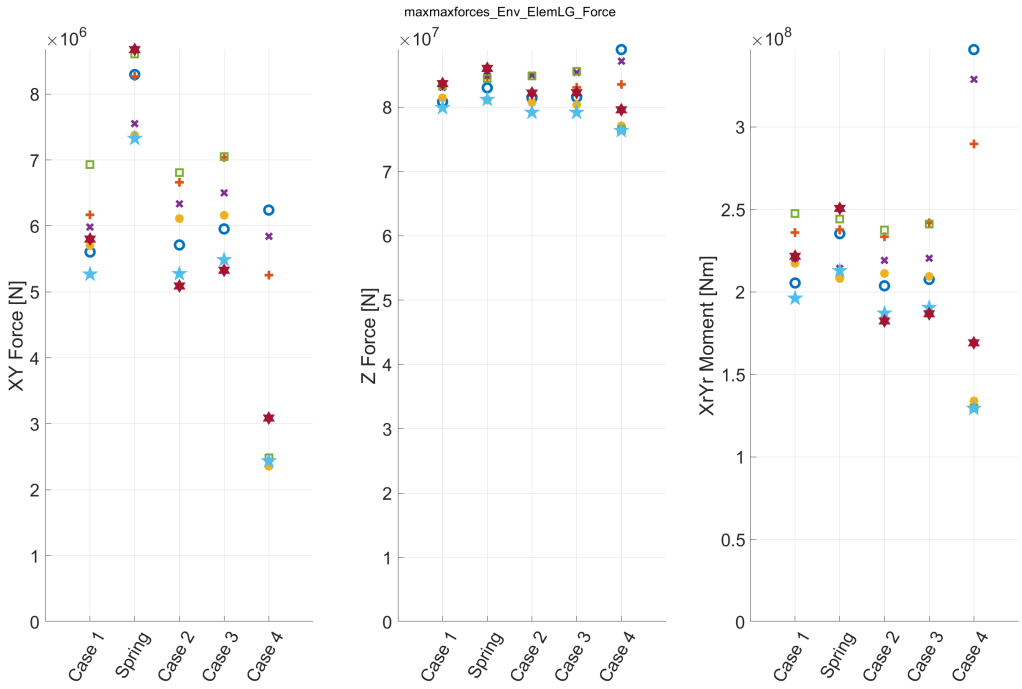

Figure 7.19: Maximum loads on the lower guide node, for all legs and angles. Separate earthquakes are represented by separate line types. Compares 4 sets of parameters and 1 linear foundation model (Taiwan-100yr)

7.4.5 Lower guide node PSD acceleration

See Figure 7.20 and Figure 7.21 for the PSD of the absolute acceleration of the lower guide node. In horizontal direction, the frequency reductions are very consistent, ranging from 0 to 0.5 rad/s. Large deviations are observed in peak height, most likely due to time-domain effects. In vertical direction, significant shifts of energy towards lower frequencies are present. Especially for case 1 and 4.

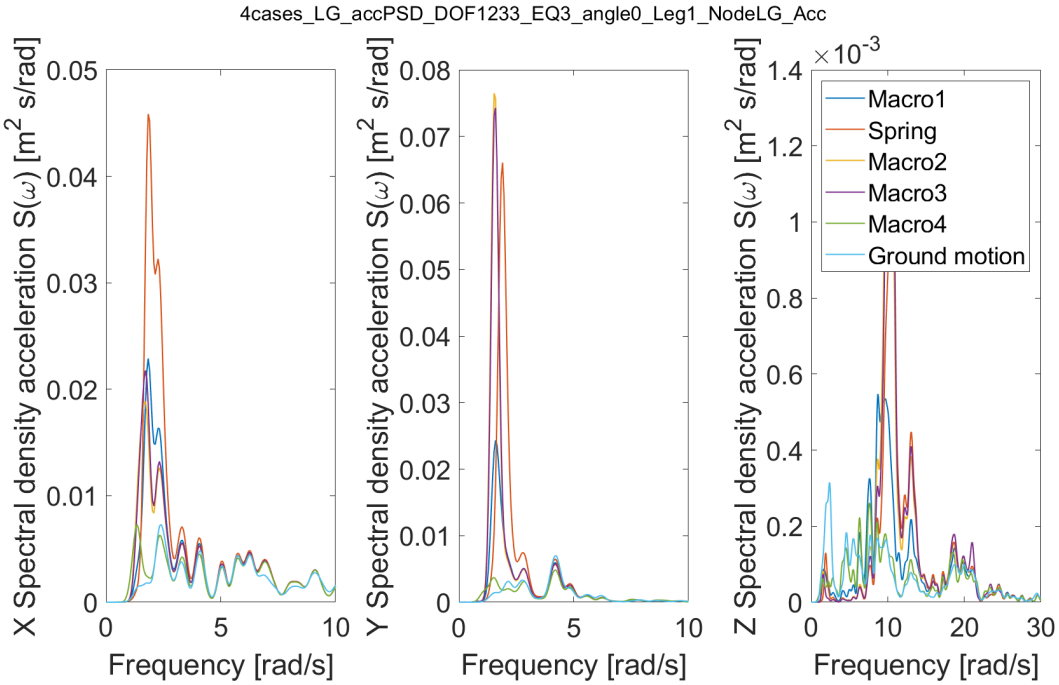

Figure 7.20: PSD of absolute lower guide acceleration. Compares 4 sets of parameters and 1 linear foundation model (Taiwan-100yr EQ3, $\theta = 0$, Leg 1)

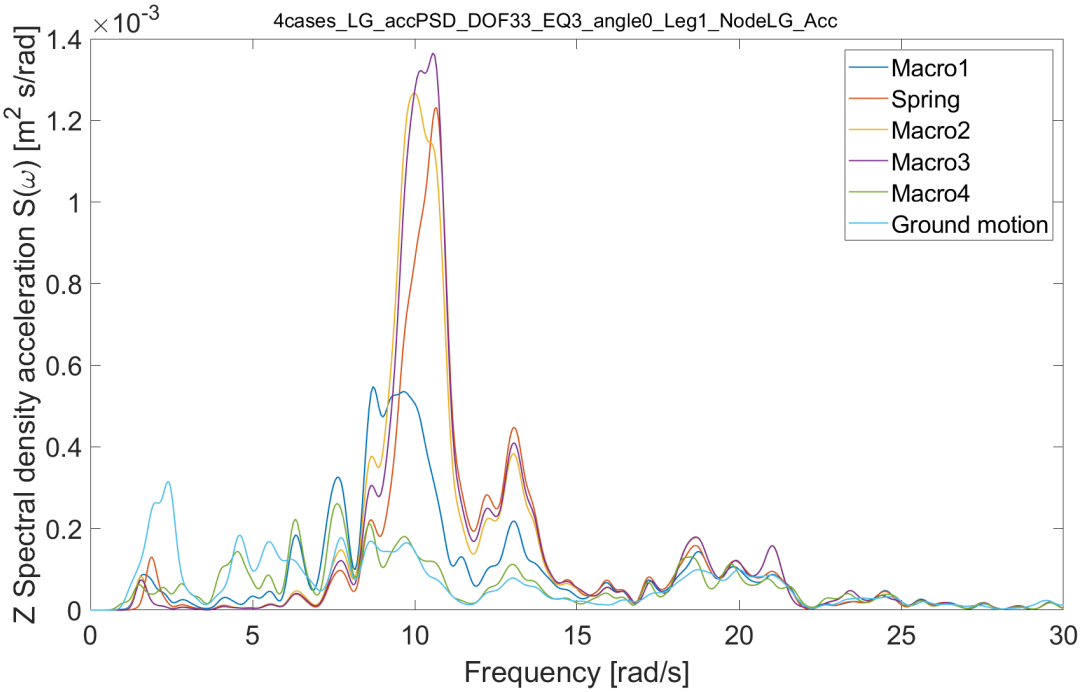

Figure 7.21: PSD of absolute lower guide vertical acceleration. Compares 4 sets of parameters and 1 linear foundation model (Taiwan-100yr EQ3, $\theta = 0$, Leg 1)

7.5 Sensitivity study

The single parameter variation aims to quantify the effect of changing parameters on the overall structural response. It verifies conclusions made in previously described simulations helps in understanding the reliability of future simulations. The analysis of the responses is condensed to a brief study of the footing displacement and an overview of maximum footing displacements and lower guide loads. More detailed investigation of the structural response is already provided for four other parameter sets in Section 7.4. The same earthquakes are used as in 7.4. The time traces and PSD of these earthquakes can be found in B.3.

7.5.1 Footing node displacement time-domain

In Appendix F.5.1 the time traces of footing node displacements for different parameter sets are provided. Only the results of earthquake 3 are displayed to demonstrate effects. Please refer to Appendix F Section F.2 for similar testing on the pile model. The conclusions that can be drawn from the footing node response, per parameter, are as follows:

- α: The shape of the plastic potential significantly changes the flow direction, and proper formulation is therefor required.
- κ: the effect of κ is only visible in the high strain regime, making its effect in visible in the earthquakes simulated. κ is therefor only expected to have a major influence during load peaks, and could cause significant differences in plastic displacement.
- m_R: This parameter has the most profound effect on the response, caused by the very early and large stiffness reduction. When equal to one, no stiffness degradation occurs during unloading. Unless further research indicates otherwise, it is recommended to set m_R between 1-3.
- m_T: From Figure F.4 in Section F.2 the strange phenomena occurring here can be explained. When equal to one, no stiffness degradation occurs during loading. Plastic penetration then only occurs during unloading. Unless proven otherwise, m_T should be chosen such that the force-displacement curve follows Masings' rule [24]. This is for values approximately equal to m_R.
- R: In the base case and many other parameter sets, extra plastic penetration occurred when the ground accelerations peaked, after which the penetration remained constant. Decreasing R makes this effect disappear. A higher R might increase the mentioned effect. It appears however that this parameter combination with this specific R-value caused this effect. Higher R-values should be evaluated.
- β_R: Increasing β_R results in increased ratcheting behaviour, larger displacement peaks but lower static penetration. Other jack-up orientations should be checked because upward plastic displacement occurs.
- χ: Reducing χ leads to more ratcheting and larger static penetration. Results are similar as in F.2. To be conservative it is recommended to choose χ larger then one, because the sensitivity to χ increases as χ decreases.

7.5.2 Lower guide forces

In Appendix F.5.2 the effect of each parameter value on maximum lower guide forces is plotted for each earthquake. To give an overview, Figure 7.22 provides the effect of parameters on the lower guide forces relative to those in the linear spring model. Here, the average of all earthquakes is used. the reduction of horizontal forces is very consistent. For some values of m_T and R, an increase of moments occurs. Please note that for R, only four earthquake simulations have produced results.

Normalised lower guide loads WRT LINEAR MODEL

		XY	Z	XrYr
	Linear foundation	0%	0%	0%
	Base case	-26%	-2%	-4%
Plastic potential	Associated	-18%	0%	6%
	Base case			
m_R	1.1	-4%	-1%	-4%
	3 bc			
	5	-34%	-3%	-7%
	10			
m_T	1.05	8%	4%	40%
	1.5 bc			
	2	0%	3%	27%
R	0.0001	10%	3%	40%
	0.005	-23%	-3%	-2%
	0.03 bc			
Beta_R	0.5	-25%	-1%	-1%
	1.0 bc			
Chi	0.5	-27%	-2%	-6%
	1	-27%	-2%	-5%
	1.5 bc			

Figure 7.22: Maximum lower guide loads as compared to linear model. Average of all earthquakes.

7.6 Conclusion

The macro-element leads to significant reductions of modelled horizontal loads regardless of parameter selection. This is caused by a combination of lower overall stiffness (reducing resonance), hysteretic damping, and an amplitude-dependent resonance-shift. the amplitude-dependent resonance-shift and hysteretic damping always have a beneficial effect on structural response, regardless of parameter selection. Only the magnitude of the effect varies with the material parameters. A lower overall stiffness is mainly caused by stiffness reduction when passing from small to medium strain. This reduction at small loads lead to a consistent reduction of vibration frequency. This generally leads to less resonance, unless there is a peak in the loading frequency below the first eigen-frequencies. On this specific site this is the case for earthquake 1 and 4, due the a resonant soil layer.
Significant settlement is observed for non-linear soils for earthquakes with a 100-yr return period. This indicates significant hardening of the soil can occur, and should be accounted for.
The non-linear model is more sensitive to numerical damping, but the effect on the superstructure is limited.
In general, the footing response is highly sensitive to parameter variation, with observed differences of one order of magnitude. Surprisingly, lower guide forces are not very sensitive to parameter variation, with some exceptions. Moment loads are very sensitive to m_T and R. Low values of m_R and high values of R are conservative. Proper definition of plastic potential is required. The response is not sensitive to χ and β_R, but this could change for more severe earthquakes.
Increasing the degree of non-linearity, especially by κ, m_R and m_T leads to much larger variation in response across earthquakes.

Chapter 8

Conclusion

The aim of this thesis is to improve foundation modelling and assess its effect on the jack-up response. The explicitly modelled radiation damping and hypoplastic foundation allow the user to improve the modelled seismic behaviour of a jack-up drastically. Non-linear foundation modelling is expected to be critical in understanding the seismic response of the jack-up. Parameter determination has proven to be a critical challenge in implementing the macro-element in the model. This research has however been able to confirm the hypothesis that linear spring foundations are overly conservative. Consistent reduction of horizontal forces in the legs and lower guides observed when using a non-linear foundation model. Additionally, non-linear foundation behaviour causes qualitatively different seismic behaviour which could lead to different governing load cases. By developing a parameter determination tool and performing extensive validation of the macro-element, a significant reduction in conservatism could be achieved.

The research questions are answered in the next section. In section 8.2 the results are interpreted and their significance is described. Recommendations for further research are made in the next chapter.

8.1 Research questions

What is the effect of explicitly incorporating linear foundation damping in the model as opposed to reduced input ground motion?
At low frequencies, no significant difference in footing response is observed. At frequencies where the first vertical modes occur, the explicitly damped system shows a larger response in all seven earthquakes. At very high frequencies, the reduced input method is too conservative as it is tuned to lower frequencies.
In the time-domain, resulting extreme vertical footing displacements are slightly larger in the new model. When the earthquake diminishes, superstructure vibrations are damped faster in the explicitly damped model. In general, the difference in Unity Checks between the two models is $<1.5\%$, with the exception of failure modes where vertical forces are governing. This occurs during the sliding case and preload exceedance case. The explicitly damped foundation is recommended for future use.

What methods are suitable for modelling nonlinear force-displacement relations in the foundation?
In the OpenSees framework, no material is available that can model non-linear foundation behaviour in a single element. Macro-elements have been widely developed by third parties, and are able to condense the behaviour of bearing soil in a single element with an acceptable accuracy. For this thesis, the REDWIN foundation models [41] and the macro-element as developed by Salciarini & Tamagnini [36] have been compared. The Salciarini model has been selected for its wider range of capabilities and available source code.

Can a suitable foundation model be implemented as a macro-element in OpenSees?
The macro-element has been successfully integrated in the OpenSees framework. This is done by modification of the ZeroLengthND element. This element is outfitted with a custom made material that provides the interface between the macro-element and the ZeroLengthND element. This interface transfers state variables and user defined properties between the macro-element and OpenSees. The successful implementation pro-

vides the user with a vast range of new OpenSees capabilities. It allows for extensive research into non-linear foundation behaviour while maintaining its industrial applicability.

What is the effect of modelling non-linear foundation behaviour on the jack-up?
Introduction of a non-linear macro-element as foundation has a profound impact on the modelled response. The most important effects are listed below:

- Smaller vibration frequency. The stiffness reduction when passing from small to medium strains is effective during practically the entire earthquake. This causes an overall decrease of the vibration frequency for all assessed parameter combinations. The vibration frequencies are therefore shifted away from the frequencies where the earthquake contains most energy and thereby reduces non-linear resonance.

- Amplitude-dependent resonance-shift. The constantly shifting resonance frequencies prevents resonance to develop, especially around load peaks. This effect is proven to have a significant beneficial effect on structural utilization for all parameter values.

- Plastic soil deformation. Vertical settlements are generally limited for 100-yr return period earthquakes, but for soft, highly non-linear soils they can increase significantly. During more severe earthquakes, hardening is expected to become significant.

- Increased variation across earthquakes. When using a non-linear foundation model, forces and displacements can accumulate. This results from the exponential stiffness reduction and differences in non-linear resonance-shift. This causes larger variations between earthquakes, especially for highly non-linear foundation models. The variation especially increases for high values of κ and m_R. When implementing non-linear foundation behaviour in the design process, this increased spread should be accounted for.

- The effect of hysteretic damping on structural response is significant. the effect is mainly visible in rapid load reductions after the earthquake diminishes

What is the sensitivity of the seismic response to empirical foundation parameters?
In general, the footing response is highly sensitive to parameter variation, with observed differences of one order of magnitude. Surprisingly, lower guide forces are not very sensitive to parameter variation, with some exceptions. Moment loads are very sensitive to m_T and R. Low values of m_R and high values of R are conservative. Proper definition of plastic potential is required. The response is not sensitive to χ and β_R, but this could change for more severe earthquakes.

What is the effect of improving foundation behaviour modelling on the modelled seismic response of a jack-up unit?
Explicitly incorporating radiation damping leads to very minor changes in structure utilization, but significantly improves the preparation time for simulations and captures occurring physical phenomena in a more correct manner. Implementation of non-linear foundation behaviour leads to major changes in the jack-up response, regardless of parameter choice. Lower horizontal loads in legs are consistently achieved, and bending moments tend to be reduced as well. If correct input parameter formulation can be achieved, it would be a major improvement of the seismic model that can greatly improve understanding of the seismic responses.

8.2 Discussion

The limitations in the findings in this thesis are discussed below, with increasing level of detail in each following section.

Jack-up model
The jack-up model is a simplification of the actual geometry of the jack-up. Most importantly, the dynamic behaviour of the crane is not included in the model. The effect of the crane on the seismic behaviour of the jack-up is considered limited. Additionally, some error has been introduced by the geometry simplification. The eigen frequencies and mass distribution have been verified with existing FE analysis, leaving a residual error in the range of $0-4\%$ for the first four eigenmodes. Although different sand properties are used in this research, the earthquake samples are based on a single location. This is not expected to lead to significant errors however, because the design site response spectra do not differ much for varying upper soil layer.

Macro-element development
The macro-element has been validated by comparison with laboratory tests. These tests consisted of monotonic load paths, cyclic load paths and two-phase swipe tests. No validation has been performed for loads as severe and complex as earthquakes. No validation has been performed on macro-scale structures.

Macro-element implementation
This macro-element has never been implemented in jack-up or seismic analysis. Available literature on hypoplastic foundation models for jack-ups is limited. No papers have been found regarding application on seismic analysis of jack-ups. Additionally, no macro-scale validation has been published for the macro-element used in this paper. This significantly increases the possibility of unknown risk.
The macro-element has been implemented parallel to the viscous radiation damper. As only the elastic part of the soil deformation is able to radiate pressure waves, this leads to an overestimation of damping. This leads to an increasing overestimation of damping when the behaviour is increasingly plastic. The damper is estimated to absorb 20% of vertical force, of which only a portion is overestimated. The vertical modes are not dominant in the jack-up response. The error is expected to be in the order of percents. When implementing the macro-element in engineering processes, it should be placed on the far end of the macro-element, parallel to a spring with the same stiffness as the elastic stiffness in the macro-element. The Rayleigh damping has been fitted to the elastic range of the macro-element, thereby overestimating the eigenfrequencies during load peaks. As a result, the modelled Rayleigh damping of the first modes (mass-dominated) is higher, and the Rayleigh damping of the higher modes is lower. As the response is dominated by the first three modes, damping is overestimated in the order of 1%. This should especially be the case for parameter sets with large overall foundation stiffness reduction. Hardening has not been included, leading to a small overestimation of plastic deformation and a small underestimation of stiffness. The material parameters used in literature and this thesis have only been defined for sand. The response on clay has not been assessed.

Other
In Section 6.2 a time-step dependent error has been identified. This error was in the range 0.5%, but could increase for severe load cases. An assessment for time-step dependence of jack-up response has not been been performed. Leg interaction effects and liquefaction have not been included.

Chapter 9

Recommendations

9.1 Damping

It is recommended to include the explicit radiation damper in design processes. It should be modelled on the far field side of the radiation damper, in parallel with a spring with stiffness equal to macro-element elastic stiffness.
To further improve the modelling of radiation damping, horizontal radiation damping could be added. Design standards only recommend the inclusion of vertical radiation damping, but academic literature does indicate horizontal radiation damping occurs. It is suspected that design standards are conservative regarding horizontal radiation damping, because plastic deformation is significant in horizontal direction. By implementing the radiation damper on the far field side, this could be accounted for. Further literature research would be required.
Rayleigh damping could be better defined by fitting it to the modes at medium-strain foundation stiffness.

9.2 Macro-element

The proposed macro-element implementation has significant effect on the seismic response of the jack-up. The implementation faces two major challenges: Validation and parameter selection. This section lays out a strategy to ensure a reliable implementation in seismic assessments. Subsequently, minor improvements are proposed and recommendations are made regarding further research and applications of the macro-element. But first, return mapping should be implemented in the material to allow for severe loading.

9.2.1 Validation

Given the tools and expertise available within GustoMSC, it is recommended to perform the validation by means of FE analyses of the soil. The pile and two-node model used in this research can provide a good basis for validation, there is no need to include the motions of the jack-up in validation of the soil. To capture jack-up behaviour under severe loading, an equivalent load could be applied to a pile or two-node model.
Before complex load cases and soil types are defined and validated, it is recommended to first validate the response on already available soil types. An FE analysis of the pile model with harmonic load on Yellow Leighton Buzzard sand (described in Nova and Montrasio [34]) should be performed. After this, loads could be gradually increased to test macro-element accuracy in highly non-linear ranges. It is expected that the model becomes less reliable as behaviour becomes increasingly non-linear. As the macro-element is not able to capture inertial effects of the soil, it should be validated in static FE analyses. When this soil type has been sufficiently validated, the macro-element has proven its potential to provide reliable non-linear results. The next step is to create a tool to quantify empirical parameters. See 9.2.1

When the parameter selection tool provides sufficient results, the validation process above can be repeated for the new soil types and stratified soils.

Parameter selection

Small-strain stiffness, capacities and hardening can be determined based on available literature. Parameters defining the force-displacement relation can easily be determined for any soil, by creating a 3D discretised soil in software such as Plaxis. A spudcan can be modelled, and a vertical force should gradually be loaded and unloaded. The occurring displacements can be recorded as a function of load. R, m_R, m_T can easily be fitted on this curve, especially if only minor loads are applied. By applying larger loads, χ and κ and β_R can be fitted. This process could also be performed for stratified soils, under the condition that the plastic behaviour occurs predominantly in the upper soil layer.

9.2.2 Transient analysis

In the pile model, interface DLL (C++) was able to retrieve the currentTime and committedTime from OpenSees, allowing the macro-element to automatically use the correct time step. In the jack-up model, this function was not working anymore, and applying VariableTransient analysis might therefore not be safe. Changing the time step now requires a change in the DLL, where the time step is explicitly defined. This bug should be addressed.

Appendix A

Macro-element foundation models

A.1 A macro-element for integrated time domain analyses representing bucket foundations for offshore wind turbines

In this section a summary of the work of [40] is presented, which was published in *Marine Structures*. This paper discusses the development of REDWIN foundation model 3, the macro-element model intended for bucket foundations of OWT's. Information in this section is derived from [40], with additional explanations from [41] (only where specified).

A.1.1 Introduction

Macro-elements developed for other structures that differ from OWT's may also be used for bucket foundation modelling by appropriate calibration of model parameters, and by modifying the yield surface criteria in tension. However, many macro-elements presented in literature lack published methodologies for adaptation of the macro-element to different soil conditions. [40] identifies this as a possible reason that macro-elements are rarely used in the design of offshore structures. The macro-element presented addresses this problem by defining a practical-oriented formulation. The macro-element captures the characteristic behaviour of a shallow foundation subjected to irregular cyclic loading. The development of the macro-element has been based on a numerical study of shallow foundations in clay.

A.1.2 Basis

A wide range of soil profiles and bucket geometries has been modelled by a series of three-dimensional (3D) FE Analyses, using PLAXIS 3D. The results from these analyses formed the "experimental" basis for the macro-element development. The soil model used in the analyses was the NGI-ADP model, which features undrained, incompressible soil. It has an anisotropic undrained shear strength failure criterion. In the FE Analysis the static undrained shear strength increased with $7[kPa/m]$. The stress strain behaviour is based on the NGI database on cyclic behavior of clays, from which an over-consolidated clay typical for North Sea offshore wind farm sites has been used. From the numerical study it is observed that the contours of plastic work do not have the same shape for all levels of mobilization. The contours reveal two very important characteristics, which should be addressed in the macro-element. Firstly, The plastic work evolve non-proportional along the three load axes. Secondly, the plastic flow direction changes not only by load path direction, but also by mobilization level.

A.1.3 Working principals

Multi-surface-plasticity

The macro-element presented in this paper has been formulated in the multi-surface plasticity framework (Mróz 1967; Iwan 1967). In this framework, the amount of plastic deformation depends on a series of nested

surfaces in the Horizontal-Vertical-Moment (HVM) load space. The hardening is defined by subsequent linear curves. The attractiveness of multi-surface plasticity comes from the easy implementation of kinematic hardening, which make the macro-element exhibit hysteretic behaviour. It is conceptually simple, robust, and allows for flexible calibration of the input parameters. In Figure A.1 the concept is explained based on a simple 1D model.

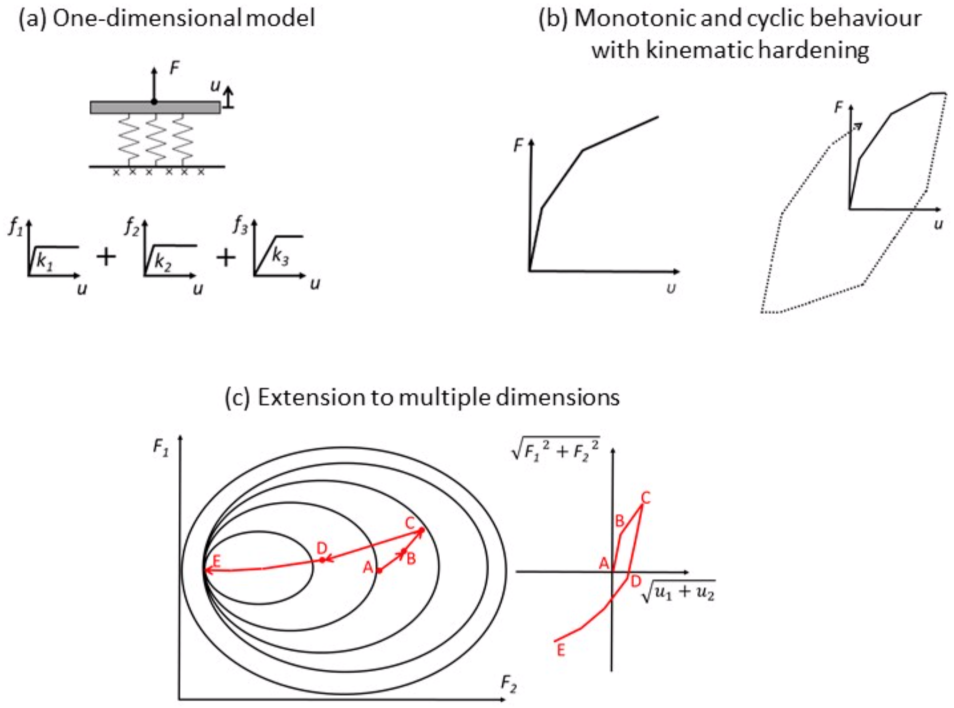

Figure A.1: The concept of multi-surface plasticity: (a) 1DOF rheological model with parallel springs, (b) graph of resulting load-displacement behaviour, (c) extension to multiple dimensions with multi-surface translation in load space. As presented in [41]

Depth of load reference point

Most macro-elements are formulated with displacements and loads located at the seabed. Specifying the depth of this Load Reference Point (z_{LRP}) as input has several advantages. Firstly, it simplifies the required mathematical equations. Secondly, z_{LRP} stores information about the coupling between the horizontal displacement and rotation. The z_{LRP} can be determined with a single FE Analysis. The paper shows that z_{LRP} varies moderately dependent on the load level, but a representative value for a given case can be defined. Add sec 5.5

Stiffness matrix, yield function and flow rule

The element uses a 3x3 diagonal elastic stiffness matrix. The coupling terms are zero because the z_{LRP} is chosen such that the forces and moments are uncoupled. For low mobilization levels, the contours of plastic work where reasonably approximated by elliptic surfaces. For the purpose of OWT assessment, this is sufficient. The elliptic surfaces are taken as the potential function as specified in Equation A.1. These surfaces are also chosen as the yield surfaces. The yield function f_i is then given by the same function imposing associated flow, for all surfaces, as in A.2. The macro-element includes hysteretic damping, but excludes radiation damping. The hysteretic damping is determined based on the three input curves, following Masing's rule. This means that the assessment should be based on either the stress-strain level or on the foundation level.

$$\frac{\delta g_i}{\delta F} = \frac{\delta f_i}{\delta F} \tag{A.1}$$

$$f_i = (\frac{V - \alpha_{i,V}}{V_{i,max}})^2 + (\frac{H - \alpha_{i,H}}{H_{i,max}})^2 + (\frac{M - \alpha_{i,M}}{M_{i,max}})^2 - 1 \tag{A.2}$$

Surface translation and hardening rule

The surface translation rule normally refers to the rule dictating the direction of translation of the surfaces. Often the direction is determined based on an image point located on an image surface. These relatively complicated rules are motivated by the overall preference of the so called "non-intersection surface criteria". For the development of the REDWIN element it was decided to formulate the surface translation without any restrictions from surrounding surfaces. A relatively simple hardening rule has been applied, which controls the relation between surface translation and plastic displacement. The hardening is a multi-linear approximation. This means that each surface i has a constant "plastic stiffness". The Koiter rule as in A.3 is used to determine the total amount of plastic displacement. In this formula k is the outermost surface being violated.

$$du^p = \sum_{i=1}^{k} du_i^p = \sum_{i=1}^{k} d\lambda_i * \frac{\delta * g_i}{\delta * F} \tag{A.3}$$

A kinematic hardening rule has been adopted in the model, which has been based on the load – displacement response in the three uniaxial directions.

In order to approximate the hardening for a combined load path, the plastic stiffness are weighted in the three uniaxial directions by the flow direction for the current load state. The formulation can be expressed for any surface i as in Equation A.4:"

$$\frac{\alpha_i}{\lambda_i} = D_i^p * \frac{\delta g_i}{\delta F} \tag{A.4}$$

Where $\frac{\delta g_i}{\delta F}$ is the plastic flow direction vector, and D_i^p is the plastic stiffness matrix for surface i. This matrix is a diagonal 3x3 matrix with the plastic stiffness in the vertical direction, horizontal direction and rotation around the out of plane axis. Note that the plastic stiffness, Di_p, is only associated with the translation of surface i. This means that for example the horizontal secant stiffness $K_{k,h}^p$ for loading between H_{kmax}, and $H_{k+1,max}$, is the combined stiffness of all surfaces being translated.

Numerical implementation

The model is required to find the solution with translation of a minimum amount of surfaces. This has been achieved by initiating the loop at the innermost surface ($i = 1$). When the convergence criteria has been met, the steps are repeated for the next surface, and so on. This continues until a solution is found involving translation of all surfaces $i = 1...k$, while the next surface, $k+1$, is not violated. This gives the elasto-plastic relation for k surfaces:

$$dF = D * (du - d * \lambda_1 * \frac{\delta g_1}{\delta F} - d * \lambda_2 * \frac{\delta g_2}{\delta F} - ...(sic) - d * \lambda_k * \frac{\delta k_1}{\delta F} = D * (du - \sum_{i=1}^{k} d\lambda_i * \frac{\delta * g_i}{\delta * F} \tag{A.5}$$

A.1.4 Required user input

The user specifies the following input:

- Three uniaxial load-displacement curves for HVM loads applied at the structure-foundation interface (SFI). These input curves are not used by thee model directly, but are transferred to a set of parameters defining the multi-surface plasticity: a linear elastic stiffness matrix D, linear "plastic stiffness matrices" D_i^p and yield function axis crossings ($V_{i,max}$, $H_{i,max}$, $M_{i,max}$). The great variety of site conditions necessitate the need for site specific definition of the load displacement curve. "The uniaxial input

response curves are used as back-bone curves. This means that the uniaxial input response curves should reflect the foundation's cyclic behaviour. The authors recommend to use FEA to establish the uniaxial response curves. The analyses can be run as quasi static analyses, but the soil's stress –strain curve should reflect a cyclic backbone curve. If laboratory data is available, these can be used directly to extract cyclic behaviour. The effect of cyclic degradation can be accounted for directly by defining the appropriate stress-strain curves. If the uniaxial load displacement curves are based upon monotonic soil data, the effect of cyclic degradation on foundation level can be approximated by the data in Skau et al. [39] or similar". If one load direction is expected to dominate the response, it is recommended to use this load axis as basis for the discretization.

- The depth of the load reference point (z_{LRP}). This is defined for both plastic and elastic deformation. z_{LRP} represents *"the depth where negligible horizontal displacement evolves when a moment load is applied to the foundation"*. It is defined in A.6, where $u_{H,SFI}$ and θ_{SFI} are the horizontal displacement and rotation, respectively.
- Number of yield surfaces.
- Numerical discretization parameters

$$z_{LRP} = \frac{u_{H,SFI}}{\theta_{SFI}} \tag{A.6}$$

A.1.5 Limitations and simplifications

Accumulation of displacement (ratcheting) and cyclic stiffness degradation are not considered. The latter is due to difficulties of estimating stiffness degradation and especially accumulation. This simplification is adopted largely because the effects occur over large time spans, while dynamic analysis of a OWT normally consider ten minutes. Pore pressure accumulation and mean stress changes are not computed internally in the model. Skau and Jostad [38] and Andersen and Berre [2] show that "the stress-strain response in sand and clay are reasonably similar if the sand response is predominately undrained during a single cycle and if the loads are relatively small, such that no significant pore- pressure accumulation occurs." The mathematical functions in this model are deliberately implemented without empirical calibration factors. These factors could benefit the accuracy, but the user availability of these factors is limited.

A.1.6 Results

Three examples have been modelled to demonstrate the performance of the macro-element. Two simplified models have different loading conditions (monotonic/irregular cyclic/cyclic), skirt lengths of 5 and 10 meters, and a soil profile consisting of homogeneous/stratified clay. The third example is a back-calculation of a field in the Bothkennar test field.

The aim of modelling the monotonically loaded bucket with 0 meter skirt in homogeneous clay was to reproduce the results computed by the FE Analysis. It resulted in a generally good agreement, with the most significant deviations in the HM-plane. This is due to the simplification of the yield and the potential function, which is less accurate in the HM-load plane. This difference cannot be completely eliminated due to the fundamentally non-symmetric nature of the HM-load plane. The modelled secant stiffness shows a good agreement with the FE Model, but damping has been lightly underestimated.

A.1.7 Conclusion

The macro-element has a simple intuitive input, and was shown to reproduce, with satisfying accuracy, the response computed in FEA and the response observed in the Bothkennar field test. Three examples have been used to illustrate the macro-element's performance. These examples show that the macro-element:

- reproduces the response computed in FE Analyses of the soil volume and the bucket foundation
- is numerically stable and does not cause numerical ratcheting

- produces a response in good agreement with a large scale field test

The macro-element was however developed with the purpose of being simple. The limited amount of input parameters compromises the accuracy, and it is therefore advised to compare some of the results with a FE Analyses.

A.2 A hypoplastic macroelement for shallow foundations subject to six-dimensional loading paths

A.2.1 Introduction

In order to model soil–foundation–superstructure–interaction (SFSI) problems of structures, one approach is to model the soil as a continuous medium, and adopting a suitable constitutive equation to reproduce the behavior of the soil. The main drawback of this method is the required discretization of a large soil volume, leading to large computational demand. In this paper, the model presented in Salciarini and Tamagnini [35] is extended to 6-dimensional loading states in order to allow more general loading specification. For the use of wind and wave loading this scenario is quite unrealistic. In the case of three-legged mobile drilling units for example, the environmental forces on the structure may apply torsional moments to the foundations. The model is validated based on the observed response in a series of laboratory tests performed at 1g on a small-scale circular foundation, subjected to complex loading paths.

A.2.2 Basis

The results were validated by means of an experimental program. A specially developed testing apparatus was used to perform a series of displacement-controlled "swipe" tests. Firstly, a 50mm flat circular footing is penetrated into sand, after which the vertical displacement is held constant and an additional rotation or translation is imposed along one of the remaining DOF's. The resulting load path is thought to closely trace the combined load capacity corresponding to the footing embedment. More complex load paths with two swipe-loading phases of different type have been used to assess the predictive capabilities of the hypo-plastic macro-element model.

A.3 Investigating six-degree-of-freedom loading of shallow foundations on sand [5]

This paper describes the experimental work carried out in order to study the response of circular flat footing on loose dry silica sand, exposed to loading in all 6 DOF. These forces are denoted as vertical (V), horizontal (H2, H3), torsion (Q) and overturning moment (M2, M3). The contents of this paper are described here to explain the working mechanisms of the Salciarini model [36] and to relate the parameters used in the Salciarini model to those described in ISO 19905-1. The paper distinguishes four components determining the responses:

- Yield surface
- Elastic behaviour within yield surface
- A hardening law that defines how the yield surface expands or contracts
- A plastic potential that describes the incremental plastic displacements at yield

The sections below describe the governing equations for each component.

A.3.1 Yield surface

In this paper the yield surface is normalised against the vertical capacity. Equation **??** is different from the one found in ISO19905-1.

Experimental work shows that the ratio of the horizontal to rotational loading influences the combined load capacity of the footing in the HM plane. For $a = 0$ the ellipse is perfectly round, and for $0 < a < 1$ it becomes more and more stretched in the HM plane until it becomes paraboidal. ISO 19905-1 does not consider this effect, thus assumes $a = 0$.

$$\left(\frac{F_{H1}/Q_V}{Q_H}\right)^2 + \left(\frac{F_{H2}/Q_V}{Q_H}\right)^2 + \left(\frac{F_{M1}/Q_V}{Q_M}\right)^2 + \left(\frac{F_{M2}/Q_V}{Q_M}\right)^2 - 2a\left(\frac{F_{H2} * F_{M2} - F_{H1} * F_{M2}}{Q_H * Q_M}\right) + \left(\frac{F_T/Q_V}{Q_T}\right)^2 - B_{12}(F_V/Q_V)^{2B_1}(1-(F_V/Q_V))^{2B_2} = 0 \quad \text{(A.7)}$$

$$B_{12} = \left[\frac{(B_1+B_2)^{(B_1+B_2)}}{B_1^{B_1}+B_2^{B_2}}\right]^2 \quad \text{(A.8)}$$

[5]

A.3.2 Elastic behaviour

The stiffness matrix is formulated as in **??**.

$$\bar{F} = 2GR * \begin{bmatrix} k & 0 & 0 & 0 & 0 & 0 \\ 0 & k & 0 & 0 & 0 & -k \\ 0 & 0 & k & 0 & k & 0 \\ 0 & 0 & 0 & k & 0 & 0 \\ 0 & 0 & k & 0 & k & 0 \\ 0 & -k & 0 & 0 & 0 & k \end{bmatrix} * \begin{bmatrix} w \\ u2 \\ u3 \\ 2R\omega \\ 2R\theta 2 \\ 2R\theta 3 \end{bmatrix} \quad \text{(A.9)}$$

A.3.3 Hardening law

Equation A.10 and A.11 describe the hardening curve with inclusion of radial hardening.

$$V_0 = k_1 * z_p \left[\frac{(1+z_p/w_1)}{(1+z_p/w_2)}\right] \quad \text{(A.10)}$$

[5]

$$\dot{z_p} = \dot{w_p} + c_1\sqrt{\dot{u}_{2p}^2 + \dot{u}_{3p}^2} + c_2\sqrt{(2R\dot{\theta_{2p}})^2 + (2R\dot{\theta_{3p}})^2} + c_3|2R\dot{\omega_p}| \quad \text{(A.11)}$$

[5]

Appendix B

Ground accelerations

B.1 Acceleration data Japan 1000-yr

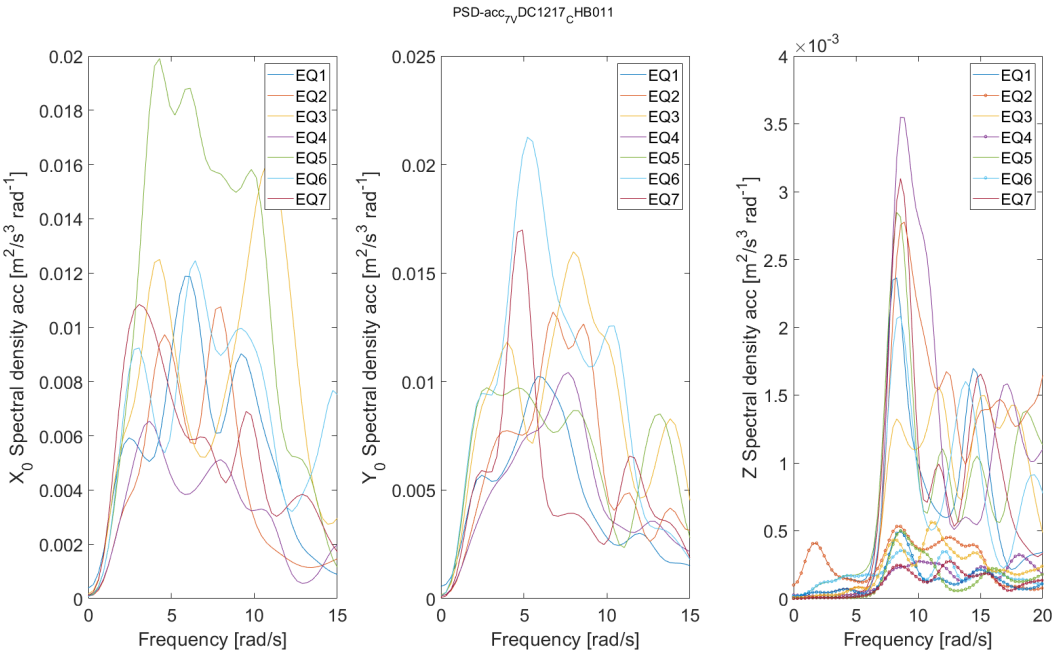

Figure B.1: PSD acceleration in all three directions for all earthquakes. Vertically damped spectrum marked with dots. Japan 1000-yr return period.

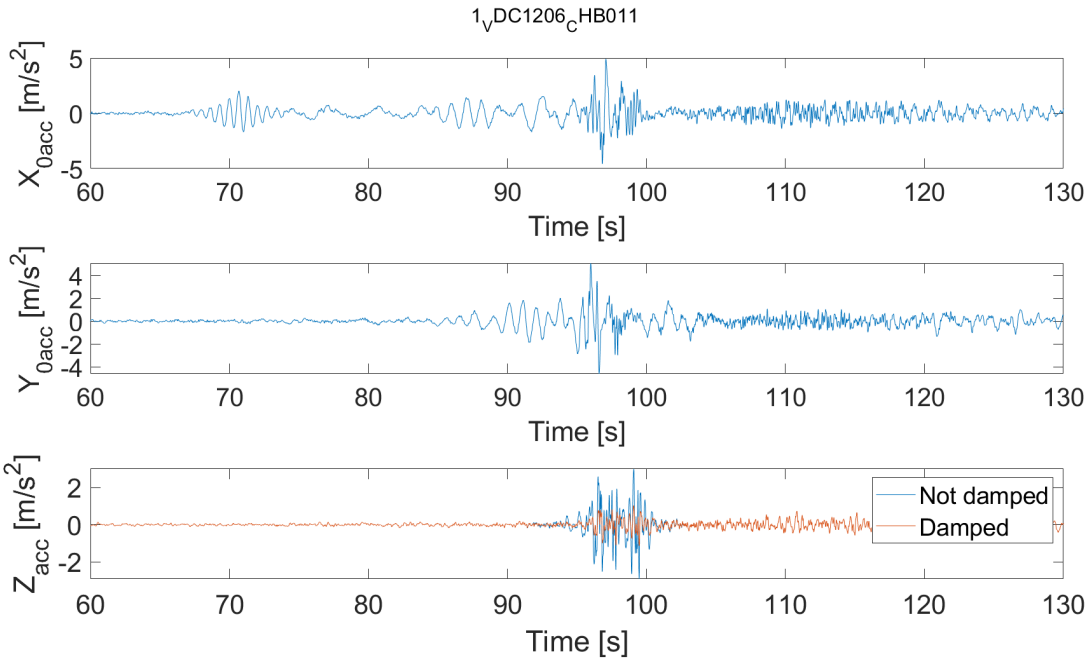

Figure B.2: Time-domain ground acceleration in all three directions. Japan 1000-yr return period, EQ1

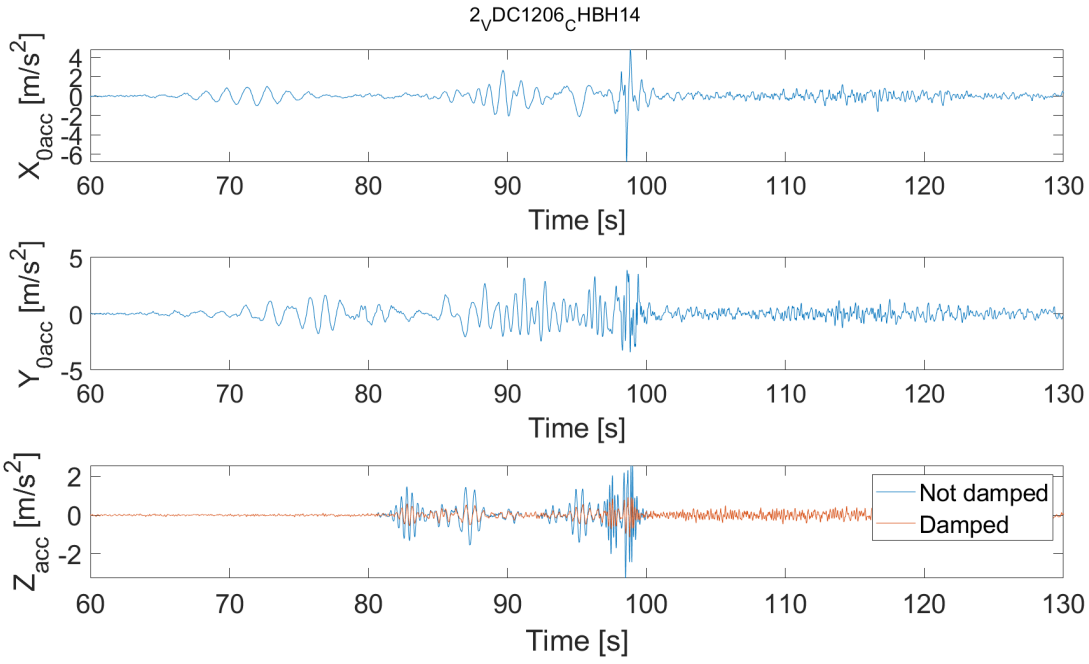

Figure B.3: Time-domain ground acceleration in all three directions. Japan 1000-yr return period, EQ2

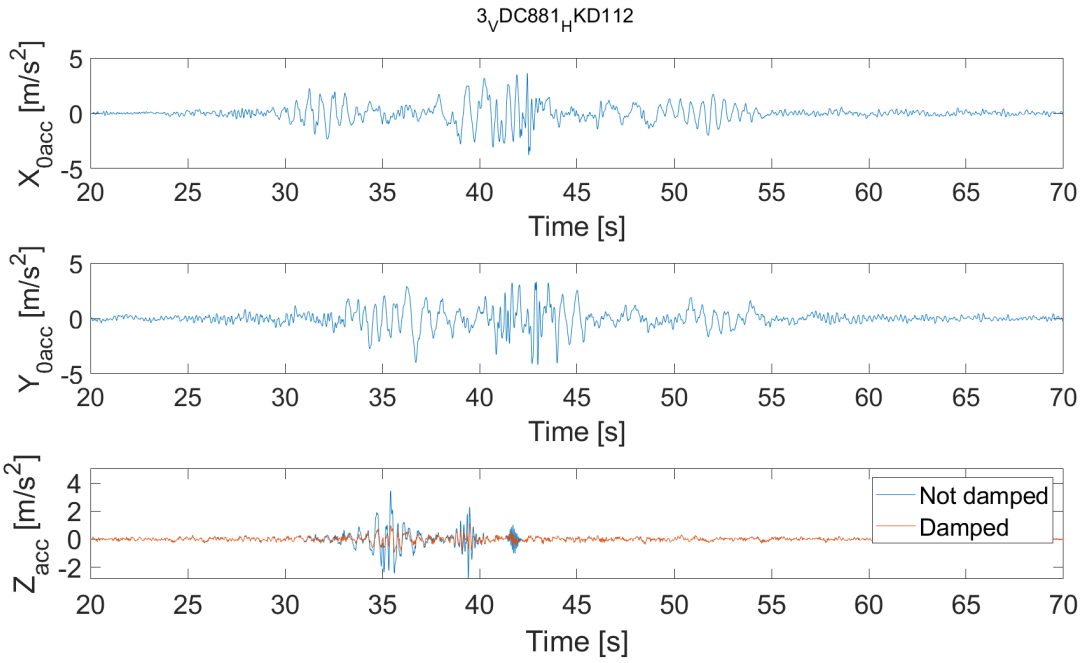

Figure B.4: Time-domain ground acceleration in all three directions. Japan 1000-yr return period, EQ3

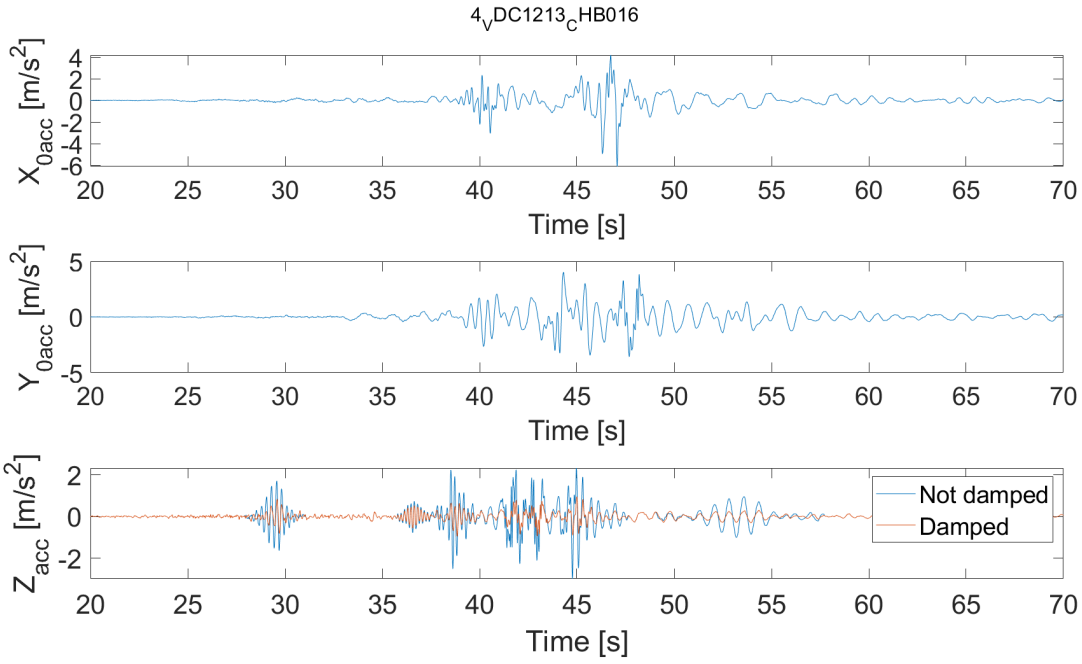

Figure B.5: Time-domain ground acceleration in all three directions. Japan 1000-yr return period, EQ4

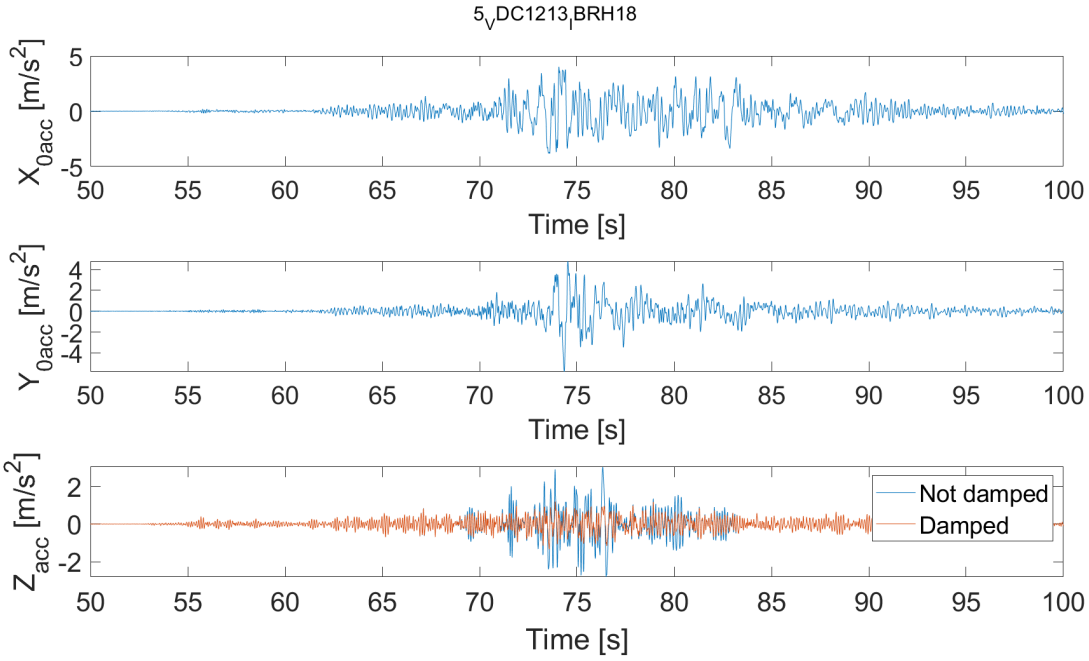

Figure B.6: Time-domain ground acceleration in all three directions. Japan 1000-yr return period, EQ5

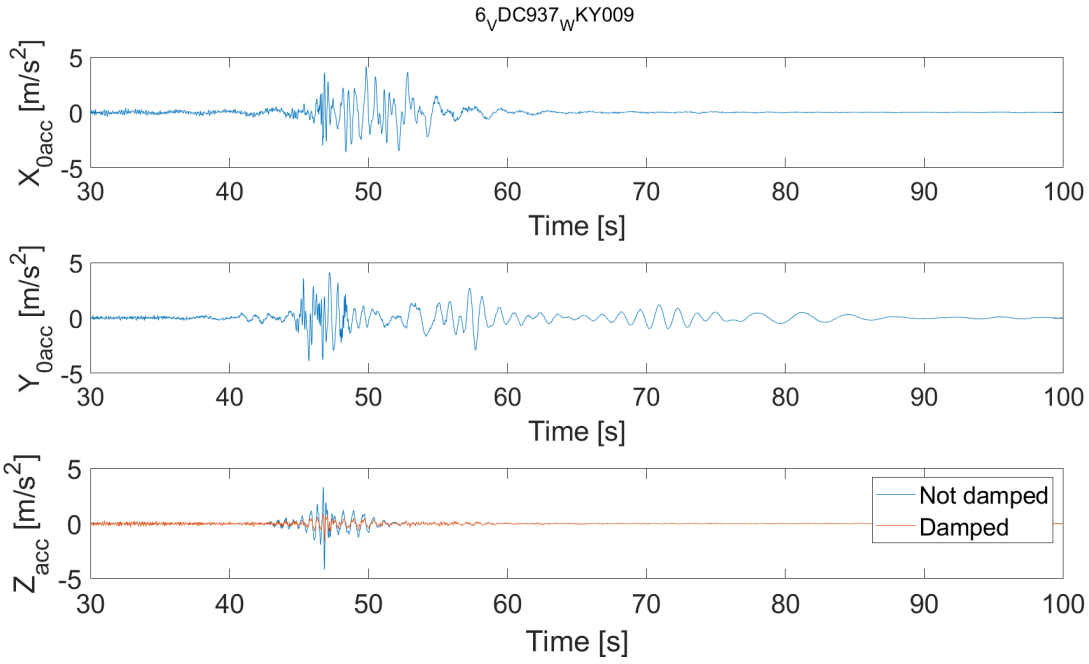

Figure B.7: Time-domain ground acceleration in all three directions. Japan 1000-yr return period, EQ6

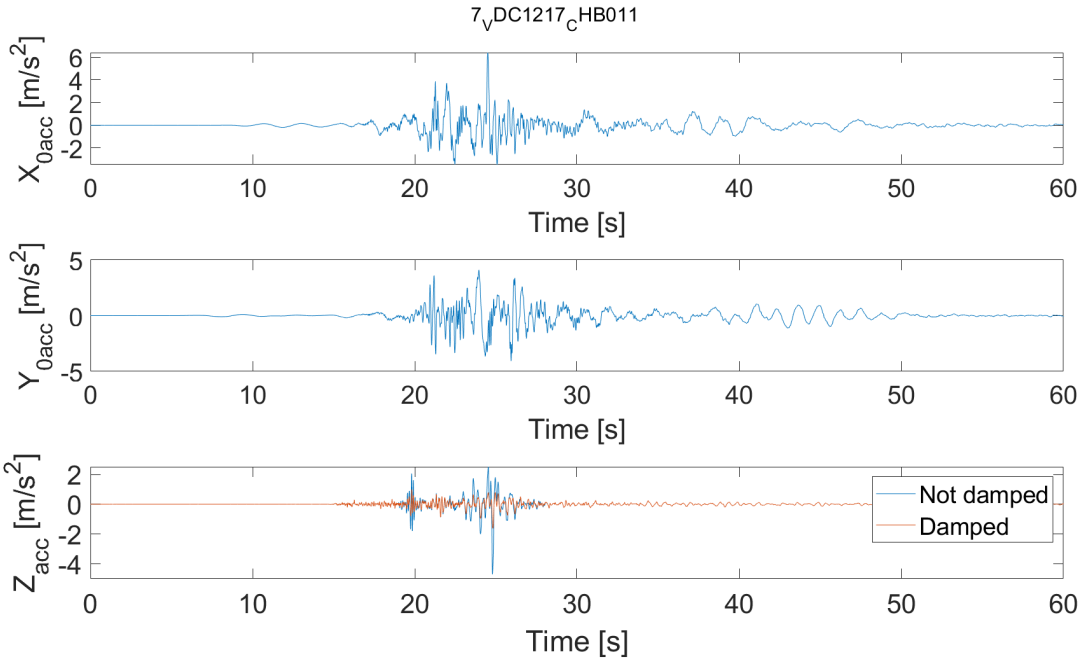

Figure B.8: Time-domain ground acceleration in all three directions. Japan 1000-yr return period, EQ7

B.2 Acceleration data Taiwan 200-yr

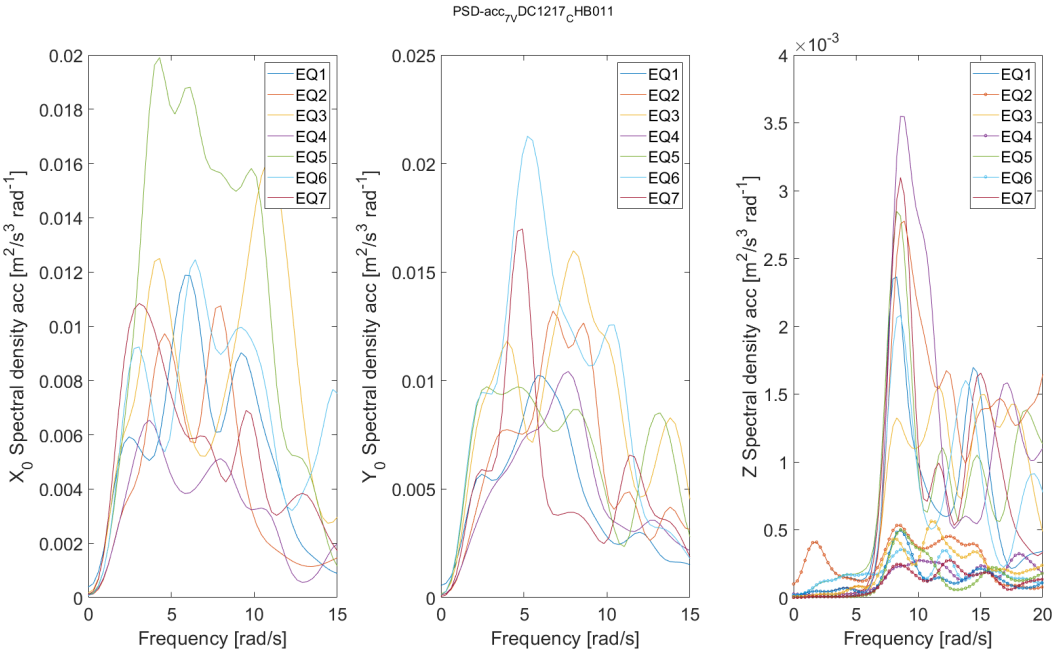

Figure B.9: PSD acceleration in all three directions for all earthquakes. Taiwan 200-yr return period.

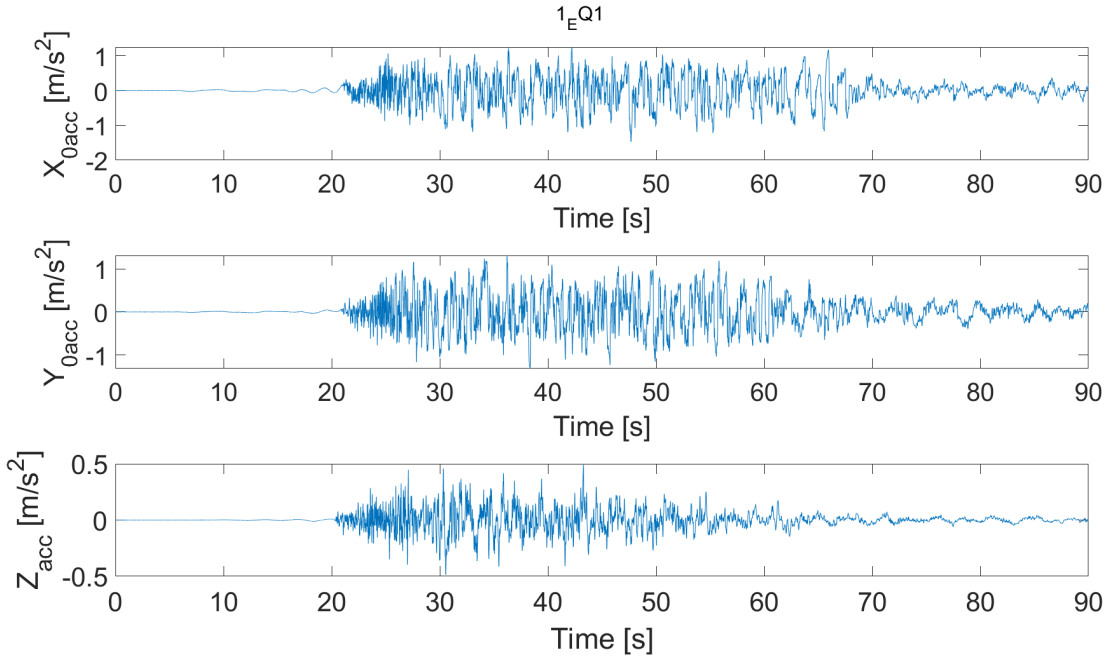

Figure B.10: Time-domain ground acceleration in all three directions. Taiwan 200-yr return period, EQ1

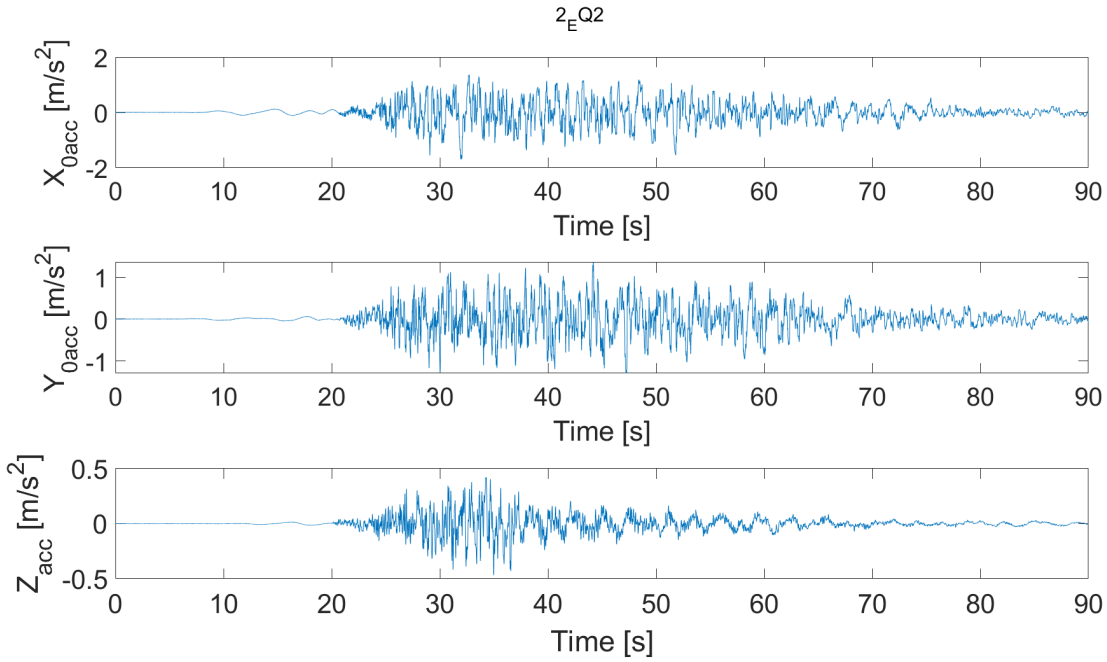

Figure B.11: Time-domain ground acceleration in all three directions. Taiwan 200-yr return period, EQ2

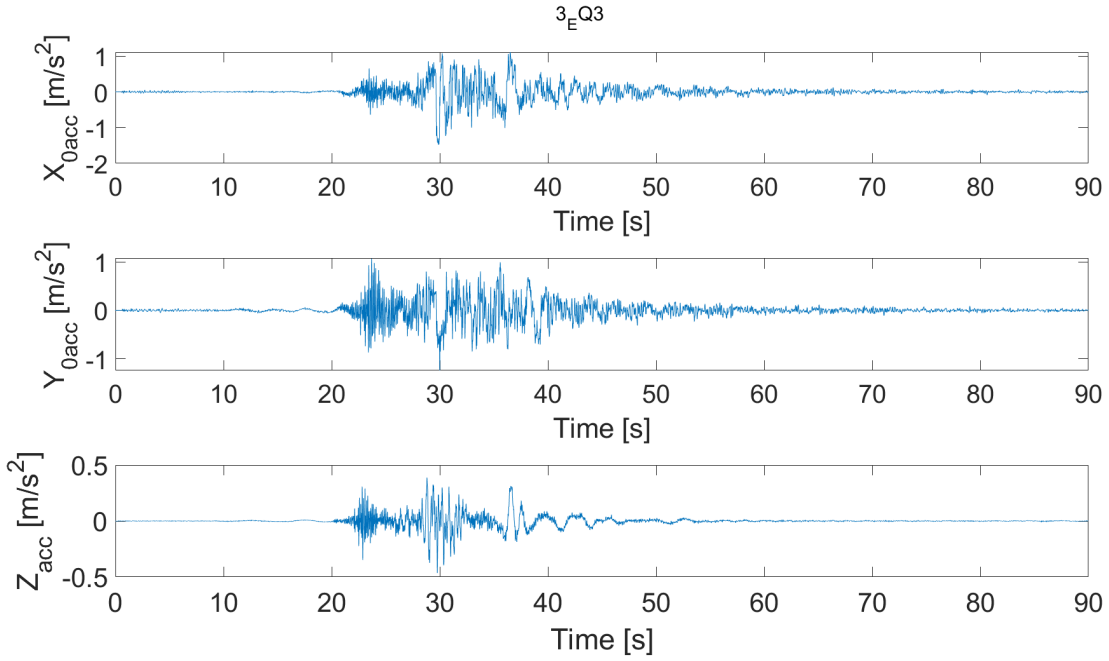

Figure B.12: Time-domain ground acceleration in all three directions. Taiwan 200-yr return period, EQ3

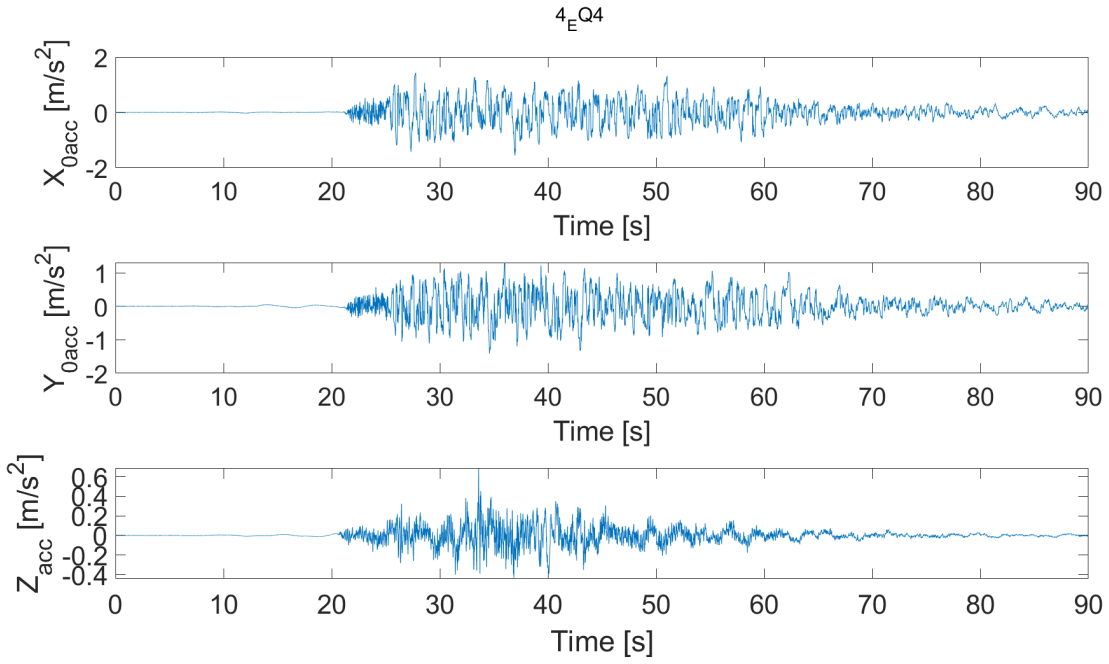

Figure B.13: Time-domain ground acceleration in all three directions. Taiwan 200-yr return period, EQ4

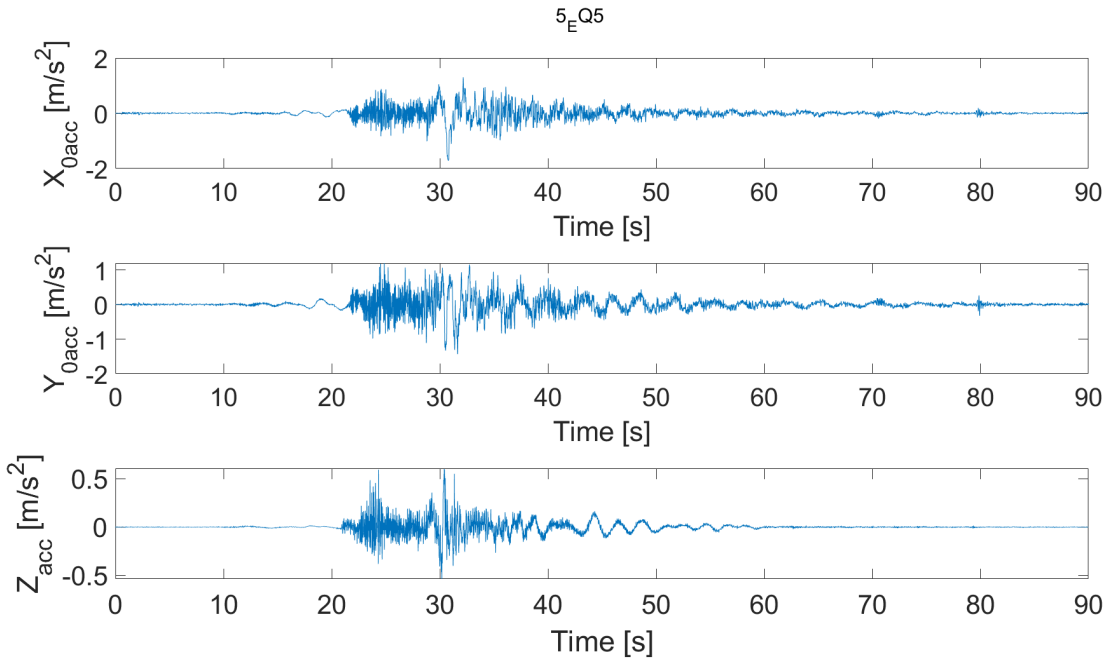

Figure B.14: Time-domain ground acceleration in all three directions. Taiwan 200-yr return period, EQ5

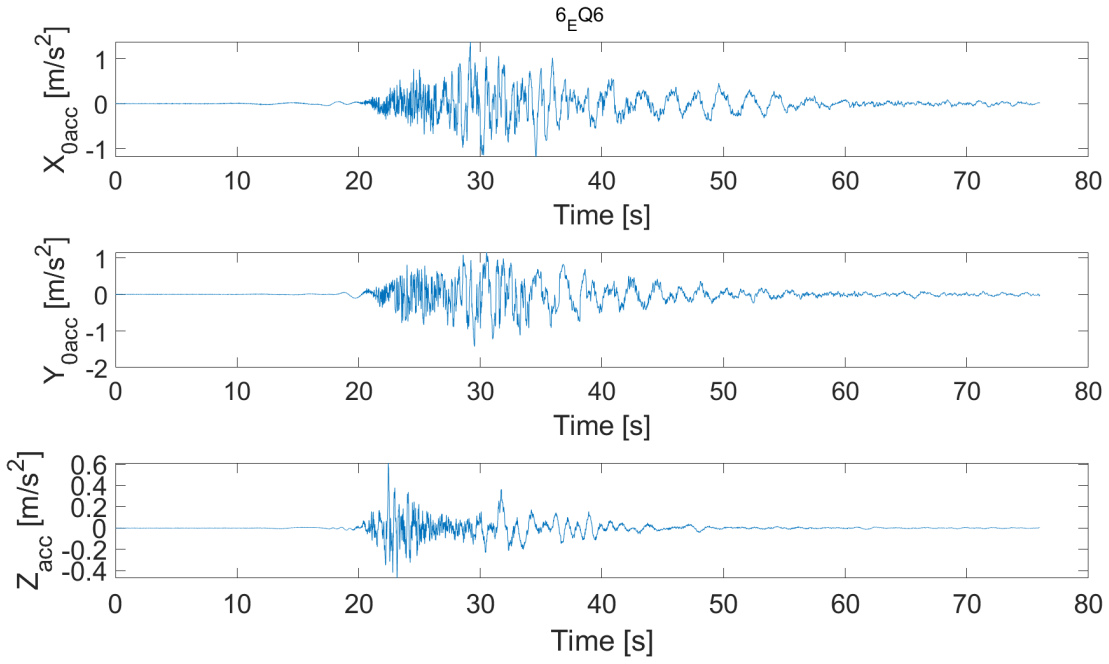

Figure B.15: Time-domain ground acceleration in all three directions. Taiwan 200-yr return period, EQ6

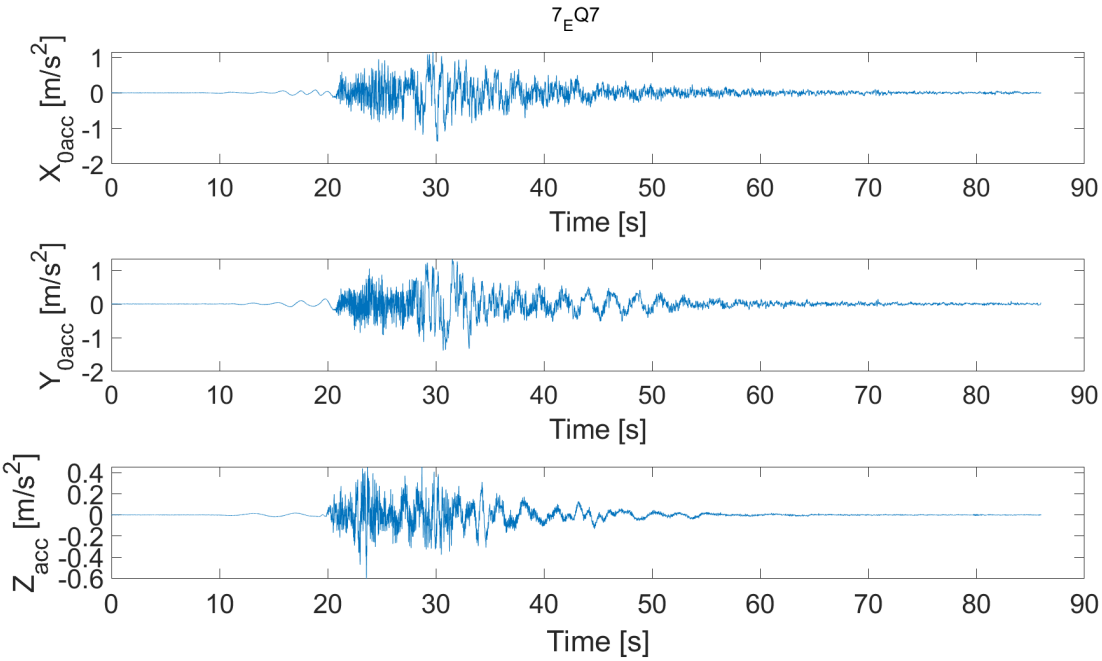

Figure B.16: Time-domain ground acceleration in all three directions. Taiwan 200-yr return period, EQ7

B.3 Acceleration data Taiwan 100-yr

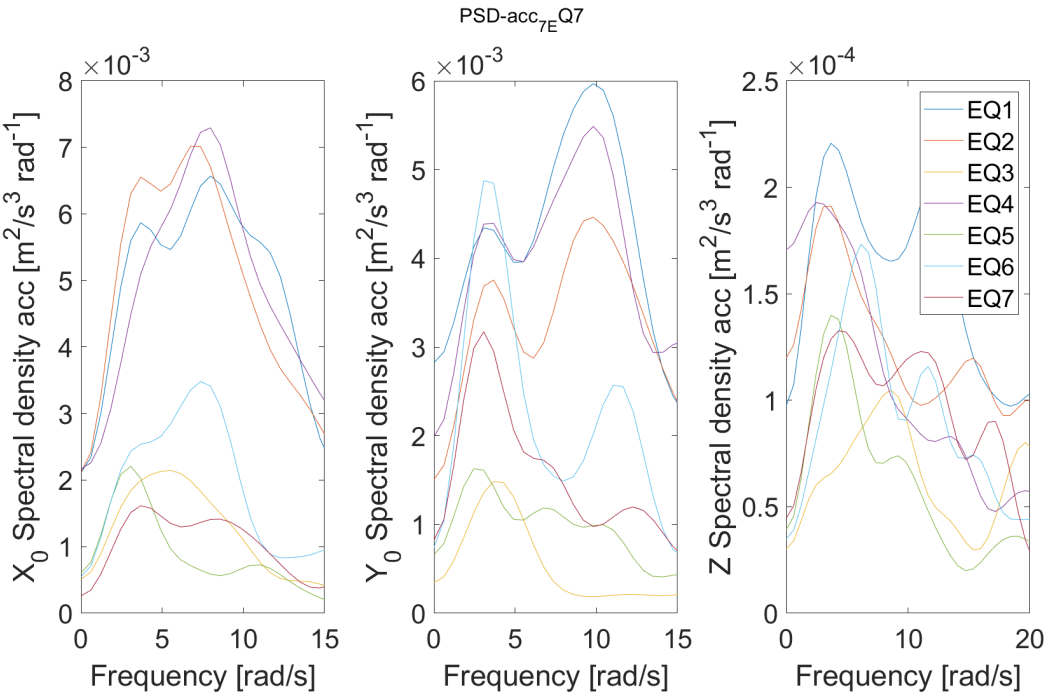

Figure B.17: PSD acceleration in all three directions for all earthquakes. Taiwan 100-yr return period.

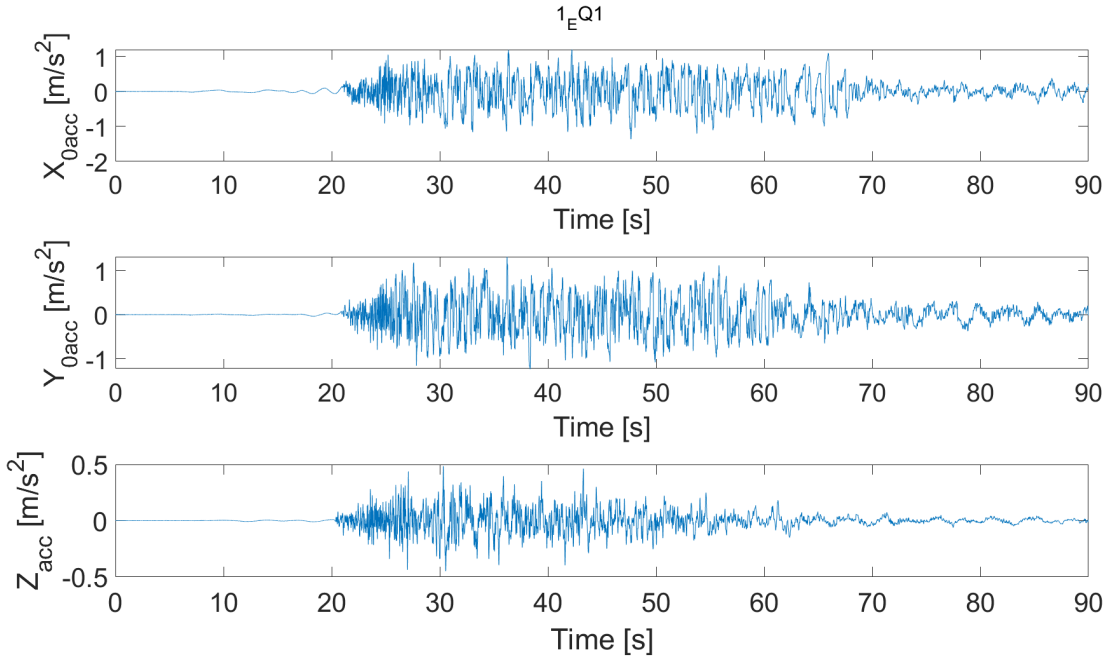

Figure B.18: Time-domain ground acceleration in all three directions. Taiwan 100-yr return period, EQ1

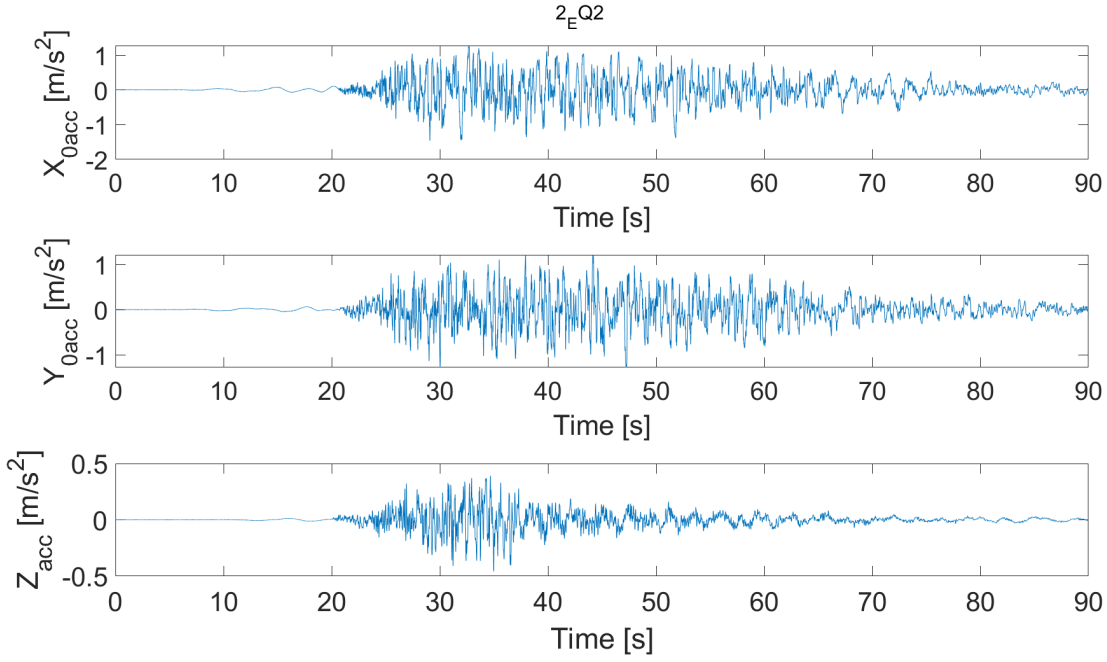

Figure B.19: Time-domain ground acceleration in all three directions. Taiwan 100-yr return period, EQ2

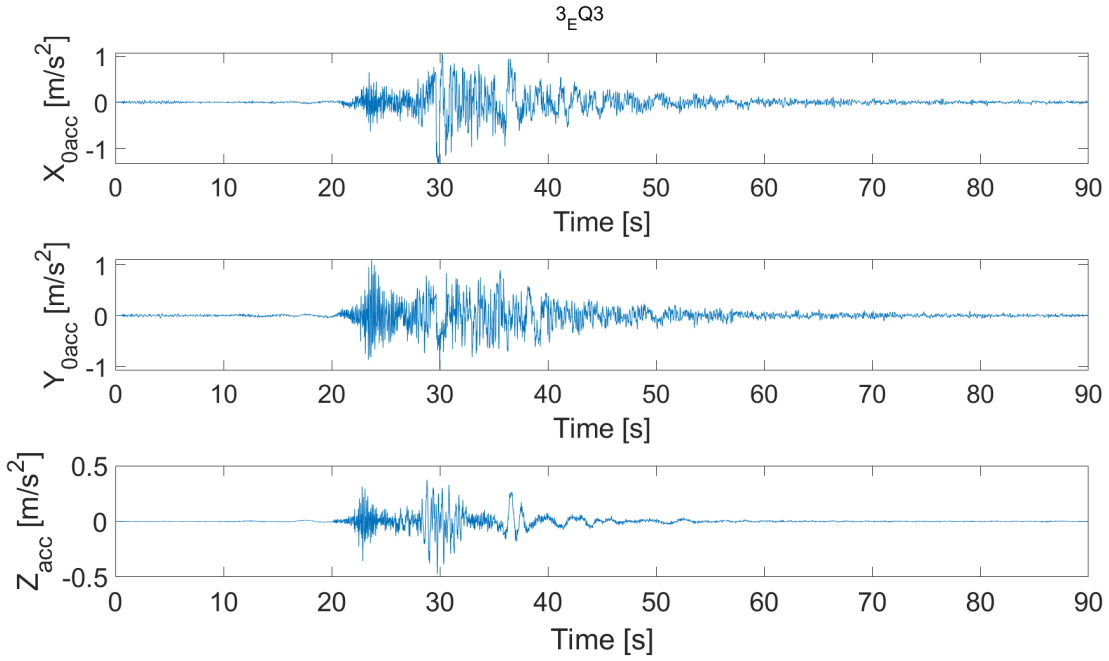

Figure B.20: Time-domain ground acceleration in all three directions. Taiwan 100-yr return period, EQ3

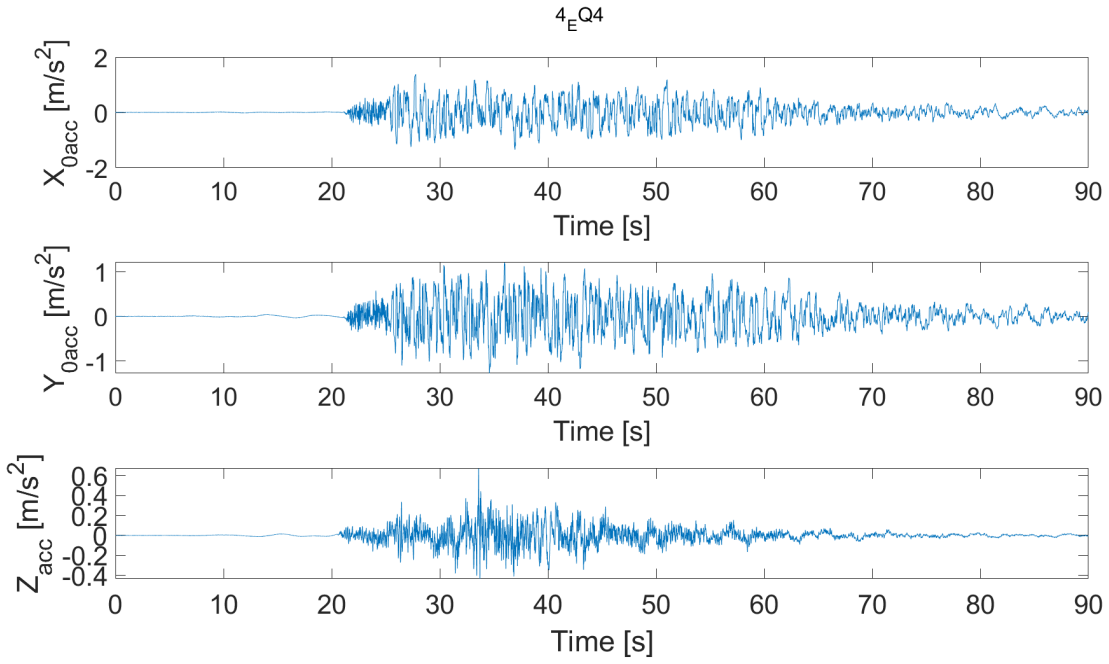

Figure B.21: Time-domain ground acceleration in all three directions. Taiwan 100-yr return period, EQ4

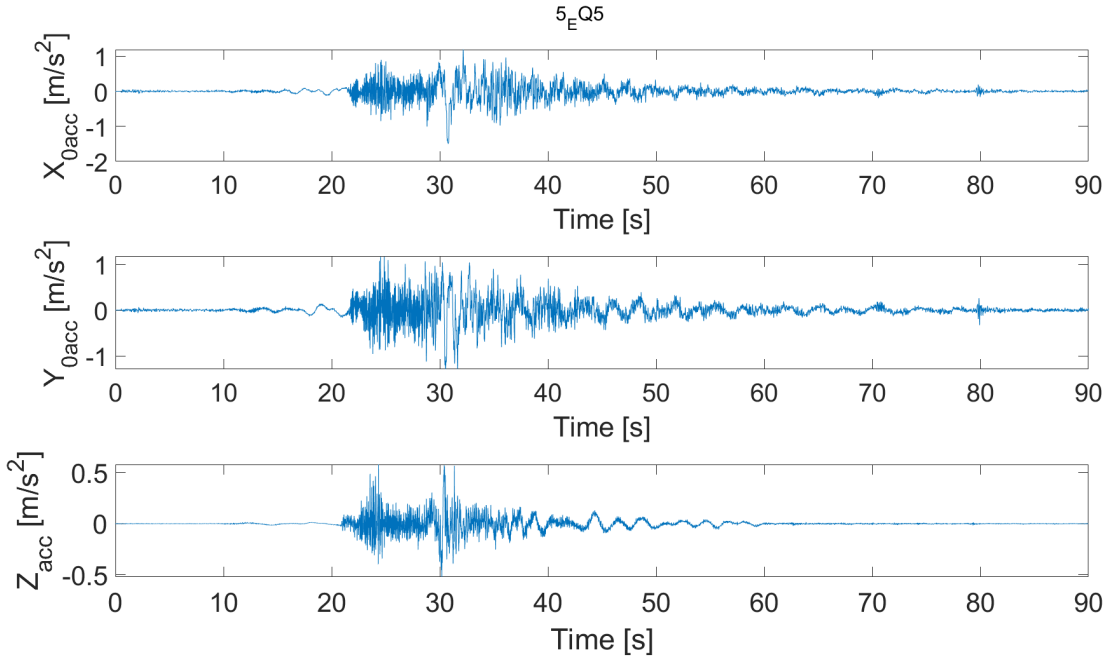

Figure B.22: Time-domain ground acceleration in all three directions. Taiwan 100-yr return period, EQ5

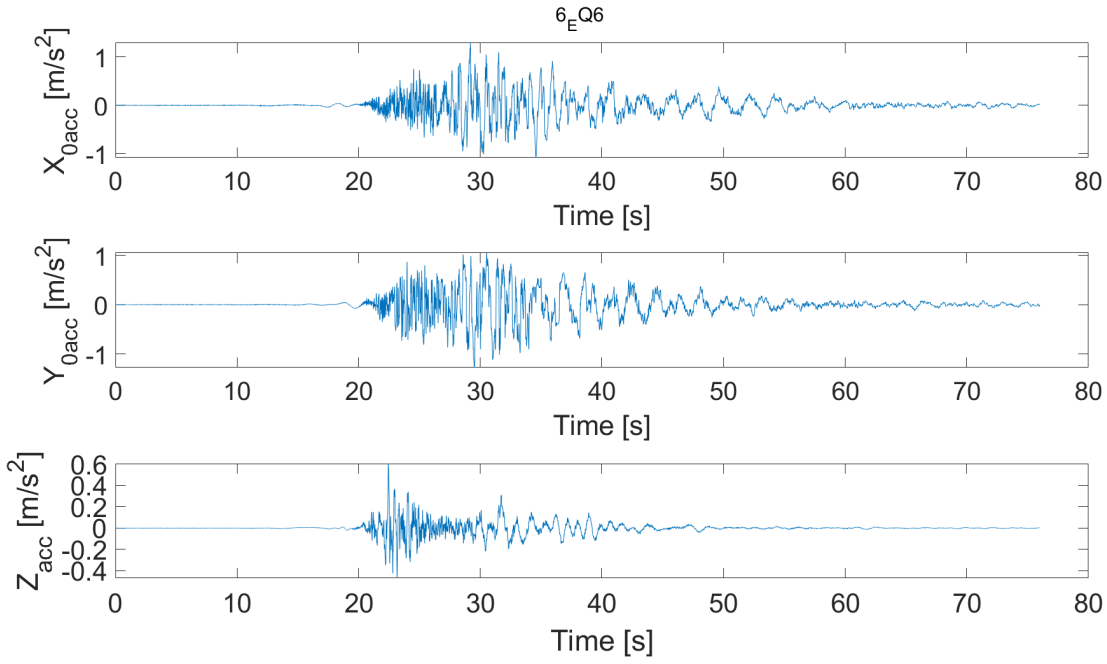

Figure B.23: Time-domain ground acceleration in all three directions. Taiwan 100-yr return period, EQ6

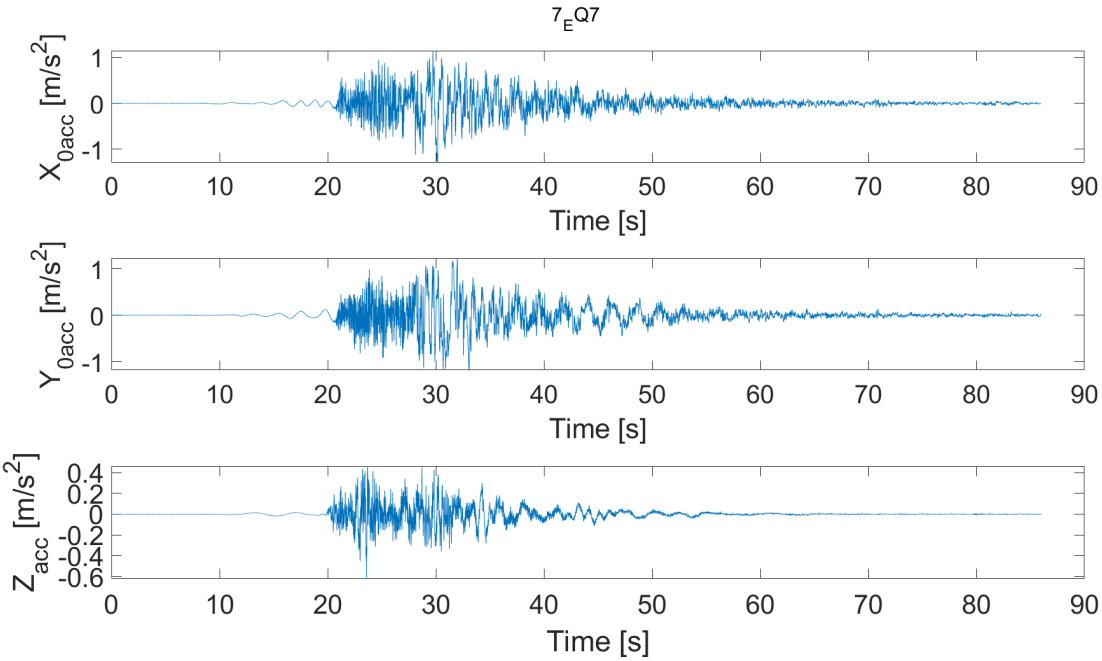

Figure B.24: Time-domain ground acceleration in all three directions. Taiwan 100-yr return period, EQ7

Appendix C

Radiation damping

C.1 Verification

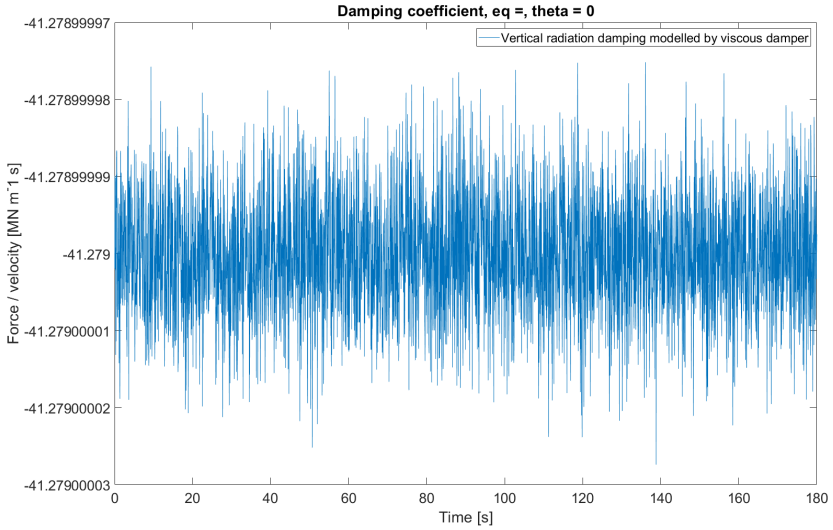

Figure C.1: Time-domain Force/velocity ($\theta = 0$, Leg 1)

C.2 Footing node Power Spectral Densities

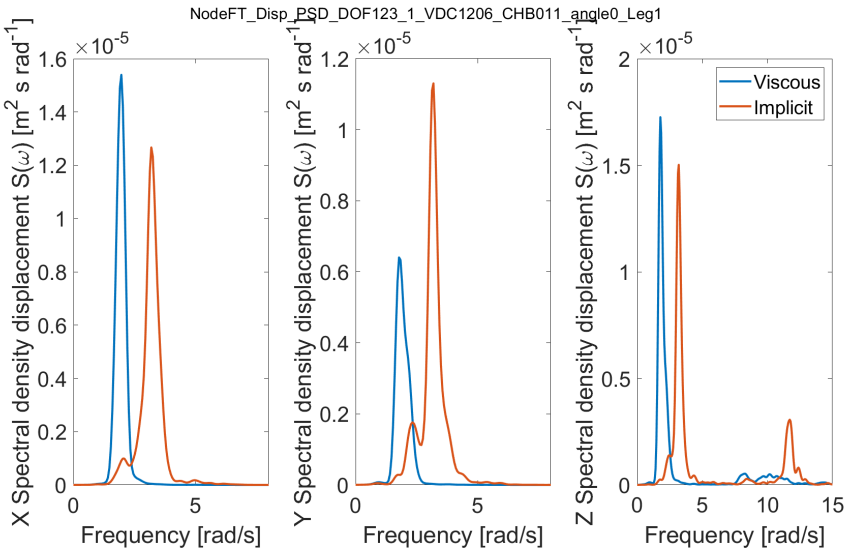

Figure C.2: Footing node displacement PSD for old (implicit) and new (viscous) model. In horizontal, horizontal and vertical direction (Japan 1000-yr, EQ1, $\theta = 0$, leg 1)

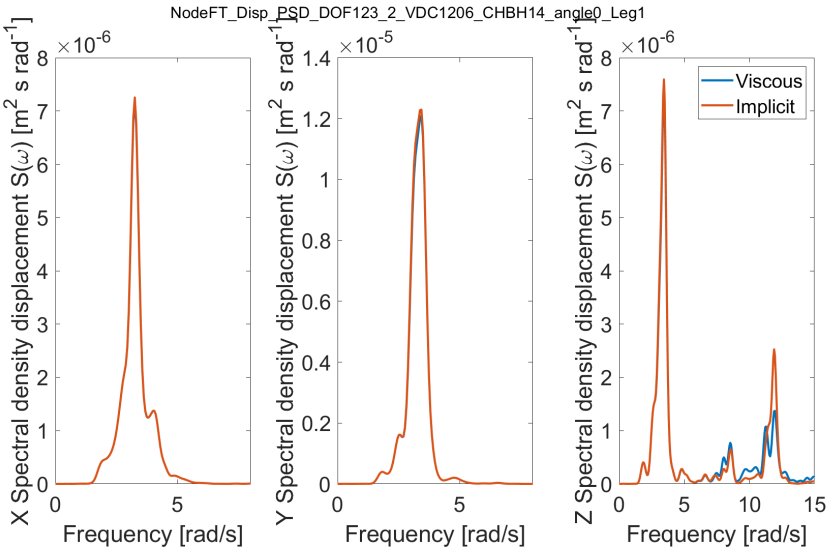

Figure C.3: Footing node displacement PSD for old (implicit) and new (viscous) model. In horizontal, horizontal and vertical direction (Japan 1000-yr, EQ2, $\theta = 0$, leg 1)

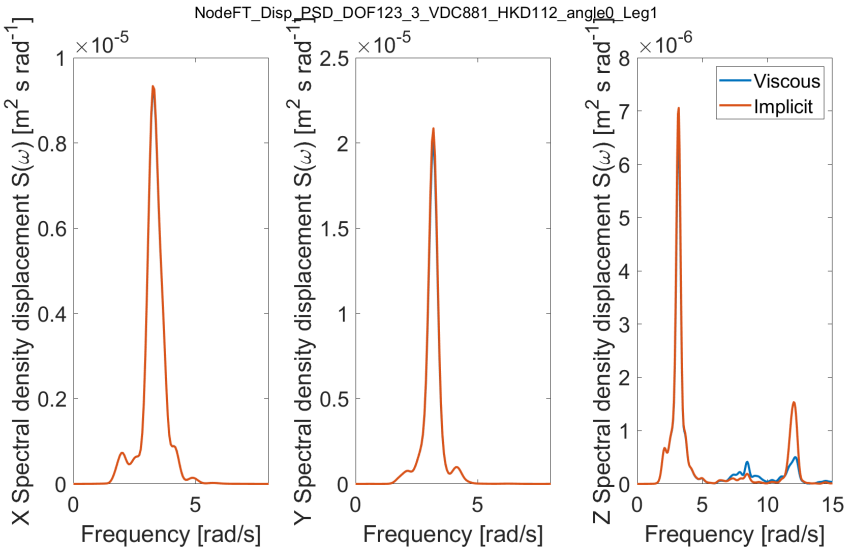

Figure C.4: Footing node displacement PSD for old (implicit) and new (viscous) model. In horizontal, horizontal and vertical direction (Japan 1000-yr, EQ3, $\theta = 0$, leg 1)

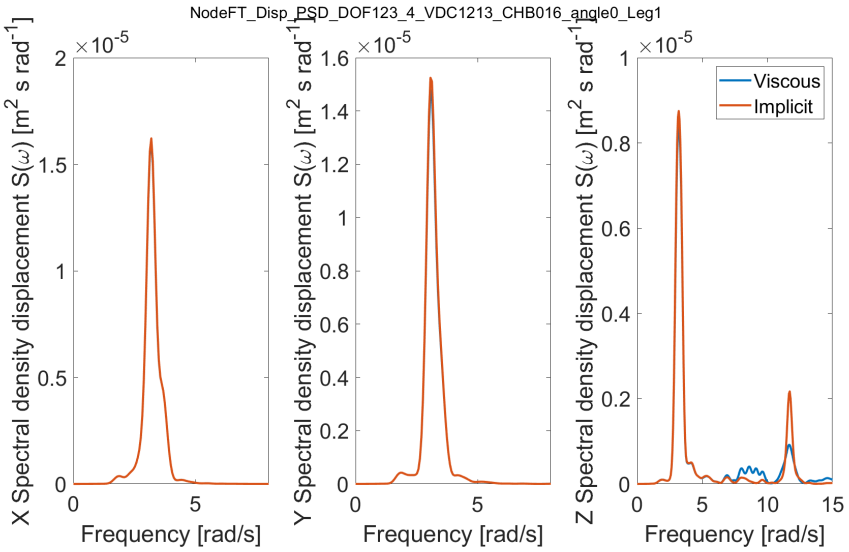

Figure C.5: Footing node displacement PSD for old (implicit) and new (viscous) model. In horizontal, horizontal and vertical direction (Japan 1000-yr, EQ4, $\theta = 0$, leg 1)

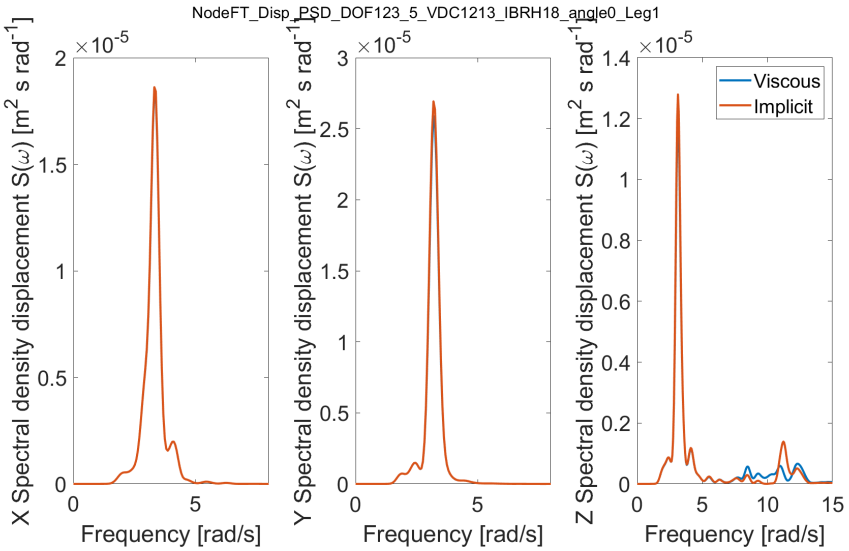

Figure C.6: Footing node displacement PSD for old (implicit) and new (viscous) model. In horizontal, horizontal and vertical direction (Japan 1000-yr, EQ5, $\theta = 0$, leg 1)

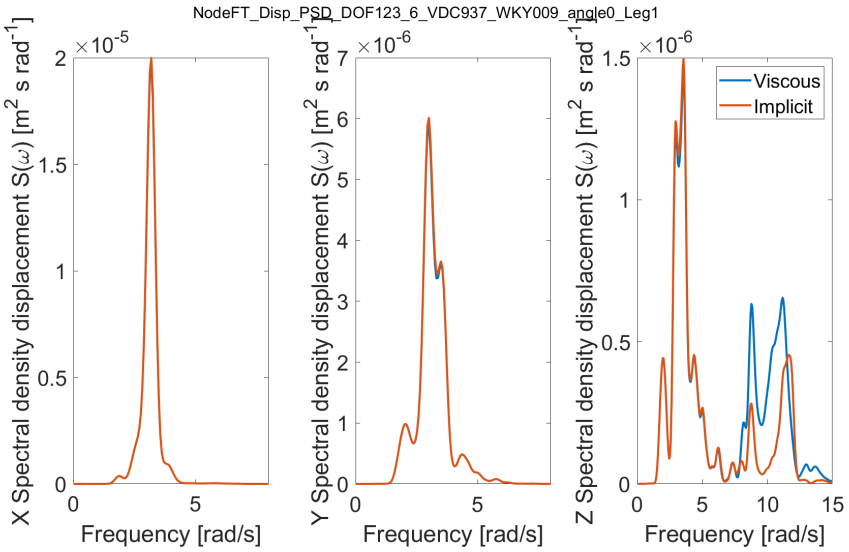

Figure C.7: Footing node displacement PSD for old (implicit) and new (viscous) model. In horizontal, horizontal and vertical direction (Japan 1000-yr, EQ6, $\theta = 0$, leg 1)

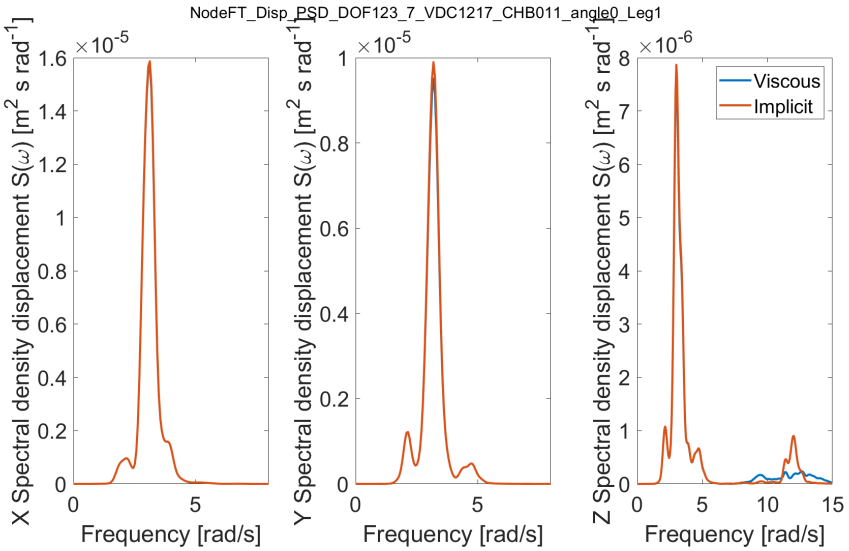

Figure C.8: Footing node displacement PSD for old (implicit) and new (viscous) model. In horizontal, horizontal and vertical direction (Japan 1000-yr, EQ7, $\theta = 0$, leg 1)

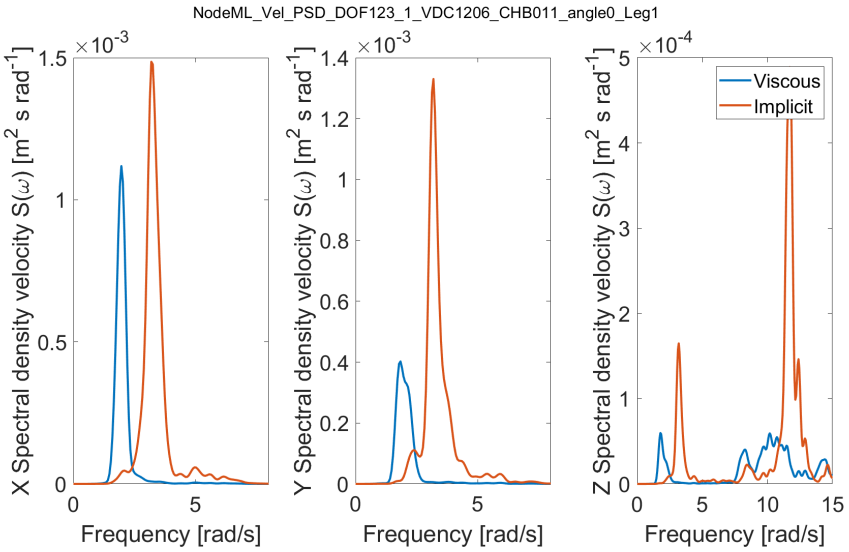

Figure C.9: Mudline node velocity PSD for old (implicit) and new (viscous) model. In horizontal, horizontal and vertical direction (Japan 1000-yr, EQ1, $\theta = 0$, leg 1)

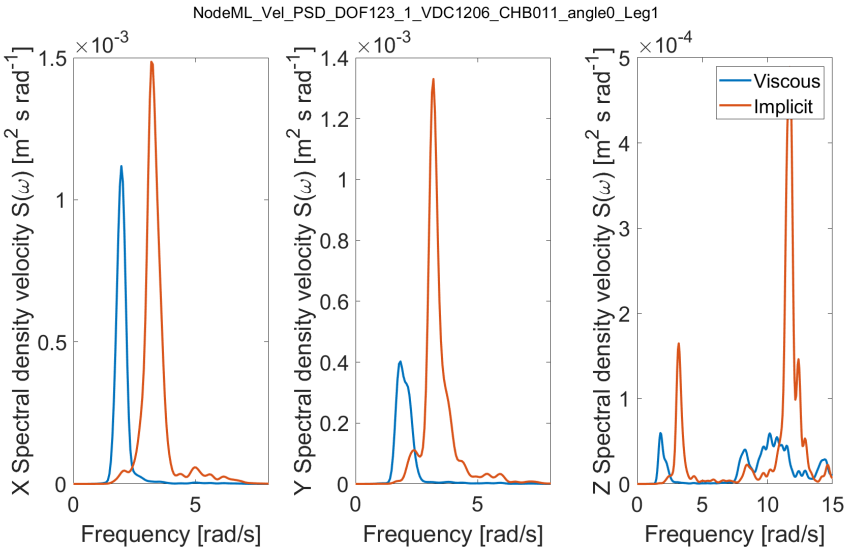

Figure C.10: Mudline node velocity PSD for old (implicit) and new (viscous) model. In horizontal, horizontal and vertical direction (Japan 1000-yr, EQ1, $\theta = 0$, leg 1)

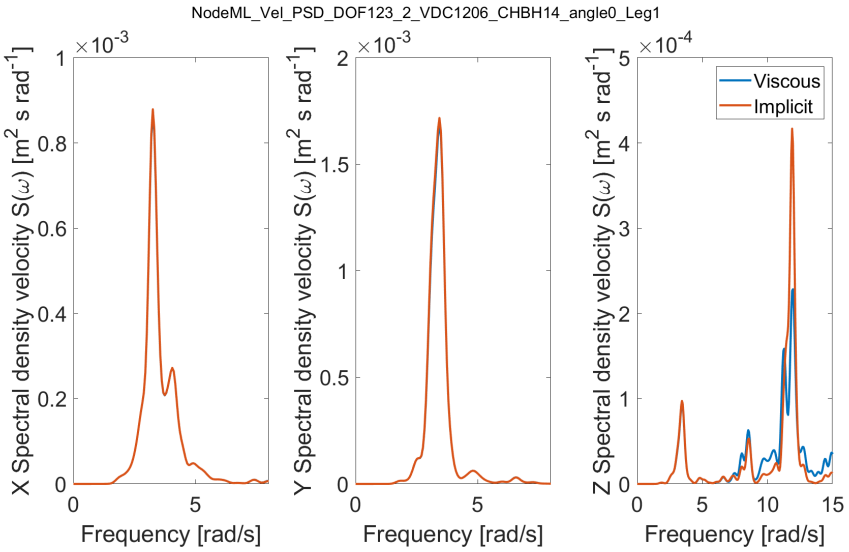

Figure C.11: Mudline node velocity PSD for old (implicit) and new (viscous) model. In horizontal, horizontal and vertical direction (Japan 1000-yr, EQ2, $\theta = 0$, leg 1)

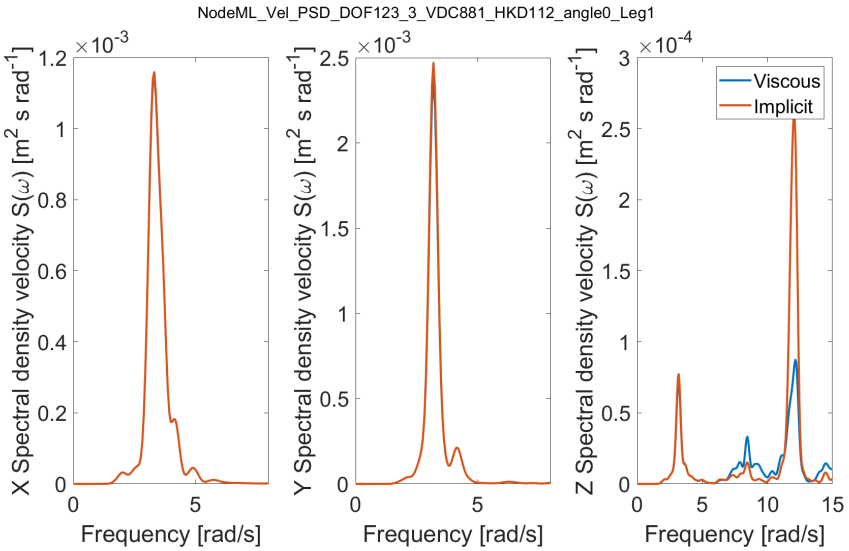

Figure C.12: Mudline node velocity PSD for old (implicit) and new (viscous) model. In horizontal, horizontal and vertical direction (Japan 1000-yr, EQ3, $\theta = 0$, leg 1)

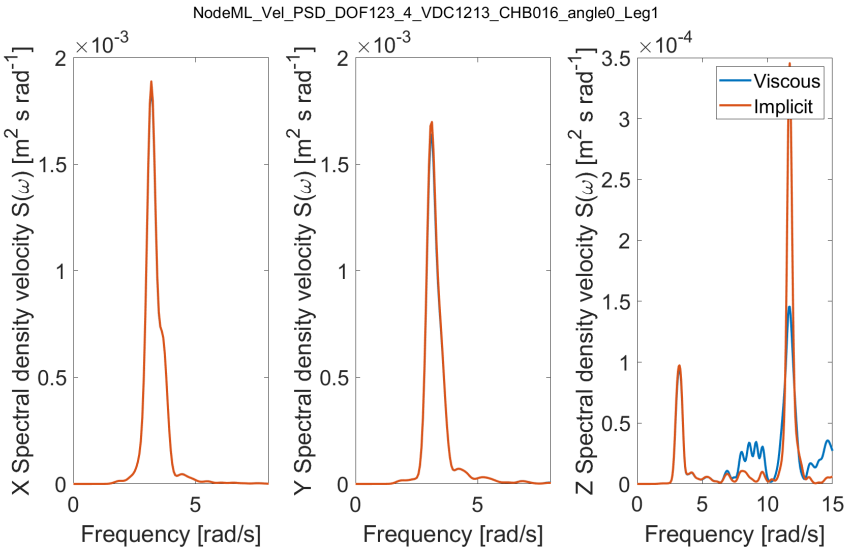

Figure C.13: Mudline node velocity PSD for old (implicit) and new (viscous) model. In horizontal, horizontal and vertical direction (Japan 1000-yr, EQ4, $\theta = 0$, leg 1)

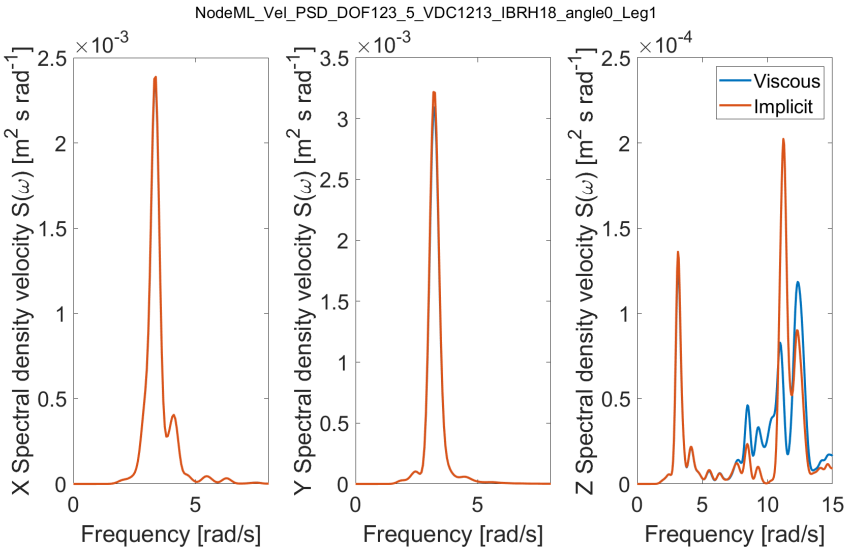

Figure C.14: Mudline node velocity PSD for old (implicit) and new (viscous) model. In horizontal, horizontal and vertical direction (Japan 1000-yr, EQ5, $\theta = 0$, leg 1)

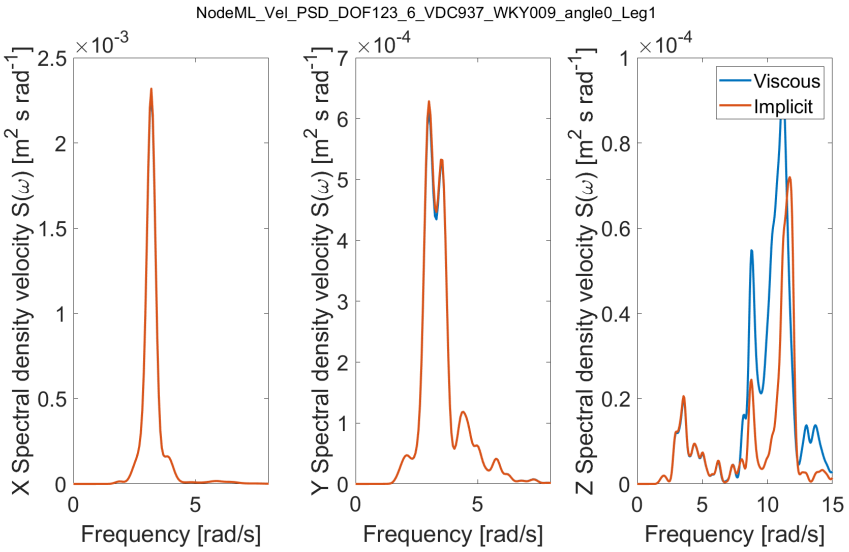

Figure C.15: Mudline node velocity PSD for old (implicit) and new (viscous) model. In horizontal, horizontal and vertical direction (Japan 1000-yr, EQ6, $\theta = 0$, leg 1)

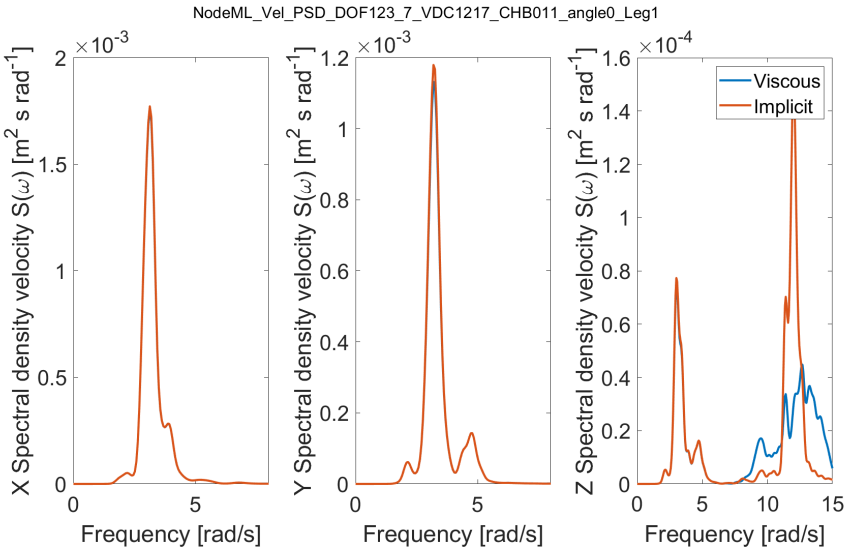

Figure C.16: Mudline node velocity PSD for old (implicit) and new (viscous) model. In horizontal, horizontal and vertical direction (Japan 1000-yr, EQ7, $\theta = 0$, leg 1)

C.3 Mudline node velocities time-domain

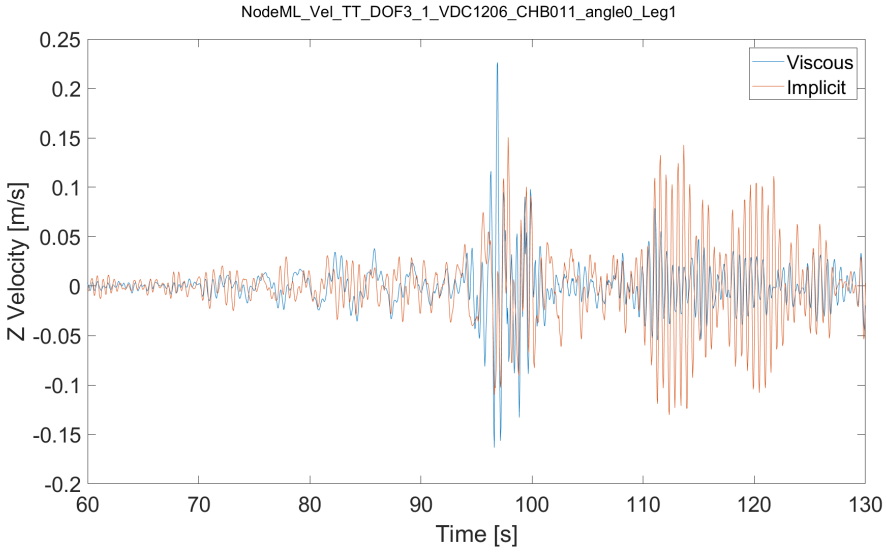

Figure C.17: Mudline node velocity for old (implicit) and new (viscous) model (Japan 1000-yr, EQ1, $\theta = 0$, leg 1)

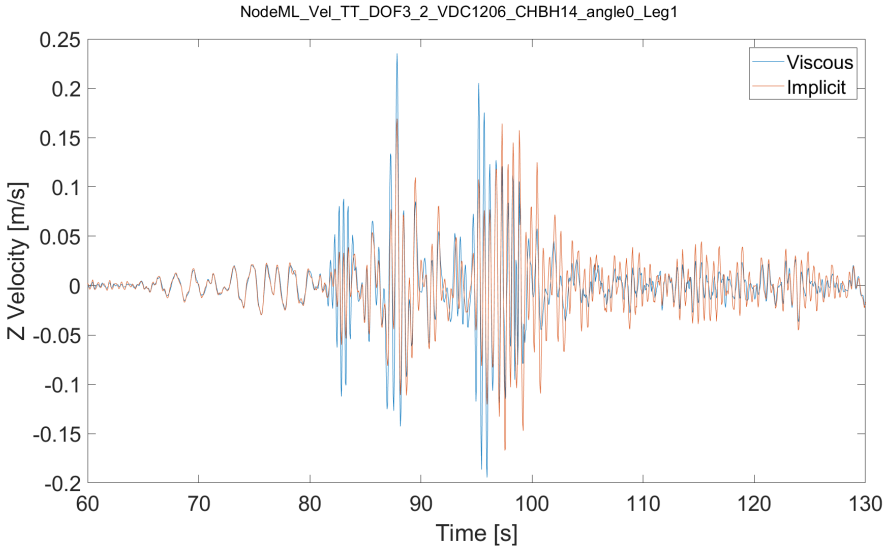

Figure C.18: Mudline node velocity for old (implicit) and new (viscous) model (Japan 1000-yr, EQ2, $\theta = 0$, leg 1)

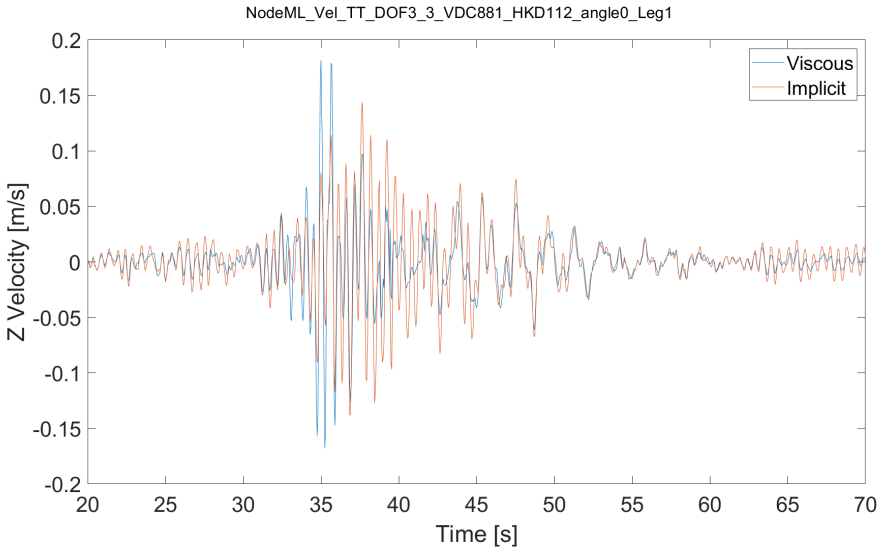

Figure C.19: Mudline node velocity for old (implicit) and new (viscous) model (Japan 1000-yr, EQ3, $\theta = 0$, leg 1)

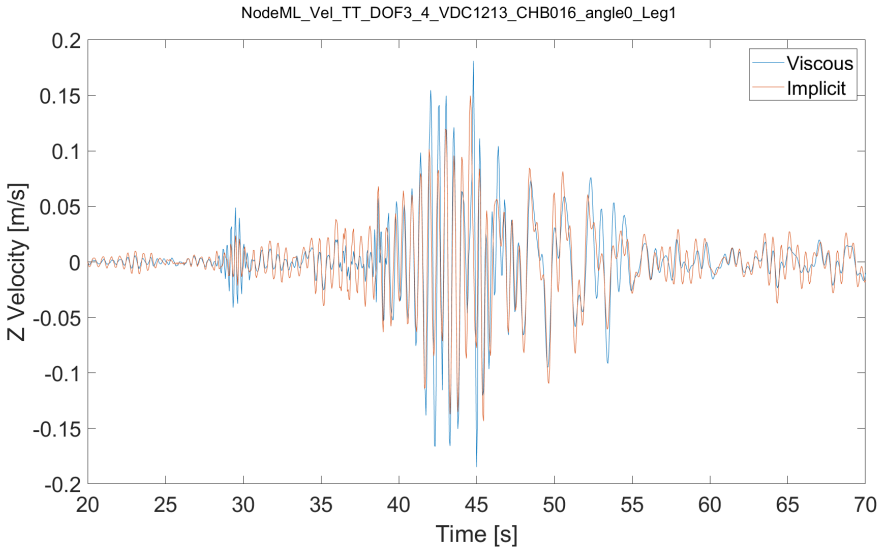

Figure C.20: Mudline node velocity for old (implicit) and new (viscous) model (Japan 1000-yr, EQ4, $\theta = 0$, leg 1)

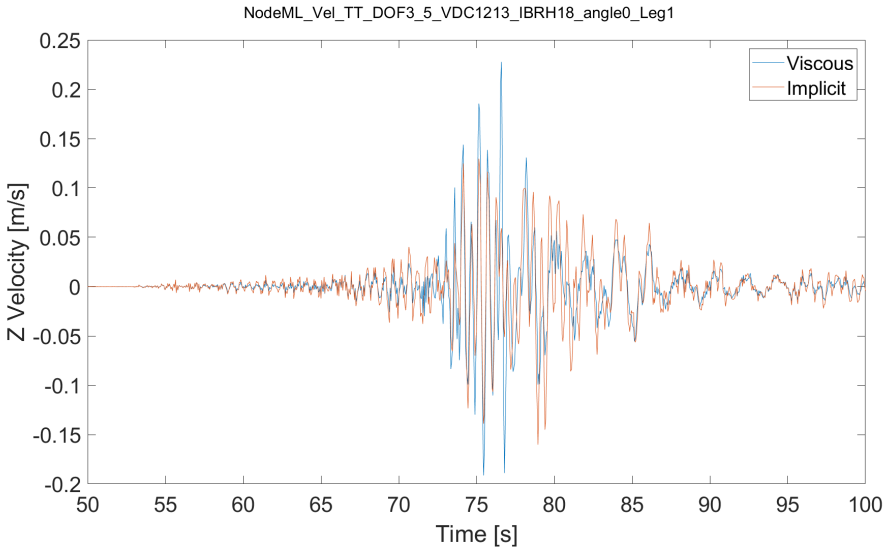

Figure C.21: Mudline node velocity for old (implicit) and new (viscous) model (Japan 1000-yr, EQ5, $\theta = 0$, leg 1)

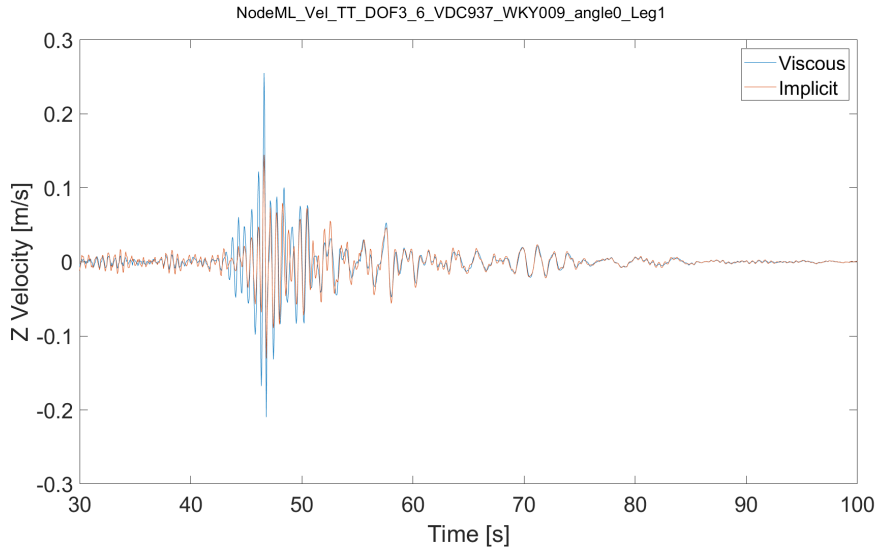

Figure C.22: Mudline node velocity for old (implicit) and new (viscous) model (Japan 1000-yr, EQ6, $\theta = 0$, leg 1)

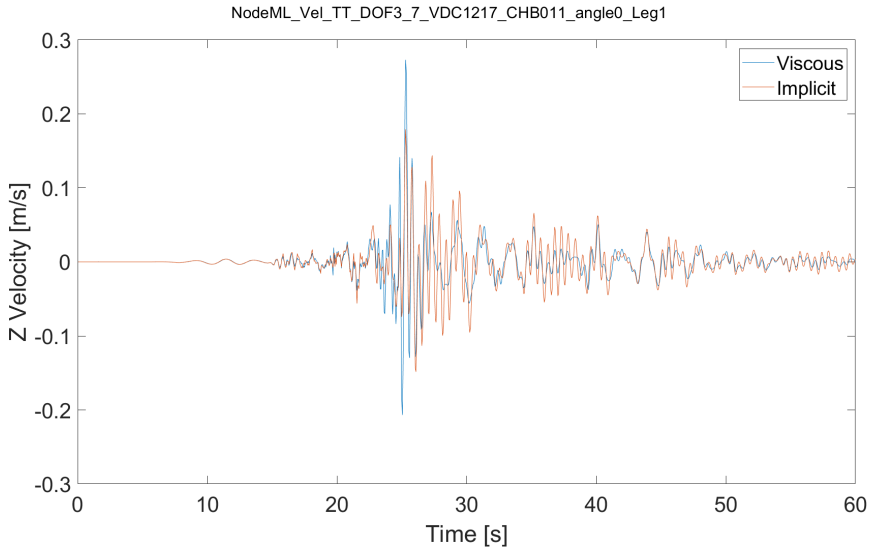

Figure C.23: Mudline node velocity for old (implicit) and new (viscous) model (Japan 1000-yr, EQ7, $\theta = 0$, leg 1)

C.4 Footing node accelerations time-domain

In this section, the footing node accelerations are compared with ground accelerations for the model with viscous radiation damping.

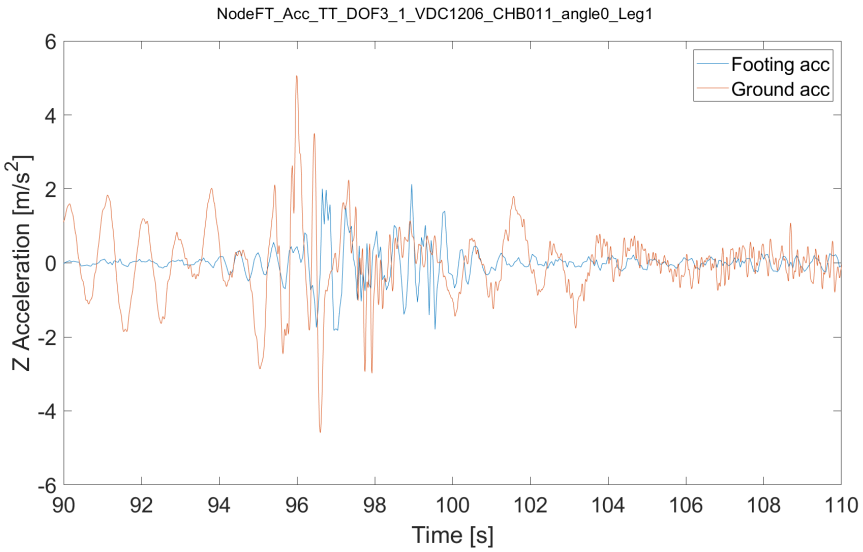

Figure C.24: Acceleration of footing and ground node during excitation peaks (Japan 1000-yr, EQ1, $\theta = 0$, leg 1)

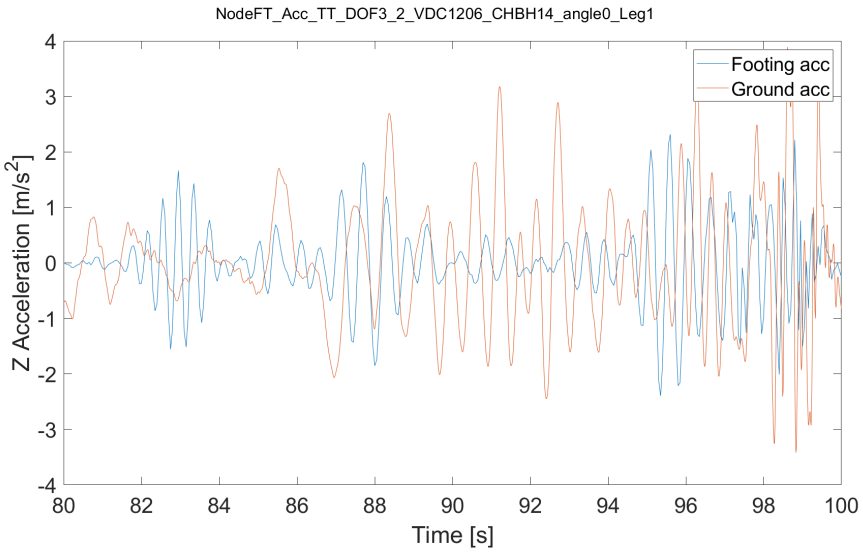

Figure C.25: Acceleration of footing and ground node during excitation peaks (Japan 1000-yr, EQ2, $\theta = 0$, leg 1)

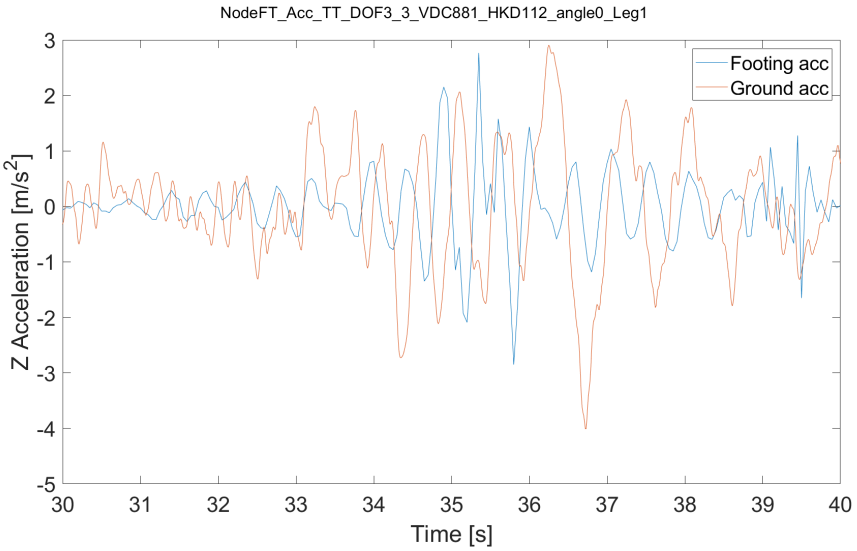

Figure C.26: Acceleration of footing and ground node during excitation peaks (Japan 1000-yr, EQ3, $\theta = 0$, leg 1)

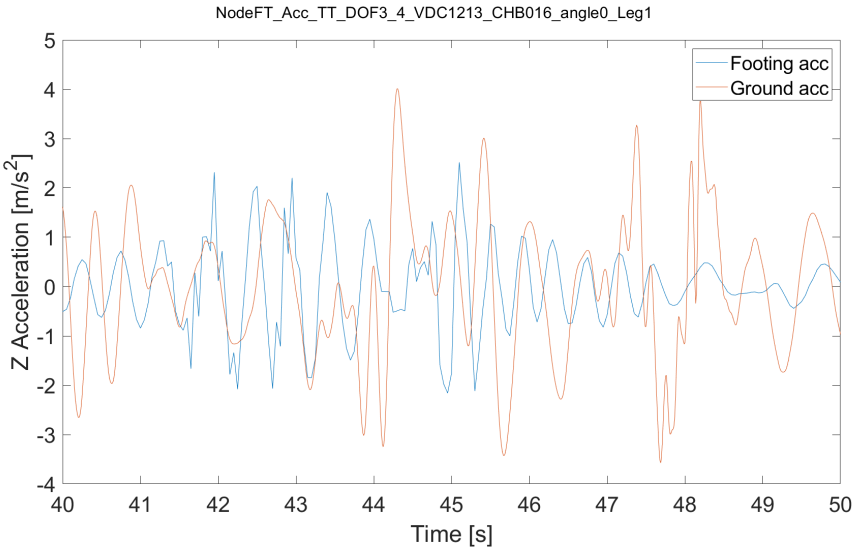

Figure C.27: Acceleration of footing and ground node during excitation peaks (Japan 1000-yr, EQ4, $\theta = 0$, leg 1)

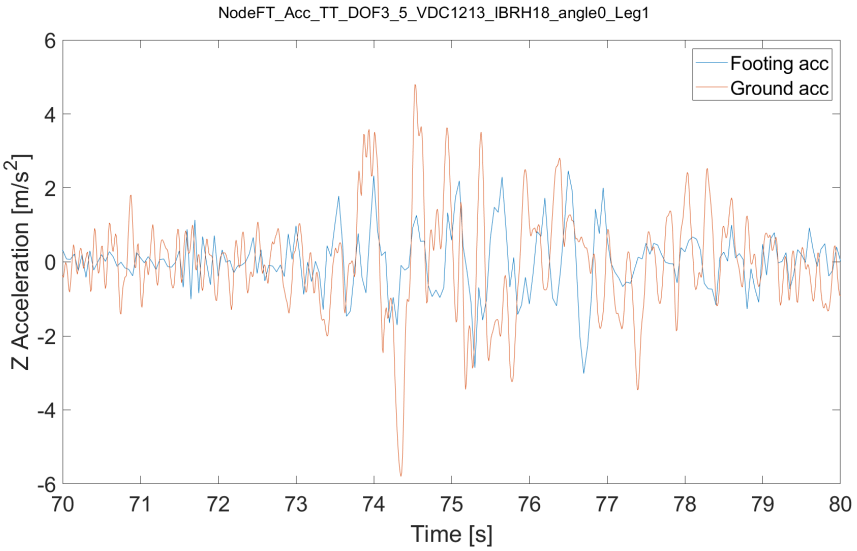

Figure C.28: Acceleration of footing and ground node during excitation peaks (Japan 1000-yr, EQ5, $\theta = 0$, leg 1)

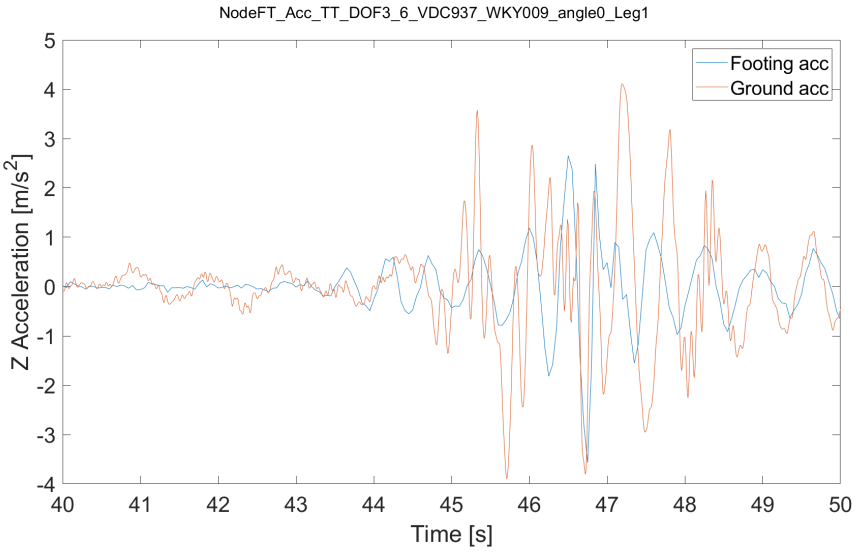

Figure C.29: Acceleration of footing and ground node during excitation peaks (Japan 1000-yr, EQ6, $\theta = 0$, leg 1)

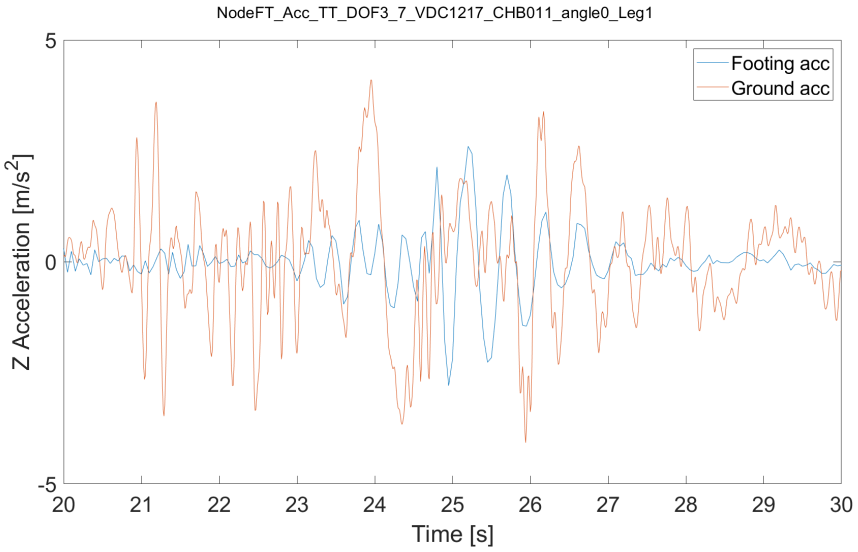

Figure C.30: Acceleration of footing and ground node during excitation peaks (Japan 1000-yr, EQ7, $\theta = 0$, leg 1)

Appendix D

Parameter combinations

D.1 Macro-element input: two-node model

D [m]	$V_0[N]$	$\zeta[m]$	k_v	k_h	k_m	k_q	k_c
10.0	1.0E9	0.0	1.0	1.0	1.0	1.0	0.0

G [Pa]	h_0	m_0	q_0	a	β_1	β_2
1.0E7	0.6	0.3	0.6	0	1.0	0.95

α_h	α_m	α_q	β_3	β_4
1.25	3.467	1.0	1.0	0.95

k_1	w_1	w_2	c_1	c_2	c_3
0	1	1	0	0	0

κ	m_R	m_T	R	β_R	χ
1.4	3.0	1.5	0.03	1.0	1.5

Table D.1: Material parameters macro-element as used in two-node model

D.2 Macro-element input: pile model

Soil as described in Yellow Leighton Buzzard Sand Cassidy et al. [5] and implemented in macro-element in [13].

D [m]	$V_0[N]$	$\zeta[m]$	k_v	k_h	k_m	k_q	k_c
12.0	3.56456E8	0.0	2.857	2.353	0.476	0.918	0.0

G [Pa]	h_0	m_0	q_0	a	β_1	β_2
4.0E7	0.6	0.3	0.6	0.0	1.0	0.95

α_h	α_m	α_q	β_3	β_4
1.25	3.467	1.0	1.0	0.95

k_1	w_1	w_2	c_1	c_2	c_3
0	1	1	0	0	0

κ	m_R	m_T	R	β_R	χ
1.4	3.0	1.5	0.03	1.0	1.5

Table D.2: Material parameters macro-element as used in pile model

D.3 Macro-element input: jack-up elastic

D [m]	$V_0[N]$	$\zeta[m]$	k_v	k_h	k_m	k_q	k_c
14.51	140.4E6	0.0	2.902	2.44	0.48	2.44	0.19

G [Pa]	h_0	m_0	q_0	a	β_1	β_2
4.0E7	36	109	36	0.0	1.0	0.95

α_h	α_m	α_q	β_3	β_4
1.25	3.467	1.0	1.0	0.95

k_1	w_1	w_2	c_1	c_2	c_3
0	1	1	0	0	0

κ	m_R	m_T	R	β_R	χ
1.4	3.0	1.5	0.03	1.0	1.5

Table D.3: Material parameters macro-element as used in jack-up model with elastic foundation

D.4 Macro-element input: jack-up basecase

D [m]	$V_0[N]$	$\zeta[m]$	k_v	k_h	k_m	k_q	k_c
14.51	140.4E6	0.0	2.902	2.44	0.48	2.44	0.19

G [Pa]	h_0	m_0	q_0	a	β_1	β_2
4.0E7	0.12	1.09	0.12	0.0	1.0	0.95

α_h	α_m	α_q	β_3	β_4
1.25	3.467	1.0	1.0	0.95

k_1	w_1	w_2	c_1	c_2	c_3
0	1	1	0	0	0

κ	m_R	m_T	R	β_R	χ
1.4	3.0	1.5	0.03	1.0	1.5

Table D.4: Material parameters macro-element as used in jack-up model for base case simulation

D.5 Macro-element input: jack-up 4 cases

D.5.1 Case 1: kappa 1.4

This parameters equal those of the base case. See Section D.4.

D.5.2 Case 2: kappa 0.25

D [m]	$V_0[N]$	$\zeta[m]$	k_v	k_h	k_m	k_q	k_c
14.51	140.4E6	0.0	2.902	2.44	0.48	2.44	0.19

G [Pa]	h_0	m_0	q_0	a	β_1	β_2
4.0E7	0.12	1.09	0.12	0.0	1.0	0.95

α_h	α_m	α_q	β_3	β_4
1.25	3.467	1.0	1.0	0.95

k_1	w_1	w_2	c_1	c_2	c_3
0	1	1	0	0	0

κ	m_R	m_T	R	β_R	χ
0.25	1.1	1.05	0.005	1.0	1.5

Table D.5: Material parameters macro-element as used in jack-up case 2

D.5.3 Case 3: kappa 0.4

D [m]	$V_0[N]$	$\zeta[m]$	k_v	k_h	k_m	k_q	k_c
14.51	140.4E6	0.0	2.902	2.44	0.48	2.44	0.19

G [Pa]	h_0	m_0	q_0	a	β_1	β_2
4.0E7	0.12	1.09	0.12	0.0	1.0	0.95

α_h	α_m	α_q	β_3	β_4
1.25	3.467	1.0	1.0	0.95

k_1	w_1	w_2	c_1	c_2	c_3
0	1	1	0	0	0

κ	m_R	m_T	R	β_R	χ
0.4	1.0	1.0	0.03	0.5	1.0

Table D.6: Material parameters macro-element as used in jack-up case 3. R has been increased to 0.03 to prevent failure of the macro-element

D.5.4 Case 4: kappa 1.1

D [m]	$V_0[N]$	$\zeta[m]$	k_v	k_h	k_m	k_q	k_c
14.51	140.4E6	0.0	2.902	2.44	0.48	2.44	0.19

G [Pa]	h_0	m_0	q_0	a	β_1	β_2
4.0E7	0.12	1.09	0.12	0.0	1.0	0.95

α_h	α_m	α_q	β_3	β_4
1.25	3.467	1.0	1.0	0.95

k_1	w_1	w_2	c_1	c_2	c_3
0	1	1	0	0	0

κ	m_R	m_T	R	β_R	χ
1.1	10.0	2.0	0.006	0.5	0.5

Table D.7: Material parameters macro-element as used in jack-up case 4

Appendix E

Results verification

E.1 Two-node model

	Force / Moment $[N/Nm]$					
Displacement	10	20	30	40	50	60
U1 [m]	1E-7	2E-7	3E-7	4E-7	5E-7	6E-7
U2 [m]	1E-7	2E-7	3E-7	4E-7	5E-7	6E-7
U3 [m]	1E-7	2E-7	3E-7	4E-7	5E-7	6E-7
U4 [rad]	1E-9	2E-9	3E-9	4E-9	5E-9	6E-9
U5 [rad]	1E-9	2E-9	3E-9	4E-9	5E-9	6E-9
U6 [rad]	1E-9	2E-9	3E-9	4E-9	5E-9	6E-9

Table E.1: Force-displacement table when single elastic force in combination with a vertical force $F_2 = 10F$

	Force / Moment $[N/Nm]$					
Displacement	10	20	30	40	50	60
U1 [m]	1E-7	2E-7	3E-7	4E-7	5E-7	6E-7
U2 [m]	1E-6	2E-6	3E-6	4E-6	5E-6	6E-6
U3 [m]	1E-7	2E-7	3E-7	4E-7	5E-7	6E-7
U4 [rad]	1E-9	2E-9	3E-9	4E-9	5E-9	6E-9
U5 [rad]	1E-9	2E-9	3E-9	4E-9	5E-9	6E-9
U6 [rad]	1E-9	2E-9	3E-9	4E-9	5E-9	6E-9

Table E.2: Force-displacement table when single elastic force in combination with a vertical force $F_2 = 10F$

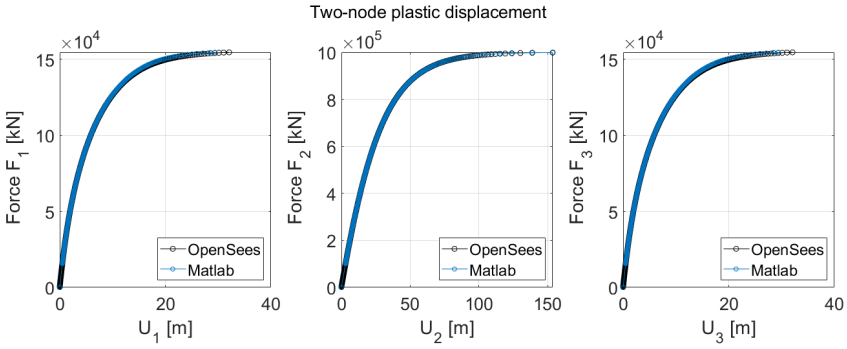

Figure E.1: Force-displacement curves up to yielding

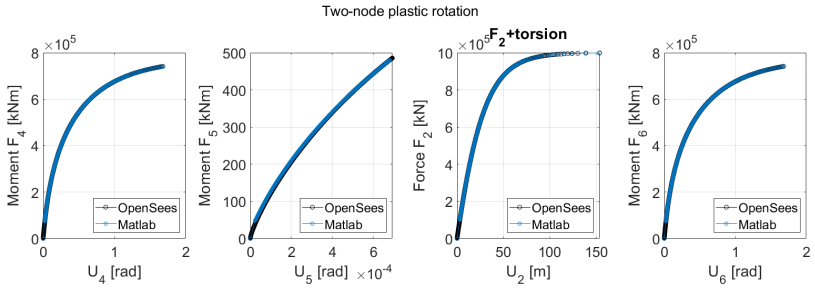

Figure E.2: Moment-rotation curves up to yielding

E.2 Pile model

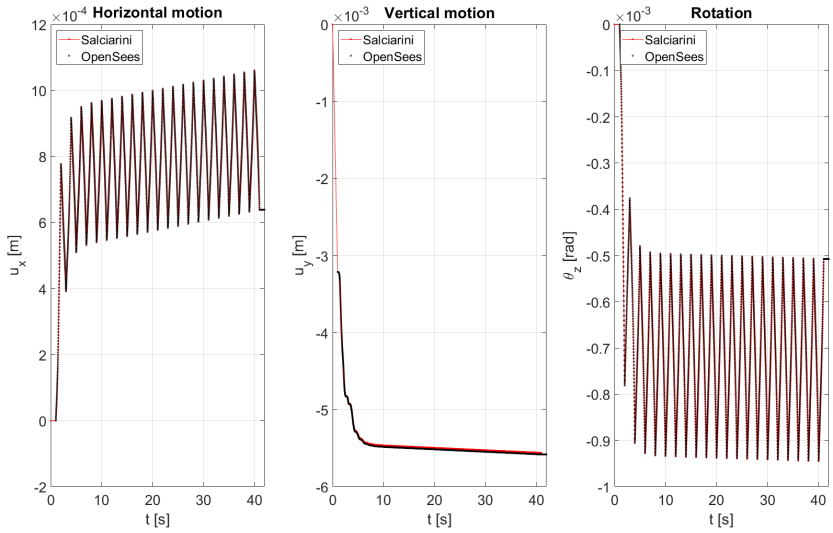

Figure E.3: Foundation motions in all three DOF as a function of time

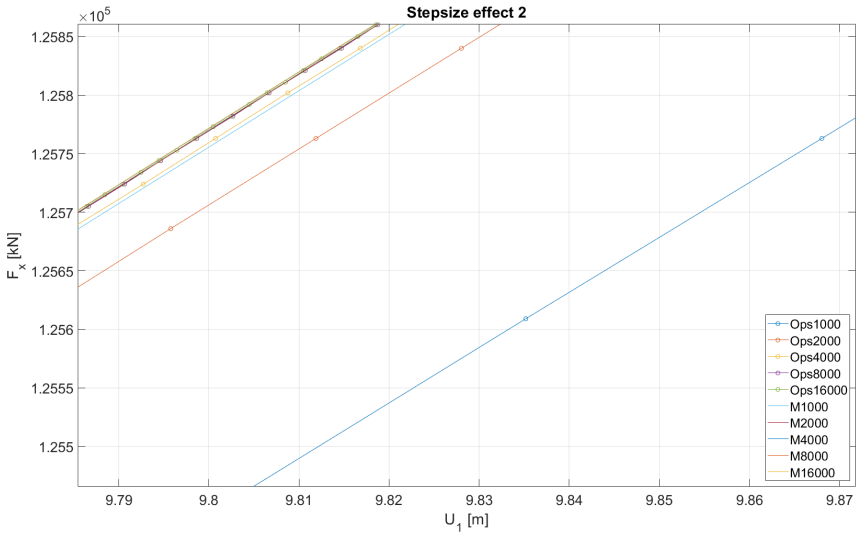

Figure E.4: F-U of OpenSees macro-element (Ops) and Matlab (M) equivalent for varying number of load steps

E.3 Elastic jack-up foundation

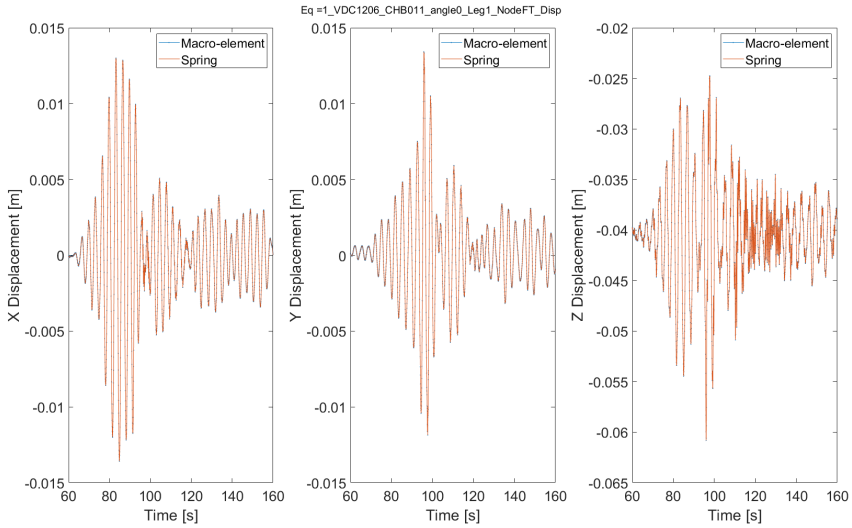

Figure E.5: Foundation motions in all three translational DOFs with fully elastic macro-element

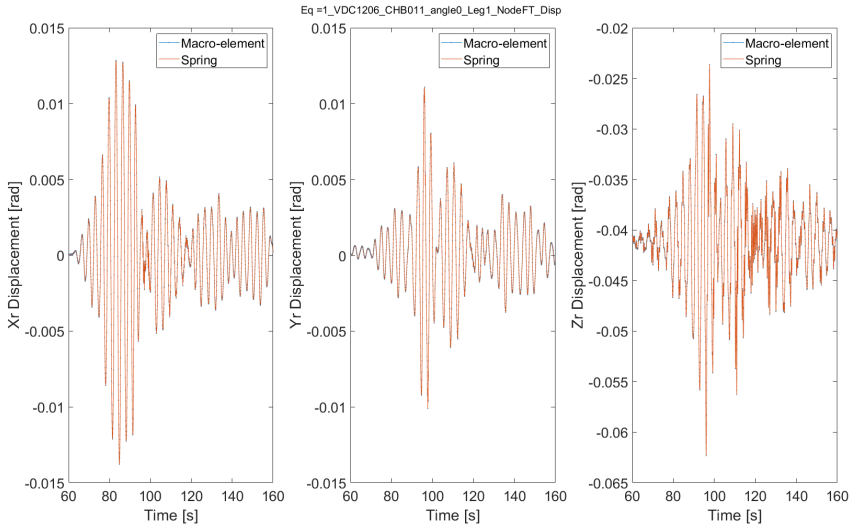

Figure E.6: Foundation motions in all three rotational DOFs with fully elastic macro-element

Appendix F

Case study and sensitivity analysis

F.1 Two-node model

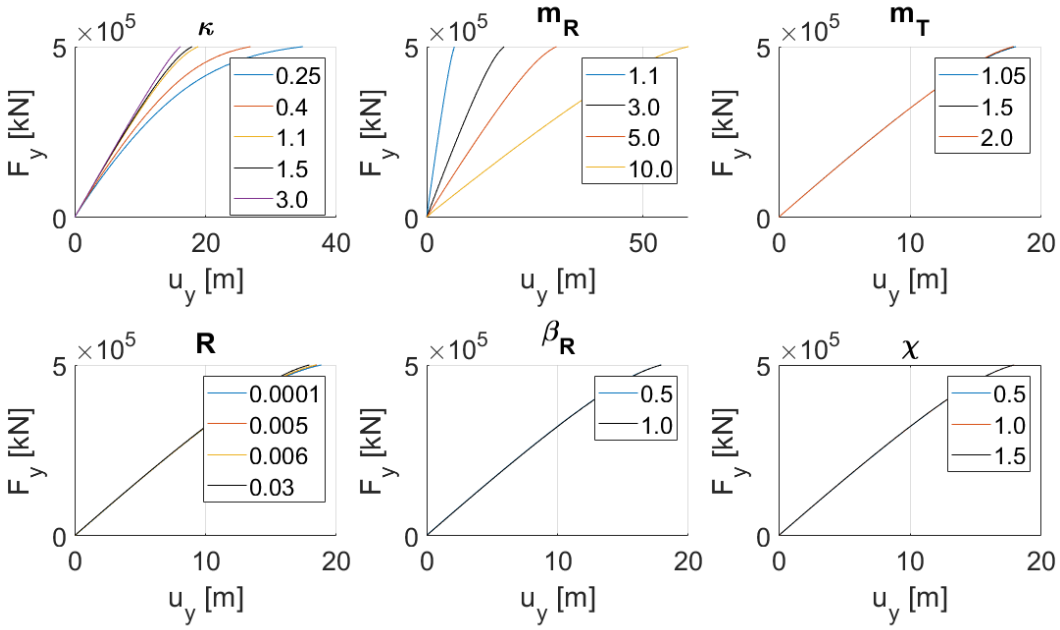

Figure F.1: Effect of varying parameters, using values from literature [35][13][43][23]

F.2 Pile model

This section compares the original response of the pile foundation (red and black), to the response after changing a single parameter.

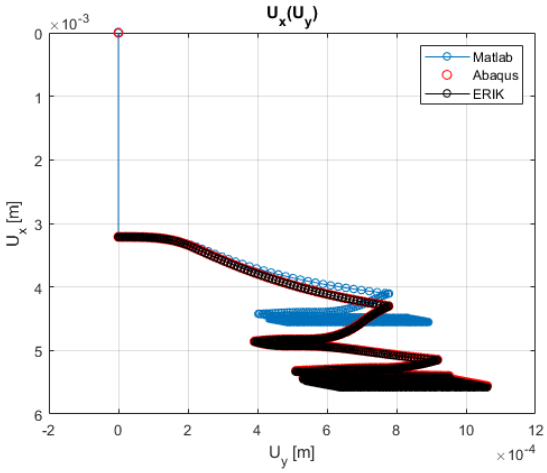

Figure F.2: $\beta_R = 0.5$ [35][13][43][23]

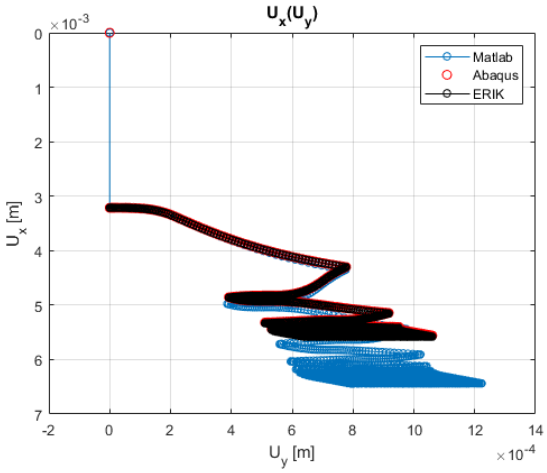

Figure F.3: $\beta_R = 1.5$ [35][13][43][23]

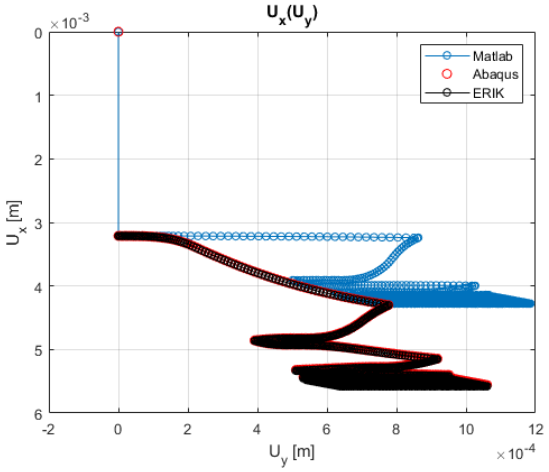

Figure F.4: $m_T = 1.0$ [35][13][43][23]

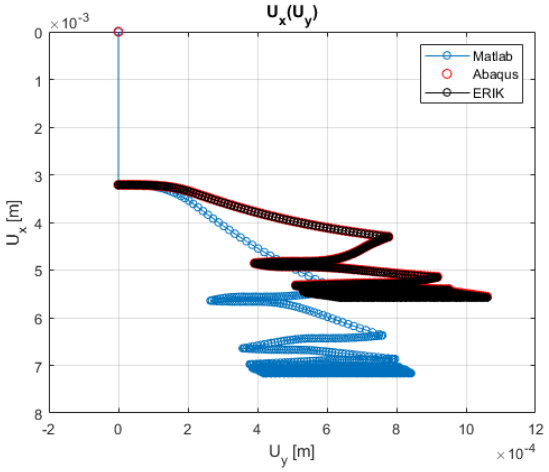

Figure F.5: $m_T = 2.5$ [35][13][43][23]

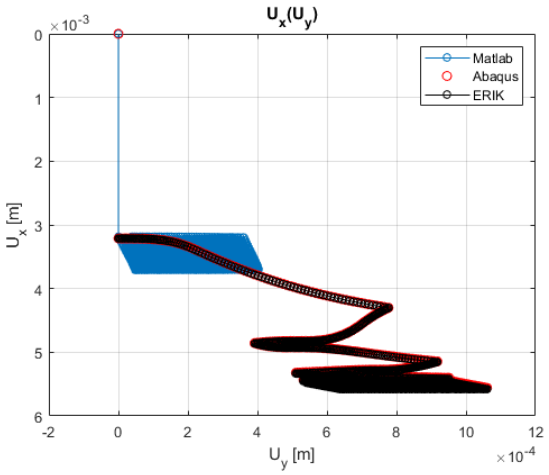

Figure F.6: $R = 0.3$ [35][13][43][23]

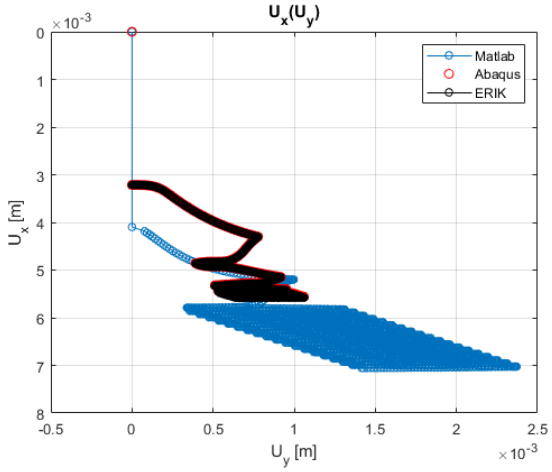

Figure F.7: $R = 0.003$ [35][13][43][23]

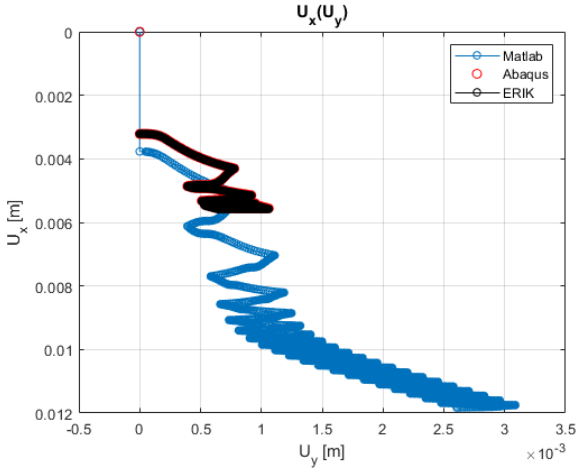

Figure F.8: $\chi = 0.5$ [35][13][43][23]

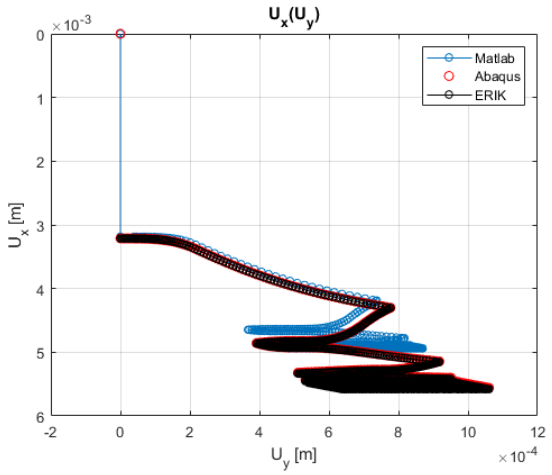

Figure F.9: $\chi = 2.5$ [35][13][43][23]

F.3 Base case

F.3.1 Footing node displacement timedomain

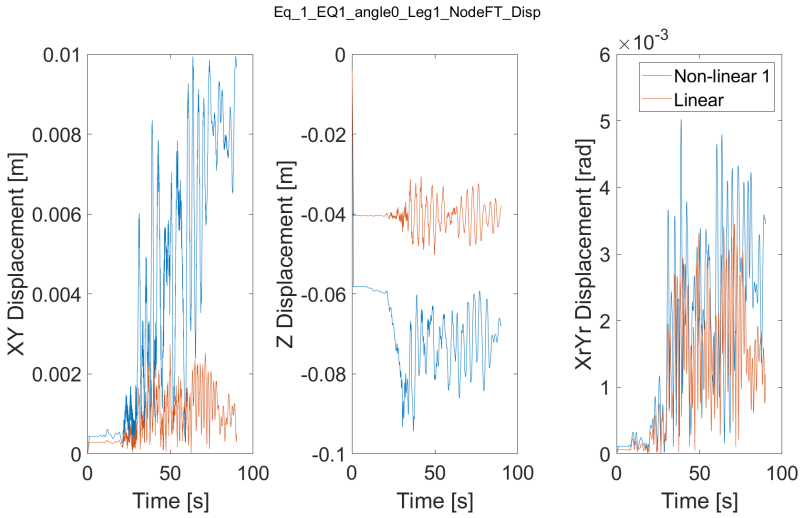

Figure F.10: Time-domain response of footing node displacement (Taiwan 200-yr EQ1, $\theta = 0$, Leg 1)

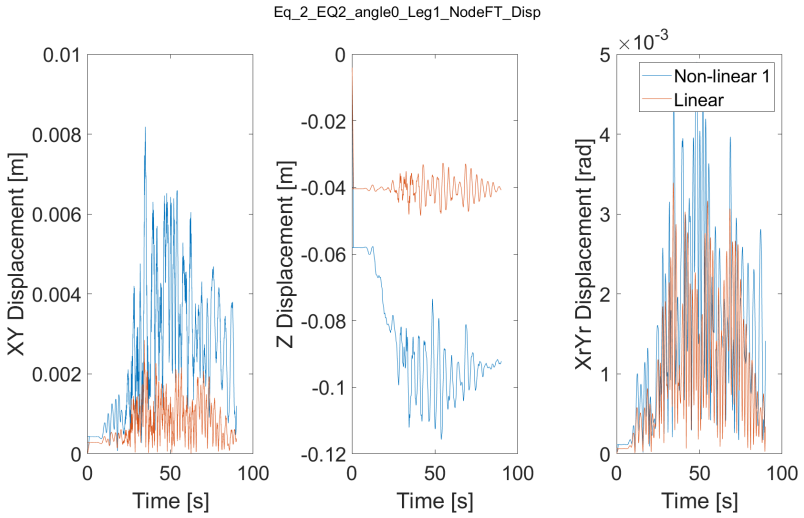

Figure F.11: Time-domain response of footing node displacement (Taiwan 200-yr EQ2, $\theta = 0$, Leg 1)

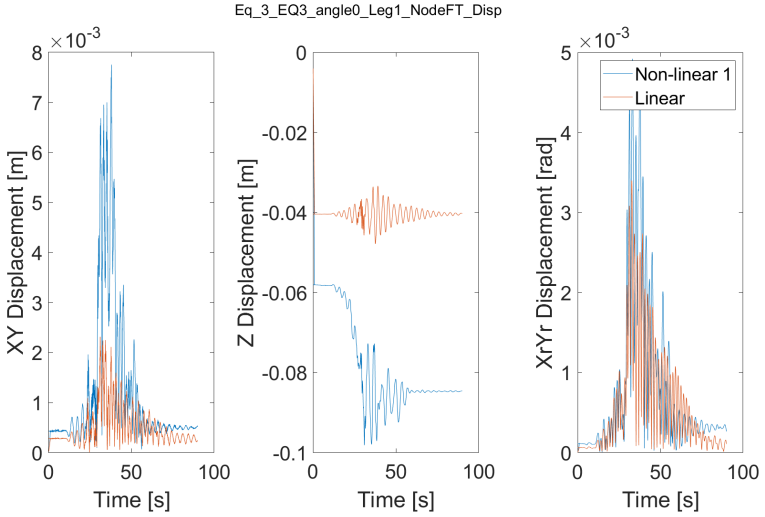

Figure F.12: Time-domain response of footing node displacement (Taiwan 200-yr EQ3, $\theta = 0$, Leg 1)

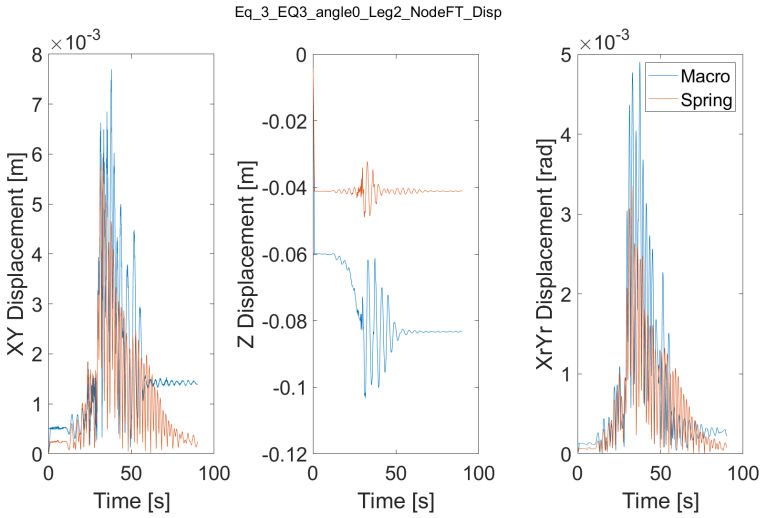

Figure F.13: Time-domain response of footing node displacement (Taiwan 200-yr EQ3, $\theta = 0$, Leg 2)

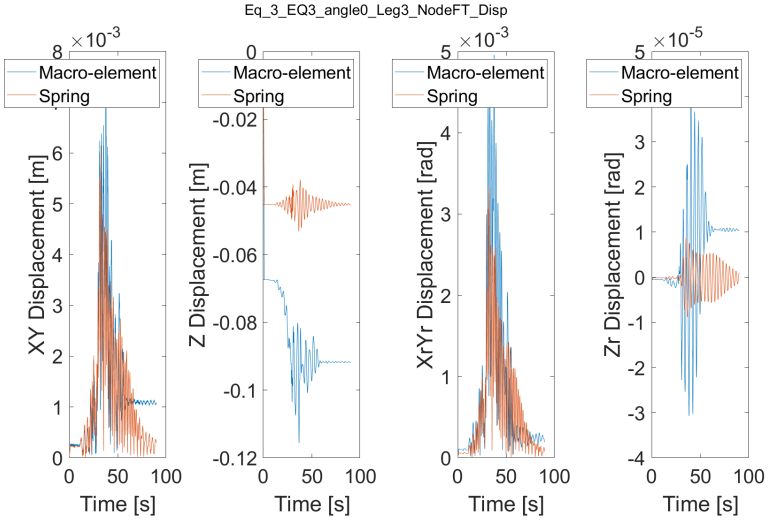

Figure F.14: Time-domain response of footing node displacement (Taiwan 200-yr EQ3, $\theta = 0$, Leg 3)

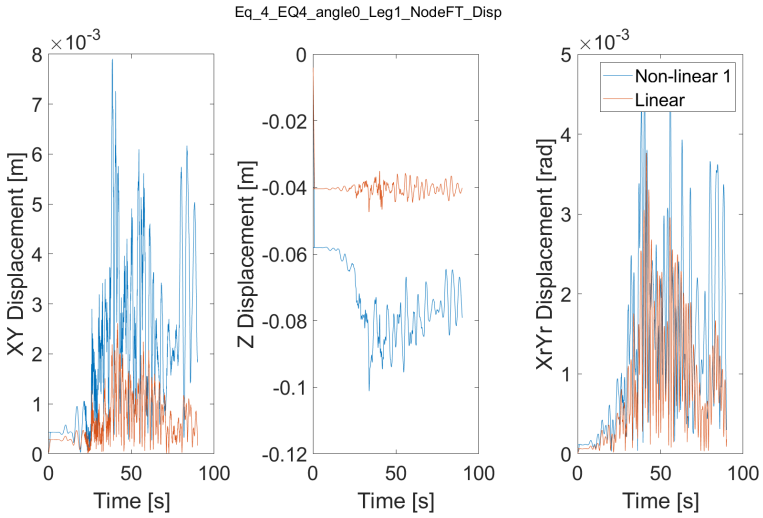

Figure F.15: Time-domain response of footing node displacement (Taiwan 200-yr EQ4, $\theta = 0$, Leg 1)

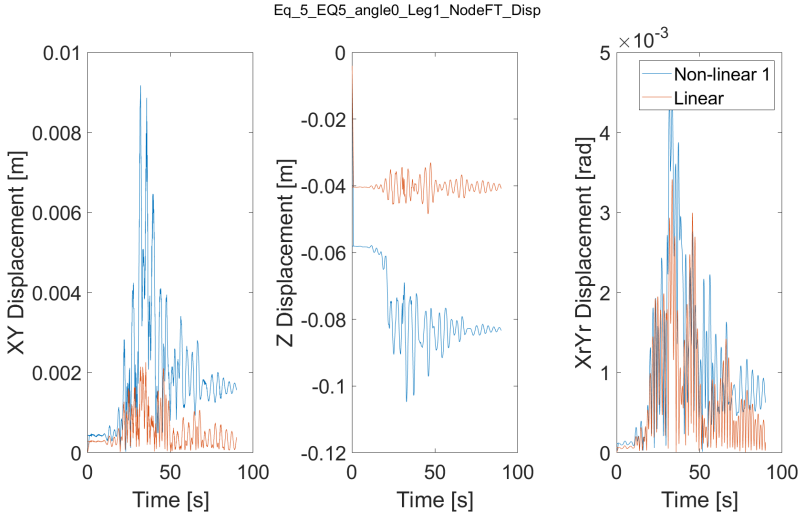

Figure F.16: Time-domain response of footing node displacement (Taiwan 200-yr EQ5, $\theta = 0$, Leg 1)

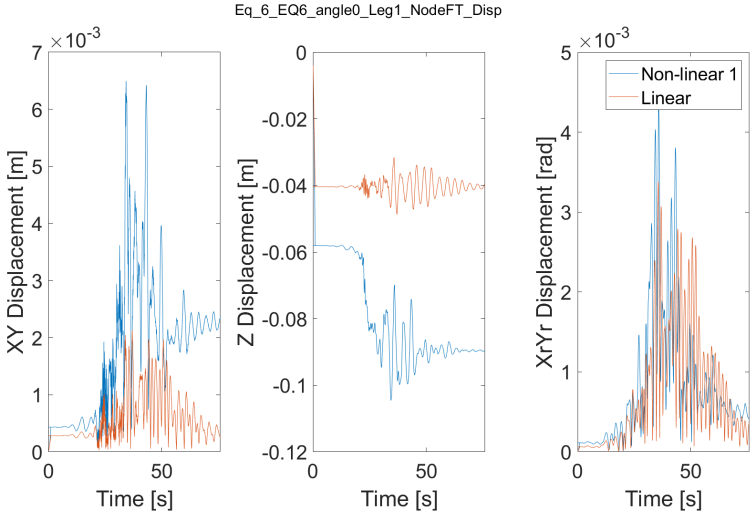

Figure F.17: Time-domain response of footing node displacement (Taiwan 200-yr EQ6, $\theta = 0$, Leg 1)

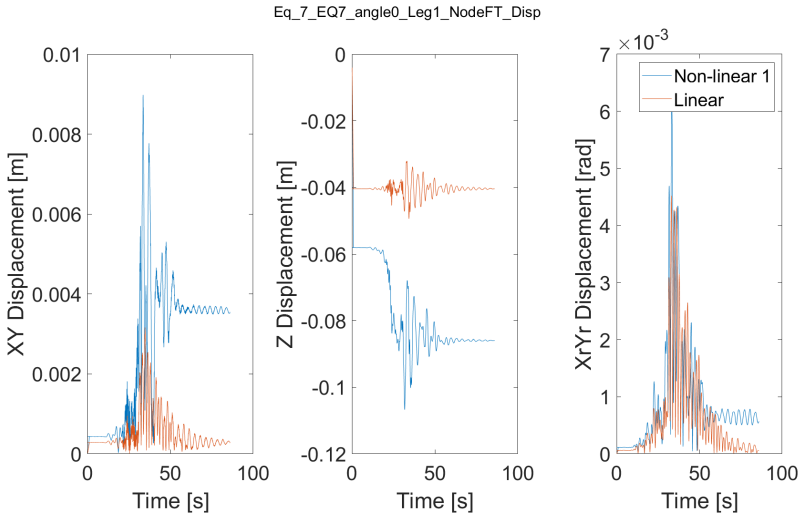

Figure F.18: Time-domain response of footing node displacement (Taiwan 200-yr EQ7, $\theta = 0$, Leg 1)

F.3.2 Macro-element loads timedomain

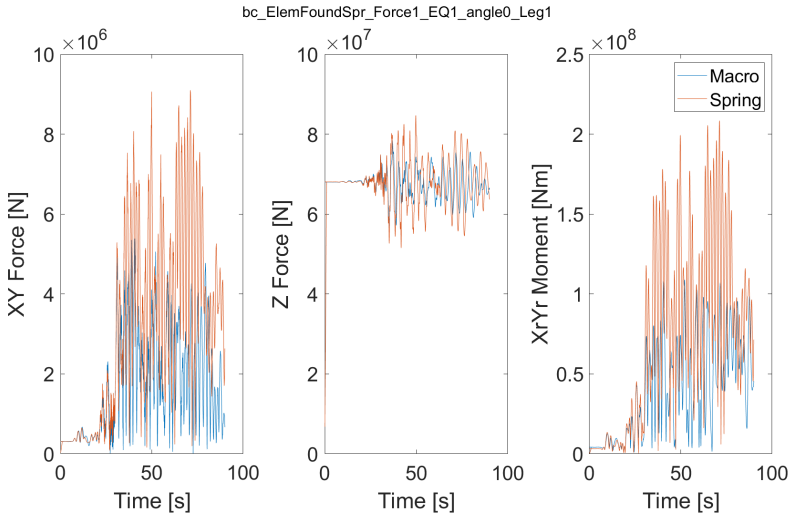

Figure F.19: Time-domain loads in macro-element (Taiwan 200-yr EQ1, $\theta = 0$, Leg 1)

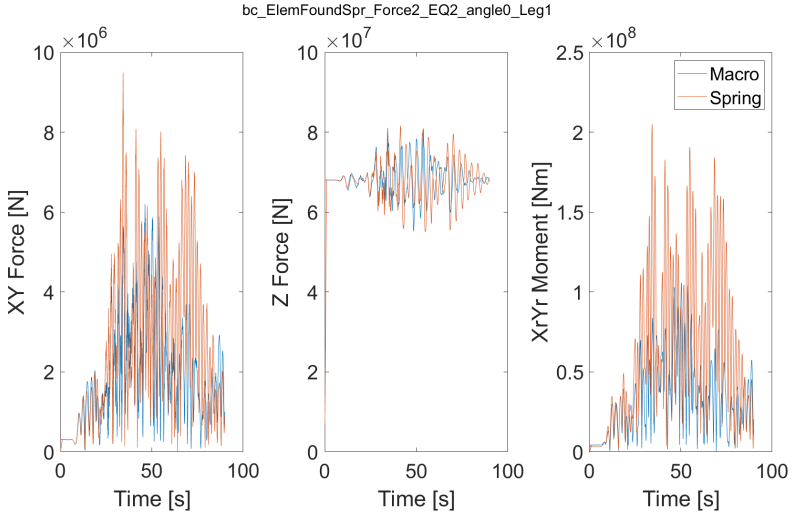

Figure F.20: Time-domain loads in macro-element (Taiwan 200-yr EQ2, $\theta = 0$, Leg 1)

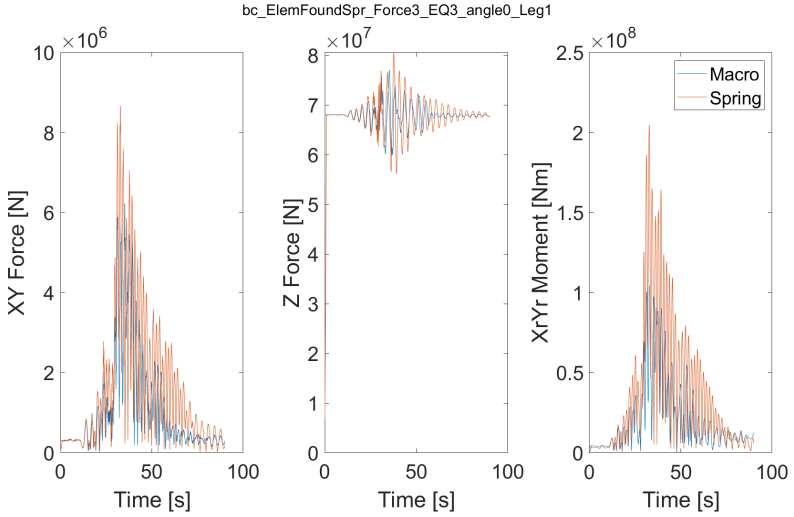

Figure F.21: Time-domain loads in macro-element (Taiwan 200-yr EQ3, $\theta = 0$, Leg 1)

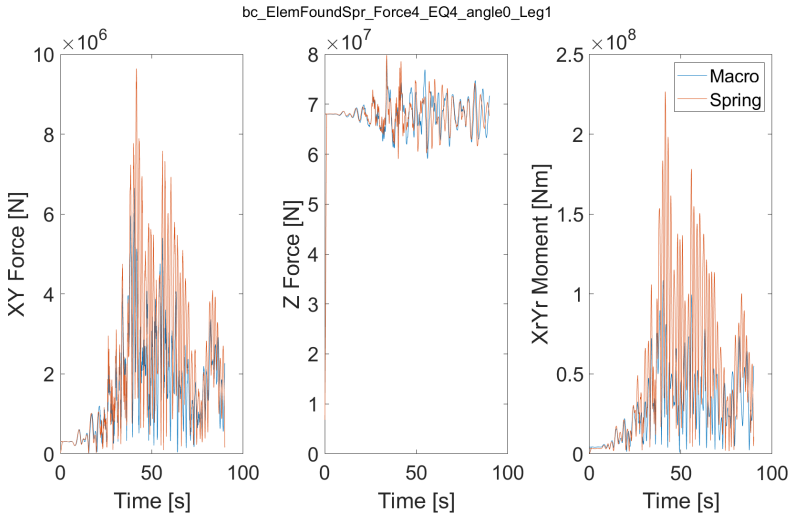

Figure F.22: Time-domain loads in macro-element (Taiwan 200-yr EQ4, $\theta = 0$, Leg 1)

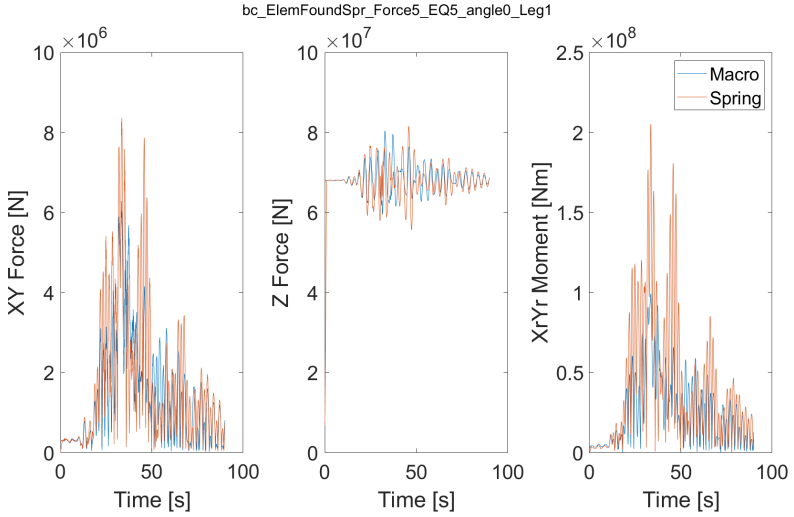

Figure F.23: Time-domain loads in macro-element (Taiwan 200-yr EQ5, $\theta = 0$, Leg 1)

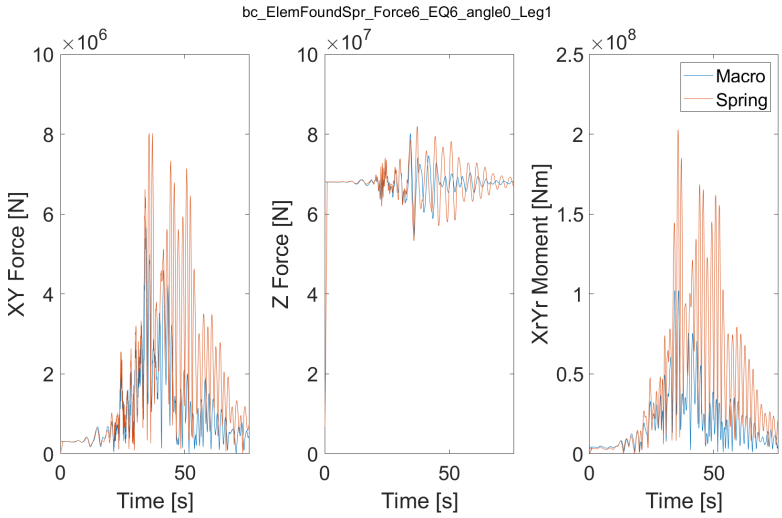

Figure F.24: Time-domain loads in macro-element (Taiwan 200-yr EQ6, $\theta = 0$, Leg 1)

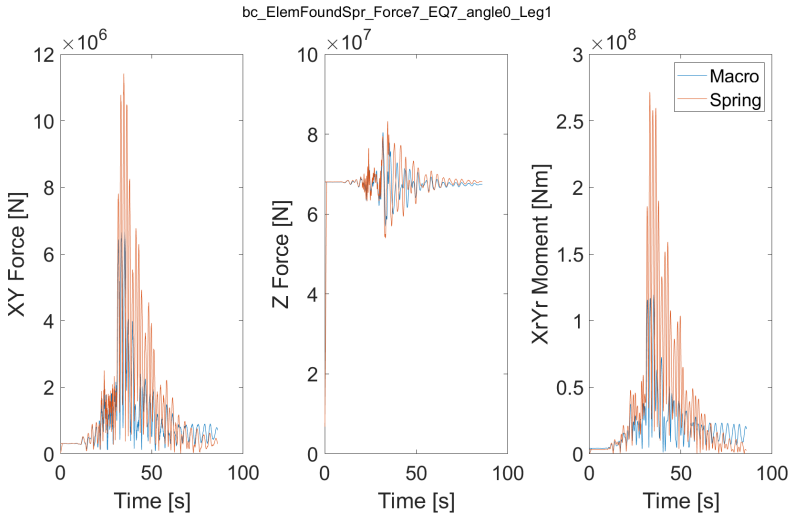

Figure F.25: Time-domain loads in macro-element (Taiwan 200-yr EQ7, $\theta = 0$, Leg 1)

F.3.3 Footing node displacement frequencydomain

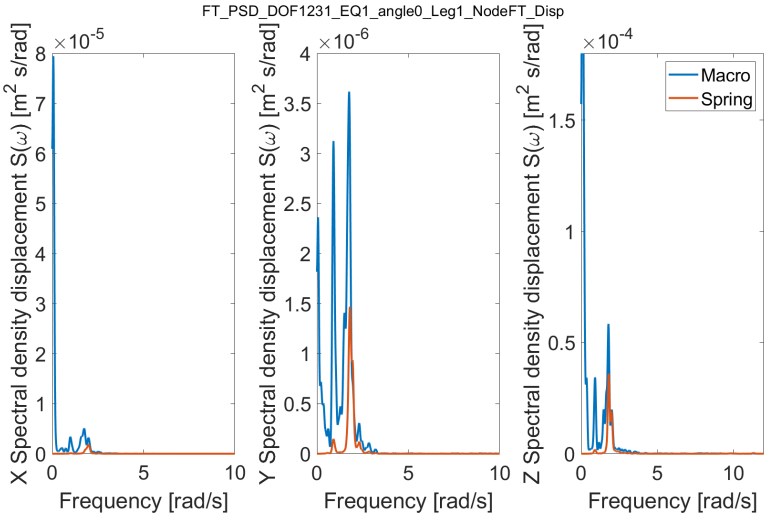

Figure F.26: PSD of footing node displacement (Taiwan 200-yr EQ1, $\theta = 0$, Leg 1)

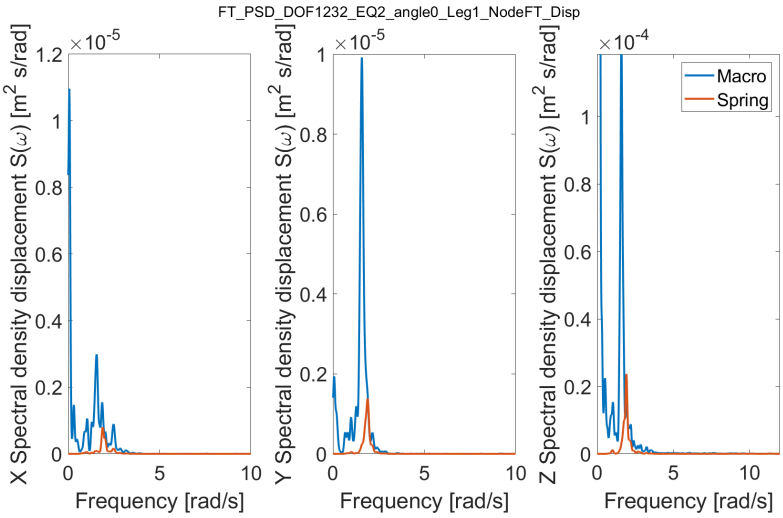

Figure F.27: PSD of footing node displacement (Taiwan 200-yr EQ2, $\theta = 0$, Leg 1)

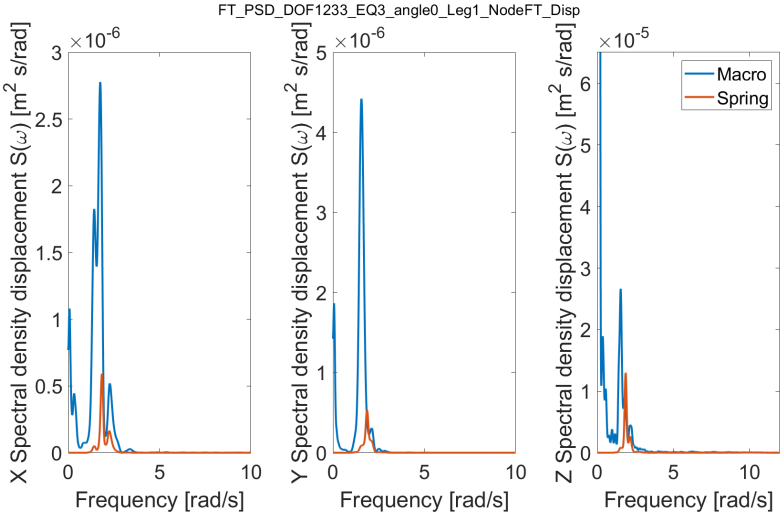

Figure F.28: PSD of footing node displacement (Taiwan 200-yr EQ3, $\theta = 0$, Leg 1)

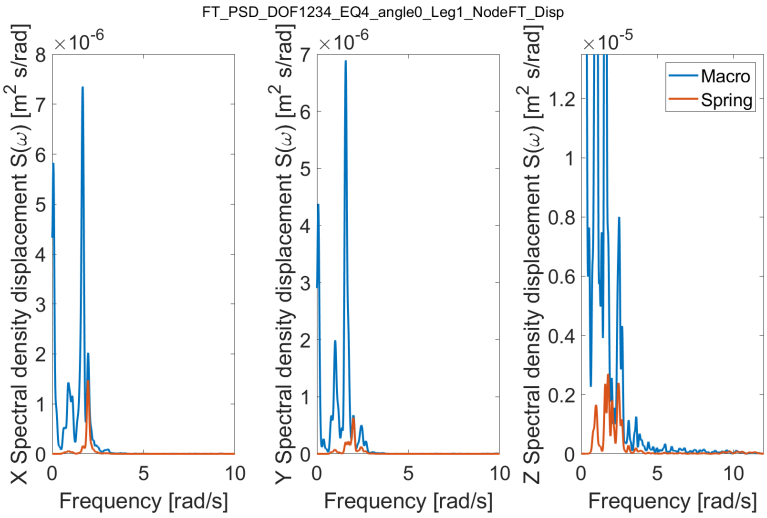

Figure F.29: PSD of footing node displacement (Taiwan 200-yr EQ4, $\theta = 0$, Leg 1)

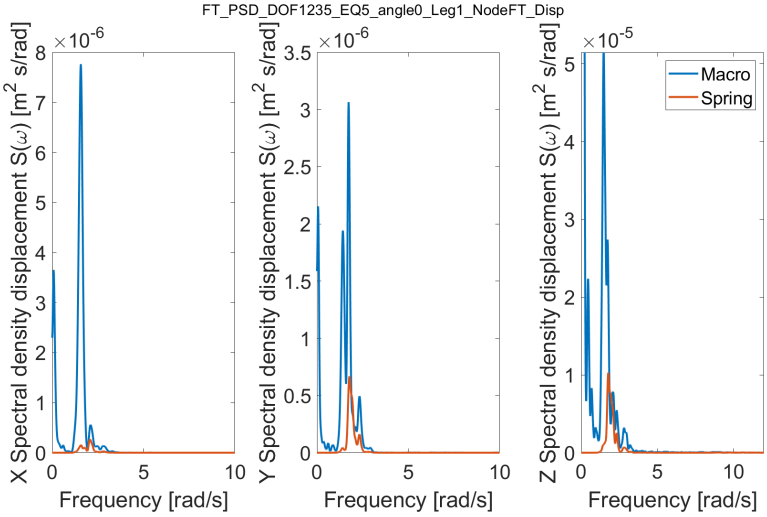

Figure F.30: PSD of footing node displacement (Taiwan 200-yr EQ5, $\theta = 0$, Leg 1)

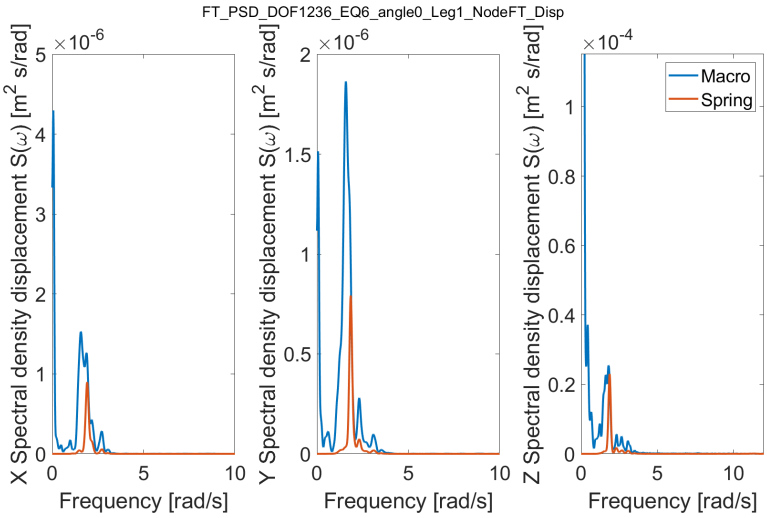

Figure F.31: PSD of footing node displacement (Taiwan 200-yr EQ6, $\theta = 0$, Leg 1)

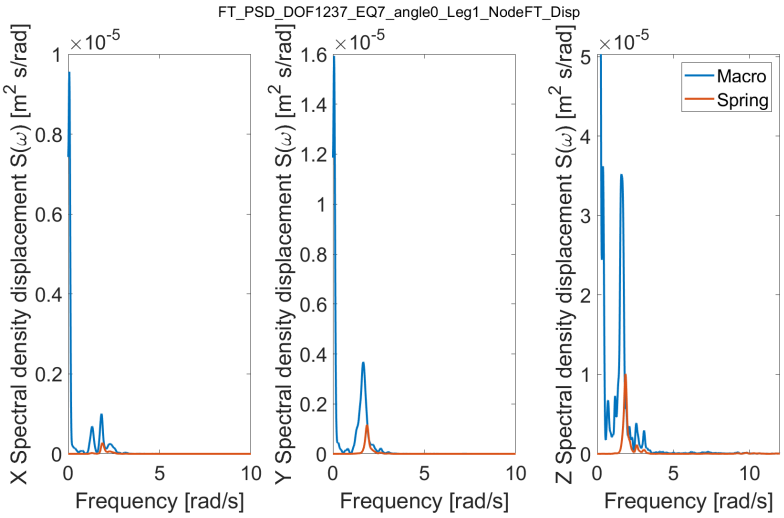

Figure F.32: PSD of footing node displacement (Taiwan 200-yr EQ7, $\theta = 0$, Leg 1)

F.3.4 Lower guide node displacement time-domain

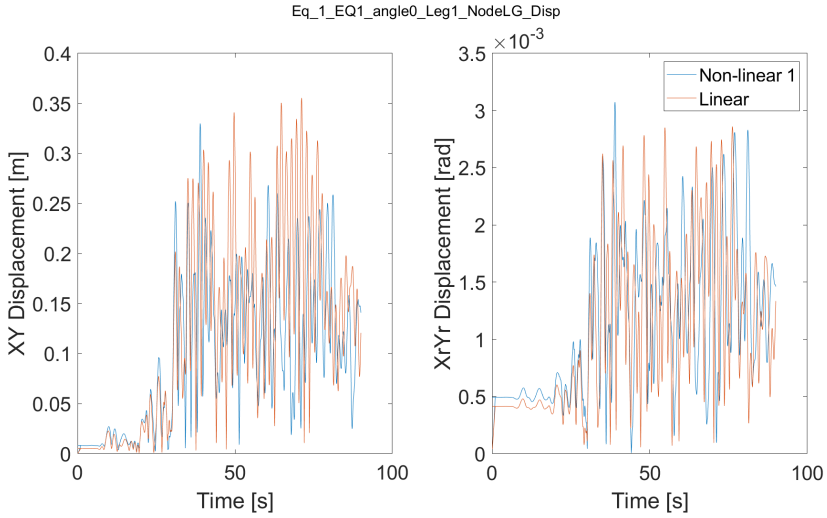

Figure F.33: Lower guide node displacement time-domain (Taiwan 200-yr EQ1, $\theta = 0$, Leg 1)

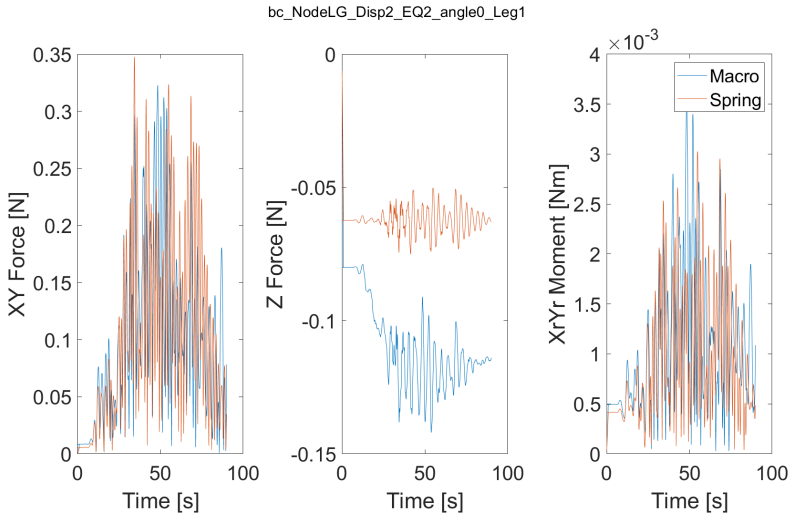

Figure F.34: Lower guide node displacement time-domain (Taiwan 200-yr EQ2, $\theta = 0$, Leg 1)

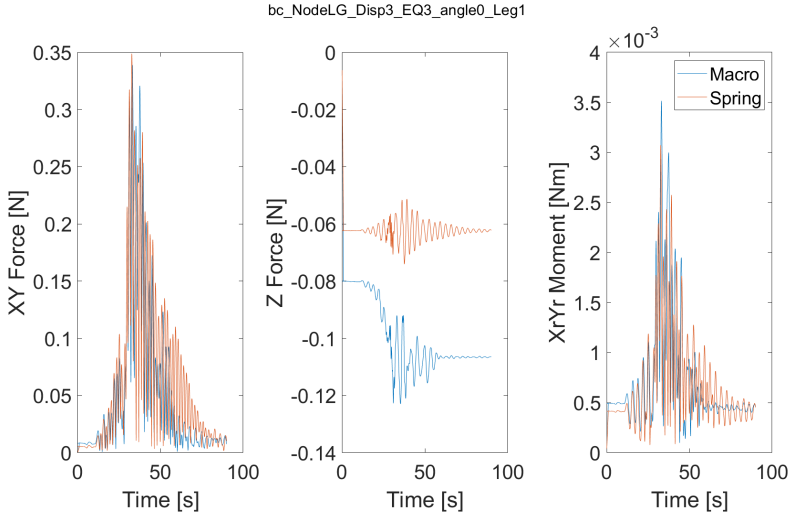

Figure F.35: Lower guide node displacement time-domain (Taiwan 200-yr EQ3, $\theta = 0$, Leg 1)

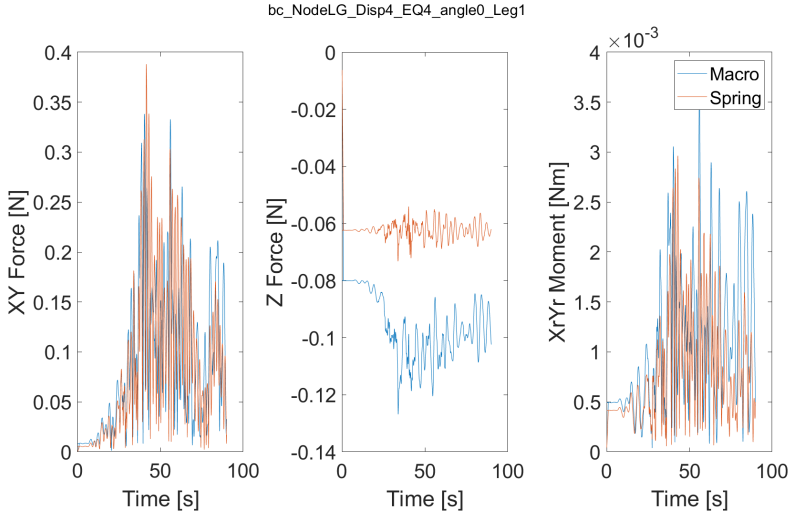

Figure F.36: Lower guide node displacement time-domain (Taiwan 200-yr EQ4, $\theta = 0$, Leg 1)

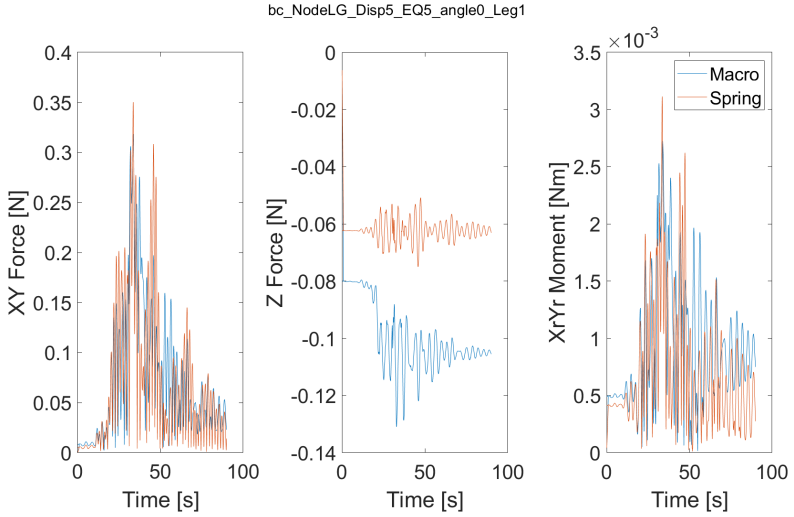

Figure F.37: Lower guide node displacement time-domain (Taiwan 200-yr EQ5, $\theta = 0$, Leg 1)

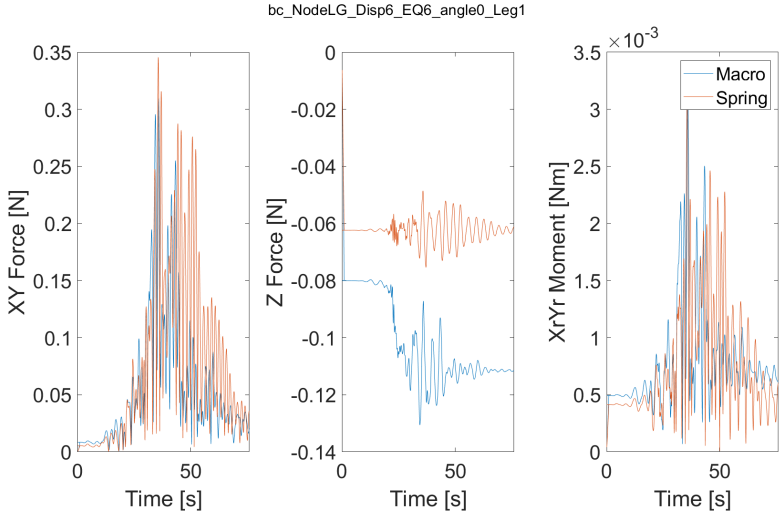

Figure F.38: Lower guide node displacement time-domain (Taiwan 200-yr EQ6, $\theta = 0$, Leg 1)

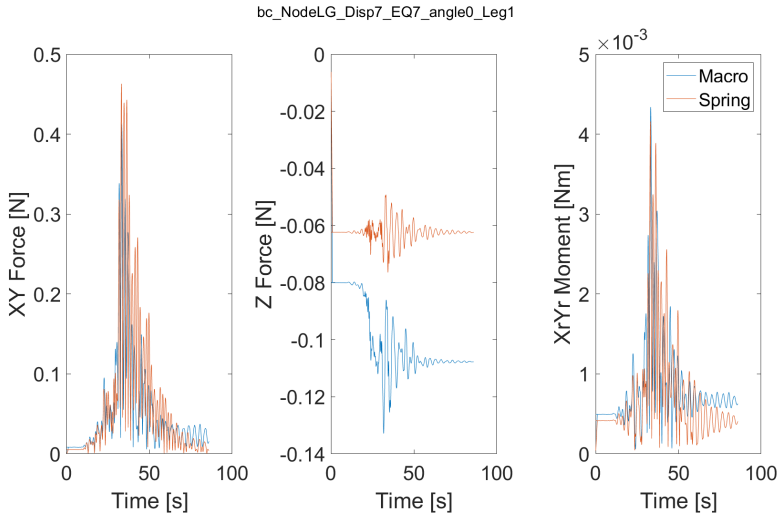

Figure F.39: Lower guide node displacement time-domain (Taiwan 200-yr EQ7, $\theta = 0$, Leg 1)

F.3.5 Lower guide node loads time-domain

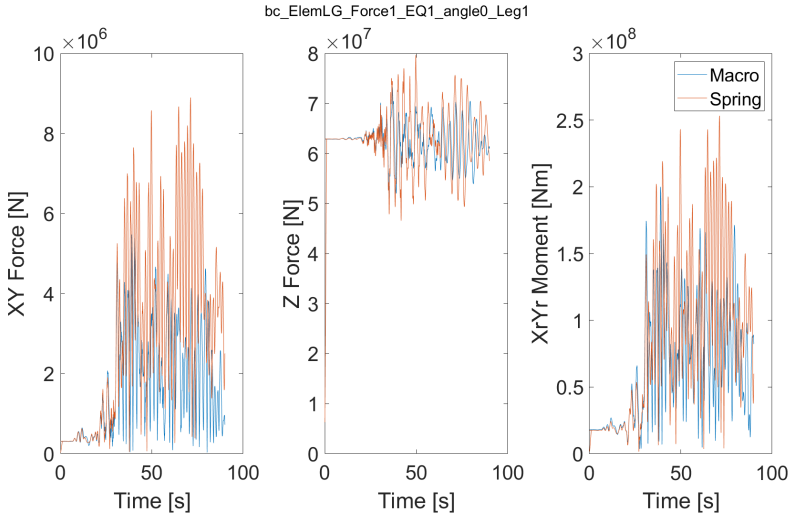

Figure F.40: Lower guide node loads time-domain (Taiwan 200-yr EQ1, $\theta = 0$, Leg 1)

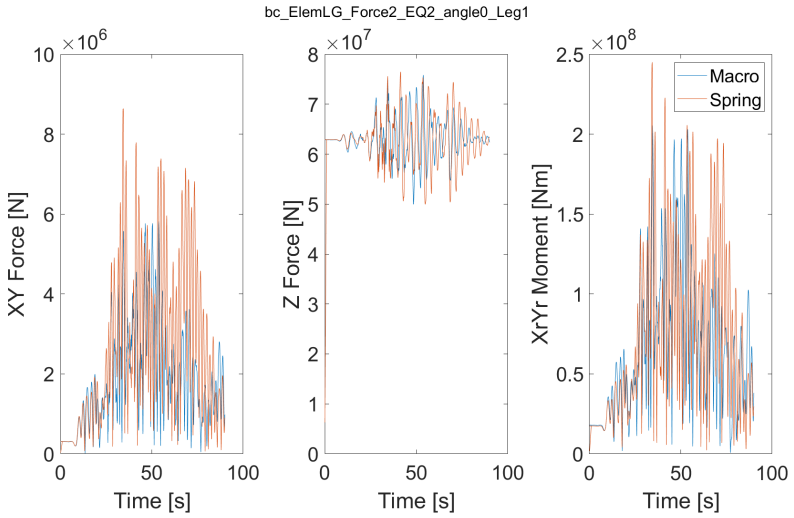

Figure F.41: Lower guide node loads time-domain (Taiwan 200-yr EQ2, $\theta = 0$, Leg 1)

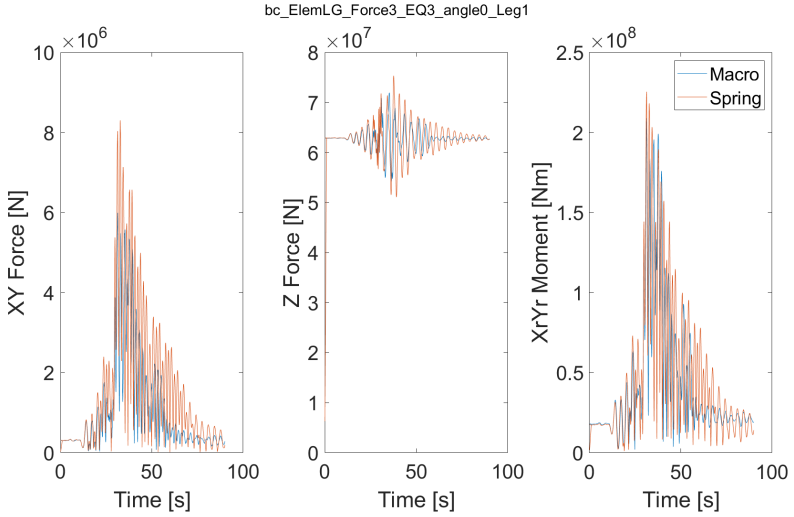

Figure F.42: Lower guide node loads time-domain (Taiwan 200-yr EQ3, $\theta = 0$, Leg 1)

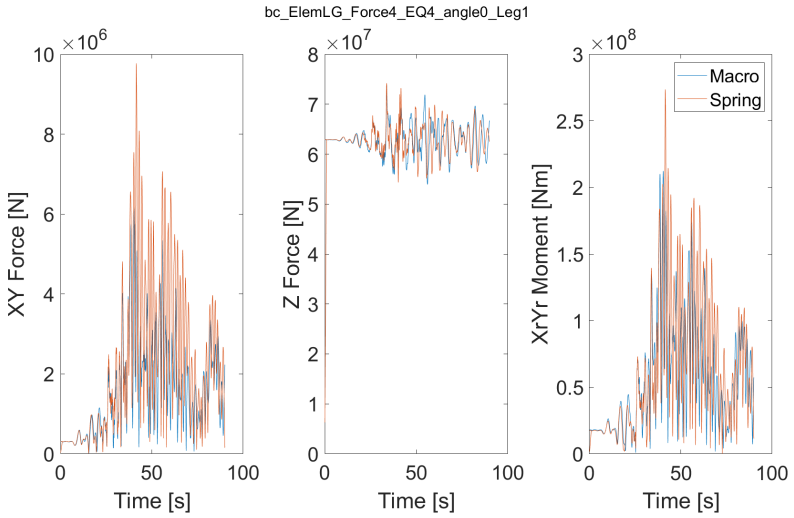

Figure F.43: Lower guide node loads time-domain (Taiwan 200-yr EQ4, $\theta = 0$, Leg 1)

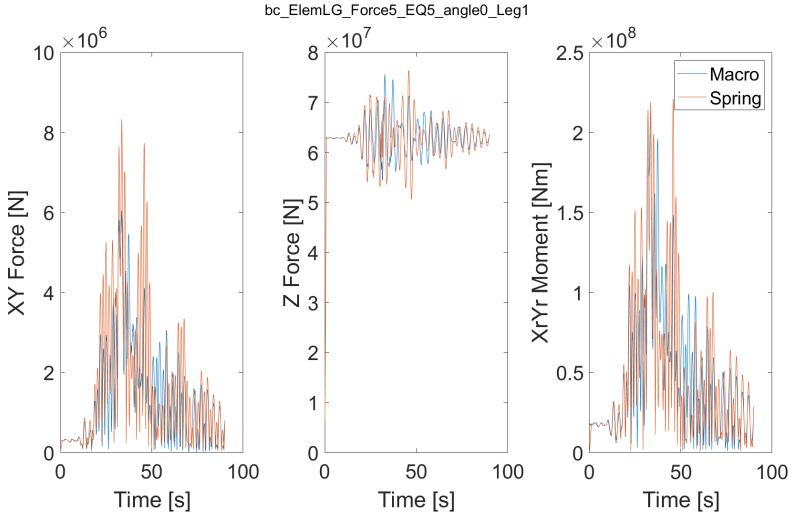

Figure F.44: Lower guide node loads time-domain (Taiwan 200-yr EQ5, $\theta = 0$, Leg 1)

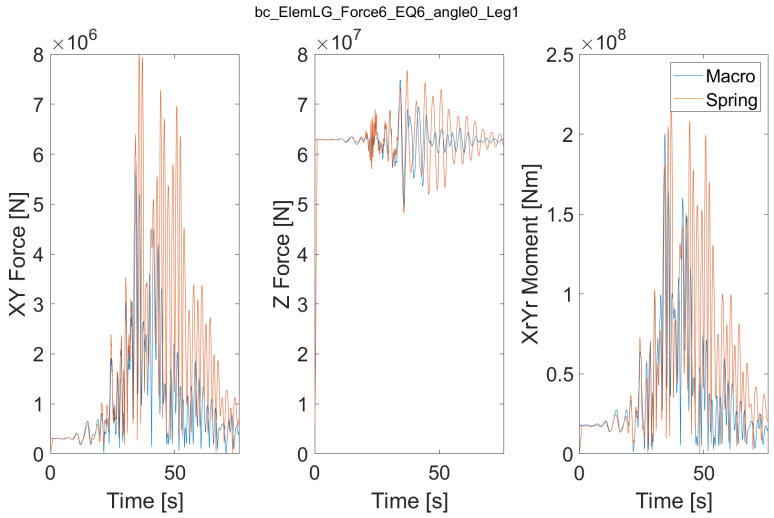

Figure F.45: Lower guide node loads time-domain (Taiwan 200-yr EQ6, $\theta = 0$, Leg 1)

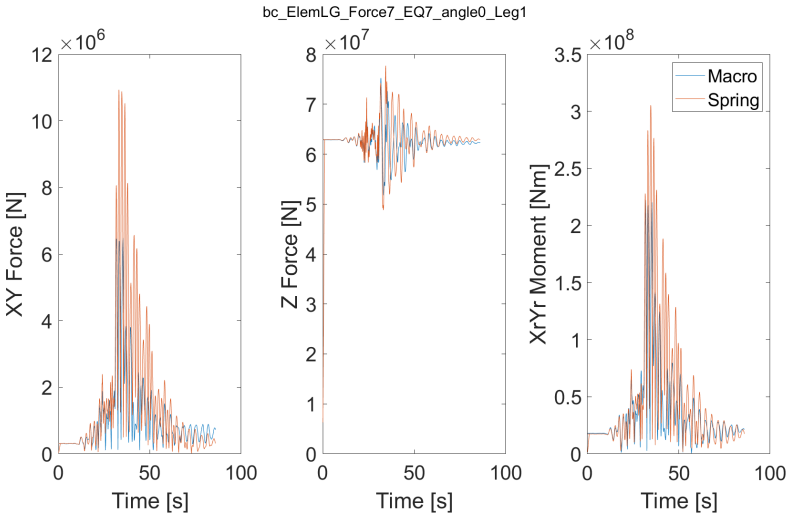

Figure F.46: Lower guide node loads time-domain (Taiwan 200-yr EQ7, $\theta = 0$, Leg 1)

F.3.6 Lower guide node acceleration frequencydomain

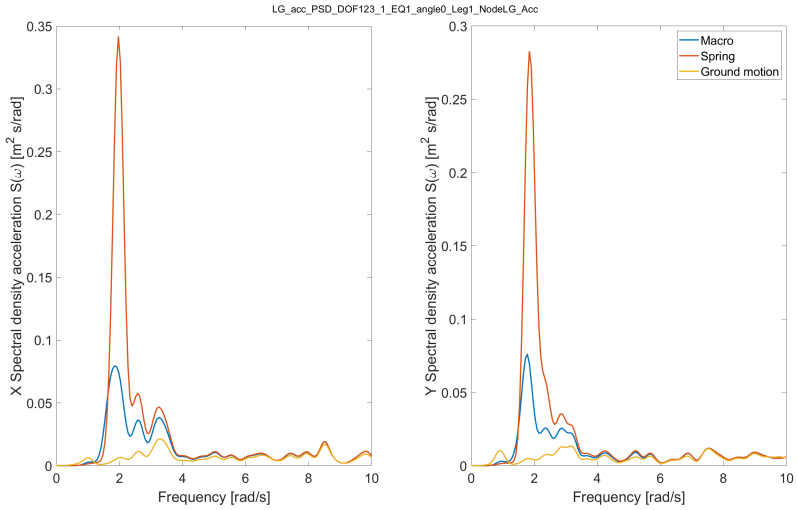

Figure F.47: PSD of lower guide node acceleration (Taiwan 200-yr EQ1, $\theta = 0$, Leg 1)

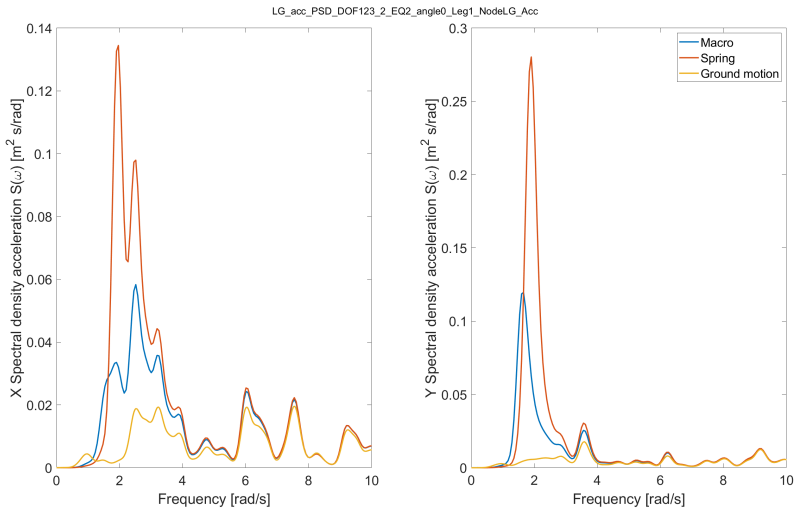

Figure F.48: PSD of lower guide node acceleration (Taiwan 200-yr EQ2, $\theta = 0$, Leg 1)

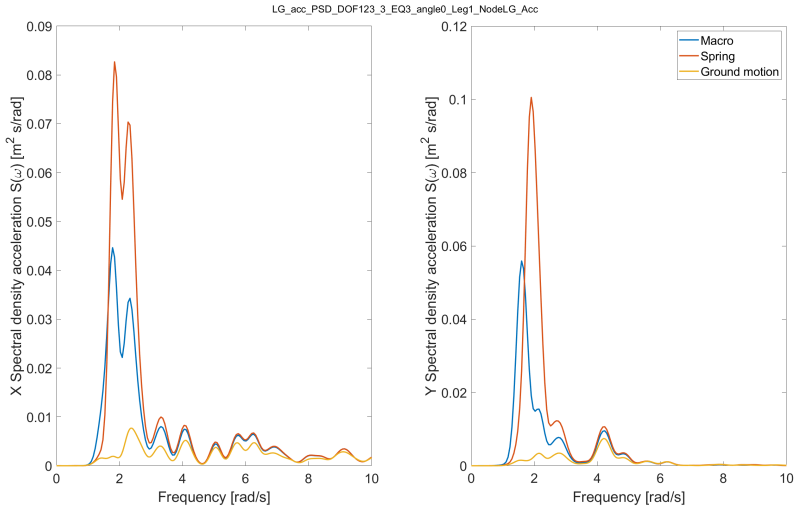

Figure F.49: PSD of lower guide node acceleration (Taiwan 200-yr EQ3, $\theta = 0$, Leg 1)

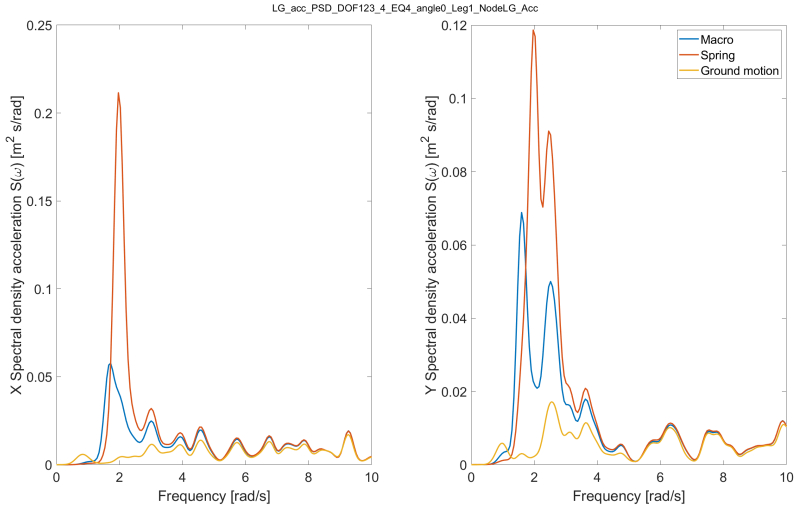

Figure F.50: PSD of lower guide node acceleration (Taiwan 200-yr EQ4, $\theta = 0$, Leg 1)

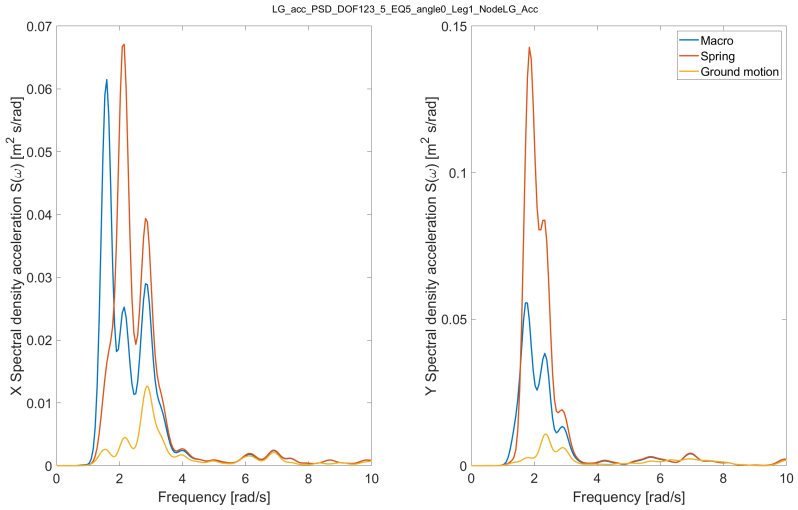

Figure F.51: PSD of lower guide node acceleration (Taiwan 200-yr EQ5, $\theta = 0$, Leg 1)

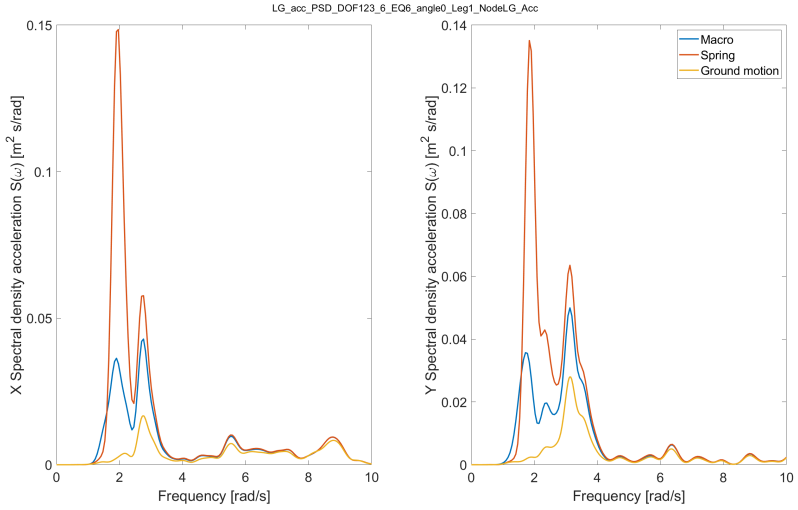

Figure F.52: PSD of lower guide node acceleration (Taiwan 200-yr EQ6, $\theta = 0$, Leg 1)

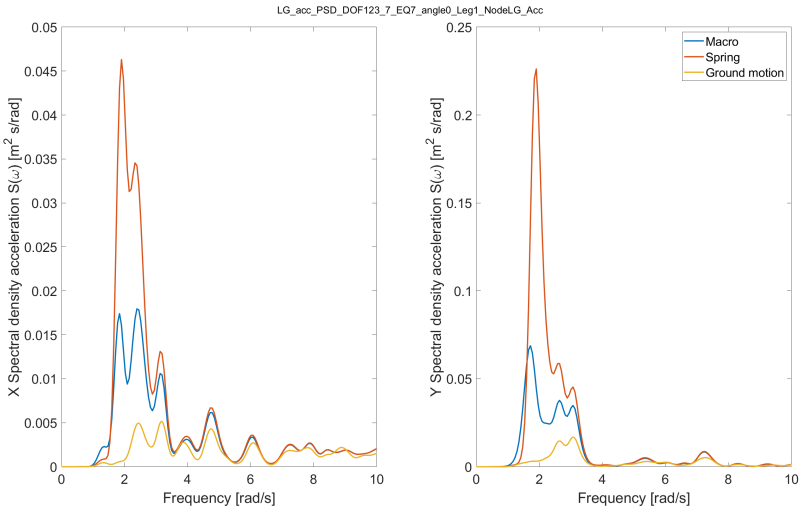

Figure F.53: PSD of lower guide node acceleration (Taiwan 200-yr EQ7, $\theta = 0$, Leg 1)

F.3.7 Numerical sensitivity

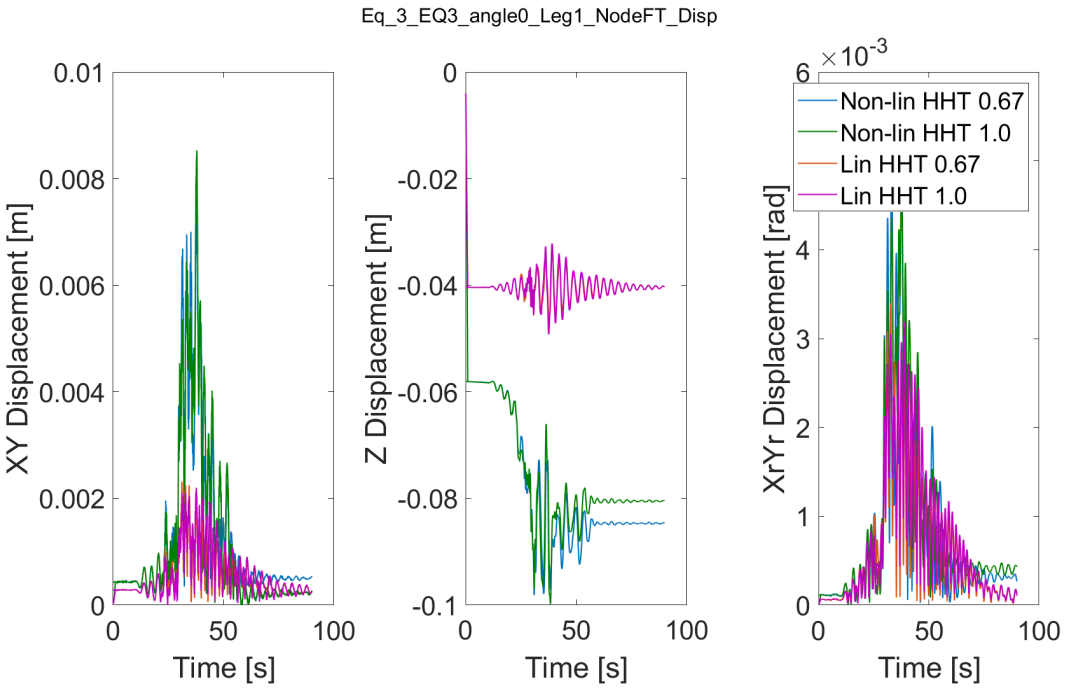

Figure F.54: Effect of varying numerical damping

F.4 Four parameter sets

F.4.1 Footing node displacement time-domain

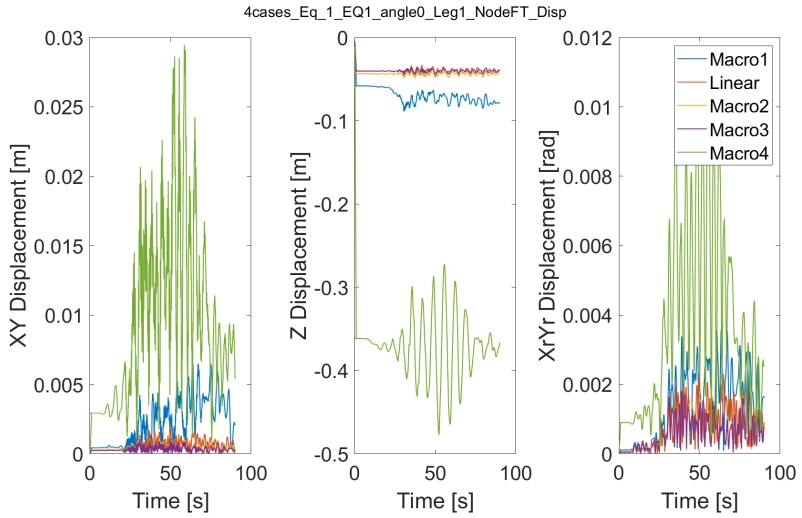

Figure F.55: Footing node displacement time-domain, 4 non-linear foundations, 1 linear foundation (Taiwan 100-yr EQ1, $\theta = 0$, Leg 1)

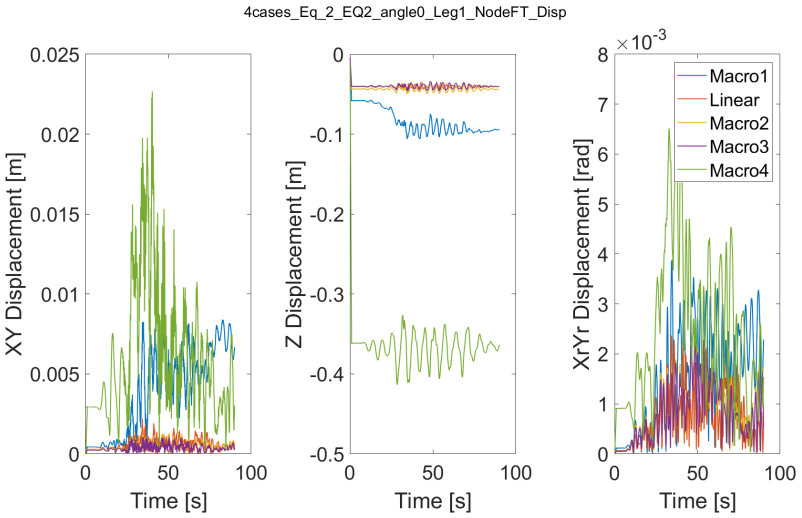

Figure F.56: Footing node displacement time-domain, 4 non-linear foundations, 1 linear foundation (Taiwan 100-yr EQ2, $\theta = 0$, Leg 1)

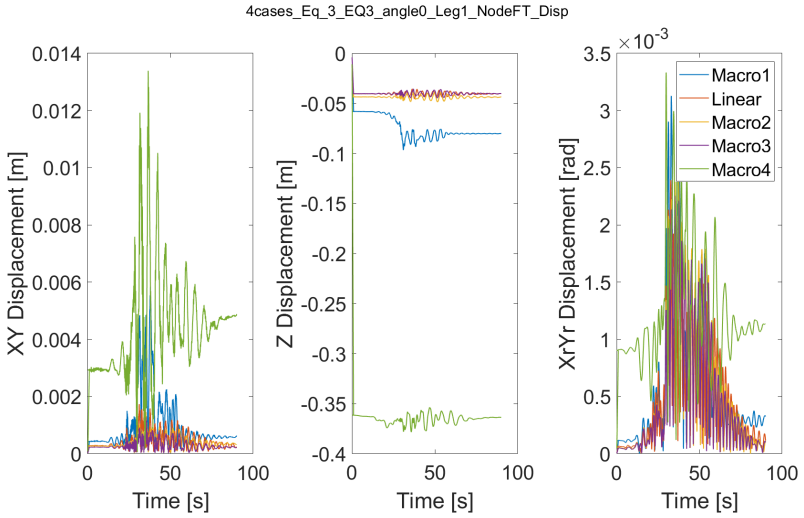

Figure F.57: Footing node displacement time-domain, 4 non-linear foundations, 1 linear foundation (Taiwan 100-yr EQ4, $\theta = 0$, Leg 1)

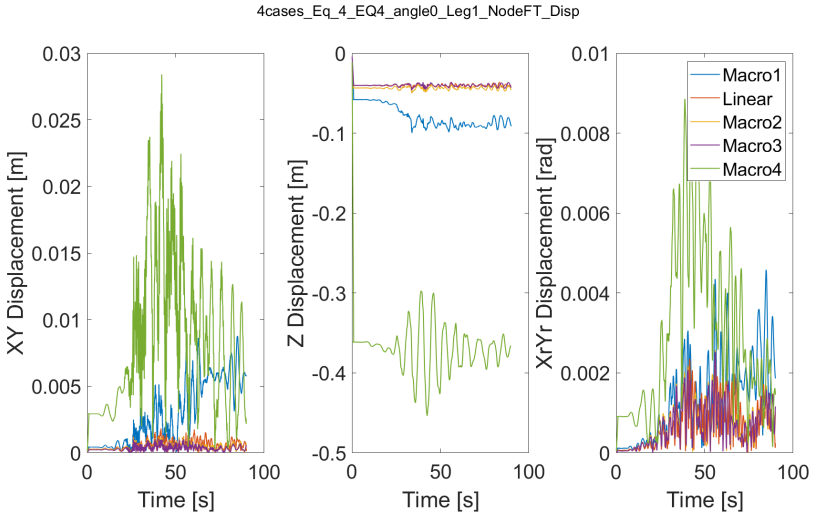

Figure F.58: Footing node displacement time-domain, 4 non-linear foundations, 1 linear foundation (Taiwan 100-yr EQ4, $\theta = 0$, Leg 1)

F.4.2 Macro-element loads time-domain

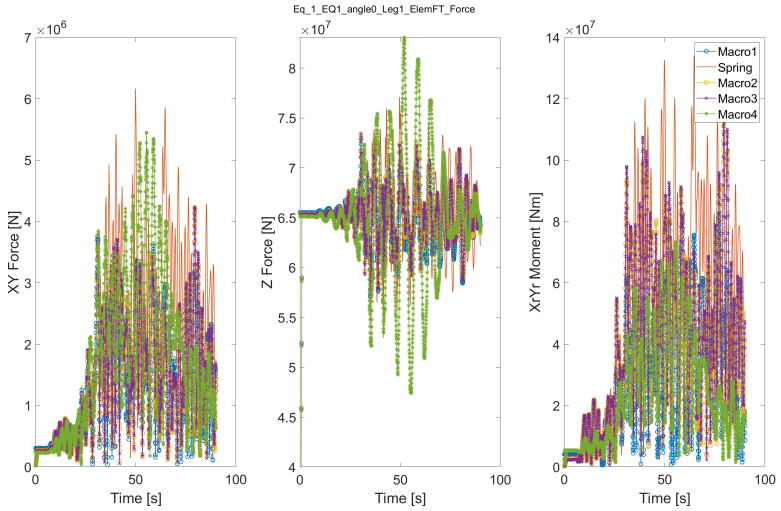

Figure F.59: Footing node loads time-domain including force damped by radiation, 4 non-linear foundations, 1 linear foundation (Taiwan 100-yr EQ1, $\theta = 0$, Leg 1)

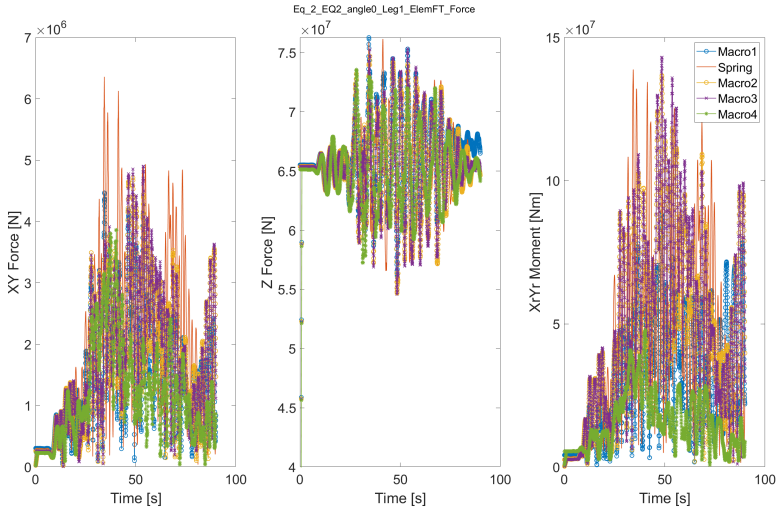

Figure F.60: Footing node loads time-domain including force damped by radiation, 4 non-linear foundations, 1 linear foundation (Taiwan 100-yr EQ2, $\theta = 0$, Leg 1)

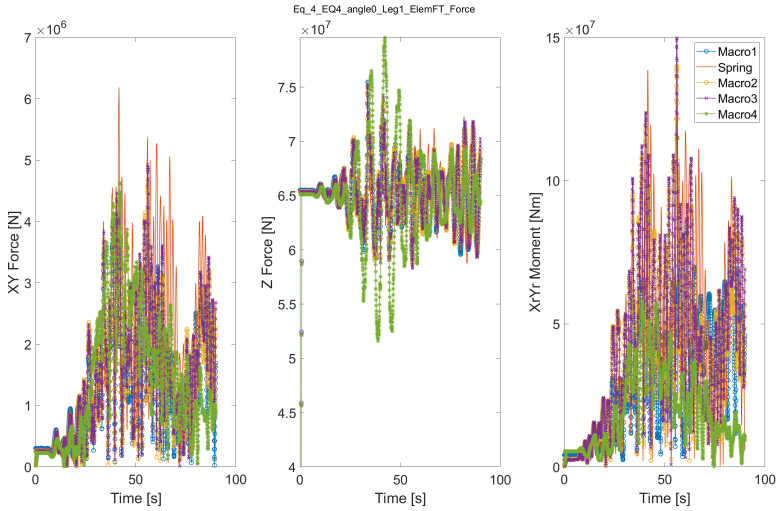

Figure F.61: Footing node loads time-domain including force damped by radiation, 4 non-linear foundations, 1 linear foundation (Taiwan 100-yr EQ4, $\theta = 0$, Leg 1)

F.4.3 Lower guide node displacements time-domain

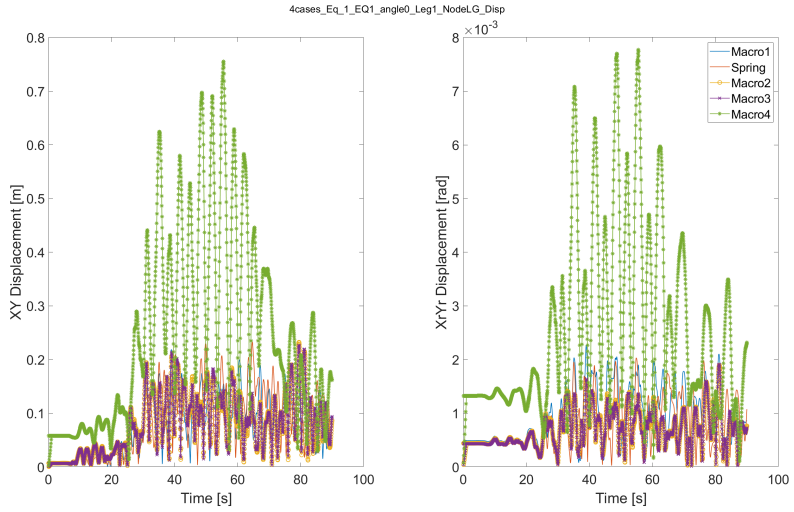

Figure F.62: Lower guide displacements time-domain, 4 non-linear foundations, 1 linear foundation (Taiwan 100-yr EQ1, $\theta = 0$, Leg 1)

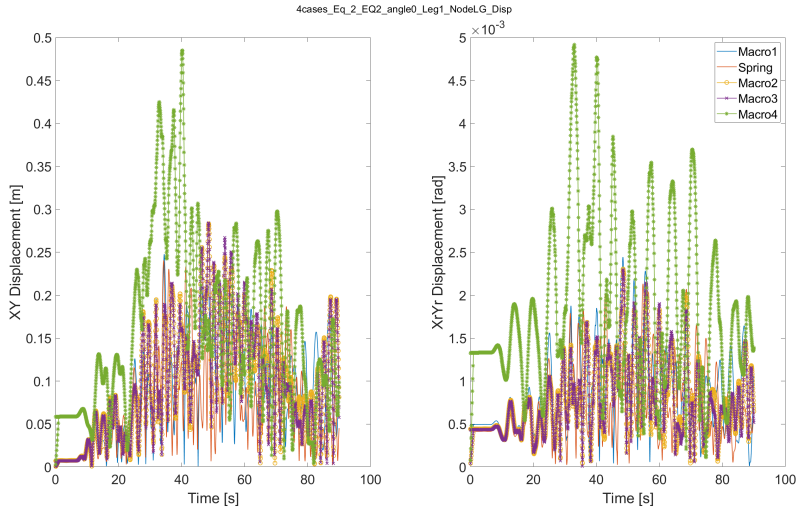

Figure F.63: Lower guide displacements time-domain, 4 non-linear foundations, 1 linear foundation (Taiwan 100-yr EQ2, $\theta = 0$, Leg 1)

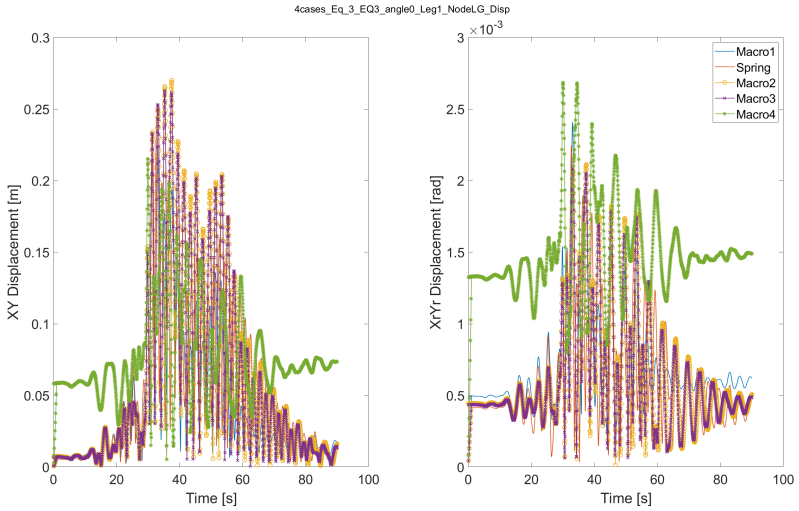

Figure F.64: Lower guide displacements time-domain, 4 non-linear foundations, 1 linear foundation (Taiwan 100-yr EQ3, $\theta = 0$, Leg 1)

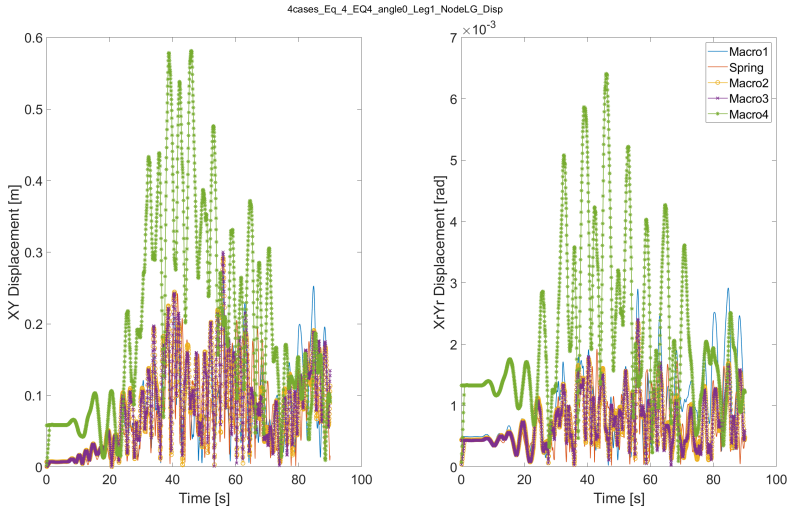

Figure F.65: Lower guide displacements time-domain, 4 non-linear foundations, 1 linear foundation (Taiwan 100-yr EQ4, $\theta = 0$, Leg 1)

F.4.4 Lower guide node loads time-domain

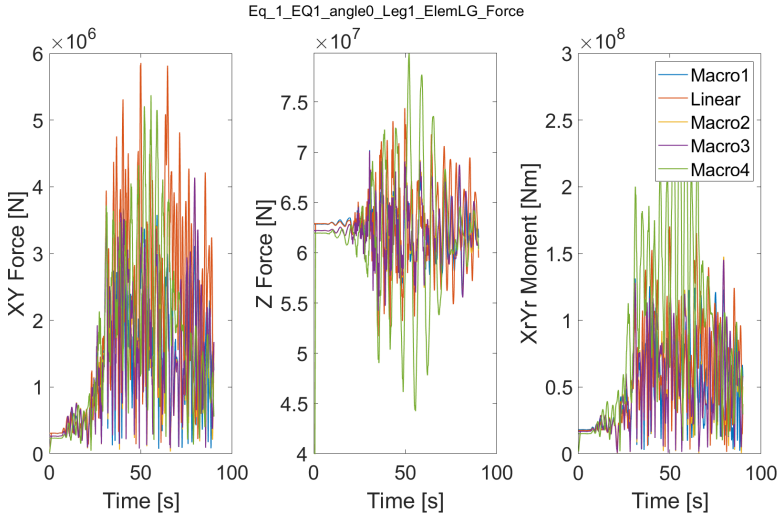

Figure F.66: Lower guide loads time-domain, 4 non-linear foundations, 1 linear foundation (Taiwan 100-yr EQ1, $\theta = 0$, Leg 1)

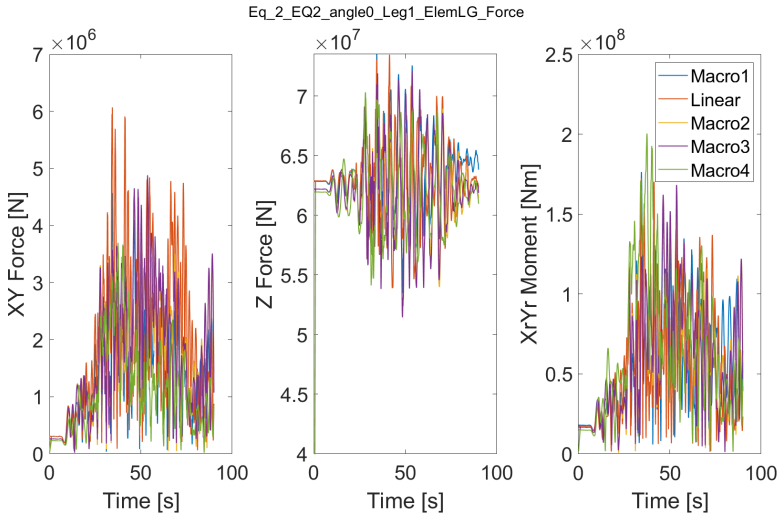

Figure F.67: Lower guide loads time-domain, 4 non-linear foundations, 1 linear foundation (Taiwan 100-yr EQ2, $\theta = 0$, Leg 1)

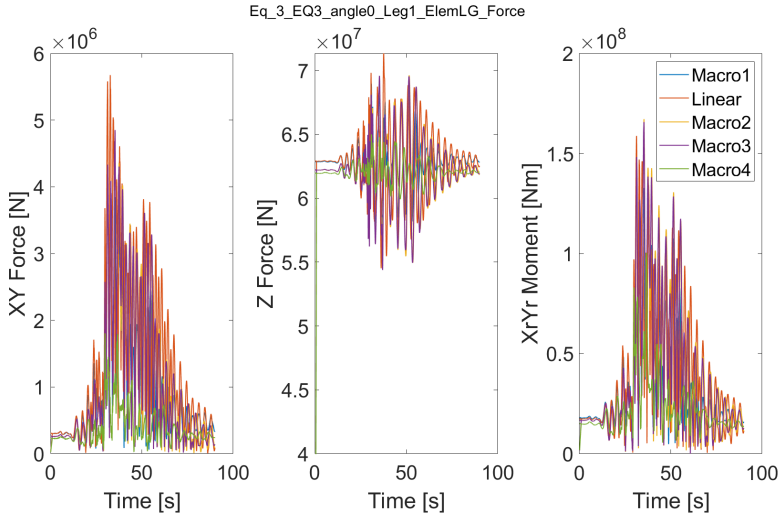

Figure F.68: Lower guide loads time-domain, 4 non-linear foundations, 1 linear foundation (Taiwan 100-yr EQ3, $\theta = 0$, Leg 1)

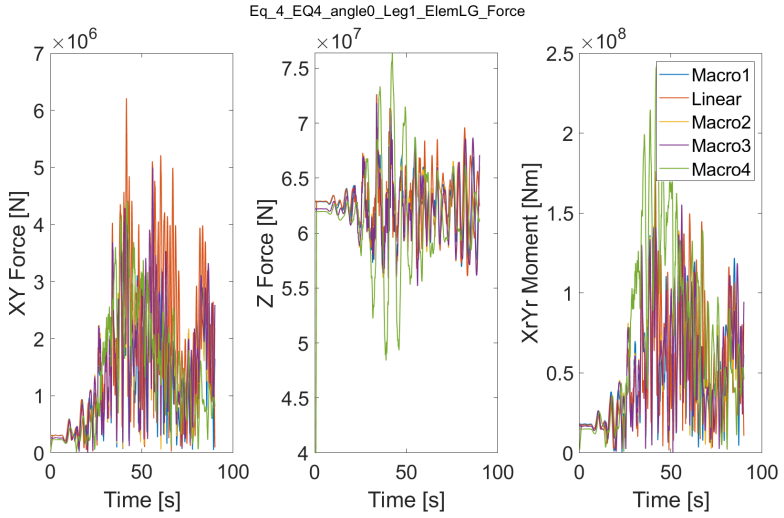

Figure F.69: Lower guide loads time-domain, 4 non-linear foundations, 1 linear foundation (Taiwan 100-yr EQ4, $\theta = 0$, Leg 1)

F.4.5 Macro-element force-displacement curves

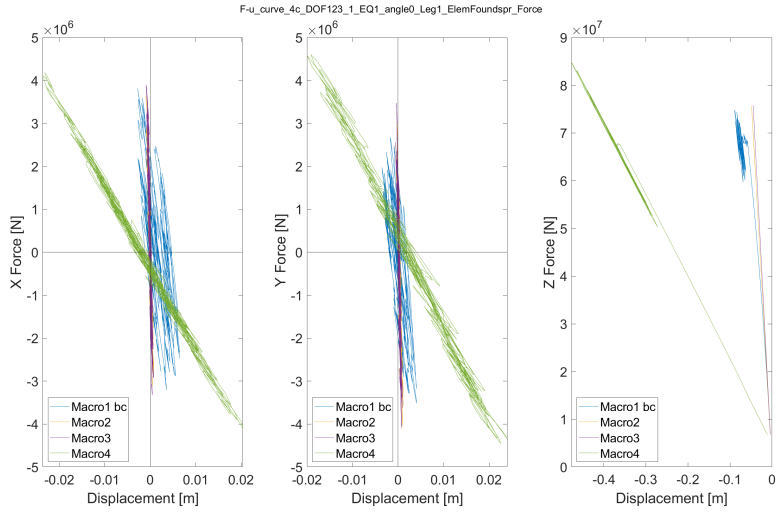

Figure F.70: F-u curve macro-element, 4 non-linear foundations (Taiwan 100-yr EQ1, $\theta = 0$, Leg 1)

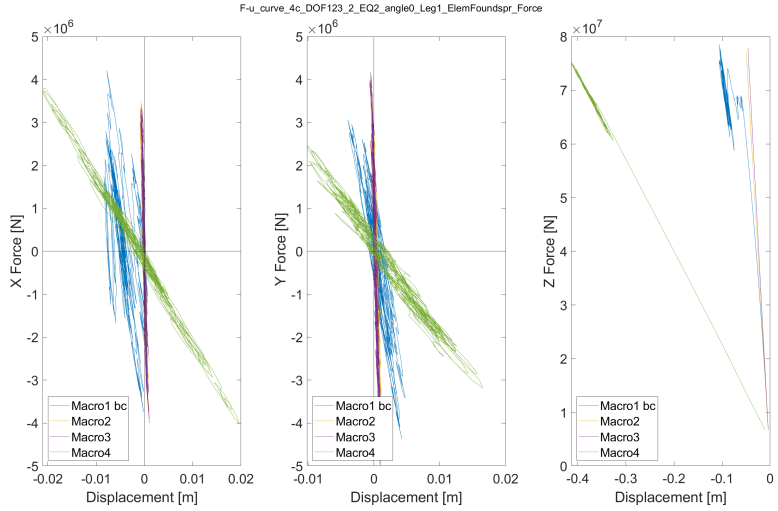

Figure F.71: F-u curve macro-element, 4 non-linear foundations (Taiwan 100-yr EQ2, $\theta = 0$, Leg 1)

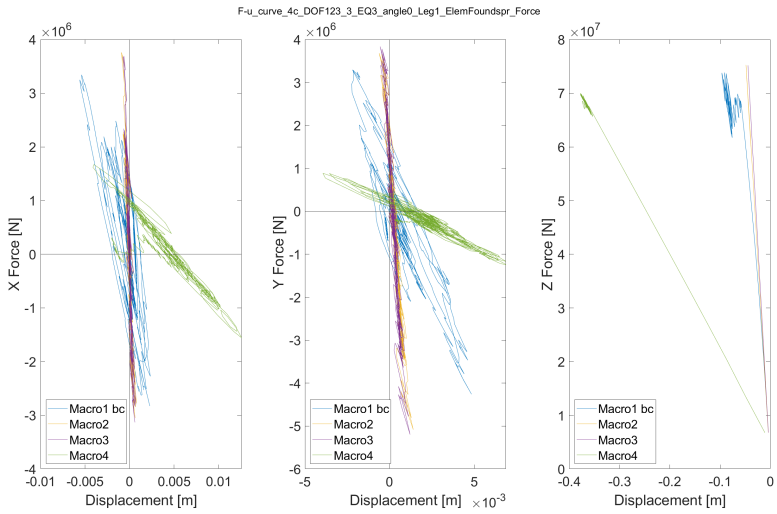

Figure F.72: F-u curve macro-element, 4 non-linear foundations (Taiwan 100-yr EQ3, $\theta = 0$, Leg 1)

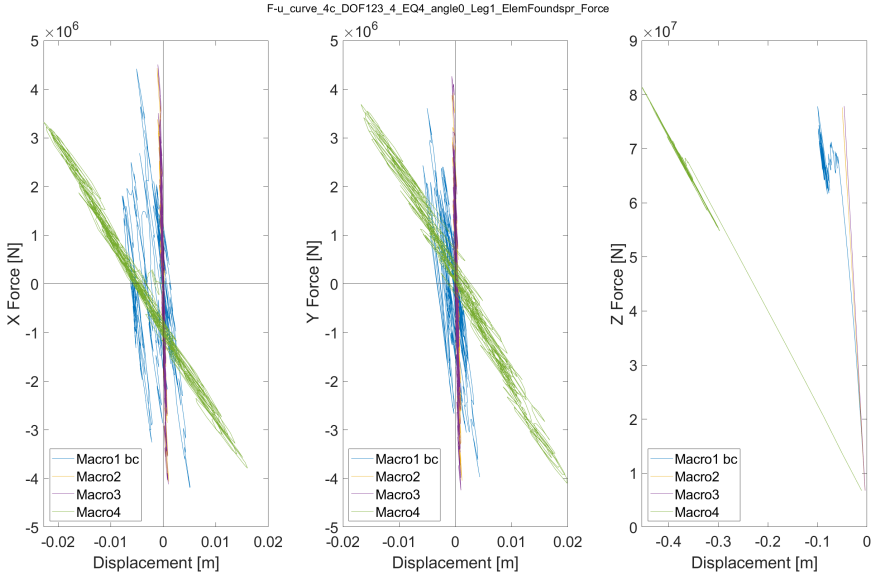

Figure F.73: F-u curve macro-element, 4 non-linear foundations (Taiwan 100-yr EQ4, $\theta = 0$, Leg 1)

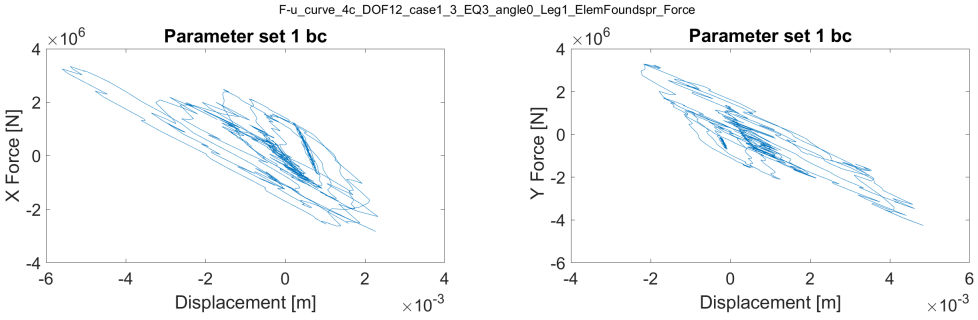

Figure F.74: F-u curve macro-element, case 1 (Taiwan 100-yr EQ3, $\theta = 0$, Leg 1)

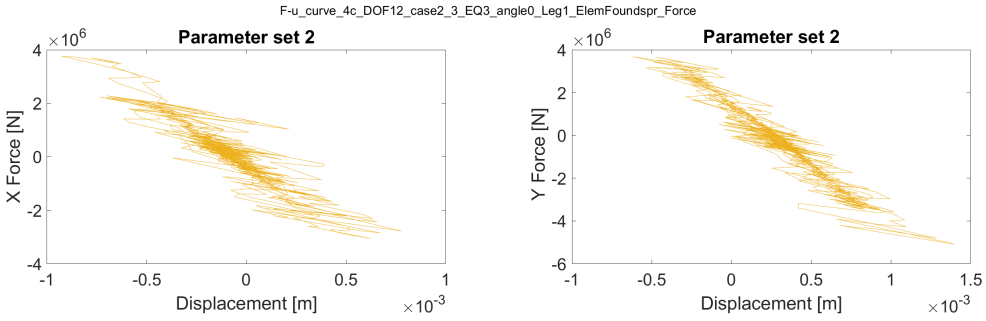

Figure F.75: F-u curve macro-element, case 2 (Taiwan 100-yr EQ3, $\theta = 0$, Leg 1)

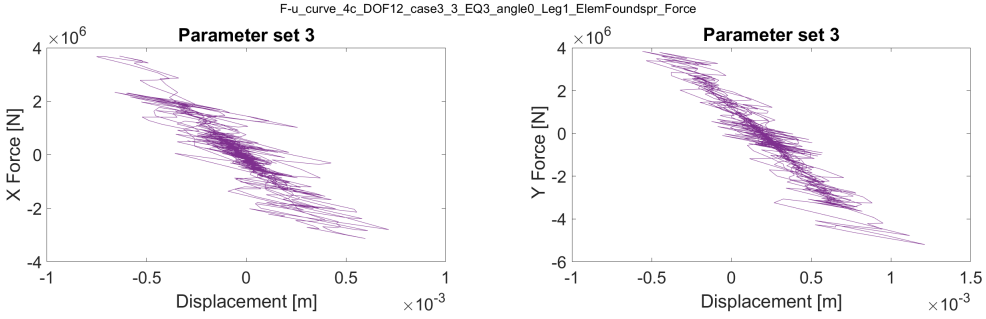

Figure F.76: F-u curve macro-element, case 3 (Taiwan 100-yr EQ3, $\theta = 0$, Leg 1)

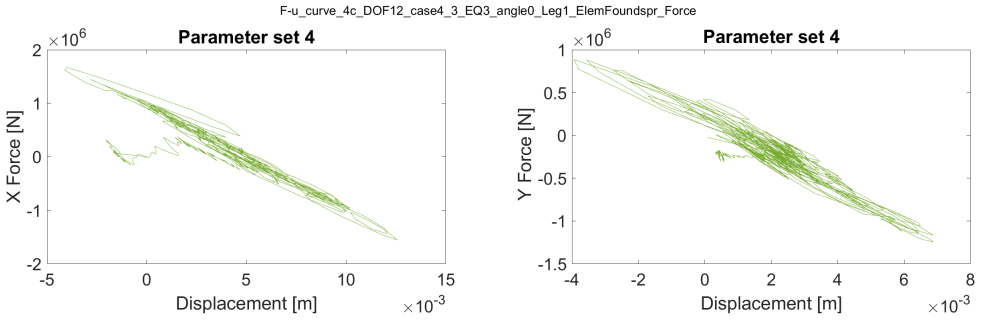

Figure F.77: F-u curve macro-element, case 4 (Taiwan 100-yr EQ3, $\theta = 0$, Leg 1)

F.4.6 Macro-element load state compared to yield surface

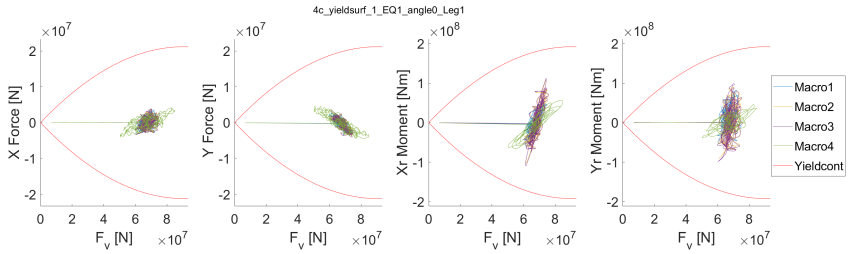

Figure F.78: Macro-element load state compared to yield surface, 4 non-linear foundations (Taiwan 100-yr EQ1, $\theta = 0$, Leg 1)

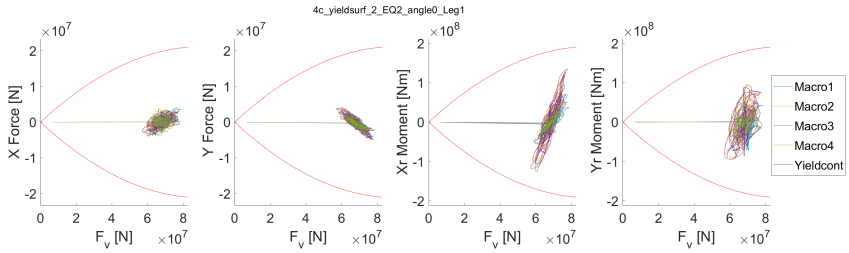

Figure F.79: Macro-element load state compared to yield surface, 4 non-linear foundations (Taiwan 100-yr EQ2, $\theta = 0$, Leg 1)

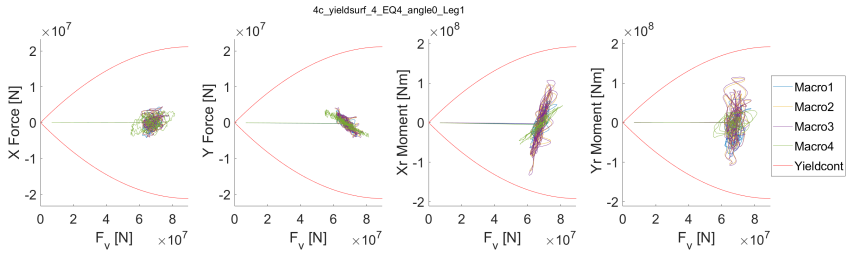

Figure F.80: Macro-element load state compared to yield surface, 4 non-linear foundations (Taiwan 100-yr EQ4, $\theta = 0$, Leg 1)

F.5 Sensitivity study

F.5.1 Footing node displacement timedomain

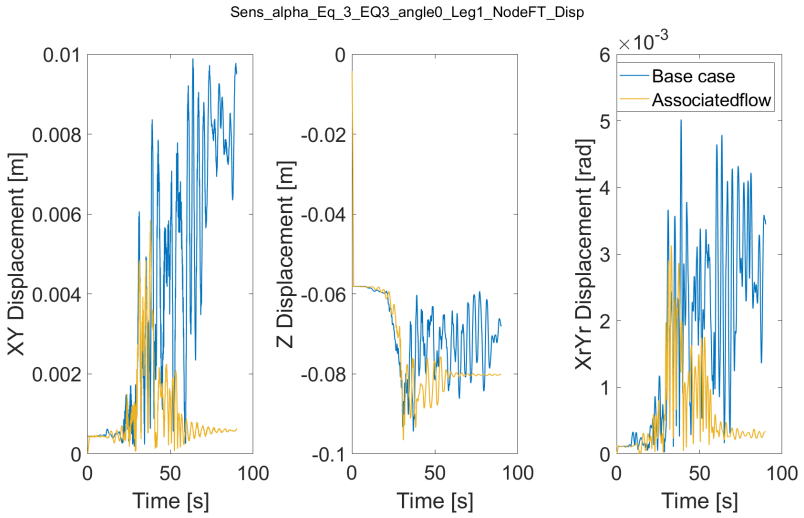

Figure F.81: Time-domain response of footing node displacement. Comparison of associated flow and α-values as defined in Grange et al. [13]. (Taiwan 100-yr EQ3, $\theta = 0$, Leg 1)

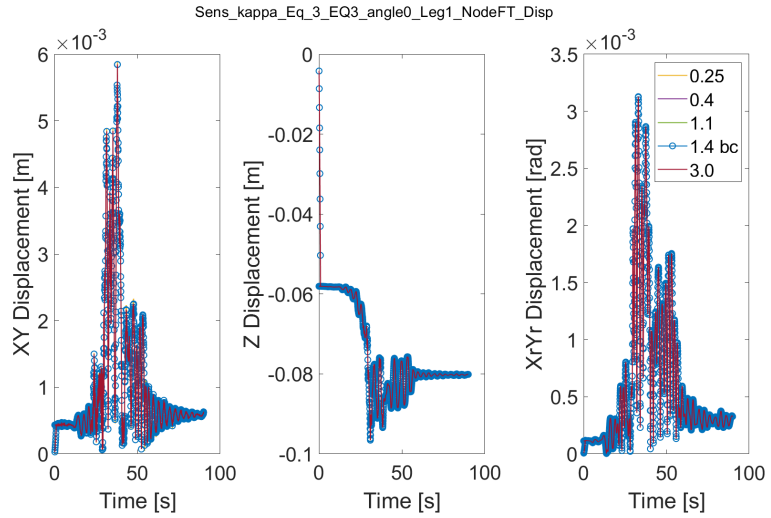

Figure F.82: Time-domain response of footing node displacement. Comparison of κ-values (Taiwan 100-yr EQ3, $\theta = 0$, Leg 1).

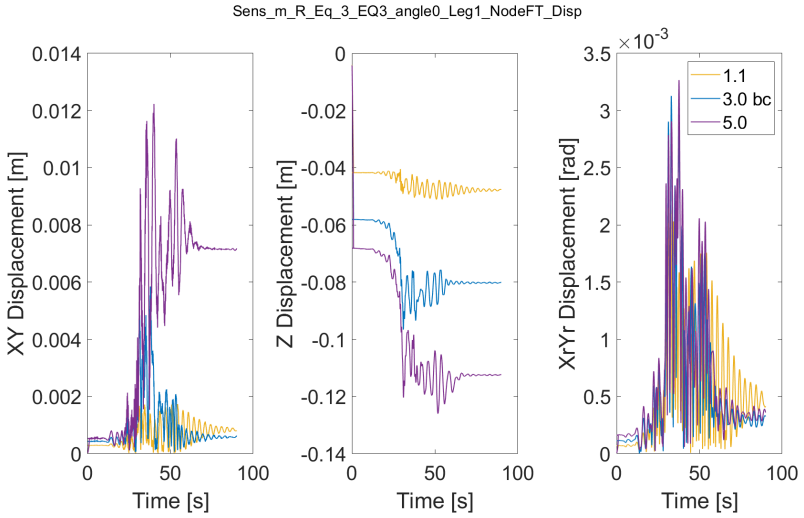

Figure F.83: Time-domain response of footing node displacement. Comparison of m_R-values (Taiwan 100-yr EQ3, $\theta = 0$, Leg 1).

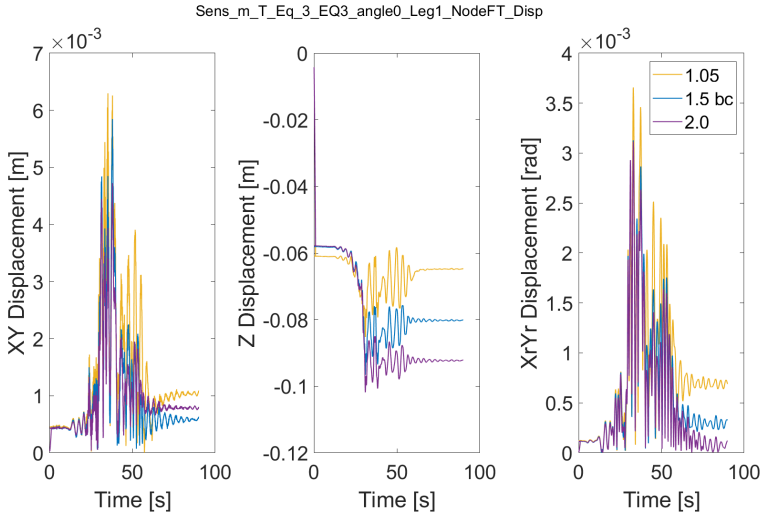

Figure F.84: Time-domain response of footing node displacement. Comparison of m_T-values (Taiwan 100-yr EQ3, $\theta = 0$, Leg 1).

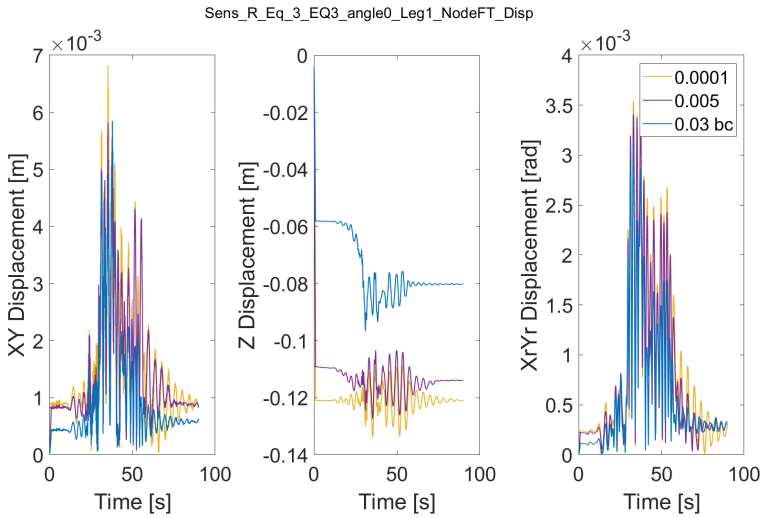

Figure F.85: Time-domain response of footing node displacement. Comparison of R-values (Taiwan 100-yr EQ3, $\theta = 0$, Leg 1).

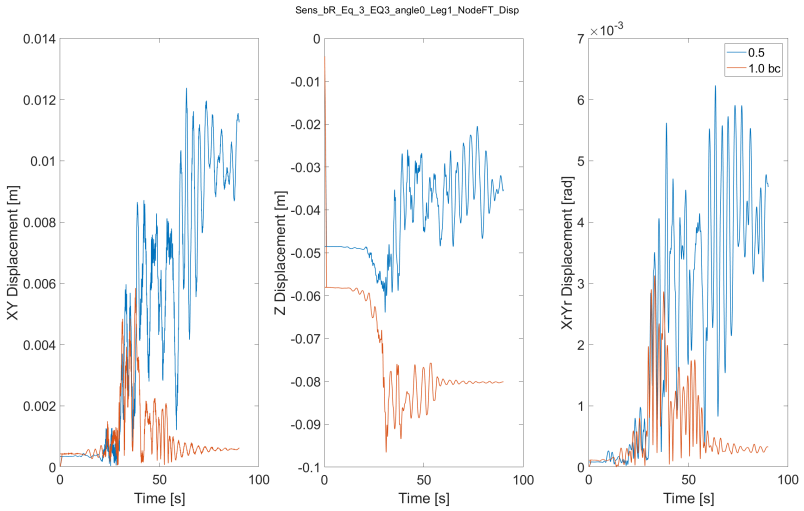

Figure F.86: Time-domain response of footing node displacement. Comparison of β_R-values (Taiwan 100-yr EQ3, $\theta = 0$, Leg 1).

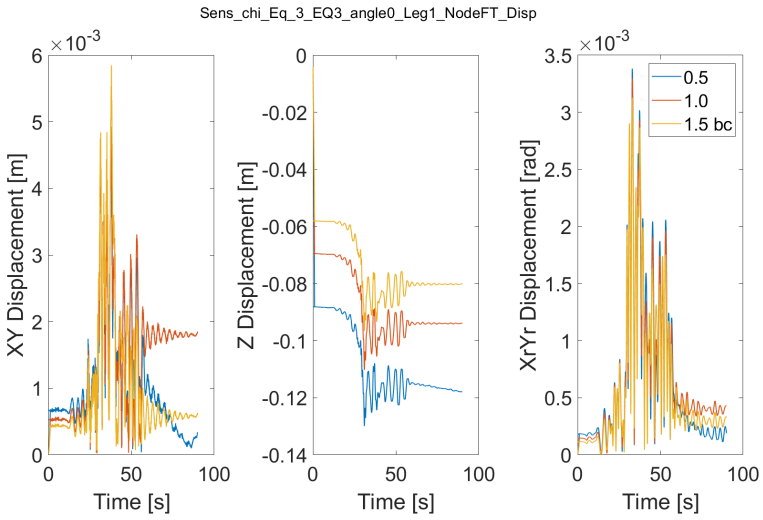

Figure F.87: Time-domain response of footing node displacement. Comparison of χ-values (Taiwan 100-yr EQ3, $\theta = 0$, Leg 1).

F.5.2 Maximum lower guide loads

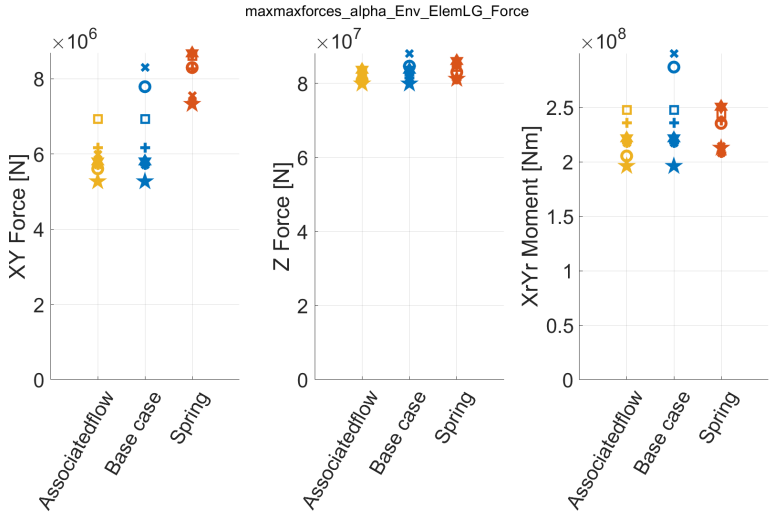

Figure F.88: Maximum lower guide loads for all orientations and legs, plotted per earthquake and varying plastic potential

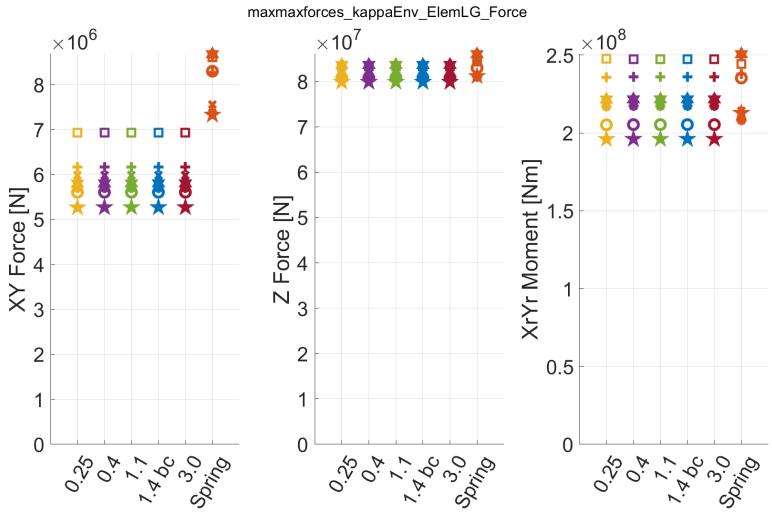

Figure F.89: Maximum lower guide loads for all orientations and legs, plotted per earthquake and varying κ

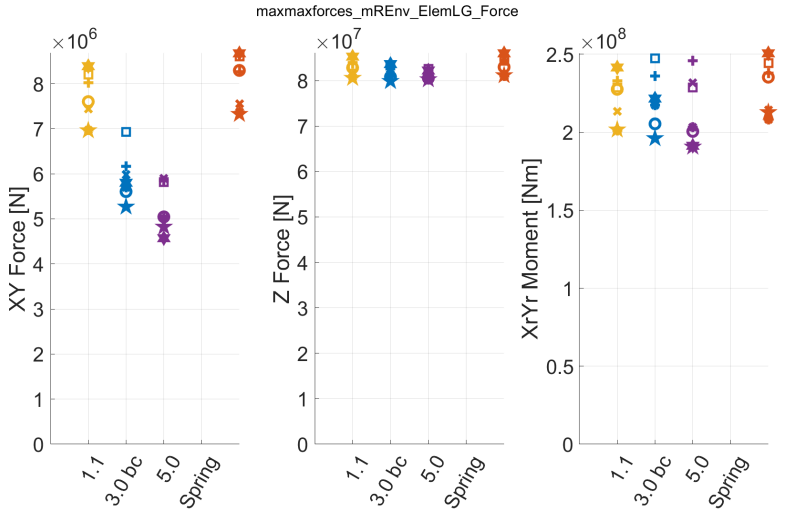

Figure F.90: Maximum lower guide loads for all orientations and legs, plotted per earthquake and varying m_R

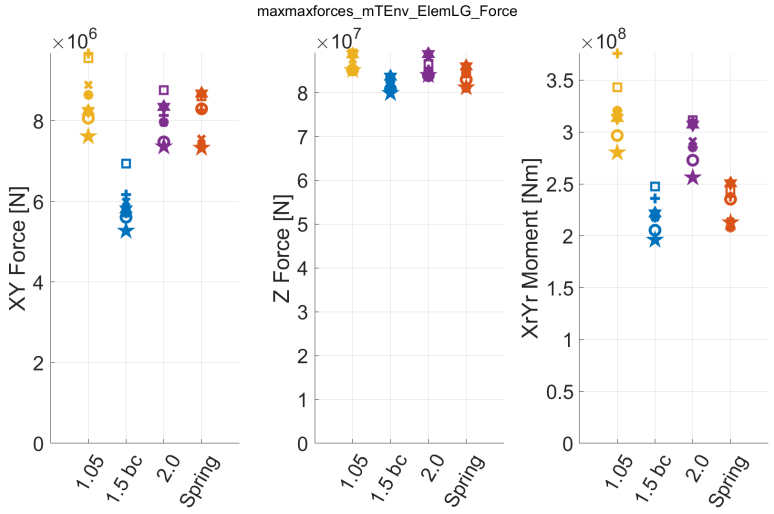

Figure F.91: Maximum lower guide loads for all orientations and legs, plotted per earthquake and varying m_T

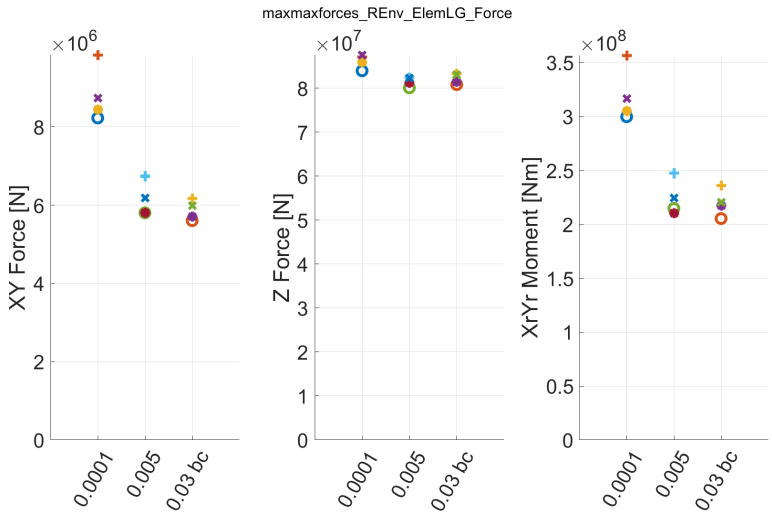

Figure F.92: Maximum lower guide loads for all orientations and legs, plotted per earthquake and varying R

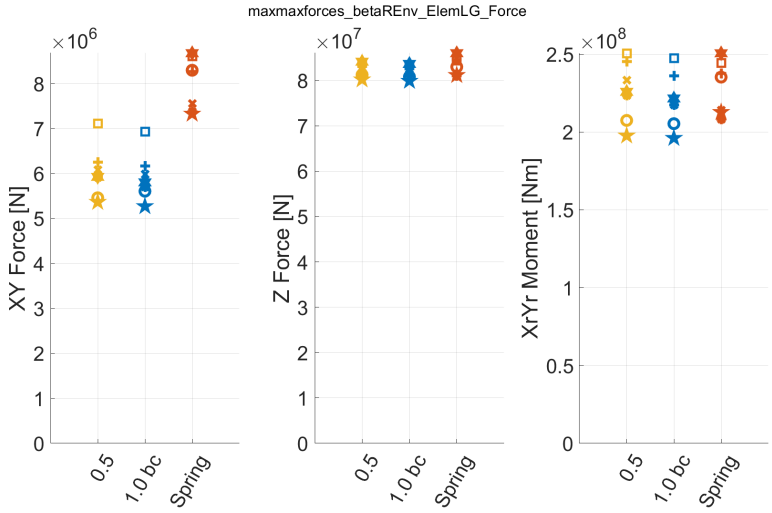

Figure F.93: Maximum lower guide loads for all orientations and legs, plotted per earthquake and varying β_R

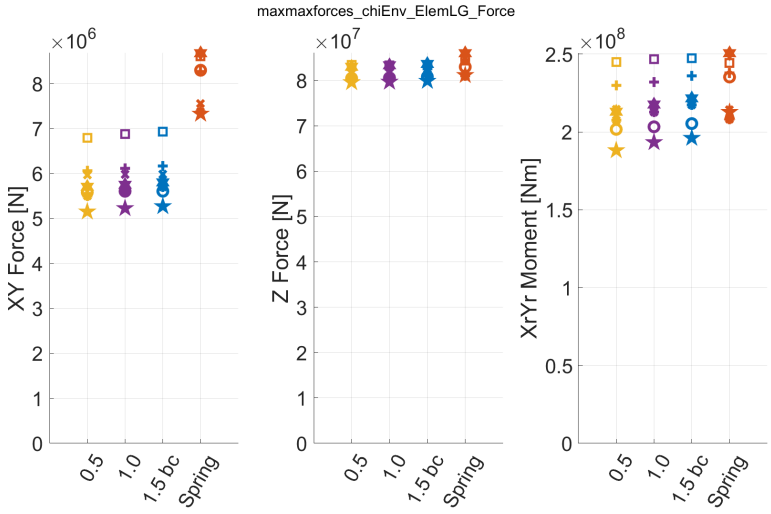

Figure F.94: Maximum lower guide loads for all orientations and legs, plotted per earthquake and varying *chi*

Appendix G

Other

G.1 Mode shapes

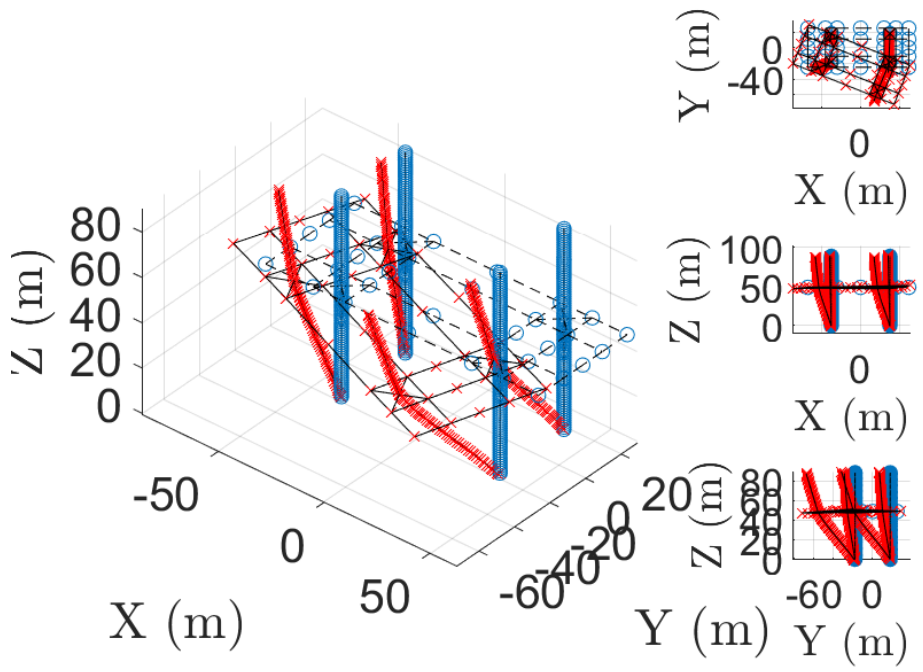

Figure G.1: Mode shape of mode 1 for parameter set D.4

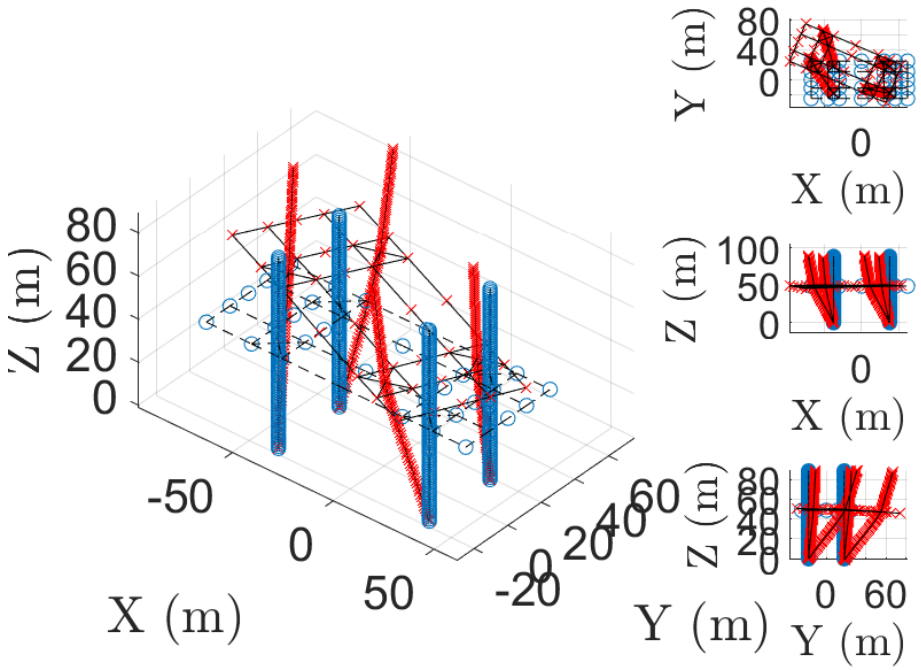

Figure G.2: Mode shape of mode 2 for parameter set D.4

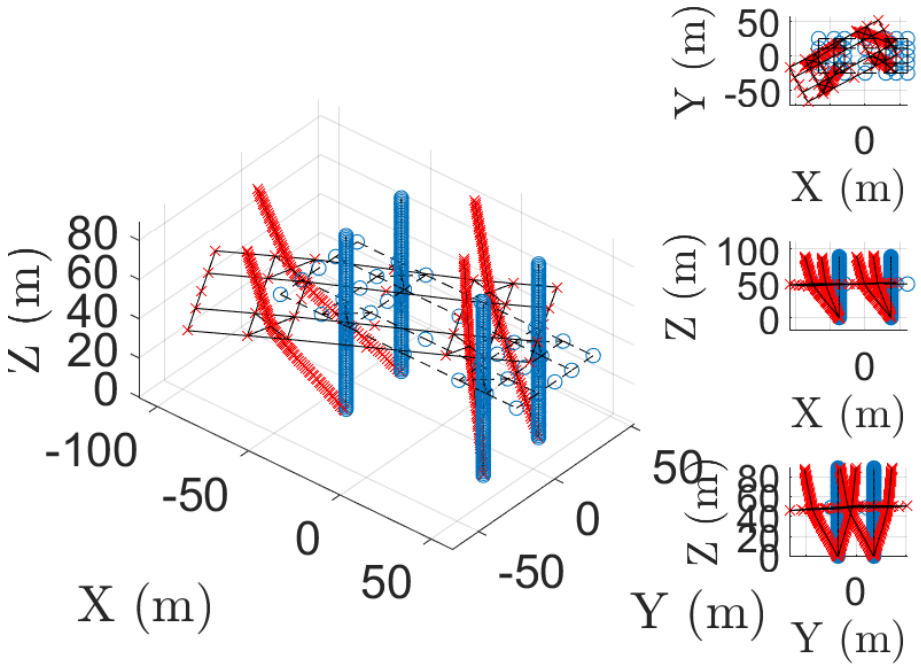

Figure G.3: Mode shape of mode 3 for parameter set D.4

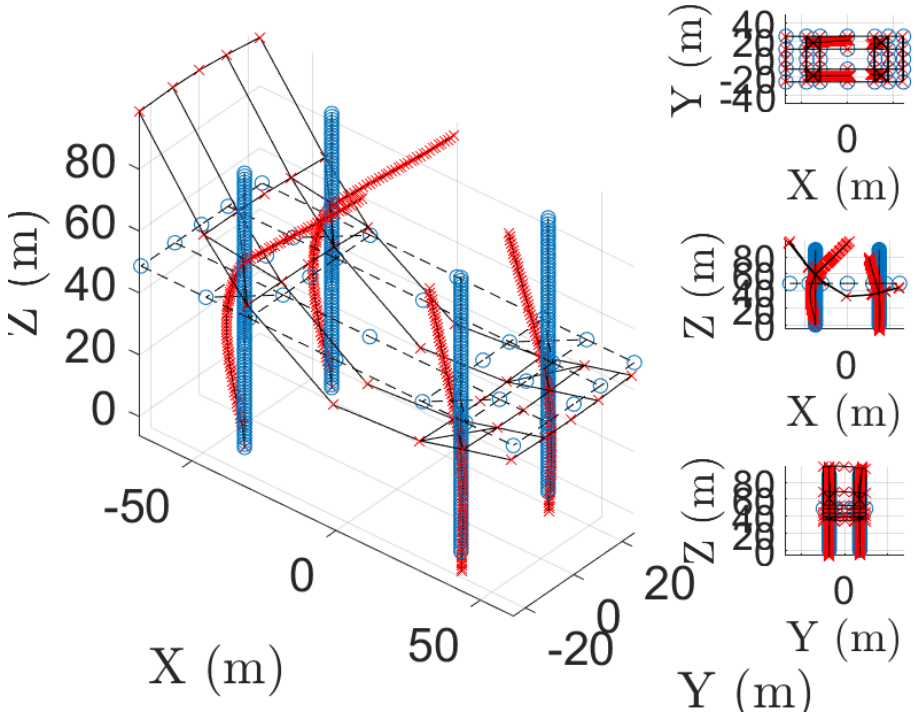

Figure G.4: Mode shape of mode 4 for parameter set D.4

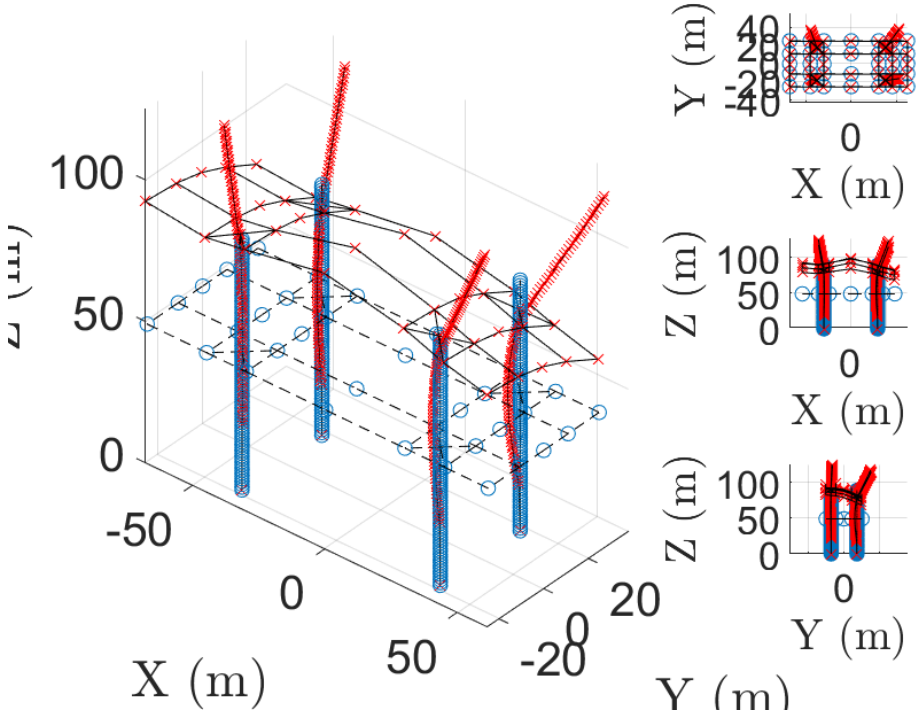

Figure G.5: Mode shape of mode 5 for parameter set D.4

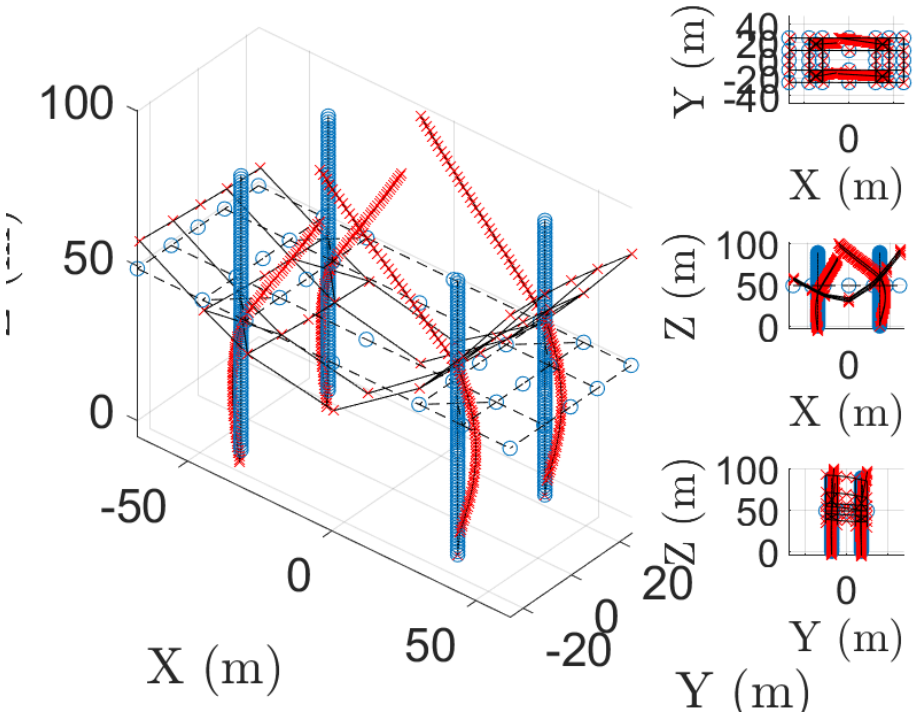

Figure G.6: Mode shape of mode 6 for parameter set D.4

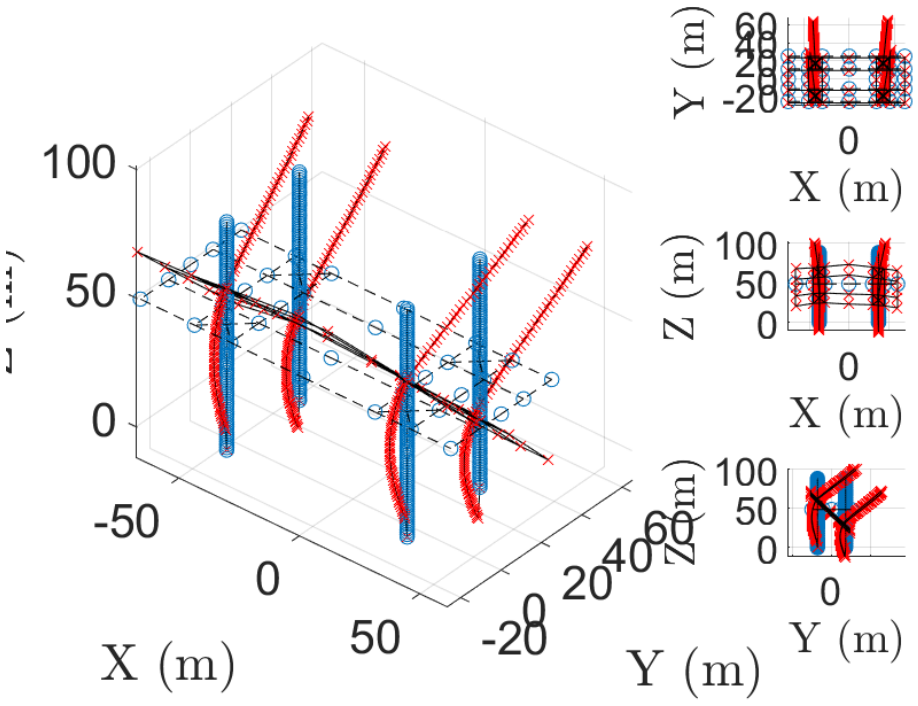

Figure G.7: Mode shape of mode 7 for parameter set D.4

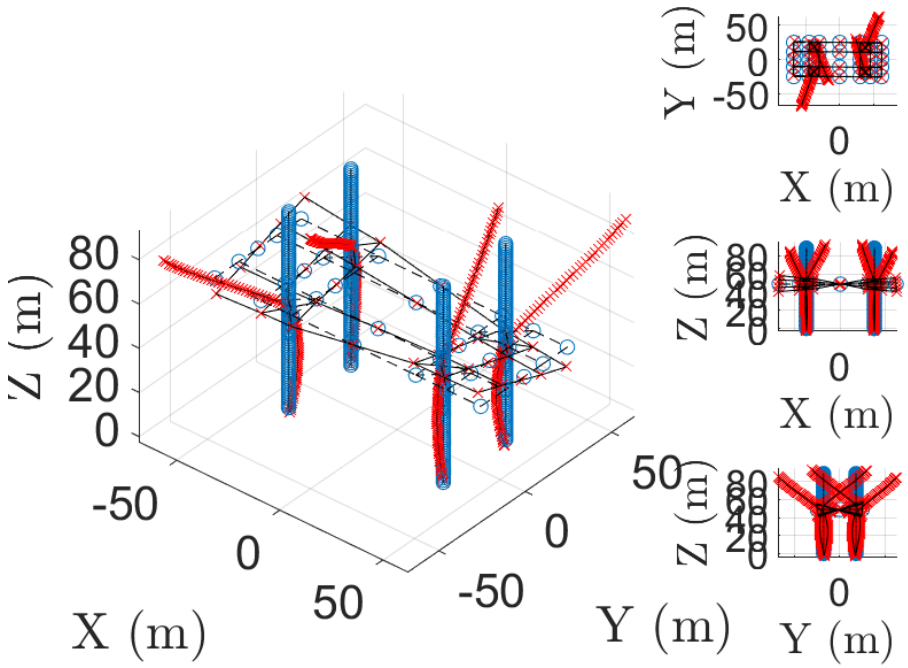

Figure G.8: Mode shape of mode 8 for parameter set D.4

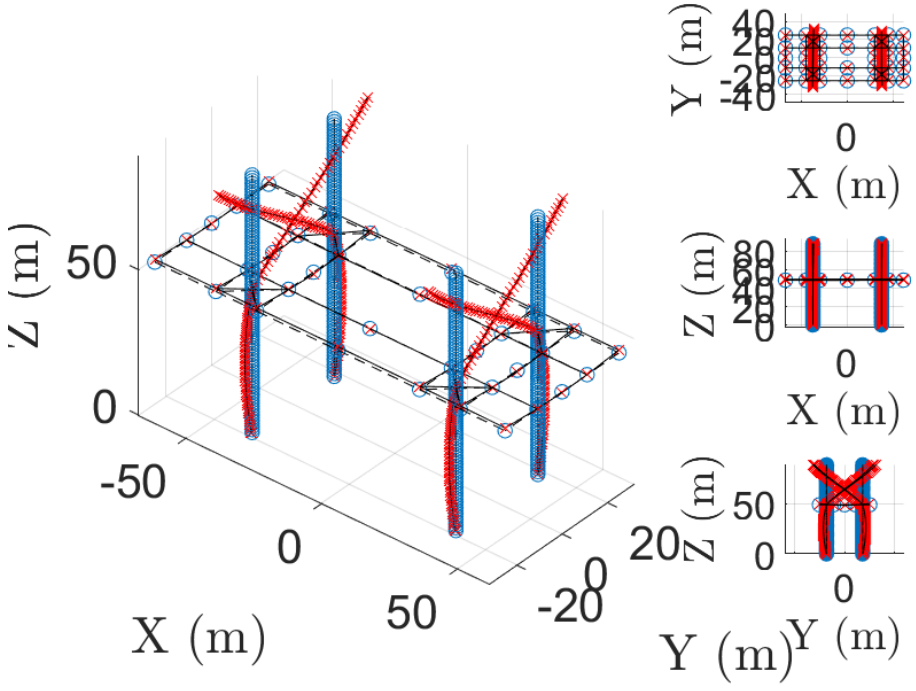

Figure G.9: Mode shape of mode 9 for parameter set D.4

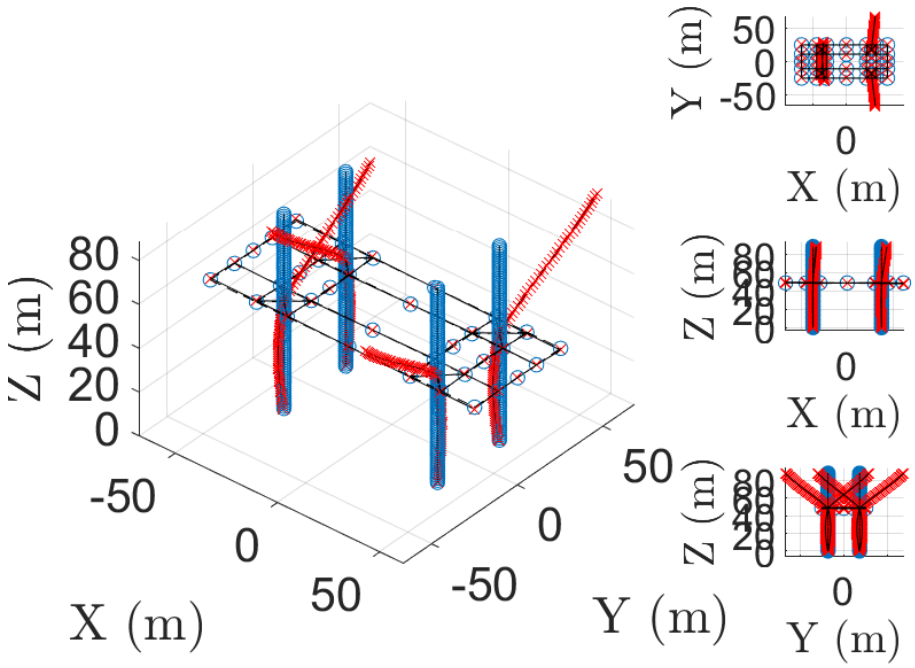

Figure G.10: Mode shape of mode 10 for parameter set D.4

G.2 Software architecture

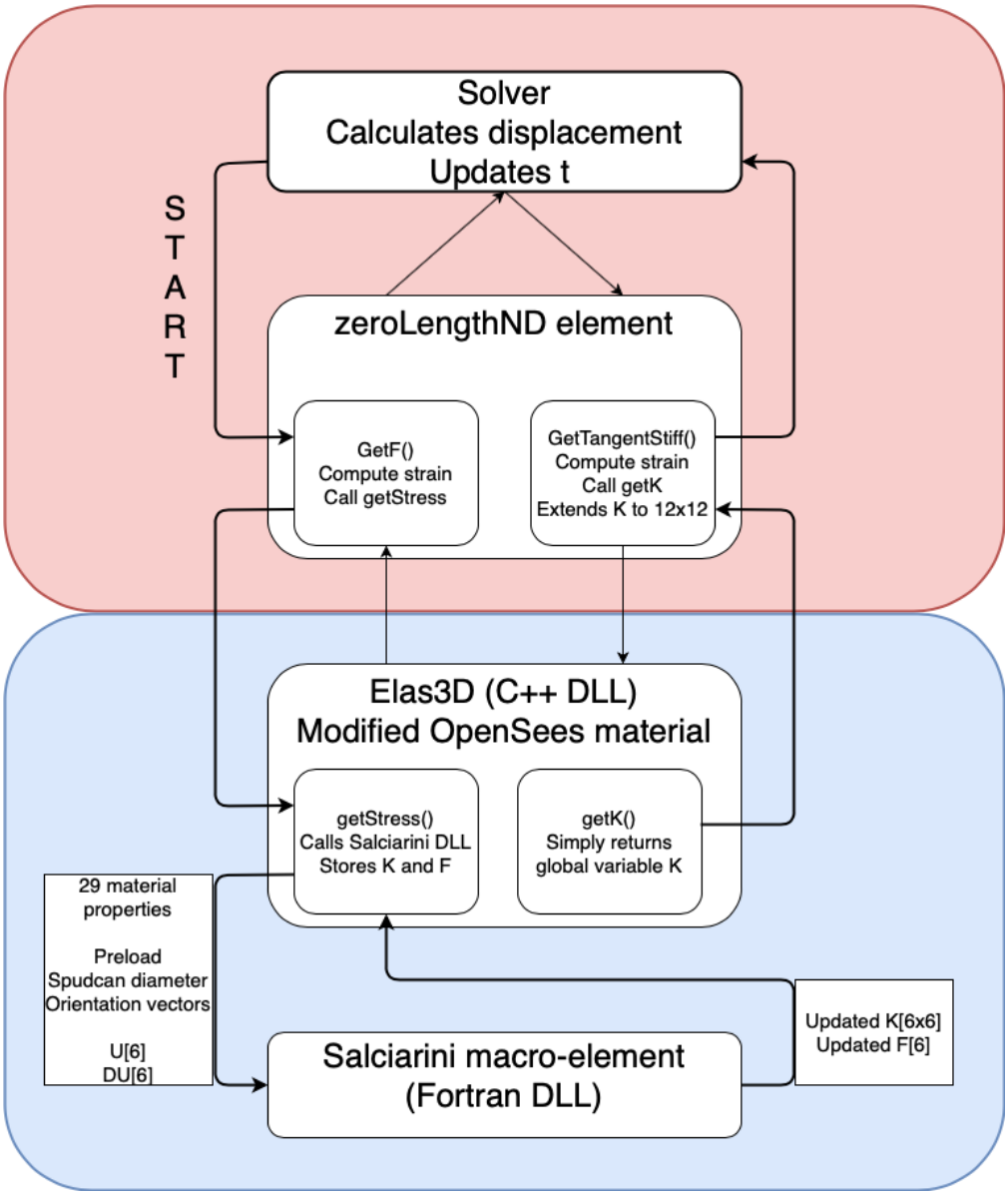

Figure G.11: Flow chart describing the implementation of the hypo-plastic macro-element. In red, the OpenSees main program. In blue, the DLL created in this research.

Bibliography

[1] K. H. Andersen. Cyclic soil parameters for offshore foundation design. *Frontiers in Offshore Geotechnics III - Proceedings of the 3rd International Symposium on Frontiers in Offshore Geotechnics, ISFOG 2015*, 2009.

[2] K. H. Andersen and T. Berre. Behavior of dense sand under monotonic and cyclic loading. 1999.

[3] M. Cassidy and B. Bienen. Three-dimensional numerical analysis of jack-up structures on sand. 05 2002.

[4] M. Cassidy, B. Byrne, and G. Houlsby. Modelling the behaviour of circular footings under combined loading on loose carbonate sand. *Geotechnique*, 52(10):705 – 712, 2002. ISSN 0016-8505. doi: 10.1680/geot.52.10.705.38846.

[5] M. Cassidy, B. Byrne, and G. Houlsby. Investigating six-degree-of-freedom loading of shallow foundation on sand. *Géotechnique*, 56:367–379, 01 2006. doi: 10.1680/geot.2006.56.6.367.

[6] M. J. Cassidy, C. M. Martin, and G. T. Houlsby. Development and application of force resultant models describing jack-up foundation behaviour. *Marine Structures*, 2004.

[7] C. Chatzigogos, A. Pecker, and J. Salençon. Macroelement modeling of shallow foundations. *Soil Dynamics and Earthquake Engineering*, 29(5):765 – 781, 2009. ISSN 0267-7261. doi: https://doi.org/10.1016/j.soildyn.2008.08.009. URL `http://www.sciencedirect.com/science/article/pii/S0267726108001383`.

[8] L. P. D.C.F., J. M., P. O., and C. A. Rate and creep effect on the stiffness of soils. *Measuring and modeling time dependent soil behavior*, (61), 1996.

[9] C. G. Di Prisco, R. Nova, and S. A. Shallow footing under cyclic loading: experimental behaviour and constitutive modelling. *Geotechnical analysis of seismic vulnerability of historical monuments*, 117, 2003. doi: http://hdl.handle.net/11311/508741.

[10] A. Durakovic. Taiwan floats plan to add 10gw more offshore wind by 2035. `https://www.offshorewind.biz/2019/11/12/taiwan-floats-plan-to-add-10gw-more-offshore-wind-by-2035/`. Accessed: 2019-09-30.

[11] G. Gazetas. *Foundation Vibrations*, pages 553–593. Springer US, 1991. ISBN 978-1-4615-3928-5. doi: 10.1007/978-1-4615-3928-5_15. URL `https://doi.org/10.1007/978-1-4615-3928-5_15`.

[12] G. Gazetas. Formulas and charts for impedances of surface and embedded foundations. *Journal of Geotechnical Engineering*, 117, 09 1991. doi: 10.1061/(ASCE)0733-9410(1991)117:9(1363).

[13] S. Grange, D. Salciarini, P. Kotronis, and C. Tamagnini. A comparison of different approaches for the modelling of shallow foundations in seismic soil-structure interaction problems. 06 2010. doi: 10.1201/b10551-75.

[14] G. Houlsby and C. Martin. Combined loading of spudcan foundations on clay: Laboratory tests. *Geotechnique*, 50:325–338, 01 2000. doi: 10.1680/geot.2000.50.4.325.

[15] G. Houlsby and C. Martin. Combined loading of spudcan foundations on clay: Numerical modelling. *Geotechnique*, 51:687–699, 01 2001. doi: 10.1680/geot.2001.51.8.687.

[16] International Association of Oil Gas Producers. Iso19902: Worldwide offshore seismic hazard maps. 2018.

[17] International Organization for Standardization. ISO19902:2007: Petroleum and natural gas industries fixed steel offshore structures. 2007.

[18] International Organization for Standardization. ISO 19901-2: Petroleum and natural gas industries — Specific requirements for offshore structures — Part 2: Seismic design procedures and criteria. 2015.

[19] International Organization for Standardization. ISO 19905-1: Petroleum and natural gas industries — Site-specific assessment of mobile offshore units — Part 1: Jack-ups. 2016.

[20] W. D. Iwan. On a Class of Models for the Yielding Behavior of Continuous and Composite Systems. *Journal of Applied Mechanics*, 34(3):612–617, 09 1967. doi: 10.1115/1.3607751. URL `https://doi.org/10.1115/1.3607751`.

[21] J. Jia. *Modern Earthquake Engineering for Offshore and Onland Structures*. 10 2015. ISBN 978-3-642-31853-5.

[22] J. Jia. *Soil Dynamics and Foundation Modeling*. Springer International Publishing AG, 2018. ISBN 978-3-319-40358-8.

[23] Z. Jin, Z.-Y. Yin, P. Kotronis, Z. Li, and C. Tamagnini. A hypoplastic macroelement model for a caisson foundation in sand under monotonic and cyclic loadings. *Marine Structures*, 66:16–26, 03 2019.

[24] A. Kaynia and K. Andersen. *Development of nonlinear foundation springs for dynamic analysis of platforms*, pages 1067–1072. 05 2015. ISBN 978-1-138-02848-7. doi: 10.1201/b18442-158.

[25] N. Lesgidis, A. Sextos, and O.-S. Kwon. A frequency-and intensity-dependent macroelement for reduced order seismic analysis of soil-structure interacting systems. *Earthquake Engineering Structural Dynamics*, 04 2018. doi: 10.1002/eqe.3063.

[26] Linklaters. Japan Offshore Wind: Approaching a Tipping Point. 2018. doi: https://www.linklaters.com/nl-nl/insights/publications/2018/october/japan-offshore-wind.

[27] J. Linthorst. Seismic analysis of cranes on Jack-Ups, 2019.

[28] Lysmer and Richart. Dynamic Response of Footings to Vertical Loading. *Journal of the Soil Mechanics and Foundations Division*, (92), 1966.

[29] C. Martin. "physical and numerical modelling of offshore foundations under combined loads". 1994.

[30] Z. Minjie. 4.13.5.25. viscous material. `https://opensees.berkeley.edu/wiki/index.php/Viscous_Material`, . Accessed: 2012-03-10.

[31] Z. Minjie. 4.2.1.1. zerolength element. `https://openseespydoc.readthedocs.io/en/latest/src/ZeroLength.html`, . Accessed: 2012-03-10.

[32] Z. Minjie. 4.2.1.2. zerolengthnd element. `https://openseespydoc.readthedocs.io/en/latest/src/zeroLengthND.html?highlight=zerolengthND`, . Accessed: 2012-03-10.

[33] Z. Mróz. On the description of anisotropic workhardening. *Journal of the Mechanics and Physics of Solids*, 15(3):163 – 175, 1967. ISSN 0022-5096. doi: https://doi.org/10.1016/0022-5096(67)90030-0. URL `http://www.sciencedirect.com/science/article/pii/0022509667900300`.

[34] R. Nova and L. Montrasio. Settlements of shallow foundations on sand. *Géotechnique*, 41(2):243–256, 1991. doi: 10.1680/geot.1991.41.2.243. URL `https://doi.org/10.1680/geot.1991.41.2.243`.

[35] D. Salciarini and C. Tamagnini. A hypoplastic macroelement model for shallow foundations under monotonic and cyclic loads. *Acta Geotechnica*, 4:163–176, 09 2009. doi: 10.1007/s11440-009-0087-2.

[36] D. Salciarini and C. Tamagnini. A hypoplastic macroelement for shallow foundations subject to six-dimensional loading paths. 04 2011.

[37] D. Salciarini and C. Tamagnini. Incorporating scale effects in shallow footings in a hypoplastic macroelement model. 06 2014. doi: 10.1201/b17017-72.

[38] K. Skau and H. Jostad. Application of the ngi-procedure for design of bucket foundations for offshore wind turbines. *Proceedings of the International Offshore and Polar Engineering Conference*, pages 189–198, 01 2014.

[39] K. Skau, Y. Chen, and H. Jostad. A numerical study of capacity and stiffness of circular skirted foundations in clay subjected to combined static and cyclic general loading, 03 2018.

[40] K. S. Skau, G. Grimstad, A. M. Page, G. R. Eiksund, and H. P. Jostad. A macro-element for integrated time domain analyses representing bucket foundations for offshore wind turbines. 2017.

[41] K. S. Skau, A. M. Page, A. M. Kaynia, F. Løvholt, K. Norén-Cosgriff, H. Sturm, H. S. Andersen, T. A. Nygard, H. P. Jostad, G. Eiksund, O. Havmøller, P. Strøm, and D. Eichler. Redwin - reducing cost of offshore wind by integrated structural and geotechnical design. 2018.

[42] C. Tamagnini, G. Viggiani, and R. Chambon. A review of two different approaches to hypoplasticity. 01 2000. doi: 10.1007/978-3-642-57018-6_5.

[43] C. Tamagnini, D. Salciarini, and R. Ragni. Implementation of a 6-dof hypoplastic macroelement in a finite element code. 08 2013.

[44] J. Templeton. Jackup Foundation Performance in Clay. *Proceedings 25th Offshore Technology Conference, Houston, OTC 18367*, 2006.

[45] J. M. T. Thompson, B. W. Byrne, and G. T. Houlsby. Foundations for offshore wind turbines. *Philosophical Transactions of the Royal Society of London. Series A: Mathematical, Physical and Engineering Sciences*, 361(1813):2909–2930, 2003. doi: 10.1098/rsta.2003.1286. URL `https://royalsocietypublishing.org/doi/abs/10.1098/rsta.2003.1286`.

[46] H. Van Langen, P. Wong, and E. Dean. Formulation and Validation of a Theoretical Model for Jack-up Foundation Load-Displacement Assessment. *Proceedings 6th International Conference on the Jack[U+2010]up Platform – Design, Construction and Operation, London*, 1997.

[47] M. Vucetic. Soil properties and seismic response. *Proceedings of the 10th world conference on earthquake engineering, Rotterdam*, 1992.

[48] P. Wong, J. Chao, J. Murff, E. Dean, R. James, A. Schofield, and Y. Tsukamoto. Jack-up Rig Foundation Modeling II. *Proceedings 25th Offshore Technology Conference, Houston, OTC 7303*, 1993.